



Graphene Paper Based Nanomaterials for Electrochemical Sensing and Energy Conversion

Zhang, Minwei

Publication date:
2016

Document Version
Publisher's PDF, also known as Version of record

[Link back to DTU Orbit](#)

Citation (APA):
Zhang, M. (2016). *Graphene Paper Based Nanomaterials for Electrochemical Sensing and Energy Conversion*. Technical University of Denmark.

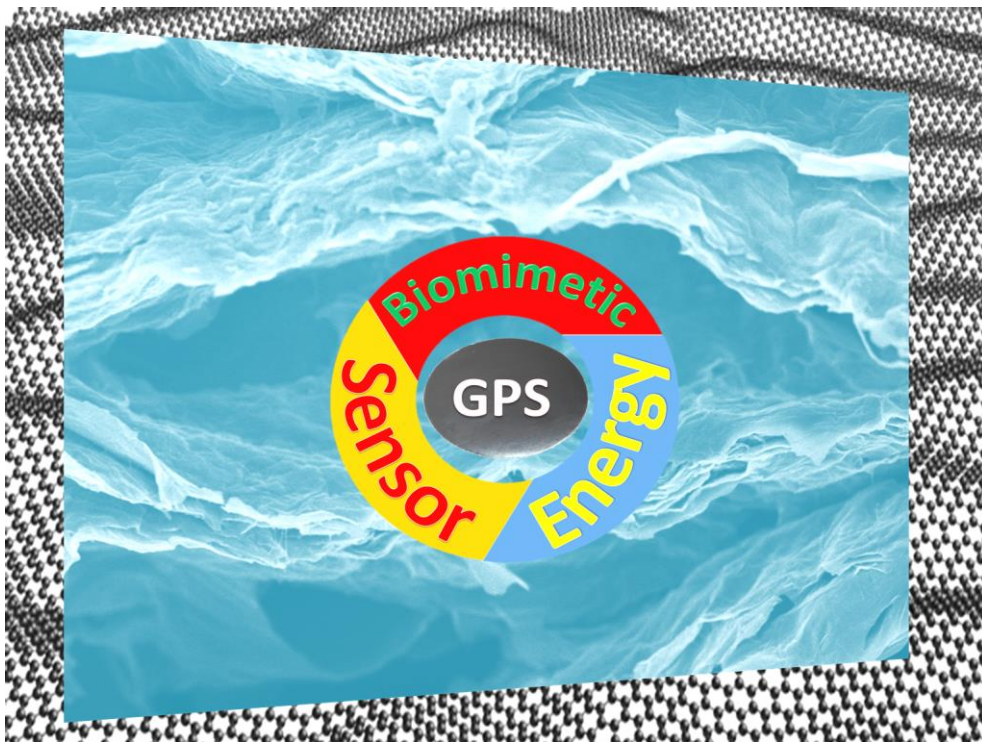
General rights

Copyright and moral rights for the publications made accessible in the public portal are retained by the authors and/or other copyright owners and it is a condition of accessing publications that users recognise and abide by the legal requirements associated with these rights.

- Users may download and print one copy of any publication from the public portal for the purpose of private study or research.
- You may not further distribute the material or use it for any profit-making activity or commercial gain
- You may freely distribute the URL identifying the publication in the public portal

If you believe that this document breaches copyright please contact us providing details, and we will remove access to the work immediately and investigate your claim.

Graphene Paper Based Nanomaterials for Electrochemical Sensing and Energy Conversion



Minwei Zhang

Ph.D thesis

Department of chemistry

Technical University of Denmark

December 2016



Technical University of Denmark

**Graphene Paper based Nanomaterials for
Electrochemical Sensing and Energy Conversion**

Minwei Zhang

Ph.D thesis

Department of Chemistry

Technical University of Denmark

December 2016

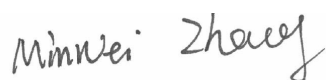
Preface and acknowledgements

This thesis is submitted in candidacy for a Ph.D degree from Technical University of Denmark (DTU). The Ph.D project was carried out in the Nanochemistry Group at DTU Chemistry with Associate Professor Qijin Chi as a principal supervisor and Professor Jens Ulstrup as a co-supervisor. We acknowledge the financial support by the Danish Research Council for Technology and Product Science, the CSC PhD scholarship, and DTU Chemistry.

Frist of all, I would like to express my intensive appreciation to my two supervisors Qijin Chi and Jens Ulstrup for their highly inspirational guidance and willingness to share their knowledge and expertise in all aspects. They give me the best possible starting point for fulfilling my PhD project and opportunities to interact with the scientific communities and to attend international conferences. I am grateful to all group members at the NanoChemistry Group for their support as well as creating a friendly and active scientific atmosphere, especially Professor Jingdong Zhang, Dr. Chengyi Hou, Dr. Christian Engelbrekt, Dr. Michal Wagner, Dr. Gunnar Olsen, Ph.D students Arnab Halder and Nedjeljko Seselj for their helps and collaborations in both taking courses and laboratory research. I should thank many people at DTU, particularly at Department of Chemistry. For example, laboratory technicians Bodil F. Holten, Lise-Lotte Jespersen and Martin Hasling Pedersen for their effective helps. I also greatly appreciate the strong support and assistance from DTU Danchip and DTU Centre of Electron Nanoscopy for XPS, SEM and TEM measurements.

Finally, I want to thank my parents for their tremendous support and understanding throughout all years for my pursuit of high educations. I sincerely thank my wife Yanan Qin for her consistent support and encouragement during the PhD study.

Sincerely



Minwei Zhang

Kongens Lyngby, Denmark.

December 2016

Abstract

Graphene has emerged as a highly interesting material since it was experimentally isolated for *the first time* in 2004. This single-atom-thick nanosheet consisting of carbon atoms arrayed in a honeycomb pattern, displays outstanding physicochemical properties, including as an excellent conductor of heat and electricity, large specific surface area, and high mechanical strength. Therefore, graphene based materials are expected to have great potential for use in the fields of sensors, catalysis, and as electrode materials for energy storage and conversion. In order to link practical applications of graphene-based materials to real world, graphene nanosheets must be assembled into macroscopic architecture with desired structures and functionality. To this end, graphene oxide (GO) is a very useful building block because it contains a significant number of oxygen-containing groups on the planar surface and at the edges. These functional groups offer various possibilities for functionalization and assembly of GO nanosheets into 2D graphene films, papers or membranes with controlled macroscopic shapes. Resulting 2D graphene films/papers/membranes can be used as ideal scaffolds for the further incorporation of functional materials with specific desired functionality. The advantages of light-weight, high flexibility, large specific surface area, tough mechanical strength, and high electrical conductivity ensure graphene-based architectures holding a wide range of applications particularly associated with sensor and energy technologies.

This PhD project is devoted to the synthesis, characterization and applications of graphene paper based nanomaterials for electrochemical sensors and energy conversion. The thesis is divided into three parts with 8 chapters in total. In Chapter 1, we provide an overview of the functional macroscopic graphene materials covering three key aspects: a) how to prepare 2D graphene films/papers, b) how to functionalize them with either polymers or other nanoscale objects, and c) what are their promising applications in the fields of molecular sieving purification, biomimetics, as flexible substrates, sensors and electrochemical energy devices. This is followed by an outline of the main experimental techniques and means used in the project (Chapter 2).

In Chapters 3-5, the focus is on graphene-*Prussian Blue* (PB) composite materials. GO or graphene paper was functionalized by PB nanostructures including nanoparticles and interlocked PB cubes. A wide range of advanced techniques such as XRD, XPS, TEM, and SEM were employed to characterize the nanocomposites. The nanocomposites were tested for the construction of high-performance, ultrasensitive and low-cost electrochemical sensors for detection of hydrogen peroxide (H₂O₂).

Graphene paper was finally explored as a sacrificial template for the synthesis of 2D ultra-fined nanostructured porous metal oxide (MO), as described in Chapters 6-8. In Chapter 6, we demonstrated that crystalline MO can be prepared by using GO papers as sacrificial templates, and furthermore layer-by-layer, nonporous and ultrathin 2D CuO nanosheets were assembled into flexible and ultralight papers as a photocathode used for photoelectrochemical catalysis of hydrogen evolution reaction. In Chapters 7 and 8, CuO-ZnO hybrid nanosheets and NiO nanosheets were synthesized, characterized and used in the fabrication of non-enzymatic electrochemical sensors for high-performance detection of glucose and urea, respectively.

Abstract in Danish

Grafen, en todimensional (2-D) sp^2 -hybridiseret type af kulstof, er blevet et af de mest interessante materialer, siden det blev opdaget i 2004. Denne enkelt-atom-tykke plade af kulstofatomer arrangeret i et bikubemønster udviser fremragende fysisk-kemiske egenskaber, nemlig fremragende ledningsevne for både varme og elektricitet og høj mekanisk styrke. Grafen udviser derfor stort potentiale til brug i sensorer, katalysatorer, elektroder, og i biologiske systemer m.v., og med videre udvikling af den teoretiske forståelse og praktiske anvendelse af grafen, vil dette materiale spille en væsentlig rolle for samfundet i moderne teknologi. Grafene-baserede materialer bør samles til makroskopiske arkitekturer med specifikke strukturelle og funktionelle egenskaber. En oxideret form af grafen, grafenoxid (GO), har en masse iltholdige funktionelle grupper, som giver mulighed for funktionalisering og konstruering af 2-D grafenfilm/papir/membraner med forskellige makroskala former gennem forskellige fabrikerings teknikker. Disse 2-D materialer kan anvendes som ideelle stilladser til indarbejdelse af andre funktionelle materialer for at opnå specifikke funktionaliteter. Fordelene ved lette, supra-fleksibilitet, stort overfladeareal, stor mekanisk styrke, og høj elektrisk ledningsevne sikrer grafene-baserede arkitekturer bred anvendelse.

I denne afhandling gives først et overblik over funktionelle makroskopiske grafenematerialer ud fra tre synspunkter; 1) hvordan man forbereder 2-D grafenfilm/papir, 2) hvordan materialet kan funktionaliseres ved hjælp af enten polymerer eller nano-objekter, og 3) lovende mulige anvendelser af 2-D grafenfilm/papir som molekylær si til oprensning, biomimisk, fleksibelt substrat, sensorer og elektrokemiske energikomponenter. Derefter præsenteres arbejdet med grafenoxid eller grafenepapir modificeret med preussisk blå nanopartikler og -kuber. Flere avancerede teknikker (XRD, XPS, TEM, SEM m.m.) blev anvendt til karakteriseringen af de fremstillede nanokompositter. Baseret på disse materialer blev nye, højtydende, ultrafølsomme og billige elektroder fremstillet og anvendt som elektrokemiske sensorer til detektering af hydrogenperoxid. Endelig blev grafenepapir designet som nedbrydelig skabelon for 2-D nanoporøse metaloxider (MO) via direkte dekomponering af GO-papir ved tilstedeværelse af metalioner. I kapitel 6 demonstreres, hvordan en række forskellige krystallinske MO kan fremstilles ved denne metode. Desuden blev lag-på-lag, nanoporøse og ultratynde 2-D CuO nanolag blev anvendt som i en fotocanode til energikonvertering. I kapitel 7 og 8 blev CuO/ZnO hybrid-nanolag og NiO nanolag designet som en ikke-enzymatisk sensor til højfølsom analytisk detektering af glukose og urea.

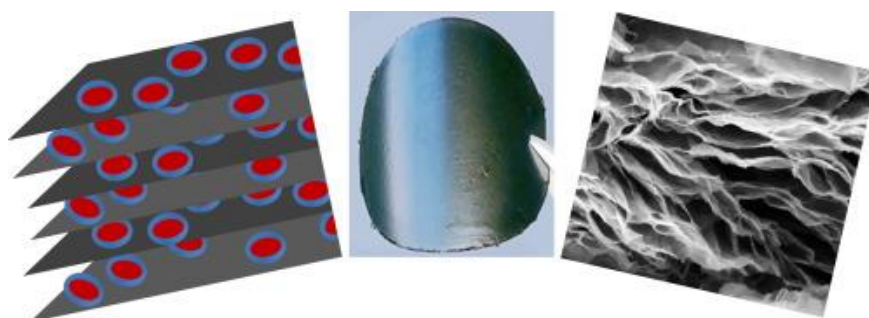
Abbreviations

AFM	Atomic Force Microscopy
AuNPs	Gold Nanoparticles
Au@PBNPs	gold@Prussian Blue Nanoparticles
CV	Cyclic Voltammogram or Cyclic Voltammetry
EIS	Electrochemical Impedance Spectroscopy
ET	Electron Transfer
GNSs	Graphene Nanosheets
GO	Graphene Oxide
GPS or GPs	Graphene Papers
LSV	Liner Sweep Cyclic Voltammogram
MO	Metal Oxide
PBNPs	Prussian Blue Nanoparticles
rGO or RGO	Reduced Graphene Oxide
rGO-PB	Prussian Blue Functionalized Reduced Graphene Oxide
SCE	Saturated Calomel Electrode
SEM	Scanning Electron Microscopy
TEM	Transmission Electron Microscopy
XPS	X-ray Photoelectron Spectroscopy
XRD	X-ray Powder Diffraction
2D	Two Dimensional
3D	Three Dimensional

Highlight of the thesis contents

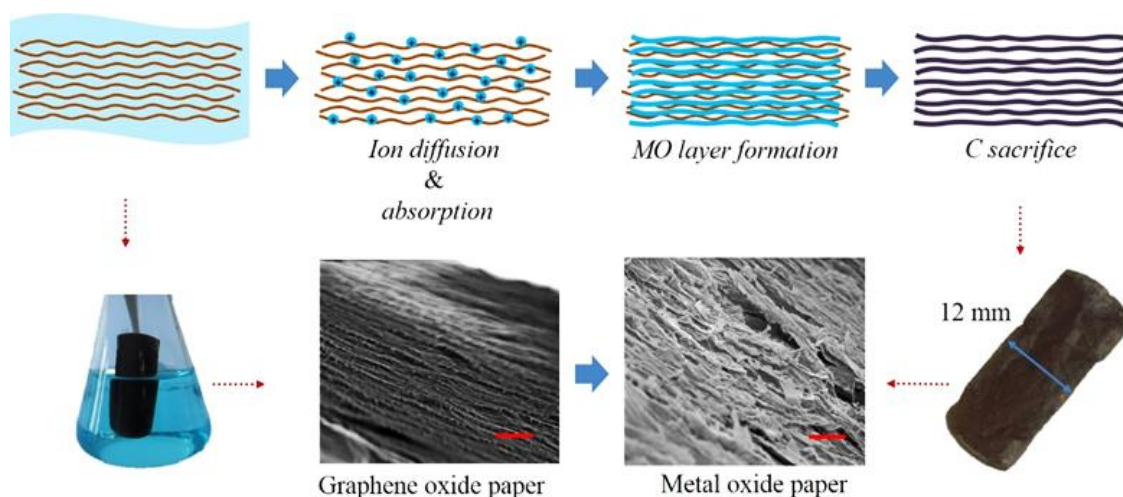
Part 1: Two chapters are included in this part. In this part, I mainly address recent advances in the design and fabrication of 2D graphene film/paper/membrane architecture and their potential applications as well as outline some key experimental methods. In the review of graphene papers related researches, we provide an overview of the functional macroscopic graphene materials from three aspects, i.e., how to prepare 2D graphene films/papers, how to functionalize them using with either polymers or nano-objects, and what they can be used in the fields of molecular sieving purification, biomimetics, as flexible substrates, sensors and electrochemical energy devices. The key instrumental methods including electrochemistry, electron microscopies, X-ray diffraction, X-ray photoelectron spectroscopy and atomic force microscopy are briefly described, in relation to their working principles and main features.

Part 2: There are three chapters in this part. In this part, I have explored the combination of redox active *Prussian Blue* (PB) nanostructures (e.g., interlocked PB nanocubes (Chapter 3) and core-shell Gold@Prussian Blue (Au@PB) nanoparticles (NPs) (Chapters 4 and 5) with chemically exfoliated graphene to prepare multifunctional composites as electrochemical catalysts and supercapacitor electrode materials. These nanocomposites were systematically characterized by AFM, SEM, TEM and XPS. The results confirmed that all PB nanostructures were combined well with graphene nanosheets. Furthermore, PB nanostructure functionalized graphene materials were fabricated into disposable paper sensors and supercapacitor electrodes. For example, Au@PBNPs hybrid GO suspension was filtered via layer-by-layer into functional GO paper, which was further converted into electrically conductive reduced GO (RGO)/Au@PB paper via hydrazine vapour reduction. Resulting sandwich functionalized graphene papers had sufficient conductivity and flexibility, and robust mechanical strength. For electrochemical measurements, the graphene paper was cut into free-standing electrodes. Such electrodes with the advantages of low cost and scalable production capacity, for example used as non-enzymatic electrochemical sensors, are of particular interest in the areas of flexible, disposable, simple and low-cost sensors.



Highlight [Fig.1](#) for part 2.

Part 3: This part includes three chapters. Transition metal oxides (MO) as pivotal important multi-functional materials have been widely used for various purposes, such as sensors, catalysis and energy storage and conversion. It is noticed that the size, morphology and structure of MO materials can significantly influence their physical and chemical properties. Well-designed and ordered MO structures have been applied for research and assembled into smart devices, due to their unique properties and desired functionality. Among various structures, ultrathin 2D nanostructure is highly desirable to obtain superior catalytic, photovoltaic and electrochemical performance, since their large surface-to-volume ratio and confined thickness in nanometer scale. Nanoporous structured MOs hold promise for their applications in adsorption, catalysis, energy conversion and storage, optoelectronic and as biological sensing platforms. Many efforts have been devoted to the synthesis and applications of MO materials with ultrathin or nanoporous structures for sensors and energy conversion and storage. However, design and control of ultrathin and nanoporous structured MO still are challenging. In this part, we have attempted to develop a novel method for preparation of 2D nanoporous MO by the GO paper templated synthesis. In Chapter 6, we demonstrated that crystalline MO nanosheets can be prepared using GO paper as a sacrificial template. Furthermore, layer-by-layer, nanoporous and ultrathin 2D CuO nanosheets were used to assemble photocathodes for photoelectrochemical water splitting. In Chapters 7 and 8, CuO/ZnO hybrid nanosheets and NiO nanosheets were synthesized, characterized and used as nonenzymatic sensing electrode materials for high performance detection of glucose and urea.



Highlight [Fig.2](#) for part 3.

Table of the Contents

Preface and acknowledgements	I
Abstract	II
Abstract in Danish.....	II
Abbreviations	IV
Highlights of the thesis contents.....	V
Part 1. Overview of research on graphene papers and experimental materials and methods.....	1
Chapter 1. Graphene papers or membranes for molecular sieving purification, sensors and energy devices ...	1
1.1 How to prepare graphene paper.....	4
1.1.1 Solution phase assembly.....	4
1.1.3 Chemical vapour deposition	9
1.1.4 Other methods	9
1.1.5 Treatment of graphene oxide paper	10
1.2 Functionalization of graphene papers	11
1.2.1 Graphene–polymer composite films/papers	11
1.2.2 Graphene–nano-object composite films/papers.....	13
1.3 Applications of graphene papers	16
1.3.1 Water Purification	16
1.3.2 Biomimetics.....	19
1.3.3 Applications in flexible substrate	21
1.3.4 Application in sensors	23
1.3.5 Application in energy device.....	30
References	33
Chapter 2: Experimental materials, methods and techniques	39
2.1 Experiment section	39
2.1.1 Chemicals and materials.....	39
2.1.2 Instrumental methods.	39
2.1.3. Experimental details of GO synthesis.....	40
2.1.4 Fabrication of electrodes.	40
2.2 Instrumental techniques	41
2.2.1 Electrochemistry.....	41
2.2.2 Electron microscopy	43

2.2.3 X-ray diffraction techniques	45
2.2.4 X-ray photoelectron spectroscopy	45
2.2.5 Atomic force microscopy	46
References	47
Part 2. <i>Prussian Blue</i> functionalized graphene composites for electrochemical sensing and energy applications.....	48
Chapter 3: Interlocked graphene- <i>Prussian blue</i> hybrid composites enable multifunctional electrochemical applications.....	49
3.1 Introduction	49
3.2 Synthesis of G-rGO-PB composite	51
3.3. Results and discussion	51
3.3.1 One-step eco-friendly synthesis of G-PB-rGO composites.....	51
3.3.2 Structural characterization of G-rGO-PB composites	53
3.3.3 Electroactivity of G-rGO-PB composites	58
3.3.4 Application of hybrid composites.....	59
3.4. Conclusions	63
References	64
Chapter 4. Size dependent self-catalytic growth and electrochemical catalysis of Au@PB Core-shell nanoparticles.....	66
4.1. Introduction	66
4.2. Experimental section	68
4.2.1 Synthesis of AuNPs.....	68
4.2.2 Synthesis and purification of Au@PB core/shell nanoparticles.....	68
4.3. Results and discussion.....	69
4.3.1 Self-catalytic formation of Au@PB nanoparticles.....	69
4.3.2 Structural mapping of Au@PB nanoparticles.....	72
4.3.3 Electroactivity of Au@PB nanoparticles.....	74
4.3.4 Size-dependent electrochemical catalysis of Au@PB nanoparticles toward reduction of H ₂ O ₂	77
4.4. Conclusions	79
References	79
Chapter 5. Free-standing and flexible graphene papers as disposable non-enzymatic electrochemical sensors	81
5.1. Introduction	81
5.2. Experimental section	81

5.2.2 Synthesis of AuNPs.....	81
5.2.3 Synthesis and purification of Au@PB core/shell nanoparticles.....	82
5.2.4 Preparation of graphene oxide.....	82
5.2.5 Preparation of graphene papers.....	82
5.3. Results and discussion.....	83
5.3.1 Synthesis, electronic properties, and structures of core/shell Au@PB NPs.....	83
5.3.2 Preparation of Au@PB NP/graphene papers.....	85
5.3.3 Characterization of Au@PB NPs graphene paper.....	87
5.3.4 Electroactivity of Au@PB NP graphene paper.....	89
5.3.5 Electrocatalytic reduction of H ₂ O ₂ by Au@PB NP graphene papers.....	90
5.4. Conclusions.....	91
References.....	92
Part 3. Low cost template methods for synthesis of 2D layered and nanoporous transition metal oxide nanosheets.....	93
Chapter 6. Ultralight and semi-transparent metal oxide papers composed of nanoporous monolayers for lightweight energy and sensing applications.....	94
6.1 Introduction.....	94
6.2 Results and discussion.....	95
6.2.1 Preparation of metal oxide.....	95
6.2.2 Structural characterization of metal oxide materials.....	96
6.2.3 The growth principle of metal oxide.....	98
6.3. Applications.....	105
6.3.1 Application of CuO as photocathode.....	105
6.3.2 Application of CuO as supercapacitor electrode materials.....	108
6.5. Conclusions.....	109
References.....	110
Chapter 7. Bottom-up method for synthesis of 2D nanoporous hybrid CuO/ZnO nanosheets for non-enzymatic biosensor.....	112
7.1. Introduction.....	112
7.2. Experimental section.....	112
7.3 Results and discussion.....	113
7.3.1 Preparation of CuO/ZnO 2D hybrid nanosheets.....	113
7.3.2 Characterization of metal oxides.....	113
7.4 Application of 2D porous CuO/ZnO nanosheets.....	118

7.5 Conclusions	121
References	121
Chapter 8. Graphene oxide templated synthesis of nickel oxide nanosheets for enzymeless detection of urea	123
8.1 Introduction	123
8.2 Experimental section	124
8.3 Results and discussion	125
8.3.1 Synthesis of 2D nanoporous NiO nanosheets.....	125
8.3.2 Structural characterization of nanosheets	126
8.3.3 Electrochemical characterization of 2D NiO nanosheets	128
8.3.4 Non-enzymatic urea sensing response.....	129
8.3.5 Interference study	130
8.4 Conclusions	131
References	131
Appendix A. Characterization data of GO material	133
Appendix B. Publication and dissemination.....	134
Appendix C. The first pages of six peer-reviewed articles.....	139

Part 1. Overview of research on graphene papers and experimental materials and methods

In [Chapter 1](#), we present an up-to-date comprehensive overview of graphene-supported papers, with the emphasis on smart assembly, purpose-driven specific functionalization and some crucial applications associated closely with sensing, environmental and energy technologies. Firstly, we give a brief introduction to graphene as a new building block and to the current status of researches on graphene papers. This is followed by addressing some crucial methods of how to prepare graphene papers. We then summarize multiple possibilities of functionalizing graphene papers, membranes or films. Finally, we evaluate some key applications of graphene papers in the areas of chemical/electrochemical sensors, bio-mimetics and energy devices. Followed the key techniques and theories that were applied in my research was briefly introduced in [Chapter 2](#), as well as the detail of synthesis graphene oxide (GO) was presented.

Chapter 1. Graphene papers or membranes for molecular sieving purification, sensors and energy devices

Graphene has attracted much interest from physicists, chemists, and material scientists. Graphene is a two-dimensional (2D) sheet of carbon atoms in a hexagonal configuration with atoms bonded by sp^2 bonds. In 2004, Andre Geim and Kostya Novoselov at the University of Manchester first isolated graphene nanosheets from bulk graphite using the Scotch tape technique¹. Although being a strictly 2D material, graphene sheet is not fully flat, but rather exhibits ripples, which provide possible locations for nanoscale objects such as nanoparticles. Owing to the oxygenated functional groups on graphene oxide (GO) basal planes and at its edges, a hybrid structure is obtained, comprised of a mixture of sp^2 and sp^3 hybridized carbon atoms^{2, 3}. Several methods have been reported for the preparation of graphene, such as peeling-off graphite, liquid phase exfoliation⁴⁻⁶, chemical vapour deposition (CVD)⁷⁻⁹, reduction of GO (rGO)¹⁰⁻¹², graphitization of silicon carbide¹³, unzipping carbon nanotubes^{14, 15}, and bottom-up organic synthesis^{16, 17}. These methods, all of which produce graphene with different size, shape, chemical composition, and environment, have different requirements for functionalization. Since 2004, graphene has been applied in electronics, energy storage and conversion (supercapacitors, batteries, fuel

cells, and solar cells), as well as in bioscience/biotechnologies because of its unique physicochemical properties: high surface area (theoretically $2630 \text{ m}^2 \cdot \text{g}^{-1}$ for single-layer graphene sheets), excellent thermal and electrical conductivity, and robust mechanical strength.

The mass production of high-quality GO can be achieved by chemical oxidation and exfoliation of low cost graphite, based on a modification of the Hummers' method, and a stable suspension of GO can be obtained by ultrasonic treatment of graphite oxide or GO in water, which is therefore a widely-studied precursor for the solution-processable synthesis of graphene based materials. The abundant hydroxyl and epoxy groups on the basal plane and the carboxyl groups at the sheet edges in the synthesis process provide the option for dispersion in water and these groups can also be replaced by other functional groups, which is a simple method to modify GO. In addition to chemically derived graphene, GO and reduced GO are promising building blocks to construct 2D graphene films/papers/membranes to obtain the collective, or enhanced, optical, electrical, and mechanical properties, which are multi-layered composite structures formed by a random stacking of GO platelets. 2D graphene films/papers/membranes are attractive candidates for novel applications and paper-like composites. It is difficult to use pristine graphene nanosheets as building blocks for a macroscopic assembly because of their low solubility in all solvents. The combined features of the planar structure and abundant processable groups of GO nanosheets allow the assembly of macroscopic architectures with hierarchical structures through various techniques. The resulting materials possess the advantages of lightweight, robust mechanical properties, and high electrical conductivity. Alternatively, graphene frameworks, with different macroscopic shapes, large surface areas, and high porosity, are ideal scaffolds for the incorporation of various functional guest nanomaterials, such as metals, semiconductors, and polymers, which enrich their functionalities and broaden the possibilities for their practical application. In this way, the synergy of the hierarchical structure and multifunctional components makes graphene-based macroscopic assemblies attractive candidates for a wide range of practical applications.

Intensive effort has devoted to assemble these well dispersed oxidized or chemically reduced (under controlled conditions, still water-dispersible) graphene nanosheets into membrane-shape ordered macrostructures, mainly through flow-directed assembly by filtration. Recently, molecular templates, Langmuir–Blodgett assembly, two-phase interfacial transfer and direct chemical vapour deposition have also been employed to obtain graphene-based or GO-based membranes on selected substrates, and these have been applied in water purification, sensing, and

energy devices. Fig.1.1 shows the results from a search of the publications as well as citations using the keywords “graphene paper or graphene membrane or graphene film” or “graphene oxide paper or graphene oxide membrane or graphene oxide film” from 2007 to 2015 using the Web-of-Science database. It is clear that the fabrication and application of graphene papers have been attracting increasing interest in recent years. Some reviews of the preparation of 2D and 3D graphene materials and their applications as biosensors, membranes, and hybrid catalysts have been summarized in previous reports¹⁸⁻²¹. I think it is timely to focus on 2D graphene paper-like materials according to the recent advancements. The overall goal of this part is to provide a critical overview of our current understanding of freestanding graphene paper. We will discuss how to fabricate, characterize, and functionalize freestanding graphene paper. We will then focus on the applications of graphene papers in sensing, biomimetics, water purification, flexible substrates, and energy devices. Fig. 1.2 shows the outline of this chapter.

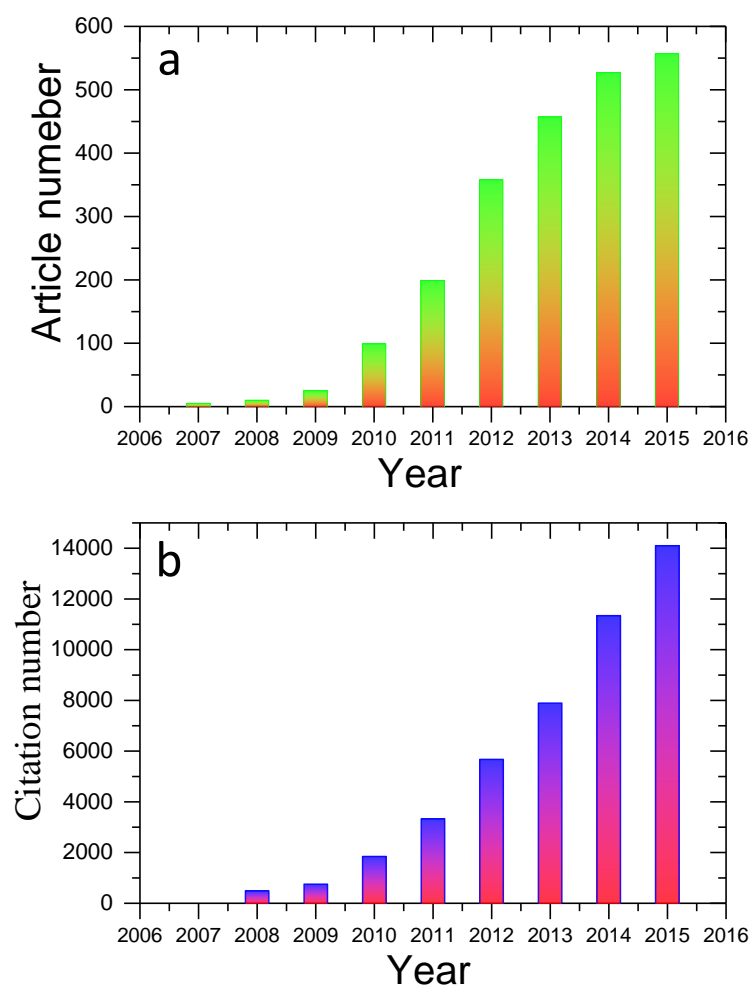


Fig. 1.1 Comparison of the annual number of scientific publications (a) and citations (b) using the keywords of graphene paper, graphene membrane, graphene film, graphene oxide paper,

graphene oxide membrane, or graphene oxide film, as searched on the Web of Science. To avoid mis-interpretation of the data, the number of publications (392) and citations (8963) for 2016 (until 31st July) is not included in the plots.

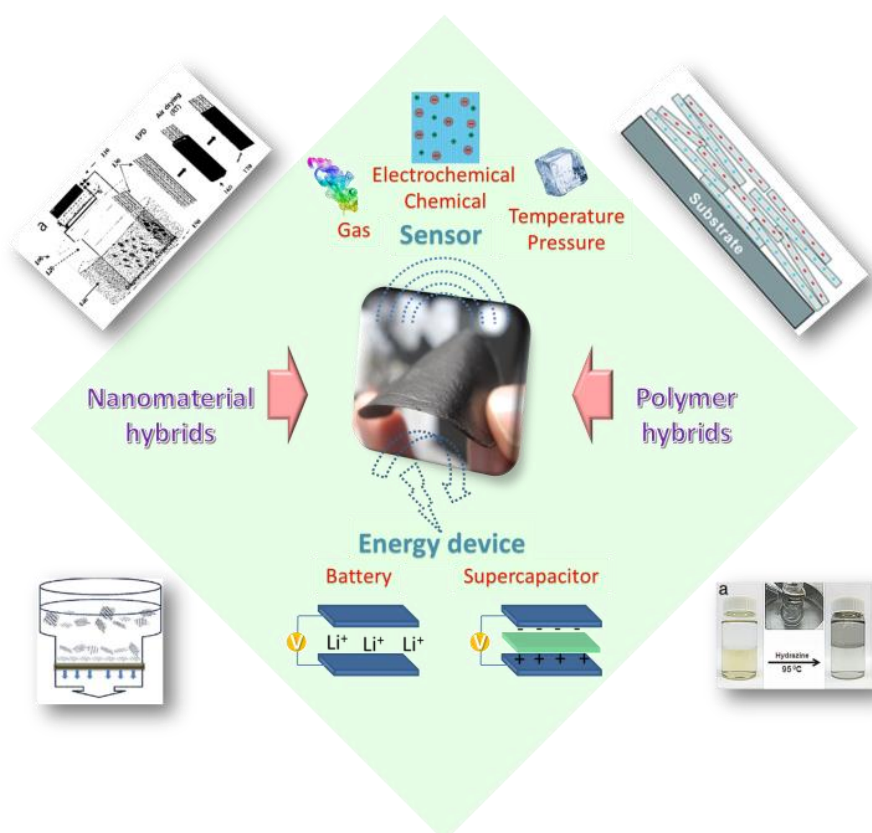


Fig. 1.2 Overview of the preparation of graphene paper and its applications.

1.1 How to prepare graphene paper

A variety of methods for the preparation of graphene paper/film/membrane have been developed, with the main procedures being solution phase assembly, electrochemical deposition, and the CVD method, the details of which are discussed in the next section.

1.1.1 Solution phase assembly

Vacuum Filtration: To arrange GO sheets into well-ordered macroscopic structures, graphene paper was first fabricated by Ruoff's group through a facile filtration method; similar to carbon nanotubes, GO sheets could be assembled into a paper-like material under a directional flow (Fig. 1.3). Vacuum filtration of colloidal dispersions of GO sheets through an anodisc membrane filter yielded free-standing GO paper with thicknesses ranging from 1 to 30 μm after drying. The physical properties of GO paper have been reported in detail. This material is uniform when the thickness is greater than 5 μm , dark brown under transmitted white light, and almost black in

reflection. The fracture edges of a GO paper sample, when imaged by scanning electron microscopy (SEM), reveal well-packed layers over almost the entire cross-section of the paper samples, sandwiched between less densely packed ‘wavy’ skin layers that were approximately 100–200 nm thick. A typical GO paper specimen corresponds to a layer-to-layer distance (d-spacing) of approximately 0.83 nm determined from the X-ray diffraction spectra. The ultimate tensile stress and strain of GO paper are higher than the corresponding values for flexible graphite foils. The work of extension to fracture for GO paper is as high as $350 \text{ kJ}\cdot\text{m}^{-3}$ and tensile test measurements show GO paper exhibits very high values of tensile modulus and fracture strength. The average modulus of GO paper was determined to be 32 GPa with the highest value being 42 ± 2 GPa, which will provide high-quality, microstructure-controllable macroscopic samples for the exploration of novel properties and the development of new applications²². As a result of its facile processability, GO paper has been popularly applied to prepare free-standing graphene paper²³⁻²⁵. Compton et al. prepared conductive “alkylated” graphene paper through the chemical reduction of post-synthesized hexylamine-modified GO paper²⁶. Lin et al. demonstrated that the giant GO sheet enabled improved performance by systematically studying the influence of the GO size on the interior structure, and the electrical and mechanical properties of the as-prepared graphene papers²⁷. Recently, researchers observed that through vacuum filtration of a frozen GO solution, followed by chemical reduction, washing and freeze drying, paper-like graphene foam could be obtained²⁸. The porous structure makes it superelastic: it can be compressed to at least 65% strain and is still able to rapidly recover most of its original thickness when the loading is removed. There are also alternative methods to fabricate paper-like graphene foams from vacuum filtration graphene membranes such as leavening and light irradiation strategies^{29,30}. However, the sizes of the films or foams prepared from the time-consuming membrane filtration method are limited, and the method is not suitable for large area production of graphene-based thin films.

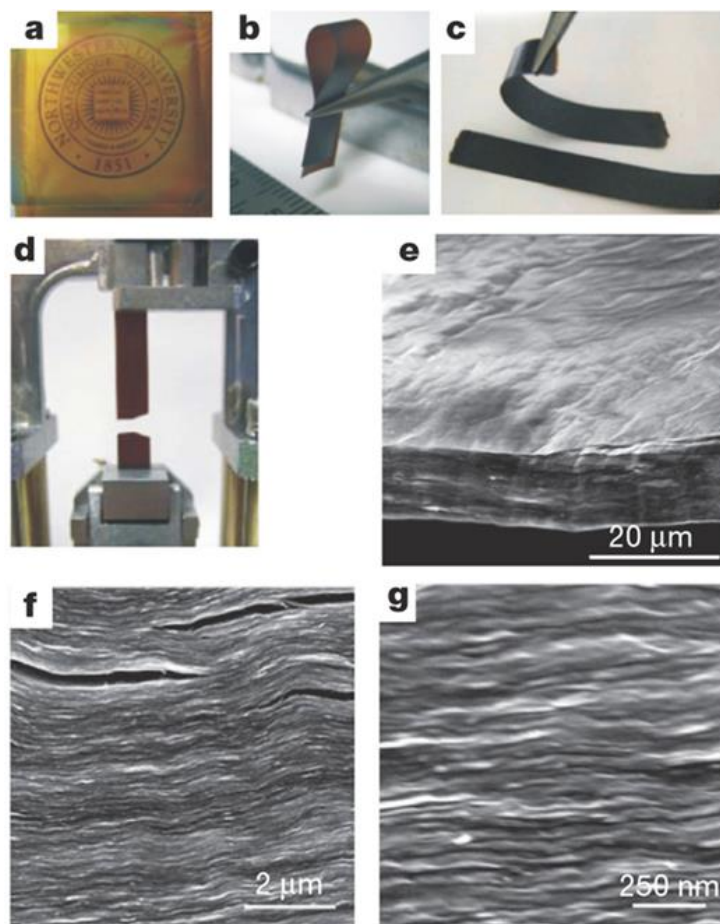


Fig. 1.3 Morphology and structure of GO paper. (a–d) Digital camera images of GO paper. a) 1-mm thick (the Northwestern University logo is beneath the paper); b) folded, 5-mm-thick semi-transparent film; c) folded, 25-mm-thick strip; d) strip after fracture from tensile loading. (e–g) Low-, middle- and high-resolution SEM side-view images of a 10- μm -thick sample²².

LbL assembly: Moreover, self-assembly, a popular approach for the preparation of films has also been applied in the deposition of GO on a substrate by electrostatic interaction³¹⁻³³. Kim et al. prepared a pure graphene film by enriching and Langmuir–Blodgett (LB) assembly of GO on a liquid/liquid or gas/liquid interface^{34, 35}. Negatively-charged functionalized GO layers were incorporated into polyelectrolyte multilayers (PEMs) through a layer-by-layer (LbL) assembly by LB deposition. These LbL-LB GO nanocomposite films were shown to be robust free-standing membranes with large lateral dimensions and a thickness of approximately 50 nm. Micromechanical measurements showed an enhancement of the elastic modulus by an order of magnitude, from 1.5 GPa for pure LbL membranes to approximately 20 GPa for 8.0 vol% GO encapsulated LbL membranes³⁶. In the same way,

transparent conductive films were constructed by LBL deposition and reduction of GO film on the flexible polymer substrate^{37, 38}.

Two-interface growth methods: Chen et al. obtained GO paper by facile self-assembly GO processes at the liquid/air interface^{39, 40}. During the heating process of the hydrosol, the Brownian motion of the GO sheets was strengthened in the aqueous suspension, and the liquid level of the hydrosol gradually decreased. Thus, there are more opportunities for GO sheets to collide and interact with each other and move up to the liquid/air interface with the water spilling out from the hydrosol. The liquid/air interface provides a smooth space for the two-dimensional GO sheets, and the nanosheets that reach the interface tend to aggregate along it. When a new sheet moves near to the interface, it will be captured by the sheets that already reside there through interlayer van der Waals forces. The membranes are thickness controlled and area adjustable, and show excellent mechanical and optical performances. Interestingly, pristine graphene can assemble on conductive pure graphene thin films through the oil/water interface and the interfacial trapping technique⁴¹.

Spin-coating: Additionally, graphene paper can easily be obtained by other methods, such as solution casting, spin coating, spray coating, and dip coating GO or rGO solution on the substrate, to prepare graphene film on substrates⁴², such as poly(ethylene terephthalate) (PET)⁴³, SiO₂/P++Si⁴⁴ and Au^{45, 46}. The graphene film prepared by this type of approach is uniform and thickness-controllable with minimal wrinkles.

1.1.2 Electrophoretic deposition

Electrophoretic deposition (EPD) has also been shown to be a useful technique to deposit graphene on conductive substrates⁴⁷, owing to the relatively short processing period and requirement of only simple and cost effective equipment to produce uniform deposits with high microstructural homogeneity and adequate control of the deposit thickness. EPD offers the possibility of scaling up to large, application relevant dimensions. Ruoff and his group used the deposition of films composed of overlapped and stacked platelets of GO to prepare graphene papers by EPD processes (Fig. 1.4). The GO platelets migrated toward the positive electrode with oxidation occurring at the anode of the electrolysis cell. The possible electrochemical reactions could be:





According to the X-ray photoelectron spectroscopy (XPS) results, the oxygen groups, such as hydroxyl and epoxide on the basal planes, and carboxylate and carbonyl functional groups at the edges and some fraction can presumably be removed by and during the EPD process. The electrical conductivity of the as-prepared graphene paper was shown to improve to $1.43 \times 10^4 \text{ S} \cdot \text{m}^{-1}$. The advantages of this method is the reduction of GO without added reductants, and under room temperature, has the potential for the high-yield, large-area, low-cost, and environmentally-friendly production of films composed of reduced GO platelets. This approach should find use in a variety of applications requiring a facile coating of complex surfaces and shapes⁴⁸. Hasan et al. prepared a transferable, tunable microstructure GO film through the EPD process. By selecting the appropriate suspension pH and deposition voltage, films composed of negatively charged GO sheets can be produced with either a smooth “rug” microstructure on the anode or a porous “brick” microstructure on the cathode⁴⁹. A nanostructural porous NiO/RGO hybrid film can also be deposited on an indium tin oxide (ITO) substrate by EPD⁵⁰. GO undergoes post-conversion by the reduction of GO and is deposited on nickel foam, ITO, stainless steel (SS), and platinum (Pt) to prepare composite films^{51, 52}. Additionally, graphene nanosheets can be directly deposited on Ni substrate through a similar process⁵³.

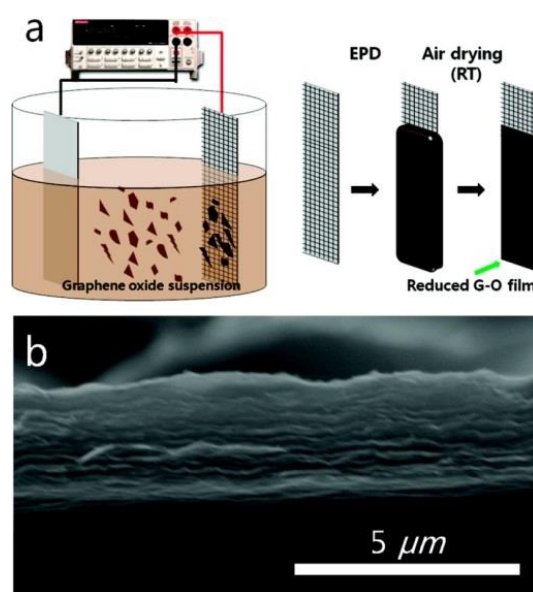


Fig.1.4 (a) Schematic diagram of the EPD process and (b) cross-sectional SEM image of EPD-GO film⁴⁸.

1.1.3 Chemical vapour deposition

To meet the requirement of large-scale, near-perfect graphene films on various substrates, the CVD technique is a direct and promising method which is attractive for electronic devices owing to their high flexibility, transparency, and electrical conductivity.^{8,54} Commonly, transition metals, such as Cu^{55, 56}, Ni⁵⁷⁻⁵⁹ and Co⁶⁰, and non-metal materials, such as SiO₂⁶¹, BN⁶² and Si₃N₄⁶³ have been used as the substrates for the CVD growth of graphene films. However, the non-metal substrate has the limitations of slow growth rate and discontinuous size. Recent advances in the direct fabrication of large-scale graphene films on a Ge substrate have overcome this problem, owing to the high carrier mobility and process compatibility of the semiconductor and the semimetal-characteristics of Ge⁶⁴.

1.1.4 Other methods

In addition, a variety of new assembly strategies have increasingly been developed for the construction of graphene films with hierarchical structures and high performances, inspired by the micro-/nano-assembled structures of materials found in nature. Cao et al. developed a simple, smart, and scalable method to simultaneously assemble and reduce GO nanosheets into large-sized chemically-converted graphene films with high conductivity and mechanical stability, triggered by the unsteady microenvironment from the reduction–oxidation reactions between GO and the active-metal substrate⁶⁵. Honeycomb structural graphene films, which were prepared by the template method, display excellent properties, such as large porosity, high conductivity, and robust chemical and mechanical stability. These films exhibit promising potential usage in various applications, including as biological scaffolds, catalysts, and sensors^{66, 67}. Bubble structural graphene film was also fabricated by using monodispersed poly(methyl methacrylate) (PMAA) latex spheres as the sacrificial templates.⁴⁰ Highly conductive, free-standing, and flexible porous carbon thin films can be prepared through chemical activation of reduced GO paper^{68, 69}, as was reported by Ruoff's group. Moreover, a novel strategy for the preparation of GO papers was developed by mechanically pressing a graphene aerogel that was obtained by freeze-drying a GO solution. This kind of graphene paper shows a unique structure with folded graphene sheets and the d-

space is 0.77 nm, which is lower than the graphene paper obtained from the vacuum filtration methods (0.83 nm)⁷⁰.

1.1.5 Treatment of graphene oxide paper

Generally, when GO paper is prepared by solution phase assembly, its conductivity is very poor owing to GO containing many oxygen groups. Such GO paper is hardly suitable for many applications related to electrochemical sensors and energy storage. Thus, the GO paper is normally subjected to the post-treatment to gain necessary conductivity. This can be achieved by chemical reduction, high-temperature annealing and electrochemical reduction. Hydrogen iodine (HI) has been used as an effective reductant to reduce GO paper for enhanced electrical conductivity. Annealing is another effective method used to remove oxygen-containing groups from GO paper to improve its conductivity. The d-space of graphene paper is approximately 1 nm, which is appropriate for the mass transportation of most ions. However, this needs to be further improved in some cases. To do so, hydrazine vapour was used as a reducing agent to create a porous structure between the interlayer graphene papers. In addition, a unique process for the preparation of highly conductive and oxygen-free graphene thin paper with a carbon/oxygen ratio reduced to 100:1 can be employed by means of Ar⁺ ion irradiation of GO papers (Fig. 1.5). The composition of graphene paper in terms of the carbon/oxygen ratio and the types of individual oxygen-containing groups is monitored throughout the process. Angle-resolved high resolution X-ray photoelectron spectroscopy (XPS) was used to investigate the depth profile of carbon and oxygen within the rGO paper. The C/O ratio of over 100 on the surface and 40 in the bulk material is observed. To provide insight into the processes of oxygen removal from GO paper by low energy Ar⁺ ion bombardment, the gases released during irradiation are analyzed by mass spectroscopy. It is found that the Ar⁺ ion beam can be applied as a technique for the fabrication of highly reduced graphene papers with high conductivity. Such highly conductive graphene papers have great potential for their applications in the construction of microelectronic and sensing devices⁷¹.

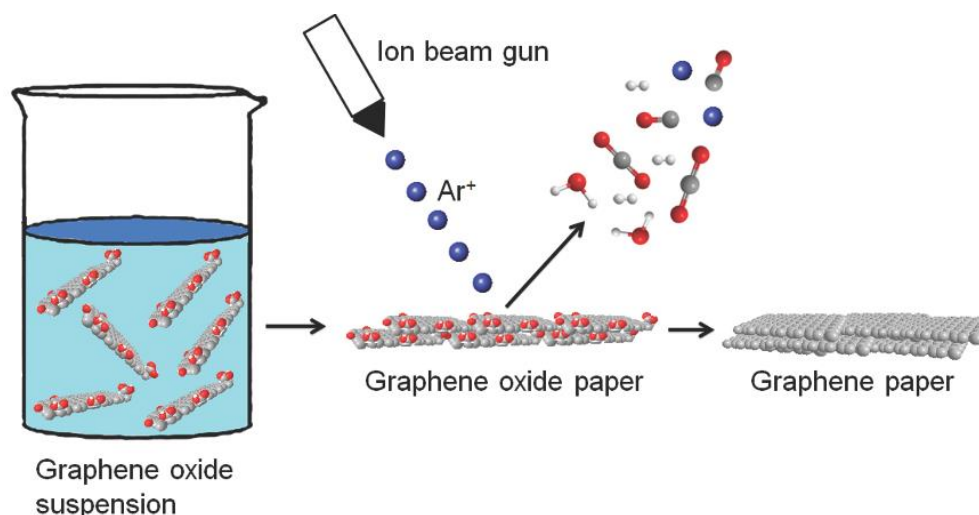


Fig.1.5 Preparation of the graphene paper by Ar^+ ion irradiation⁷¹.

1.2 Functionalization of graphene papers

The emerging field of freestanding and flexible paper-like materials based on graphene sheets has become the focus of considerable research in recent years because of the scientific and technological significance of these materials. In particular, multifunctional flexible graphene-based films or papers are in high demand for various applications.

1.2.1 Graphene–polymer composite films/papers

Polymers, as important components in the nanoworld, have been applied in sensor energy conversion and storage, and are popular tools for the functionalization of graphene paper to improve conductivity, biocompatibility, and mechanical property⁷²⁻⁷⁴. In general, the polymer is stabilized with graphene paper through electrostatic, hydrogen bond, and π - π stacking interactions. The layer-by-layer assembly method is a facile, low-cost way to fabricate polymer hybrid/graphene paper with precise control over the structure and thickness on both the micro- and nanoscales, and has the great advantage of being able to fabricate graphene–polymer composite films through the electrostatic interaction of the oppositely-charged objects or hydrogen bonding. A variety of polymers have been incorporated into graphene-based films with a uniform multilayer structure and novel functionality, such as polyaniline⁷³, poly(sodium 4-styrenesulfonate)⁷⁴, poly(diallyldimethylammonium)⁷⁵, poly(p-phenylene vinylene)⁴³ and poly(sodium 4-styrenesulfonate)⁷⁶. This technology was used to fabricate GO-PEI films consisting of a

poly (ethylene terephthalate) substrate (Fig. 1.6) as a gas barrier. Nanostructure and oxygen barrier properties of the GO-PEI film were shown to be highly dependent on the pH. Using a GO suspension with a pH of 3.5 resulted in assembly of a film that exhibited very dense and ordered structures and delivered very low oxygen transmission rates (the lowest was $<0.05 \text{ cm}^3 \text{ m}^{-2} \text{ day}^{-1}$)⁷⁷.

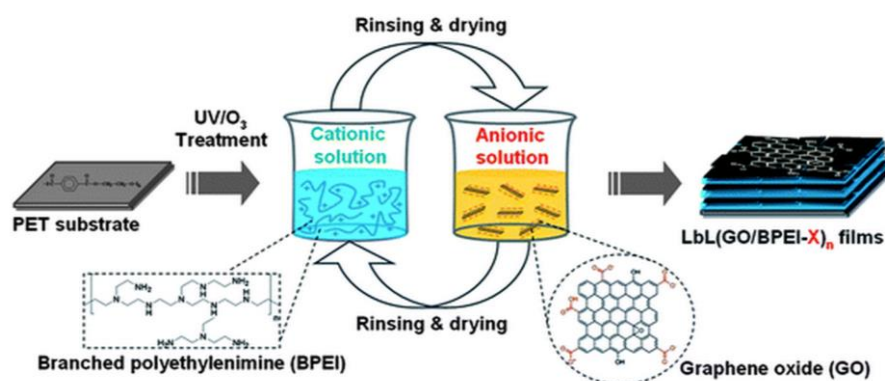


Fig. 1.6 Schematic of the preparation of GO/BPEI films through layer-by-layer self-assembly.

Solution-casting is a popular method to assemble polymer/graphene paper owing to the advantages of easily-obtained, simple apparatus and size-controllability. Recently, PVDF (polyvinylidene fluoride), PVP (polyvinyl pyrrolidone)^{78, 79}, PANi⁸⁰, poly (benzimidazole)⁸¹ and poly (VDF-TrFE)⁷² modified graphene paper have been synthesized by the solution-casting approach. A PANi nanorod array was electrodeposited on graphene paper that was prepared by the solution-casting assembly strategy, and the thickness of PANi was controlled by electropolymerization time. In addition, free-standing, flexible, conductive, reduced GO/Nafion (RGON) hybrid films were obtained by a solution chemistry that involved self-assembly and directional convective-assembly. These films display high conductivity facilitated electron transfer (ET), low interfacial resistance, and are excellent performance electrochemical biosensing platforms for organophosphate (OP) detection⁸³. Given the relative sparseness of usable functionality on pure carbon materials, forming covalent linkages between the polymer matrix and such surfaces (when used as composite filler) may be quite challenging. However, G–O platelets contain surfaces rich in reactive functional groups, and a number of approaches for introducing covalent bonds between G–O platelets and polymers have been demonstrated. For instance, both the grafting-from and grafting-to approaches have been used for the attachment of a broad range of polymers. Dopamine hydrochloride and PEI, as good reducing agents, were used to reduce and functionalize GO, and then assemble the formation of graphene papers^{84, 85}.

In addition, hybrid materials of polycaprolactone (PCL)/graphene papers were fabricated based on a PCL brush on the surface by polymerization of caprolactone from the functional groups on graphene⁸⁶.

1.2.2 Graphene–nano-object composite films/papers

Graphene displays extremely useful physicochemical properties, but it also possesses a weakness in the expected functions, such as catalysis, redox performance, or energy storage. From the viewpoint of a practical fabrication, it is necessary to decorate graphene with functional groups. Graphene is highly compatible with different solvents, and graphene paper or films offer a large surface area owing to multiple interactions in the film. Additionally, graphene obtained by the reduction of GO may still possess some oxygen groups, which enable the loading or growing of a nano-object.

Several methods have been reported to effectively fabricate functionalized nano-objects with graphene paper or films. Graphene paper has been functionalized with nano-objects mainly by the procedures in the following list.

1) Some inorganic functional materials mainly cover the surface rather than bind to the interior of the graphene sheet. These nano-objects functionalize graphene hybrid materials mostly obtained by the growth of metal and semiconductor nanostructures on graphene film by various processes. Such highly transparent conducting films can be obtained by spin-coated⁸⁷, physical vapour⁸⁸ and pulse electrochemical⁸⁹ Ag nanowires or nanocrystals on the graphene film to significantly enhance the electrical properties and surface plasmon signal of the graphene film. Pulse laser deposition was applied to deposit V₂O₅ film on the graphene paper surface to yield flexible energy storage devices⁹⁰. MS (NiS and CoS)⁹¹, Ni(OH)₂ and NiOOH⁹²⁻⁹⁴, TiO₂^{95, 96}, indium–gallium–zinc–oxide⁹⁷, and Au@PtNPs, PtNPs, or PtNPs/MnO₂ nanowires⁹⁸⁻¹⁰¹ are well-designed for depositing on graphene paper surface through advanced techniques. Furthermore, Duck Hyun Lee presented a well-designed carbon hybrid film that was prepared by self-assembly of versatile growth carbon nanotubes on graphene films (Fig. 1.7)⁵⁴, which displayed good mechanical property and high performance for the bending test.

More interesting, AuNPs¹⁰² and NiO^{103, 104} can be in-situ grown on the graphene paper surface to form multifunctional hybrid graphene paper.

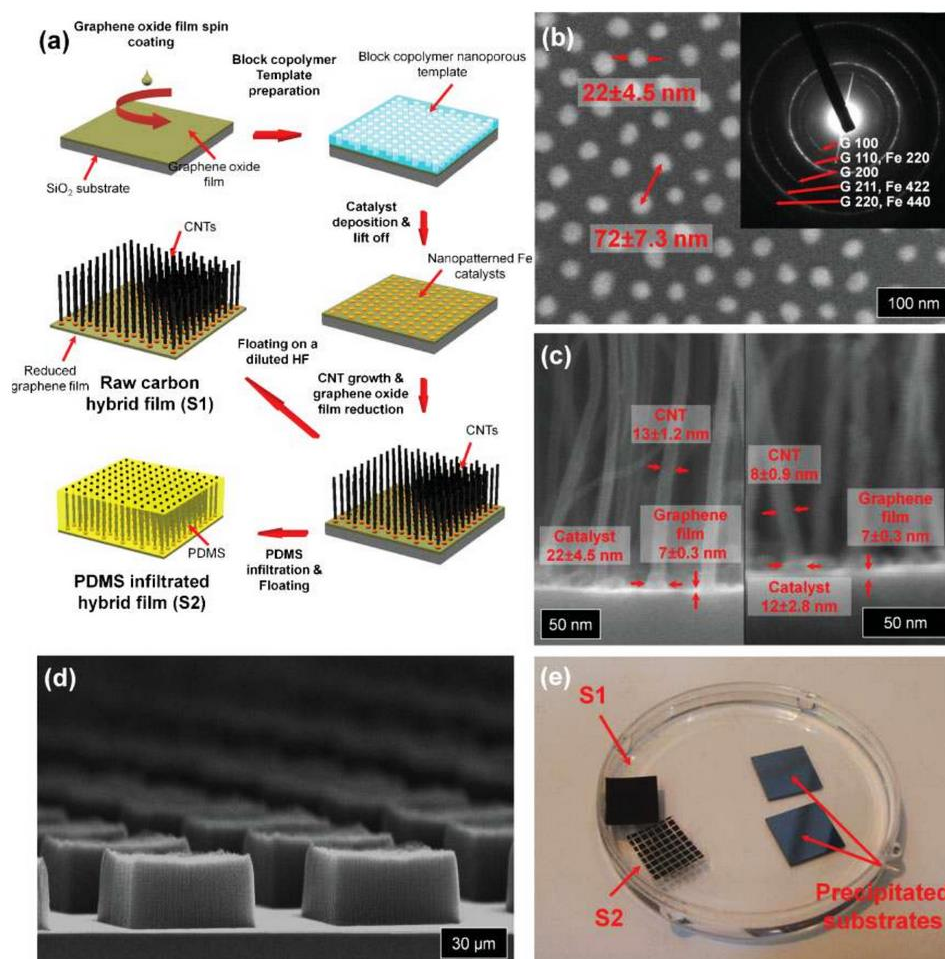


Fig. 1.7 a) Schematic illustration of the fabrication process for carbon hybrid films. A multilayer graphene oxide film is spin-coated onto a SiO_2/Si substrate from an aqueous dispersion. The following block-copolymer lithography creates a nanopatterned iron catalyst array on the graphene oxide film. Highly aligned vertical CNT arrays are grown by catalytic PE-CVD. The underlying graphene oxide film is reduced and becomes electrically conductive during this high temperature PE-CVD growth. b) SEM image of iron catalyst particles on graphene film. The inset image shows the electron diffraction pattern. c) Cross-sectional SEM images of hybrid films. d) SEM image of a square-patterned CNT array on the graphene film. e) Photograph of graphene film floating on a water surface.

2) Loading NPs into the interiors of graphene sheets (Fig. 1.8). To insert a nano-object into the interlayer graphene paper, flow-directed assembly is the most efficient way to prepare nano-object (Prussian blue nanoparticles (PBNPs)²⁴, Au@PBNPs ¹⁰⁵, $\text{Na}_{2/3}\text{Fe}_{1/2}\text{Mn}_{1/2}\text{O}_2$ nanoparticles¹⁰⁶ and SnO_2 nanoparticles¹⁰⁷) hybrid graphene paper. Flow-directed assembly of a mixture of graphene and Fe_3O_4 nanoparticles have also been used to prepare graphene paper. The hybrid graphene paper was reported with high contents of Fe_3O_4 , reaching up to 10 percent. The hybrid graphene paper also exhibited excellent electrical conductivity and mechanical strength. The most important characteristic is the super paramagnetism, which

can easily be tuned through modulation of the loading of Fe_3O_4 nanoparticles¹⁰⁸. Moreover, graphene/ MnO_2 paper was fabricated by filtration of the chemically reduced mixture of GO solution with $\text{Mn}(\text{NO}_3)_2$ and KMnO_4 ¹⁰⁹.

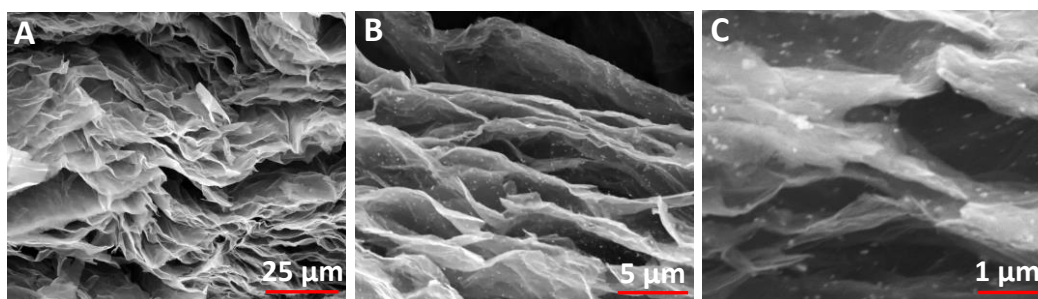


Fig. 1.8 Cross-sectional SEM images of Au@PB NP rGO papers with various magnifications.

A homogeneous mixture of a GO suspension with Au NPs self-assembles at the air/liquid interface, resulting in multi-layered GO–Au NP composite films. The reduced GO–Au NP film shows increased electrode kinetics and a cyclic voltammetric response in proportion to the amount of Au NPs, and an enhancement of anodic peak current was observed compared with that of the reduced GO films¹¹⁰. Transparent and flexible thin film transistors with high performance, based on solution processed graphene nanosheets (GNS)–amorphous indium–gallium–zinc-oxide composites, have been developed¹¹¹.

In addition, Haitao Zhang et al. reported a facile, rapid, scalable, and environmentally-friendly method of making rGO/ $\text{Ni}(\text{OH})_2$ paper by the EPD process⁵¹. NiCo_2O_4 has been grown on the surfaces of porous N-doped graphene sheets through hydrogen bonding, van der Waals forces, or covalent interactions with the functional groups of graphene, such as $-\text{COOH}$. The as-prepared hierarchically porous graphene paper with NiCo_2O_4 has shown a remarkable OER catalytic activity¹¹². N-doped graphene- SnO_2 papers have been prepared by inducing the 7,7,8,8-tetracyanoquinodimethane anion as both the nitrogen source and complexing agent to format a sandwich structure, which exhibits a large capacity, high rate capability, and excellent cycling stability¹¹³. In addition, AuNPs–embedded porous graphene thin films for electrochemical sensing of H_2O_2 were prepared by LBL self-assembly and subsequent annealing technologies¹¹⁴.

Not only some foreign groups can endow graphene paper with special functions, the special structures that can be obtained during the preparation process, such as porous and

bubble structures¹¹⁵ were also used to functionalize graphene paper. Moreover, free-standing elemental-doped (N)¹¹⁶ graphene film was prepared by CVD.

1.3 Applications of graphene papers

Graphene papers, with the advantages of low price, high quality, and simple synthesis process, have a potential to overcome the gap from nanoscale graphene to real macro-scale applications of graphene.

1.3.1 Water Purification

Graphene derivative papers or membranes for molecular sieving purification permeation through nanometer pores are important in the design of materials for use in filtration and separation techniques. To achieve high solvent permeability, filtration membranes must be as thin as possible, while retaining their high mechanical strength and solvent resistance. Papers or membranes made from GO are particularly interesting candidates in this subject. In this section, we discuss recently demonstrated graphene derivative papers or membranes which are used for molecular sieving purification.

Grossman et al. reported that nanometer-scale pores in single-layer freestanding graphene can effectively filter out NaCl salt from water¹¹⁷. The graphene membrane's ability to prevent the salt passage depends critically on pore diameter with adequately sized pores allowing for water flow while blocking ions (Fig. 1.9). Additionally, they investigated the role of chemical functional groups bonded to the edges of graphene pores. The results suggest that commonly occurring hydroxyl groups can roughly double the water flux owing to their hydrophilic character. The water permeability of this graphene membrane is several orders of magnitude higher than conventional reverse osmosis membranes.

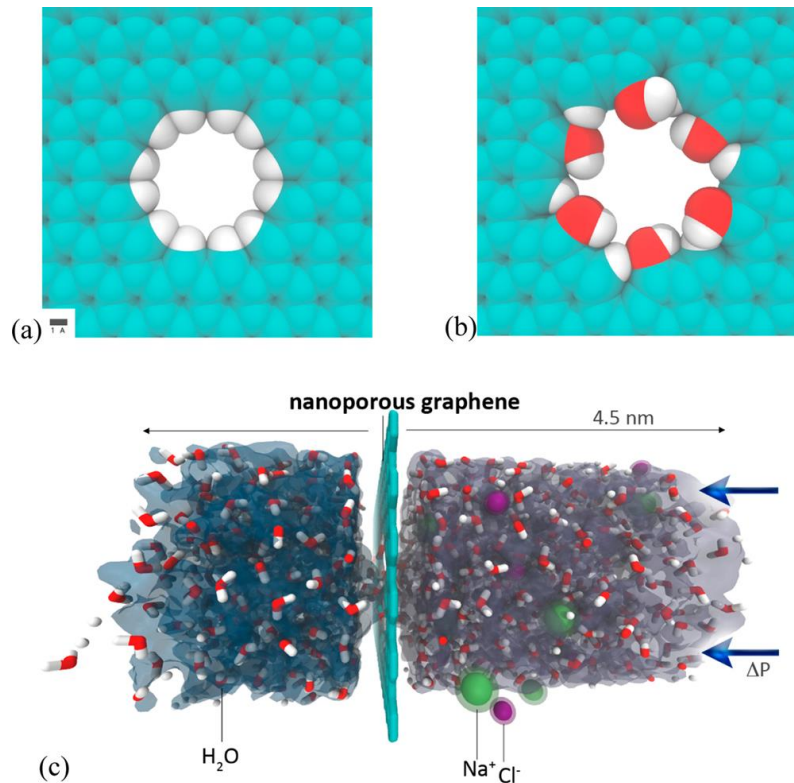


Fig. 1.9 (a) Hydrogenated and (b) hydroxylated graphene pores, and (c) side view of the computational system investigated in this work.

Another option for molecular sieving is the low-friction flow of solvent through two-dimensional capillaries formed by closely spaced graphene sheets. R.R. Nair et al. observed that submicrometer-thick GO membranes can be completely impermeable to liquids, vapours, and gases, including helium, but allow unimpeded permeation of water¹¹⁸. They commented on the mechanism involved as: A monolayer water proceeds through the capillaries formed in GO membranes. GO laminates consist of crystallites stacked on top of each other. The groups attached to the graphene sheets lead to a relatively large d-spacing. Importantly, such groups tend to cluster and leave large, percolating regions of graphene sheets not oxidized. Therefore, GO laminates are likely to have empty spaces between the non-oxidized regions of graphene sheets. Because d for reduced GO is approximately 4 \AA , the width of the empty space δ can be estimated as approximately 5 \AA , which is sufficient to accommodate a monolayer of water (Fig. 1.10). The described GO membranes can be used as barrier films in the design of filtration and separation materials and for the selective removal of water.

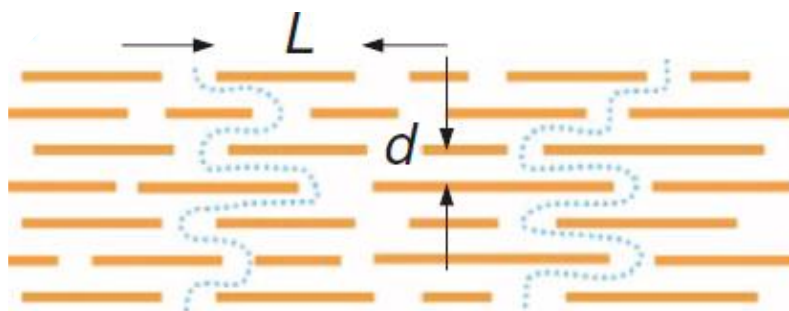


Fig. 1.10 Schematic view for the possible permeation through GO laminates. Typical L/d is ~ 1000 ¹¹⁸.

The nearly frictionless surface of the non-oxidized GO facilitates the extremely fast flow of water molecules. Joshi et al. further reported that ions smaller in size than the GO nanochannel can permeate in the GO membrane at a speed orders of magnitude faster than would occur through simple diffusion¹¹⁹. Size exclusion appears to be the dominant sieving mechanism. Indeed, the GO membrane represents the next generation of ultrathin, high-flux, energy-efficient membranes for precise ionic and molecular sieving in aqueous solution; however, as commented by B. Mi¹²⁰, further research is still needed to thoroughly understand the transport of water and solutes in the GO membrane, especially to fundamentally elucidate other potential separation mechanisms in addition to size exclusion. In addition to the porous graphene monolayer and GO membranes, diamond-like carbon (DLC) is a promising alternative in the permeation of solvents¹²¹. DLC was made just over 40 years ago by Aisenberg and Chabot¹²². Thin transparent films made from compounds very similar to diamond were initially synthesized by means of an ion-beam deposition method. Currently, the widely-used technique for DLC deposition is plasma chemical vapour deposition using organic compounds. S. Karan et al. demonstrated that DLC membranes can be prepared to exhibit extremely high solvent permeability while maintaining considerable mechanical strength¹²¹. They reported the ultrafast permeation of organic solvents through DLC nanosheets, which were free-standing amorphous carbon membranes with a thickness ranging from 10 to 40 nm. Furthermore, the membranes exhibit an excellent separation performance for organic solutes. Interestingly, the solvent flux was mainly affected by the viscosity of the solvent, rather than their molecular size or dipole moment.

1.3.2 Biomimetics

Graphene paper also displayed a potential application in actuators, electromagnetic-free generators, robots and artificial muscles^{42, 123-125}, since it displays a fast response to external stimuli. J. Mu et al.^{125,126} developed a series of graphene monolayer (GM) papers with a gradient reduced graphene oxide/graphene oxide (rGO/GO) structure. In the gradient GM paper, the GO region could readily adsorb/desorb water molecules in response to the environmental humidity, temperature, or light, which resulted in swelling/shrinking of the GO sheets. In contrast, the rGO region was inert to water molecules. Considering this behaviour, together with the excellent photothermal properties of rGO and GO, as well as its high flexibility and mechanical robustness, this graphene paper provides great potential for photoresponsive actuator application. J Mu et al. exploited these properties to produce GM paper with reversible, fast (~ 0.3 s), powerful (7.5×10^5 N \cdot kg⁻¹ force output), and controllable mechanical deformation and recovery, in response to moisture, heat, and light. The response of this water-driven actuator to multiple stimuli allows the fabrication of artificial muscles and electric generators. Furthermore, it was shown that with a programmed dual-gradient (vertical and lateral) structure, a self-folding all-graphene origami could be developed to demonstrate three capabilities: (i) production of pre-designed shapes, (ii) walking, and (iii) turning a corner (Fig. 1.11).

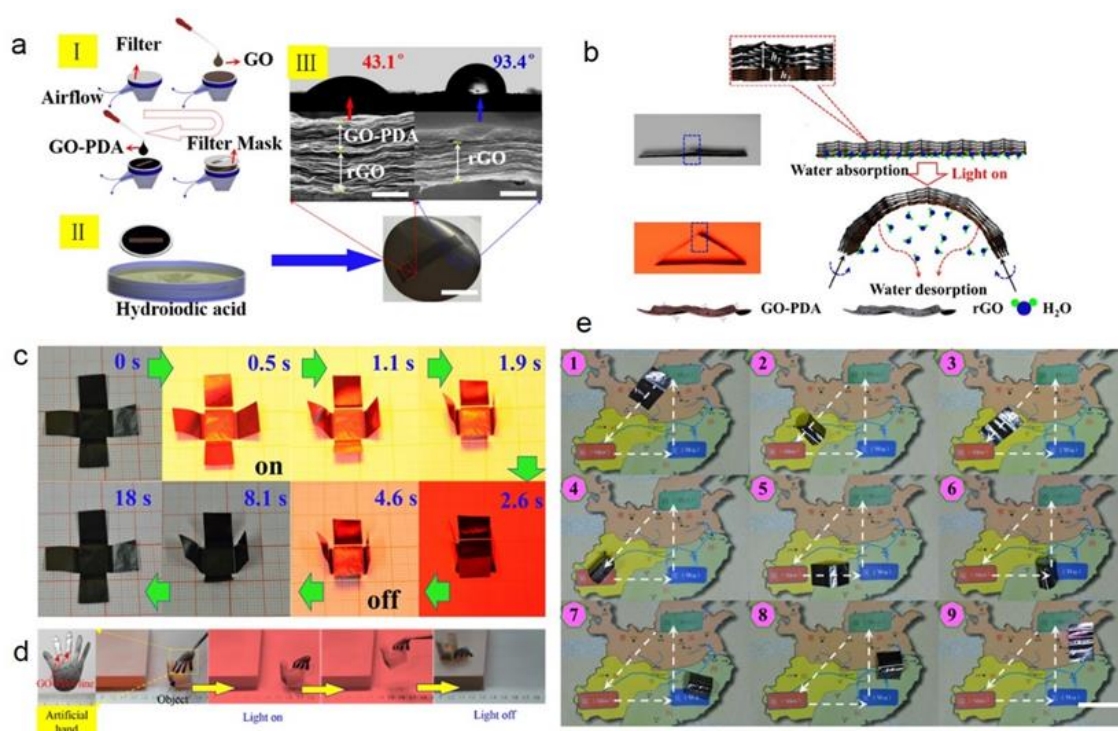


Fig. 1.11. (a) I. Schematic illustration of the mask-assisted filtration process (scale bar, 2 cm). II. Cross-sectional SEM images of GO-PDA/rGO and rGO regions following reduction by HI (scale bar,

1 μm). III.CA measurement of the GO-PDA/rGO surface (43.1°) and rGO surface (93.4°) of dual-gradient GM. (b) Schematic representations of the structures and mechanisms of the graphene paper. With no NIR light irradiation, the GO-PDA/rGO region flattens. A flat freestanding GO-PDA/rGO region starts to bend immediately upon exposure to NIR light irradiation. This bending/unbending mechanism is completely reversible over many cycles. (c) Time profiles of self-folding movements of a cross-shaped piece of paper with and without NIR light irradiation. The sample was placed on the platform and illuminated with NIR light ($100 \text{ mW}\cdot\text{cm}^{-2}$) normal to its surface (light is incident from above). (d) Optical images showing an artificial/robotic hand holding an object driven by light irradiation. (e) Optical images showing the “micro robot” walking and turning on a map driven by light irradiation^{125,126}.

The skin is highly sensitive to pressure and temperature, and is therefore an important feedback source of crucial information. Considering its excellent mechanical, electrical, and thermoelectric properties, graphene papers have attracted increasing attention to mimic the sensing behaviour of natural skin. Hou et al. reported the first graphene paper-based self-healing, mechanically strong and stretchable, pressure-sensing device¹²⁷. It consisted of a piezoelectric polymer layer and a porous graphene layer with a healing substrate. The integrated graphene/polymer hybrid film mimics both the mechanical self-healing and pressure sensitivity behaviour of natural skin without the requirement of an external power supply (Fig. 1.12). Its ultimate strain and tensile strength were even two and ten times larger than the corresponding values of human skin, respectively.

More recently, Hou et al. reported novel paper-like graphene foam that is free-standing, flexible and elastic. It demonstrated temperature sensitivity based on the thermoelectric effects of graphene. Furthermore, this elastic graphene foam exhibited a pressure sensing behaviour under finger pressure. A proof-of-concept graphene pressure sensor pad was manufactured that could locate finger-pressure points and measure the pressure levels. All of the above sensing abilities were demonstrated without the need for an internal/external power supply. The unique passive all-graphene flexible thin-film sensor may open up new opportunities for the development of electronic skin.

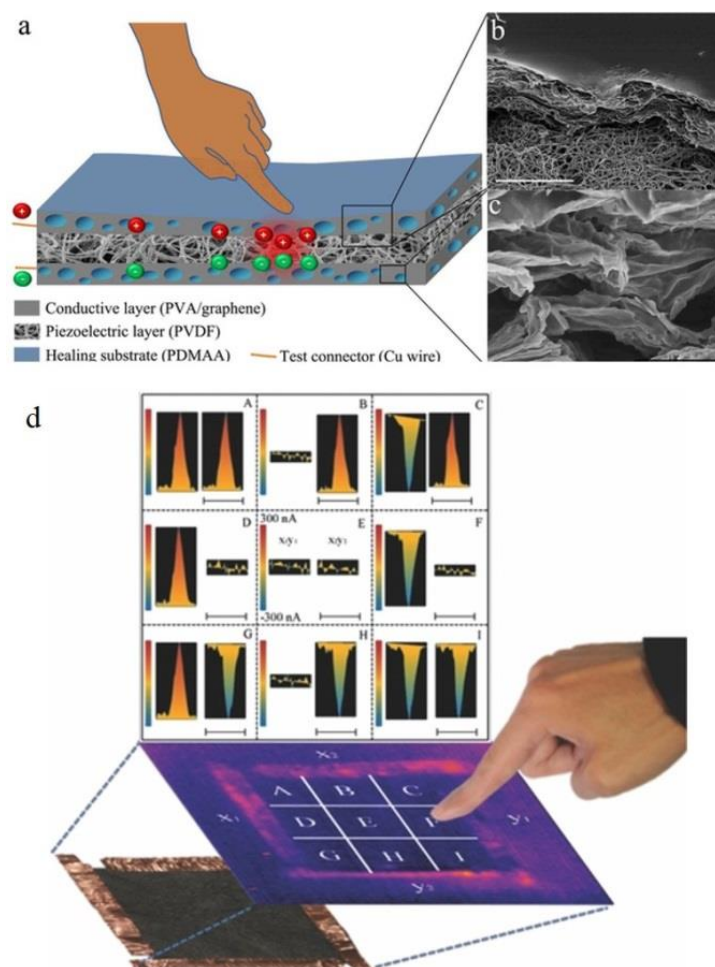


Fig. 1.12 Schematic illustration and images of the graphene-paper based touch sensors. (a-c) A self-healing and stretchable PDMAA/PVA/graphene-PVDF sandwiched thin-film sensor.¹²⁷ (d) A compressive graphene sensor pad.

1.3.3 Applications in flexible substrate

Graphene films that have recently become available on a large scale exhibit good optical transparency, electrical and thermal conductivities, and high temperature stability and mechanical flexibility. Therefore, graphene film, as a solid substrate conducting platform to support functional groups, has attracted a lot of interest. For the fabrication of light-emitting diodes, high-quality GaN/ZnO co-axial nanorod heterostructures have been grown directly on graphene films. The nanostructure LEDs exhibit strong blue emission, even under room illumination⁹⁷. In another study, ZnO nanowire functionalized graphene film was used as an optical device for a constructed nanostructure LED light (Fig. 1.13)¹²⁸. Transparent macroporous graphene thin films (MGTFs) were prepared by using ice crystal-induced phase separation. They have shown wide application to substrates as they can be used as

porous scaffolds with high conductivity for electrochemical deposition of various semiconductors and rare metal nanoparticles, such as CdSe, ZnO, and Pt, as well as successive deposition of different materials. Notably, the macroporous structures bestow the MGTFs and the nanoparticle-decorated MGTFs (i.e., Pt@MGTF and CdSe@MGTF) with an enhanced performance as electrodes for the oxygen reduction reaction and photoelectrochemical H₂ generation¹²⁹. Gyu-Chul Yi's group successfully grew ZnO on a graphene film. They demonstrated the position- and morphology-controlled growth of ZnO nanostructures on graphene layers without using any growth mask or metal catalyst¹³⁰. The microstructures of epitaxial GaN thin films grown on graphene layers using ZnO nanowalls were then investigated. The predominant dislocations in the GaN thin films grown on ZnO-coated graphene layers were mixed-type dislocations. The typical threading dislocation density in the films was determined to range from 1.2×10^9 to 2.4×10^9 cm⁻², which is comparable to that of GaN on Si substrates and slightly higher than that of GaN on sapphire substrates.¹³¹ Fully-flexible and transparent 3-D structure nanogenerators were fabricated by depositing 1-D ZnO nanorods on a 2-D graphene film. This type of nanocomposite is suitable for self-powered RT device applications, such as flexible self-powered touch sensors, wearable artificial skin, fully flexible display mobile devices, and battery supplements for wearable cellular phones¹³². In another study, the power-generating phenomenon of a single GO film with a preformed oxygen-containing group gradient was reported. The GO film was prepared by a moisture/electric field co-induced gradient process of oxygen-containing groups on a vacuum-filtrating GO film, and this strategy that was developed was called moisture–electric annealing. The as-prepared GO film was able to provide a moisture-enabled voltage output of approximately 35 mV with a power density of approximately $4.2 \text{ mW} \cdot \text{m}^{-2}$ by harvesting energy from moisture diffusion with an energy conversion efficiency of up to approximately 62%. This efficiency surpassed the fluidic–electric generators and was even better than those of piezoelectric generators with optimized structure. More interestingly, an extra-power-free respiratory monitor has been built by using the moisture flow of human breath as a clean and renewable power source¹³³.

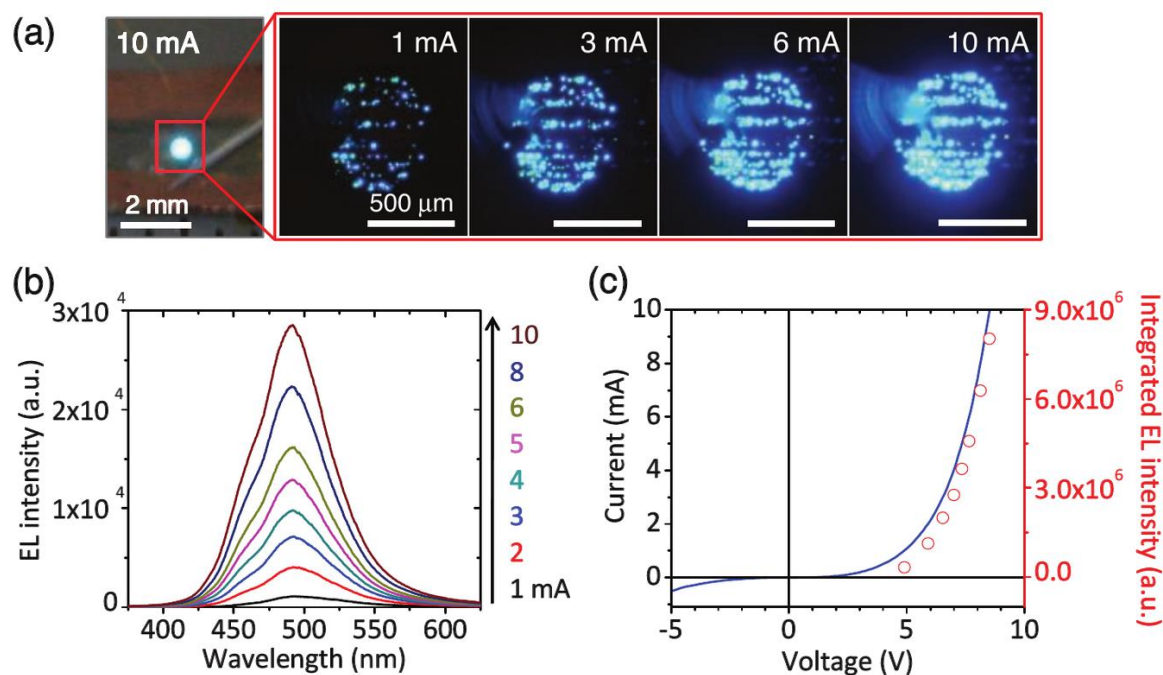


Fig.1.13 Visible nanostructure LEDs on graphene films. a) Photograph and optical microscopy images of the light emission from the LED at different applied currents. b) Power-dependent EL spectra at applied currents of 1–10 mA. c) I – V characteristic curve of the LED (black solid line) and a plot of the integrated EL intensity (red open circles) as a function of the applied bias voltage. a.u., arbitrary unit.

Graphene paper, as a flexible substrate, has not only been used for the growth of nano-objects, but also as a good supporting material for fixing enzymes and growth bacteria to build a membrane-free biofuel cell¹³⁴⁻¹³⁶.

1.3.4 Application in sensors

The self-assembled 2-D graphene paper/film/membrane, functionalized with nano-objects, polymers, and biomolecules, are promising candidates for sensing application. In particular, in the field of electrochemical biosensors with high sensitivity, these candidates have found widespread uses in clinic diagnosis, environment monitoring, and for quality control in industrial, food, and agricultural products.

1.3.4.1 Electrochemical sensors

GO paper has a good mechanical property, which will provide high-quality, microstructure-controllable, free-standing paper electrodes for the detection of small molecules,¹³⁷ bacteria,^{138,139} organophosphates,⁸³ and even viruses¹⁴⁰.

Graphene paper as a sensing platform for detection of H₂O₂ and glucose (Table 1.1) has been attractive owing to its high conductivity bio-compostable, sufficient flexibility, and robust mechanical strength. Based on the graphene film-GOD (glucose oxidase) electrochemical sensor for the detection of glucose, other detectors have been built. For example, LBL self-assembly of glucose oxidase and chitosan nitrogen-doped graphene to fabricate a glucose biosensor was prepared. The biosensor operates at a low potential of -0.2 V (vs Ag/AgCl), exhibiting a high sensitivity of $10.5 \mu\text{A cm}^{-2} \text{mM}^{-1}$, and detection limit of $64 \mu\text{M}$ ¹⁴¹. A GOD-AuNPs-PBNPs-chitosan complex¹⁴² or PANI/AuNPs¹⁴³ as electron transfer media and assistant group to combine GOD with graphene paper, has been proposed as a method for the determination of glucose concentration in whole blood samples within the physiological range (3.9–7.8 mM). Based on the CVD of a graphene film modified by GOD, field-effect transistors for real-time glucose and glutamate sensing have been built¹⁴⁴. Moreover, graphene paper has been functionalized by non-enzymatic catalysts by different techniques, such as PtNPs/MnO₂ nanowires/graphene paper as a free-standing paper electrode for non-enzymatic detection of H₂O₂ enables its use for monitoring H₂O₂ with a linear dynamic range of 2.0 μM to 13.33 mM and LOD down to 1.0 μM (S/N=3)⁹⁸. The sensor response is linear to glucose concentrations in the range from 0.1 mM to 30.0 mM with a detection limit of 0.02 mM (S/N=3) and detection sensitivity of $58.54 \text{mA cm}^{-2} \text{mM}^{-1}$. In addition to that mentioned above, dip-coating gold nanoparticles¹⁴⁵, NiO nanoparticles loaded on graphene paper using the EPD process⁹³, AgNCs directly grown controllably on graphene paper⁸⁹ and LBL self-assembly of AuNPs-embedded porous graphene thin films¹¹⁴ have been used to build a sensing platform for the detection of glucose or H₂O₂.

Our group has successfully fabricated graphene paper doped with chemically compatible Prussian blue nanoparticles and Au@PB NPs¹⁰⁵ as a nanohybrid electrocatalyst. Prussian blue was loaded on the graphene nanosheet by electrostatic attraction. The hybrid materials were characterized by AFM, SEM, and TEM (Figs. 1.14 and 1.15), and indicate that the graphene nanosheet was successfully decorated by PBNPs. However, the surface of the graphene paper was very smooth, and water molecules were also trapped together with the PBNPs on the graphene paper, which could provide a microenvironment for the

accommodation of bio-macromolecules. Cyclic voltammograms (CVs) reveal that heterogeneous electron transfer (ET) reactions arising from the confined PBNPs were reversible and ET kinetics were controlled by mixed diffusion and surface confinement. Using the hybrid materials as a platform for the detection of H_2O_2 , the electrocatalytic reduction of H_2O_2 started at 0.4 V (vs SCE) and tended to reach a maximum effect at potentials more negative than -0.1 V, and a linear relation between electrocatalytic current density and H_2O_2 concentration was observed in the range of 1–7 mM, with the detection limit of approximately $5 \mu\text{M}^{24}$.

Electrochemiluminescence (ECL) sensors are very important. Therefore, ECL sensors have recently been developed based on graphene paper. For example, a novel biosensor was developed using immobilized $\text{Ru}(\text{bpy})_3^{2+}$ and alcohol dehydrogenase (ADH) on a graphene/bovine serum albumin composite film for the detection of ethanol¹³⁷. Xu YH et al. used a poly(sodium 4-styrenesulfonate) functionalized graphene/Nafion composite film to prepare a paper-based solid-state electrochemiluminescence sensor and applied it to detect tripropylamine. A low detection limit (S/N=3) of 5.0 nM was obtained. It also exhibited excellent reproducibility (relative standard deviations of 0.63% for continuous 45 cycles) and long-term stability ($\sim 80\%$ of its initial ECL intensity could be retained over 3 months). Furthermore, highly porous Fe_3O_4 nanocrystal clusters as well as poly(sodium 4-styrenesulfonate) were used to hybridize graphene paper. This type of graphene paper showed high performance to compounds containing tertiary amino groups and DNA with guanine and adenine, when it was applied as an ECL sensor^{146, 147}.

Impedimetric immunosensors for the detection of bacteria have been a hot topic because of the frequency of food safety accidents. An efficient, low-cost, and robust impedimetric immunosensor for the rapid and sensitive detection of *Escherichia coli* O157:H7 (*E. coli* O157:H7) was developed by using a gold nanoparticles hybrid free-standing graphene paper electrode. The graphene paper was prepared by chemical reduction of GO paper obtained from the vacuum filtration method. The gold nanoparticles were grown on the surface of the graphene paper electrode by a one-step electrodeposition technique. Immobilization of anti-*Escherichia coli* O157:H7 antibodies on the paper electrode were performed using the biotin-streptavidin system. Electrochemical impedance spectroscopy was used to detect *E. coli* O157:H7 captured on the paper electrode with a broad linear range (1.5×10^2 – 1.5×10^7 cfu mL^{-1}) and low detection limit (1.5×10^2 cfu mL^{-1})¹³⁸.

Photoelectrochemical sensing is another key technique as a branch of electrochemical sensing, based on a TiO₂–graphene complex nanopaper. An advanced photoelectrochemical biosensing device for the detection of carcinoembryonic antigens has been proposed working at a relatively low applied potential¹⁴⁸.

Moreover, a microfluidic biochip was prepared by graphene paper and functionalized with antibodies, enzymes, and aptamers as a biosensor for the multiplexed detection of different metabolites, such as glucose, lactate, xanthine, and cholesterol. The results showed that the graphene biosensor arrays can detect multiple metabolites on a microfluidic paper sensitively, rapidly, and simultaneously¹⁴⁹.

Table 1.1 Summary of the graphene paper based platforms for detection of glucose and H₂O₂

Materials	catalyst	Analyst	methods	LOD	ref
AuNPs/Graphene paper	AuNPs	Glucose	Chronoamperometry	5 μ M	145
AuNPs/PANI/graphene paper- GOD	AuNPs	Glucose	DPV		143
PBNPs/Graphene paper-GOD	GOD	Glucose	Chronoamperometry	10 μ M	24
Chitosan/graphene-GOD	GOD	Glucose	Chronoamperometry	64 μ M	141
SiO ₂ @CeO ₂ /graphene paper-GOD	GOD	Glucose	Colorimetric	0.2 mM	150
PtNPs/MnO ₂ nanowires/graphene paper	PtNPs	Glucose	Chronoamperometry	0.02mM	99
NiO/graphene paper	NiO	Glucose	Chronoamperometry	0.1 μ M	93
PBNPs/Graphene paper-GOD	GOD	Glucose	Chronoamperometry	8.4 μ M	151
AuNPs/graphene-GOD	GOD	Glucose	Chronoamperometry	4.1 μ M	152
PtNPs/graphene film	PtNPs	Glucose	Chronoamperometry	1 μ M	100
ZrO ₂ /graphene film-GOD	GOD	Glucose	Chronoamperometry	45.6 μ M	153
GOD-AuNPs-PBNPs chitosan/graphene	GOD	Glucose	Chronoamperometry	10 μ M	142
AuNPs/PANI/graphenepaper- GOD	AuNPs	H ₂ O ₂	DPV		143
AuNPs/Graphene paper	AuNPs	H ₂ O ₂	Chronoamperometry	2 μ M	145
PBNPs/Graphene paper-	PBNPs	H ₂ O ₂	Chronoamperometry	5 μ M	24
SiO ₂ @CeO ₂ /graphene paper		H ₂ O ₂	Colorimetric	9nM	164
PtNPs/MnO ₂ nanowires/graphene paper	PtNPs	H ₂ O ₂	Chronoamperometry	1 μ M	98
HRP/graphene film	HRP	H ₂ O ₂	CVs	1.17 mM	154
PBNPs/Graphene paper	PBNPs	H ₂ O ₂	Chronoamperometry	1.5 μ M	151
AgNCs/graphene film	AgNCs	H ₂ O ₂	Chronoamperometry	3 μ M	89
AuNPs-Embedded Porous Graphene Thin Films	AuNPs	H ₂ O ₂	Chronoamperometry	0.1 μ M	114
PtNPs/graphene film	PtNPs	H ₂ O ₂	Chronoamperometry	0.2 μ M	100

1.3.4.2 Chemical sensors

The two-dimensional structure of graphene makes the electron transport through graphene highly sensitive to the adsorption of gas molecules. The adsorption of gas molecules on graphene's surface leads to changes in its electrical conductivity that can be attributed to the change in the local carrier concentration induced by the surface adsorbates, which act as electron donors or acceptors. O. Leenaerts et al. reported a gas (NH₃, CO, NO₂, and NO) sensor based on the absorption of gas on graphene film using first-principles calculations¹⁵⁵. The film, with a thickness of 1.5 nm, displayed high chemical sensitivity in the range of tens of ppb owing to the enriched hole-like carrier concentration through the electron transfer from a p-type electron withdrawing graphene to NO₂ acceptors adsorbed on graphene (Fig.1. 16)¹⁵⁶. Samsonau et al. fabricated a gas sensor based on a CVD graphene-like film for the detection of NO₂¹⁵⁷. A low cost conductometric sensing device, based on

using rGO as the sensing material on a porous paper substrate, was presented. The sensor exhibited high sensitivity towards NO_2 , and the detection limit was well in the sub-ppm level. The thickness of the rGO film affected the sensitivity of the sensor in such a way that the thinner (10 nm) films exhibited a better performance¹⁵⁸. Freestanding three-dimensional graphene network structure graphene paper was fabricated by the CVD method to build graphene paper sensors for the detection of NH_3 . The detection principle was ascribed to the effective charge carrier transport between the foam with large porosity and the few-layer graphene component and the adsorbed gas species¹⁵⁹. Furthermore, to improve the sensitivity and selectivity, nano-objects (AuNPs ¹⁶⁰ and Au@PtNPs ¹⁰¹) and pyrenebutyric acid¹⁵⁶ were combined with graphene paper by electrostatic or covalent-bond physical absorption to build a flexible biosensor to real-time monitor live cell secretion of nitric oxide with a broad linear range, low detection limit, high sensitivity, and good selectivity against interferences often existing in biological systems. Moreover, based on the pyrenebutyric acid functionalized free-standing graphene film, a new type of flexible H_2S sensor with high selectivity was presented by Dong et al. using Fe_2O_3 nanoparticles-modified graphene paper^{161, 162}.

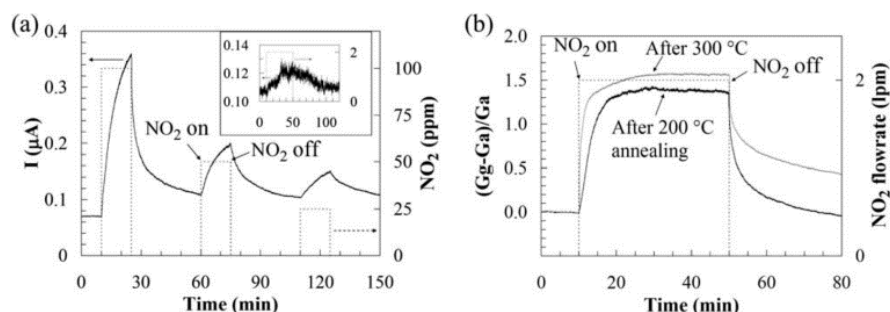


Fig. 1.16 (a) Room-temperature sensing behavior of GO after annealing in Ar at 200 °C for 1 h. (b) 300 °C annealing improved sensitivity and response time but lengthened recovery time, compared to 200 °C annealing¹⁵⁶.

Moreover, based on the reflectance change with the varied optical and geometric properties of the sensing layers absorbing the gas molecules, Some et al. constructed a new type of one-headed polymer optical sensor array with hydrophilic GO and hydrophobic rGO for sensing volatile organics¹⁶³. The sensing device offered the ability to distinguish between THF and dichloromethane, owing to the strong interactions of oxygenated groups of GO with polar organic THF¹⁶⁴. Furthermore, the GO sensor displayed a high sensitivity under

extreme conditions, such as strongly acidic or basic conditions, or a high humidity environment.

In addition to the gas species, GO-based assemblies showed high sensitivity to moisture^{42, 124}, this can be attributed to the planar structure and abundance of oxygen-containing groups on the GO sheets. Park et al. constructed a smart paper actuator composed of adjacent GO and CNT films, based on the sensitivity of GO to humidity¹⁶⁵.

Graphene paper colorimeter sensors display a lot of advantages, such as visualization, low cost simplicity, rapidity, and high sensitivity. A new kind colorimeter sensor for the detection of hazardous volatile organics, including tetrahydrofuran (THF), chloroform, methanol, and dimethylformamide (DMF), was developed based on a graphene–polydiacetylene (PDA) composite film. First, graphene film was immersed in PCDA solution and PCDA was fixed on the graphene nanosheet through π – π stacking. After UV illumination treatment, the precursor self-assembled to “blue-phase” PDA. Owing to the merits of the large surface area and high transparency of the graphene film as an efficient support, the colorimetric response from the structural conformation changes of PDA could be visually investigated at a relatively high concentration of organics. The well-fitting relationship between the chromatic response and the organic concentration in the range of 0.01–10% quantitatively provides the foundation for organic detection in practical applications¹⁶⁶.

In addition, due to its good biocompatibility, the freestanding hybrid film sensor would be a promising candidate for biological, medical, and pharmaceutical applications. Caryn L. Heldt et al. fabricated a microdevice sensor for the detection of proteins in solution by measuring the surface electrical resistivity of graphene/cellulose composite paper as a function of protein concentration¹⁶⁷. Different kinds of bioactive (glucose oxidase, cholesterol oxidase, cholesterol esterase, lactate oxidase, and HRP) functionalized SiO₂@CeO₂/graphene were used for the colorimetric detection of lactate, uric acid, cholesterol and glucose.¹⁵⁰ Ping Zuo et al. presented microfluidic systems for the detection of two infectious pathogens—*Staphylococcus aureus* and *Salmonella enterica*—using fluorescence marked aptamer-functionalized graphene paper¹⁴⁹. A pH sensor was built using upconversion luminescence nanomaterials hybrid graphene paper¹⁶⁸ and high-performance flexible potentiometric sensing devices using freestanding graphene paper functional with ions-selective electrodes have been constructed¹⁶⁹.

1.3.5 Application in energy device

Increasing research efforts have been focused on developing flexible, lightweight, and even wearable energy systems because of their potential applications in wearable electronic devices such as flexible displays, paper-like mobile phones, and other collapsible functional devices. Here I summarized several types of wearable energy systems, including batteries, supercapacitors, and fuel cells, based on graphene papers, in my thesis I mainly address to applied graphene paper in supercapacitor materials.

Supercapacitors (SCs), state-of-the-art charge–storage systems, also known as electrochemical capacitors, have attracted much attention as a result of their promising features, such as high power densities, fast charge–discharge rates, reliable cycling lives, safe operation, and simple two-electrode ‘sandwich’ configuration¹⁷⁰⁻¹⁷². The macroscopic construction of the cell system, as well as the microstructures of electrodes, greatly influences the energy and power densities of SCs. According to the equation $E = 1/2CV^2$, the energy density (E) of an SC can be enhanced by increasing the device capacitance (C) and/or increasing the cell voltage (V). An efficient way to increase the energy density is to fabricate asymmetric SCs (so called hybrid electrochemical capacitors), which can provide a wider operating voltage. Graphene has been widely used as electrode materials in SCs. Normally, graphene-based powder materials are compressed into graphene membrane electrodes. Therefore, there is an obvious boundary between graphene nanomaterial electrodes and graphene paper electrodes, except for some specific cases.

S.O. Kim et al. reported the development of flexible graphene/mesoporous carbon films, which show a specific capacitance value of $86.7 \text{ F}\cdot\text{g}^{-1}$ in $1 \text{ M H}_2\text{SO}_4$ solution¹⁷³. Later, D. Mitlin et al. reported a sponge-like graphene based supercapacitor, which showed an extremely high power density of $48 \text{ kW}\cdot\text{kg}^{-1}$ ¹⁷⁴.

In addition to pure graphene, activated graphene materials have proven to be more promising as candidates for SC electrodes. R.S. Ruoff et al. reported that the specific surface area of the graphene prepared by microwave exfoliation of GO was significantly enhanced to $3100 \text{ m}^2\cdot\text{g}^{-1}$ after activation by KOH. The activation treatment of graphene not only increased its specific surface area but also enabled a superior supercapacitor performance. A rectangle-like CV behaviour was maintained at a scan rate as high as $500 \text{ mV}\cdot\text{s}^{-1}$ in an organic electrolyte. Graphene paper was prepared by holey graphene (h-graphene) to improve the accessibility of electrolytes and ions to the graphene surface. The ultracapacitor

electrodes based on h-graphene showed a remarkably improved volumetric capacitance with an approximately 700% increase compared to that of regular graphene electrodes¹⁷⁵.

Boron, nitrogen, phosphorus, oxygen, and sulphur are the most used elements for doping graphene. This could lead to an increase of the charge carrier concentration, specific surface area, and enhanced capacitance retention. Among these elements, a maximum proton loading can be achieved with boron substitution, further establishing the ability of B doping to enhance the interfacial capacitance¹⁷⁶. However, previous studies indicate that the actual capacitive performance is much lower than the anticipated value estimated from the ultrahigh theoretical surface area, which arises from the aggregation and restacking of graphene nanosheets in graphene papers. Therefore, various graphene-based composites/hybrids, including metal oxide nanoparticle/graphene and polymer chain/graphene papers, have been demonstrated to solve the above problem. Wang's group demonstrated a simple method for preparing flexible, freestanding, three-dimensional porous graphene/MnO₂ nanorod and graphene/Ag hybrid thin-film electrodes. These graphene hybrid films accelerate ion and electron transport by providing lower ion-transport resistances and shorter diffusion-distances, thus exhibiting high specific capacitances and power performances, and also having excellent mechanical flexibility¹⁷⁷.

Graphene/manganese dioxide (MnO₂) composite papers (GMCP) have been fabricated by a simple three-step route: preparation of the GO/MnO₂ composite (GOMC) dispersion, subsequent vacuum filtration of the GOMC dispersion to achieve GO/MnO₂ composite paper (GOMCP), and finally, thermal reduction of GOMCP to generate GMCP. The morphology and microstructure of the prepared samples were characterized by field-emission scanning electron microscopy, transmission electron microscopy, Raman spectroscopy, Fourier transformation infrared spectroscopy, thermal gravimetric analysis, and X-ray photoelectron spectroscopy. Moreover, as a binder-free and flexible electrode material for supercapacitors, the electrochemical properties of the prepared GMCP were evaluated by cyclic voltammetry and galvanostatic charge/discharge tests. As a result, the specific capacitance of the GMCP with the MnO₂ weight ratio of 24% (GMCP-24) reached 256 F•g⁻¹ at a current density of 500 mA•g⁻¹, and also showed good cycle stability, indicating a promising potential application as an effective electrode material for supercapacitors¹⁷⁸.

Asymmetric SC can be fabricated by using different graphene composite/hybrid papers as positive and negative electrodes, respectively. Compared with conventional symmetric SCs, asymmetric SCs can make full use of the different potential windows of the two electrodes to broaden the maximum operating voltage of the cell system, which leads to an obvious improvement in the specific capacitance and energy density. The ability to fabricate flexible electrodes that exhibit very large surface areas and unusual or novel physical and electronic properties, and that can be assembled into asymmetric SCs, is therefore necessary for applications.

Polymer/graphene composite papers have also attracted great attention because of their relatively high strength when compared to pure inorganic based electrodes. Moreover, when applying graphene in conductive polymers, the conductivity of the polymers would also be increased. G. Shi et al. reported a flexible SC based on a polyaniline/graphene film¹⁷⁹. The conductivity of polyaniline fibres was found to be increased up to 44% when the composite was made with graphene. This flexible composite SC had a specific capacitance of $210 \text{ F}\cdot\text{g}^{-1}$ at a current density of $0.3 \text{ A}\cdot\text{g}^{-1}$.

Supercapacitor performance is significantly affected by the transport rates of electrons and ions, which usually depend on the microstructure and conductive characteristics of the electrode materials. These can be improved by fabricating interconnected electrode materials with a high conductivity and porous structure.²¹ 3-D graphene materials, consisting of micro-, meso-, and even macroporous networks, can provide high surface area, light-weight, and fast ion/electron transport.

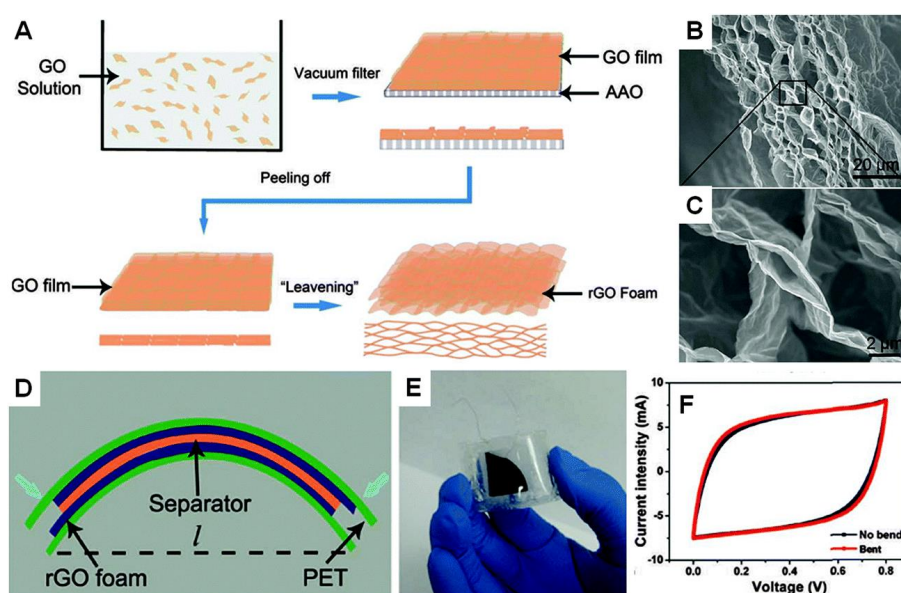


Fig. 1.17 (A) Schematic drawings illustrating the process to prepare RGO foams. (B and C) Cross-sectional SEM images of RGO foams. (D and E) Schematic diagram and optical image of the flexible RGO foam supercapacitor. (F) CV curves of the RGO foam supercapacitor before bending and while bent.

The rGO foam supercapacitor is able to bend. For example, Chen et al. reported a “leavening” process to transform compact graphene paper to porous graphene film (Fig. 1.17)²⁹. They used a filtration assembled graphene paper as dough and hydrazine vapour as foaming and reducing agent. Cross-sectional SEM images indicated the formation of an open porous graphene foam network with pore sizes in the range of sub-micrometer to several micrometers. They concluded that the hydrazine vapour induced gaseous species (such as H₂O and CO₂) were responsible for the formation of the porous structure. They built flexible supercapacitors by using freestanding rGO foams as both current collectors and electrodes. The specific capacitance of the resulting rGO foam was 110 F•g⁻¹. It was found that there was only a very slight difference in the CV curves when the distance between the two sides of the supercapacitor was changed from 3 to 2 cm under bending.

Scale-up assembly of nanomaterials such as graphene and its derivatives is a promising way to enable the materials being connected to real-world applications. In our work, Nano-structured *Prussian Blue* was used as redox group loading to graphene paper to fabricate a new kind paper-like electrode in Chapters 3-5. In Chapters 6-8, graphene papers were used as a sacrificial template to synthesize ultralight 2D metal oxide papers.

References

1. K. S. Novoselov, A. K. Geim, S. V. Morozov, D. Jiang, Y. Zhang, S. V. Dubonos, I. V. Grigorieva and A. A. Firsov, *Science*, 2004, **306**, 666-669.
2. K. S. Novoselov, D. Jiang, F. Schedin, T. J. Booth, V. V. Khotkevich, S. V. Morozov and A. K. Geim, *PNAS*, 2005, **102**, 10451-10453.
3. K. S. Novoselov, A. K. Geim, S. V. Morozov, D. Jiang, M. I. Katsnelson, I. V. Grigorieva, S. V. Dubonos and A. A. Firsov, *Nature*, 2005, **438**, 197-200.
4. Y. Hernandez, V. Nicolosi, M. Lotya, F. M. Blighe, Z. Sun, S. De, I. T. McGovern, B. Holland, M. Byrne, Y. K. Gun'ko, J. J. Boland, P. Niraj, G. Duesberg, S. Krishnamurthy, R. Goodhue, J. Hutchison, V. Scardaci, A. C. Ferrari and J. N. Coleman, *Nat. Nanotechnol.*, 2008, **3**, 563-568.
5. C. Valles, C. Drummond, H. Saadaoui, C. A. Furtado, M. He, O. Roubeau, L. Ortolani, M. Monthieux and A. Penicaud, *J. Am. Chem. Soc.*, 2008, **130**, 15802-15804.
6. A. B. Bourlinos, V. Georgakilas, R. Zboril, T. A. Steriotis and A. K. Stubos, *Small*, 2009, **5**, 1841-1845.
7. Y. Hao, M. S. Bharathi, L. Wang, Y. Liu, H. Chen, S. Nie, X. Wang, H. Chou, C. Tan, B. Fallahzad, H. Ramanarayan, C. W. Magnuson, E. Tutuc, B. I. Yakobson, K. F. McCarty, Y. Zhang, P. Kim, J. Hone, L. Colombo and R. S. Ruoff, *Science*, 2013, **342**, 720-723.

8. X. Li, W. Cai, J. H. An, S. Kim, J. Nah, D. Yang, R. Piner, A. Velamakanni, I. Jung, E. Tutuc, S. K. Banerjee, L. Colombo and R. S. Ruoff, *Science*, 2009, **324**, 1312-1314.
9. Z. Sun, Z. Yan, J. Yao, E. Beitler, Y. Zhu and J. M. Tour, *Nature*, 2010, **468**, 549-552.
10. G. Eda, G. Fanchini and M. Chhowalla, *Nat. Nanotechnol.*, 2008, **3**, 270-274.
11. S. Stankovich, D. A. Dikin, G. H. B. Dommett, K. M. Kohlhaas, E. J. Zimney, E. A. Stach, R. D. Piner, S. T. Nguyen and R. S. Ruoff, *Nature*, 2006, **442**, 282-286.
12. X. Fan, W. Peng, Y. Li, X. Li, S. Wang, G. Zhang and F. Zhang, *Adv. Mater.*, 2008, **20**, 4490-4493.
13. K. V. Emtsev, A. Bostwick, K. Horn, J. Jobst, G. L. Kellogg, L. Ley, J. L. McChesney, T. Ohta, S. A. Reshanov, J. Roehrl, E. Rotenberg, A. K. Schmid, D. Waldmann, H. B. Weber and T. Seyller, *Nat. Mater.*, 2009, **8**, 203-207.
14. L. Y. Jiao, L. Zhang, X. R. Wang, G. Diankov and H. J. Dai, *Nature*, 2009, **458**, 877-880.
15. D. V. Kosynkin, A. L. Higginbotham, A. Sinitskii, J. R. Lomeda, A. Dimiev, B. K. Price and J. M. Tour, *Nature*, 2009, **458**, 872-875.
16. A. Rouhanipour, M. Roy, X. L. Feng, H. J. Rader and K. Mullen, *Angew. Chem. Int. Ed.*, 2009, **48**, 4602-4604.
17. L. J. Zhi and K. Mullen, *J. Mater. Chem.*, 2008, **18**, 1472-1484.
18. G. Liu, W. Jin and N. Xu, *Chem. Soc. Rev.*, 2015, **44**, 5016-5030.
19. H. Gao and H. Duan, *Biosens. Bioelectron.*, 2014, **65**, 404-419.
20. X. Zhao, P. Zhang, Y. Chen, Z. Su and G. Wei, *Nanoscale*, 2015, **7**, 5080-5093.
21. Y. Shao, M. F. El-Kady, L. J. Wang, Q. Zhang, Y. Li, H. Wang, M. F. Mousavi and R. B. Kaner, *Chem. Soc. Rev.*, 2015, **44**, 3639-3665.
22. D. A. Dikin, S. Stankovich, E. J. Zimney, R. D. Piner, G. H. B. Dommett, G. Evmenenko, S. T. Nguyen and R. S. Ruoff, *Nature*, 2007, **448**, 457-460.
23. G. Wang, X. Sun, F. Lu, H. Sun, M. Yu, W. Jiang, C. Liu and J. Lian, *Small*, 2012, **8**, 452-459.
24. N. Zhu, S. Han, S. Gan, J. Ulstrup and Q. Chi, *Adv. Funct. Mater.*, 2013, **23**, 5297-5306.
25. H. Chen, M. B. Mueller, K. J. Gilmore, G. G. Wallace and D. Li, *Adv. Mater.*, 2008, **20**, 3557-3561.
26. O. C. Compton, D. A. Dikin, K. W. Putz, L. C. Brinson and S. T. Nguyen, *Adv. Mater.*, 2010, **22**, 892-896.
27. X. Y. Lin, X. Shen, Q. B. Zheng, N. Yousefi, L. Ye, Y. W. Mai and J. K. Kim, *ACS Nano*, 2012, **6**, 10708-10719.
28. C. Hou, H. Wang, Q. Zhang, Y. Li and M. Zhu, *Adv. Mater.*, 2014, **26**, 5018-5024.
29. Z. Niu, J. Chen, H. H. Hng, J. Ma and X. Chen, *Adv. Mater.*, 2012, **24**, 4144-4150.
30. Q. Shi, C. Hou, H. Wang, Q. Zhang and Y. Li, *J. Mater. Chem. A*, 2015, **3**, 9882-9889.
31. G. K. Ramesha and S. Sampath, *J. Phys. Chem. C*, 2009, **113**, 7985-7989.
32. M. A. Raj and S. A. John, *J. Phys. Chem. C*, 2013, **117**, 4326-4335.
33. S. L. Yang, B. F. Xu, J. Q. Zhang, X. D. Huang, J. Ye and C. Z. Yu, *J. Phys. Chem. C*, 2010, **114**, 4389-4393.
34. L. J. Cote, F. Kim and J. Huang, *J. Am. Chem. Soc.*, 2009, **131**, 1043-1049.
35. F. Kim, L. J. Cote and J. Huang, *Adv. Mater.*, 2010, **22**, 1954-1958.
36. D. D. Kulkarni, I. Choi, S. Singamaneni and V. V. Tsukruk, *ACS Nano*, 2010, **4**, 4667-4676.
37. Q. Zheng, W. H. Ip, X. Lin, N. Yousefi, K. K. Yeung, Z. Li and J. K. Kim, *ACS Nano*, 2011, **5**, 6039-6051.
38. X. Lin, J. Jia, N. Yousefi, X. Shen and J.-K. Kim, *J. Mater. Chem. C*, 2013, **1**, 6869-6877.
39. C. Chen, Q. Yang, Y. Yang, W. Lv, Y. Wen, P. Hou, M. Wang and H. Cheng, *Adv. Mater.*, 2009, **21**, 3007-3011.
40. C. Chen, Q. Zhang, C. Huang, X. Zhao, B. Zhang, Q. Kong, M. Wang, Y. Yang, R. Cai and D. Su, *Chem. Commun.*, 2012, **48**, 7149-7151.
41. S. J. Woltornist, A. J. Oyer, J. M. Carrillo, A. V. Dobrynin and D. H. Adamson, *ACS Nano*, 2013, **7**, 7062-7066.
42. S. Borini, R. White, D. Wei, M. Astley, S. Haque, E. Spigone, N. Harris, J. Kivioja and T. Ryhanen, *ACS Nano*, 2013, **7**, 11166-11173.

43. B. H. Wee and J. D. Hong, *Adv. Funct. Mater.*, 2013, **23**, 4657-4666.
44. X. Li, G. Zhang, X. Bai, X. Sun, X. Wang, E. Wang and H. Dai, *Nat. Nanotechnol.*, 2008, **3**, 538-542.
45. T. Li, J. R. Hauptmann, Z. Wei, S. Petersen, N. Bovet, T. Vosch, J. Nygard, W. P. Hu, Y. Q. Liu, T. Bjornholm, K. Norgaard and B. W. Laursen, *Adv. Mater.*, 2012, **24**, 1333-1339.
46. S. Seo, M. Min, J. Lee, T. Lee, S. Y. Choi and H. Lee, *Angew. Chem. Int. ed.*, 2012, **51**, 108-112.
47. A. Chavez-Valdez, M. S. Shaffer and A. R. Boccaccini, *J. Phys. Chem. B.*, 2013, **117**, 1502-1515.
48. S. An, Y. Zhu, S. H. Lee, M. D. Stoller, T. Emilsson, S. Park, A. Velamakanni, J. An and R. S. Ruoff, *J. Phys. Chem. Lett.*, 2010, **1**, 1259-1263.
49. S. A. Hasan, J. L. Rigueur, R. R. Harl, A. J. Krejci, I. Gonzalo-Juan, B. R. Rogers and J. H. Dickerson, *ACS Nano*, 2010, **4**, 7367-7372.
50. G. F. Cai, J. P. Tu, J. Zhang, Y. J. Mai, Y. Lu, C. D. Gu and X. L. Wang, *Nanoscale*, 2012, **4**, 5724-5730.
51. H. Zhang, X. Zhang, D. Zhang, X. Sun, H. Lin, C. Wang and Y. Ma, *J. Phys. Chem. B*, 2013, **117**, 1616-1627.
52. S. Liu, J. Ou, J. Wang, X. Liu and S. Yang, *J. Appl. Electrochem.*, 2011, **41**, 881-884.
53. Y. Chen, X. Zhang, P. Yu and Y. Ma, *J. Power Sources*, 2010, **195**, 3031-3035.
54. D. H. Lee, J. E. Kim, T. H. Han, J. W. Hwang, S. Jeon, S. Y. Choi, S. H. Hong, W. J. Lee, R. S. Ruoff and S. O. Kim, *Adv. Mater.*, 2010, **22**, 1247-1252.
55. B. Aleman, W. Regan, S. Aloni, V. Altoe, N. Alem, C. Girit, B. S. Geng, L. Maserati, M. Crommie, F. Wang and A. Zettl, *ACS Nano*, 2010, **4**, 4762-4768.
56. S. Lee, K. Lee and Z. H. Zhong, *Nano Lett.*, 2010, **10**, 4702-4707.
57. K. S. Kim, Y. Zhao, H. Jang, S. Y. Lee, J. M. Kim, K. S. Kim, J. H. Ahn, P. Kim, J. Y. Choi and B. H. Hong, *Nature*, 2009, **457**, 706-710.
58. A. Reina, X. Jia, J. Ho, D. Nezich, H. Son, V. Bulovic, M. S. Dresselhaus and J. Kong, *Nano Lett.*, 2009, **9**, 30-35.
59. M. Losurdo, M. M. Giangregorio, P. Capezzuto and G. Bruno, *Phys. Chem. Chem. Phys.*, 2011, **13**, 20836-20843.
60. M. E. Ramon, A. Gupta, C. Corbet, D. A. Ferrer, H. C. P. Movva, G. Carpenter, L. Colombo, G. Bourianoff, M. Doczy, D. Akinwande, E. Tutuc and S. K. Banerjee, *ACS Nano*, 2011, **5**, 7198-7204.
61. H. Bi, S. Sun, F. Huang, X. Xie and M. Jiang, *J. Mater. Chem.*, 2012, **22**, 411-416.
62. Z. Liu, L. Song, S. Zhao, J. Huang, L. Ma, J. Zhang, J. Lou and P. M. Ajayan, *Nano Lett.*, 2011, **11**, 2032-2037.
63. J. Chen, Y. Guo, Y. Wen, L. Huang, Y. Xue, D. Geng, B. Wu, B. Luo, G. Yu and Y. Liu, *Adv. Mater.*, 2013, **25**, 992-997.
64. G. Wang, M. Zhang, Y. Zhu, G. Ding, D. Jiang, Q. Guo, S. Liu, X. Xie, P. Chu, Z. Di and X. Wang, *Sci. Rep.-UK*, 2013, **3**, 2465.
65. X. Cao, D. Qi, S. Yin, J. Bu, F. Li, C. F. Goh, S. Zhang and X. Chen, *Adv. Mater.*, 2013, **25**, 2957-2962.
66. S. Y. Yin, Y. Goldovsky, M. Herzberg, L. Liu, H. Sun, Y. Zhang, F. B. Meng, X. Cao, D. Sun, H. Chen, A. Kushmaro and X. Chen, *Adv. Funct. Mater.*, 2013, **23**, 2972-2978.
67. S. Y. Yin, Y. Y. Zhang, J. H. Kong, C. J. Zou, C. M. Li, X. H. Lu, J. Ma, F. Y. C. Boey and X. D. Chen, *ACS Nano*, 2011, **5**, 3831-3838.
68. L. Zhang, X. Zhao, M. D. Stoller, Y. Zhu, H. Ji, S. Murali, Y. Wu, S. Perales, B. Clevenger and R. S. Ruoff, *Nano Lett.*, 2012, **12**, 1806-1812.
69. Y. Zhu, S. Murali, M. D. Stoller, K. J. Ganesh, W. Cai, P. J. Ferreira, A. Pirkle, R. M. Wallace, K. A. Cychoz, M. Thommes, D. Su, E. A. Stach and R. S. Ruoff, *Science*, 2011, **332**, 1537-1541.
70. F. Liu, S. Song, D. Xue and H. Zhang, *Adv. Mater.*, 2012, **24**, 1089-1094.
71. P. Simek, Z. Sofer, O. Jankovsky, D. Sedmidubsky and M. Pumera, *Adv. Funct. Mater.*, 2014, **24**, 4878-4885.
72. S. H. Bae, O. Kahya, B. K. Sharma, J. Kwon, H. J. Cho, B. Ozyilmaz and J. H. Ahn, *ACS Nano*, 2013, **7**, 3130-3138.

73. J. Shang, Y. Zhang, L. Yu, X. Luan, B. Shen, Z. Zhang, F. Lv and P. K. Chu, *J. Mater. Chem. A*, 2013, **1**, 884-890.
74. N. Ruecha, R. Rangkupan, N. Rodthongkum and O. Chailapakul, *Biosens. Bioelectron.*, 2014, **52**, 13-19.
75. A. K. Sarker and J. D. Hong, *Langmuir*, 2012, **28**, 12637-12646.
76. S. Liu, X. Liu, Z. Li, S. Yang and J. Wang, *New J. Chem.*, 2011, **35**, 369-374.
77. D. K. Huang, B. Y. Zhang, Y. B. Zhang, F. Zhan, X. B. Xu, Y. Shen and M. K. Wang, *J. Mater. Chem. A*, 2013, **1**, 1415-1420.
78. W. Qi, Z. Xue, W. Yuan and H. Wang, *J. Mater. Chem. B*, 2014, **2**, 325.
79. J. T. Chen, Y. J. Fu, Q. F. An, S. C. Lo, S. H. Huang, W. S. Hung, C. C. Hu, K. R. Lee and J. Y. Lai, *Nanoscale*, 2013, **5**, 9081-9088.
80. X. Yan, J. Chen, J. Yang, Q. Xue and P. Miele, *ACS Appl. Mater. Inter.*, 2010, **2**, 2521-2529.
81. Y. Wang, J. Yu, L. Chen, Z. Hu, Z. Shi and J. Zhu, *RSC Adv.*, 2013, **3**, 20353.
82. H. Cong, X. Ren, P. Wang and S. Yu, *Energy Environ. Sci.*, 2013, **6**, 1185-1191.
83. B. G. Choi, H. Park, T. J. Park, M. Yang, J. S. Kim, S. Jang, N. S. Heo, S. Y. Lee, J. Kong and W. H. Hong, *ACS Nano*, 2010, **4**, 2910-2918.
84. X. Hu, R. Qi, J. Zhu, J. Q. Lu, Y. Luo, J. Jin and P. Jiang, *J. Appl. Polym. Sci.*, 2014, **131**, 39754.
85. H. Liu, T. Kuila, N. H. Kim, B. Ku and J. H. Lee, *J. Mater. Chem. A*, 2013, **1**, 3739-3746.
86. T. D. Dao, J. E. Hong, K. S. Ryu and H. M. Jeong, *Chem. Eng. J.*, 2014, **250**, 257-266.
87. H. O. Choi, D. W. Kim, S. J. Kim, S. B. Yang and H. T. Jung, *Adv. Mater.*, 2014, **26**, 4575-4581.
88. P. Mulpur, R. Podila, K. Lingam, S. K. Vemula, S. S. Ramamurthy, V. Kamiseti and A. M. Rao, *J. Phys. Chem. C*, 2013, **117**, 17205-17210.
89. L. J. Zhong, S. Y. Gan, X. G. Fu, F. H. Li, D. X. Han, L. P. Guo and L. Niu, *Electrochim. Acta*, 2013, **89**, 222-228.
90. H. Gwon, H.-S. Kim, K. U. Lee, D.-H. Seo, Y. C. Park, Y.-S. Lee, B. T. Ahn and K. Kang, *Energy Environ. Sci.*, 2011, **4**, 1277-1283.
91. H. Bi, W. Zhao, S. Sun, H. Cui, T. Lin, F. Huang, X. Xie and M. Jiang, *Carbon*, 2013, **61**, 116-123.
92. G. F. Cai, J. P. Tu, J. Zhang, Y. J. Mai, Y. Lu, C. D. Gu and X. L. Wang, *Nanoscale*, 2012, **4**, 5724-5730.
93. Y. Zhang, X. Xiao, Y. Sun, Y. Shi, H. Dai, P. Ni, J. Hu, Z. Li, Y. Song and L. Wang, *Electroanalysis*, 2013, **25**, 959-966.
94. B. Zhan, C. Liu, H. Chen, H. Shi, L. Wang, P. Chen, W. Huang and X. Dong, *Nanoscale*, 2014, **6**, 7424-7429.
95. H.-B. Yao, L.-H. Wu, C.-H. Cui, H.-Y. Fang and S.-H. Yu, *J. Mater. Chem.*, 2010, **20**, 5190.
96. X. Sun, M. Xie, J. J. Travis, G. Wang, H. Sun, J. Lian and S. M. George, *J. Phys. Chem. C*, 2013, **117**, 22497-22508.
97. C. H. Lee, Y. J. Kim, Y. J. Hong, S. R. Jeon, S. Bae, B. Hong and G. Yi, *Adv. Mater.*, 2011, **23**, 4614-4619.
98. F. Xiao, Y. Li, X. Zan, K. Liao, R. Xu and H. Duan, *Adv. Funct. Mater.*, 2012, **22**, 2487-2494.
99. F. Xiao, Y. Li, H. Gao, S. Ge and H. Duan, *Biosens. Bioelectron.*, 2013, **41**, 417-423.
100. B. Liang, L. Fang, Y. Hu, G. Yang, Q. Zhu and X. Ye, *Nanoscale*, 2014, **6**, 4264-4274.
101. X. Zan, Z. Fang, J. Wu, F. Xiao, F. Huo and H. Duan, *Biosens. Bioelectron.*, 2013, **49**, 71-78.
102. Y. K. Kim, H. K. Na and D. H. Min, *Langmuir*, 2010, **26**, 13065-13070.
103. S. Chen, J. Duan, J. Ran, M. Jaroniec and S. Z. Qiao, *Energy Environ. Sci.*, 2013, **6**, 3693-3699.
104. S. Chen, J. Zhu, L. Qiu, D. Li and X. Wang, *Chem. Eur. J.*, 2013, **19**, 7631-7636.
105. M. Zhang, A. Halder, C. Hou, J. Ulstrup and Q. Chi, *Bioelectrochemistry*, 2016, **107**, 87-94.
106. H. Zhu, K. T. Lee, G. T. Hitz, X. Han, Y. Li, J. Wan, S. Lacey, A. V. Cresce, K. Xu, E. Wachsman and L. Hu, *ACS Appl. Mater. Inter.*, 2014, **6**, 4242-4247.
107. J. Liang, Y. Zhao, L. Guo and L. Li, *ACS Appl. Mater. Inter.*, 2012, **4**, 5742-5748.
108. J. Liang, Y. Xu, D. Sui, L. Zhang, Y. Huang, Y. Ma, F. Li and Y. Chen, *J. Phys. Chem. C*, 2010, **114**, 17465-17471.

109. A. Sumboja, C. Y. Foo, X. Wang and P. S. Lee, *Adv. Mater.*, 2013, **25**, 2809-2815.
110. F. Liu, Y. Piao, K. S. Choi and T. S. Seo, *Carbon*, 2012, **50**, 123-133.
111. M. Dai, J. Lian, T. Lin and Y. Chen, *J. Mater. Chem. C*, 2013, **1**, 5064-5071.
112. S. Chen and S. Qiao, *ACS Nano*, 2013, **7**, 10190-10196.
113. X. Wang, X. Cao, L. Bourgeois, H. Guan, S. Chen, Y. Zhong, D. Tang, H. Li, T. Zhai, L. Li, Y. Bando and D. Golberg, *Adv. Funct. Mater.*, 2012, **22**, 2682-2690.
114. Q. Xi, X. Chen, D. G. Evans and W. Yang, *Langmuir*, 2012, **28**, 9885-9892.
115. L. Sheng, Y. Liang, L. Jiang, Q. Wang, T. Wei, L. Qu and Z. Fan, *Adv. Funct. Mater.*, 2015, **25**, 6545-6551.
116. G. R. S. Iyer, J. Wang, G. Wells, M. P. Bradley and F. Borondics, *Nanoscale*, 2015, **7**, 2289-2294.
117. D. Cohen-Tanugi and J. C. Grossman, *Nano Lett.*, 2012, **12**, 3602-3608.
118. R. R. Nair, H. A. Wu, P. N. Jayaram, I. V. Grigorieva and A. K. Geim, *Science*, 2012, **335**, 442-444.
119. R. K. Joshi, P. Carbone, F. Wang, V. G. Kravets, Y. Su, I. V. Grigorieva, H. Wu, A. K. Geim and R. R. Nair, *Science*, 2014, **343**, 752-754.
120. B. Mi, *Science*, 2014, **343**, 740-742.
121. S. Karan, S. Samitsu, X. Peng, K. Kurashima and I. Ichinose, *Science*, 2012, **335**, 444-447.
122. Aisenber.S and R. Chabot, *J. Appl. Phys.*, 1971, **42**, 2953-2958.
123. H. Cheng, J. Liu, Y. Zhao, C. Hu, Z. Zhang, N. Chen, L. Jiang and L. Qu, *Angew. Chem. Int. Ed.*, 2013, **52**, 10482-10486.
124. D. W. Boukhvalov, M. I. Katsnelson and Y. W. Son, *Nano Lett.*, 2013, **13**, 3930-3935.
125. J. Mu, C. Hou, B. Zhu, H. Wang, Y. Li, and Q. Zhang, *Sci. Rep.-UK*, 2015, **5**, 9503.
126. C. Hou, T. H. Huang, H. Wang, Q. Zhang and Y. Li, *Sci. Rep.-UK*, 2013, **3**, 3138.
127. J. Mu, C. Hou, H. Wang, Y. Li, Q. Zhang and M. Zhu, *Sci. Adv.*, 2015, **1**, e1500533.
128. K. Hasan, M. O. Sandberg, O. Nur and M. Willander, *Adv. Opt. Mater.*, 2014, **2**, 326-330.
129. J. Sun, M. A. Memon, W. Bai, L. Xiao, B. Zhang, Y. Jin, Y. Huang and J. Geng, *Adv. Funct. Mater.*, 2015, **25**, 4334-4343.
130. Y. J. Kim, H. Yoo, C. H. Lee, J. B. Park, H. Baek, M. Kim and G. C. Yi, *Adv. Mater.*, 2012, **24**, 5565-5569.
131. H. Yoo, K. Chung, Y. S. Choi, C. S. Kang, K. H. Oh, M. Kim and G. C. Yi, *Adv. Mater*, 2012, **24**, 515-518.
132. D. Choi, M. Y. Choi, W. M. Choi, H. J. Shin, H. K. Park, J. S. Seo, J. Park, S. M. Yoon, S. J. Chae, Y. H. Lee, S. W. Kim, J. Y. Choi, S. Y. Lee and J. M. Kim, *Adv. Mater.*, 2010, **22**, 2187-2192.
133. F. Zhao, H. Cheng, Z. Zhang, L. Jiang and L. Qu, *Adv. Mater*, 2015, **27**, 4351-4357.
134. Y. Song, C. Chen and C. Wang, *Nanoscale*, 2015, **7**, 7084-7090.
135. C. Liu, S. Alwarappan, Z. Chen, X. Kong and C. Z. Li, *Biosens. Bioelectron.*, 2010, **25**, 1829-1833.
136. A. S. Campbell, Y. J. Jeong, S. M. Geier, R. R. Koepsel, A. J. Russell and M. F. Islam, *ACS Appl. Mater. Inter.*, 2015, **7**, 4056-4065.
137. W. Gao, Y. Chen, J. Xi, S. Lin, Y. Chen, Y. J. Lin and Z. Chen, *Biosens. Bioelectron*, 2013, **41**, 776-782.
138. Y. Wang, J. Ping, Z. Ye, J. Wu and Y. Ying, *Biosens. Bioelectron.*, 2013, **49**, 492-498.
139. Z. Zheng, Y. Du, Z. Wang, Q. Feng and C. Wang, *Analyst*, 2013, **138**, 693-701.
140. F. Liu, K. S. Choi, T. J. Park, S. Y. Lee and T. S. Seo, *BioCchip J.*, 2011, **5**, 123-128.
141. M. M. Barsan, M. David, M. Florescu, L. Tugulea and C. M. A. Brett, *Bioelectrochemistry*, 2014, **99**, 46-52.
142. X. Zhong, R. Yuan and Y. Q. Chai, *Sens. Actuators B Chem.*, 2012, **162**, 334-340.
143. F. Kong, S. Gu, W. Li, T. Chen, Q. Xu and W. Wang, *Biosens. Bioelectron.*, 2014, **56**, 77-82.
144. Y. Huang, X. Dong, Y. Shi, C. Li, L. J. and P. Chen, *Nanoscale*, 2010, **2**, 1485-1488.
145. F. Xiao, J. Song, H. Gao, X. Zan, R. Xu and H. Duan, *ACS Nano*, 2012, **6**, 100-110.
146. Y. Xu, B. Lou, Z. Lv, Z. Zhou, L. Zhang and E. Wang, *Anal. Chim. Acta*, 2013, **763**, 20-27.

147. Y. Xu, Z. Lv, Y. Xia, Y. Han, B. Lou and E. Wang, *Anal. Bioanal. Chem.*, 2013, **405**, 3549-3558.
148. Y. Zhang, L. Ge, S. Ge, M. Yan, J. Yan, D. Zang, J. Lu, J. Yu and X. Song, *Electrochim. Acta*, 2013, **112**, 620-628.
149. P. Zuo, X. Li, D. C. Dominguez and B. Ye, *Lab on Chip*, 2013, **13**, 3921-3928.
150. L. Deng, C. Chen, C. Zhu, S. Dong and H. Lu, *Biosens. Bioelectron.*, 2014, **52**, 324-329.
151. X. Bai, G. Chen and K. Shiu, *Electrochim. Acta*, 2013, **89**, 454-460.
152. X. Cao, Y. Ye, Y. Li, X. Xu, J. Yu and S. Liu, *J. Electroanal. Chem.*, 2013, **697**, 10-14.
153. C. Cai, M. Xu, S. Bao, C. Lei and D. Jia, *RSC Adv.*, 2012, **2**, 8172-8178.
154. Q. Zhang, Y. Qiao, L. Zhang, S. Wu, H. Zhou, J. Xu and X. Song, *Electroanalysis*, 2011, **23**, 900-906.
155. O. Leenaerts, B. Partoens and F. Peeters, *Phys. Rev. B*, 2008, **77**, 125416.
156. G. Lu, L. E. Ocola and J. Chen, *Appl. Phys. Lett.*, 2009, **94**, 083111.
157. S. V. Samsonau, S. D. Shvarkov, F. Meinerzhagen, A. D. Wieck and A. M. Zaitsev, *Sens. Actuators B Chem.*, 2013, **182**, 66-70.
158. J. Hassinen, J. Kauppila, J. Leiro, A. Maattanen, P. Ihalainen, J. Peltonen and J. Lukkari, *Anal. Bioanal. Chem.*, 2013, **405**, 3611-3617.
159. F. Yavari, Z. Chen, A. V. Thomas, W. Ren, H. Cheng and N. Koratkar, *Sci. Rep.-UK*, 2011, **1**, 166.
160. M. Xu, J. Wu and G. Zhao, *Sensors*, 2013, **13**, 7492-7504.
161. C. Guo, S. R. Ng, S. Y. Khoo, X. Zheng, P. Chen and C. Li, *ACS Nano*, 2012, **6**, 6944-6951.
162. Z. Jiang, J. Li, H. Aslan, Q. Li, Y. Li, M. Chen, Y. Huang, J. P. Froning, M. Otyepka, R. Zboril, F. Besenbacher and M. Dong, *J. Mater. Chem. A*, 2014, **2**, 6714-6717.
163. S. Some, Y. Xu, Y. Kim, Y. Yoon, H. Qin, A. Kulkarni, T. Kim and H. Lee, *Sci. Rep.-UK*, 2013, **3**, 1868.
164. O. C. Compton, S. W. Cranford, K. W. Putz, Z. An, L. C. Brinson, M. J. Buehler and S. T. Nguyen, *ACS Nano*, 2012, **6**, 2008-2019.
165. S. Park, J. An, J. W. Suk and R. S. Ruoff, *Small*, 2010, **6**, 210-212.
166. X. Wang, X. Sun, P. A. Hu, J. Zhang, L. Wang, W. Feng, S. Lei, B. Yang and W. Cao, *Adv. Funct. Mater.*, 2013, **23**, 6044-6050.
167. C. L. Heldt, A. K. Sieloff, J. P. Merrillat, A. R. Minerick, J. A. King, W. F. Perger, H. Fukushima and J. Narendra, *Sens. Actuator B Chem.*, 2013, **181**, 92-98.
168. L. A. Yan, Y. N. Chang, W. Y. Yin, X. D. Liu, D. B. Xiao, G. M. Xing, L. N. Zhao, Z. J. Gu and Y. L. Zhao, *Phys. Chem. Chem. Phys.*, 2014, **16**, 1576-1582.
169. J. Ping, Y. Wang, K. Fan, W. Tang, J. Wu and Y. Ying, *J. Mater. Chem. B*, 2013, **1**, 4781-4791.
170. L. Zhang and X. Zhao, *Chem. Soc. Rev.*, 2009, **38**, 2520-2531.
171. M. Winter and R. J. Brodd, *Chem. Rev.*, 2004, **104**, 4245-4269.
172. P. Simon and Y. Gogotsi, *Nat. Mater.*, 2008, **7**, 845-854.
173. S. H. Lee, H. W. Kim, J. O. Hwang, W. J. Lee, J. Kwon, C. W. Bielawski, R. S. Ruoff and S. O. Kim, *Angew. Chem. Int. Ed.*, 2010, **49**, 10084-10088.
174. Z. Xu, Z. Li, C. M. B. Holt, X. Tan, H. Wang, B. S. Amirkhiz, T. Stephenson and D. Mitlin, *J. Phy. Chem. Lett.*, 2012, **3**, 2928-2933.
175. X. Han, M. R. Funk, F. Shen, Y. C. Chen, Y. Li, C. J. Campbell, J. Dai, X. Yang, J. W. Kim, Y. Liao, J. W. Connell, V. Barone, Z. Chen, Y. Lin and L. Hu, *ACS Nano*, 2014, **8**, 8255-8265.
176. T. Liao, C. Sun, Z. Sun, A. Du, D. Hulicova-Jurcakova and S. C. Smith, *J. Mater. Chem.*, 2012, **22**, 13751-13755.
177. Y. L. Shao, H. Z. Wang, Q. H. Zhang and Y. G. Li, *J. Mater. Chem. C*, 2013, **1**, 1245-1251.
178. Z. Li, Y. Mi, X. Liu, S. Liu, S. Yang and J. Wang, *J. Mater. Chem.*, 2011, **21**, 14706-14711.
179. Q. Wu, Y. Xu, Z. Yao, A. Liu and G. Shi, *ACS Nano*, 2010, **4**, 1963-1970.

Chapter 2: Experimental materials, methods and techniques

2.1 Experiment section

2.1.1 Chemicals and materials.

Potassium hexacyanoferrate (III) ($K_3[Fe(CN)_6]$, 99%), sodium citrate dehydrate (99%), hydrogen chloride (HCl, 25 %) and potassium chloride (KCl, $\geq 99\%$) were obtained from Merck. Iron (III) chloride ($FeCl_3$, 98%) from Riedel-deHaën was used. Hydrogen peroxide (H_2O_2 , 34.5-36.5 %), sodium borohydride ($NaBH_4$ 99.995%) and gold (III) chloride tri-hydrate ($HAuCl_4 \cdot 3H_2O$ 99.9%) were from Sigma-Aldrich. Graphite power ($< 20 \mu m$, synthetic), sulfuric acid (H_2SO_4 , 95–97%), potassium persulfate ($K_2S_2O_8$, $\geq 99\%$), phosphorus pentoxide (P_2O_5 , $\geq 98\%$), and potassium permanganate ($KMnO_4$, $\geq 99\%$) were from Sigma-Aldrich. All chemicals were used as received. Milli-Q water ($18.2 M\Omega cm$) was used throughout.

2.1.2 Instrumental methods.

UV-vis measurements were carried out using an Agilent Instrument Exchange Service Model G1103A. A 5500 atomic-force microscopy (AFM) system (Aligent Technology) was used for all AFM imaging. Images were recorded in the tapping mode. Transmission electron microscopy (TEM) imaging was performed using a Tecnai G2 T20, and EDS mapping images were obtained by Titan Analytical 80-300ST TEM (STEM dark-mode) from FEI Company (Oregon, USA). Scanning electron microscope (SEM) and energy-dispersive X-ray spectroscopy (EDS) mapping images were obtained by Quanta FEG 200 ESEM (with ETD and BSE detector) from FEI Company (Oregon, USA). XPS spectra were recorded on Thermo Scientific X-ray photoelectron spectrometer with an Al K-Alpha (1486 eV) x-ray source. All XPS samples were prepared by drop casting materials on polished Si-wafer. In all measurements, X-ray spot area was set to $400 \mu m$ and a flood gun was used for charge compensation. Electrochemical measurements were carried out at room temperature ($23 \pm 2 \text{ }^\circ C$) using an Autolab System (Eco Chemie, Netherlands) controlled by the Nova software or/and using a CHI 760C electrochemical workstation. A three-electrode system consisting of a saturated calomel electrode (SCE) as reference electrode, a platinum coiled wire as counter electrode, and a glassy carbon electrode (GCE) modified with target materials as working electrode was used throughout.

2.1.3. Experimental details of GO synthesis

GO was prepared by the modified Hummer's method. The procedure involved two major steps. Pre-oxidized graphite was prepared in the first step. In a typical sampling, graphite powder (5.0 g) was slowly added to concentrated H_2SO_4 (8.5 mL) containing P_2O_5 (2.5 g) and $\text{K}_2\text{S}_2\text{O}_8$ (2.5 g) and the mixture kept in a hot water bath (80°C) under strong stirring for 3 h. After cooling to room temperature and diluting with Milli-Q water, the dark green mixture was filtered and washed several times until waste solution pH had reached neutral. The pre-oxidized graphite powder was collected and dried in an oven at 50°C overnight.

In the second step, pre-oxidized graphite powder (1.0 g) was slowly added to concentrated H_2SO_4 (23 mL) in an ice-water bath (0°C). KMnO_4 (3.0 g) was then added to the mixture under slow stirring and keeping the whole process below 20°C . After removing the ice-water bath, the mixture was left to react at 35°C for 2 h with stirring, and Milli-Q water (46 mL) was added to stop reaction. After a few minutes, Milli-Q water (137.5 mL) and 2.5 mL 30% H_2O_2 solution were further added to the mixture, causing the solution color to change rapidly to bright yellow. The mixture was then washed with 1:10 HCl solution (v/v, 250 mL) and filtered to remove residual metal ions. The crude GO suspended in Milli-Q water was centrifuged at high rotation speed ($12000\text{ rpm min}^{-1}$), and the supernatant containing highly dispersed and stable GO nanosheets collected. To remove residual salts and acids, the supernatant was further dialyzed using a dialysis tube (with a cut-off molecular mass of 12000-14000) for at least one week, changing the water bath regularly (2-3 times per day). The concentration of GO was calculated after centrifugation of 1 ml (5 x) GO solution and discarding the supernatant. The pellets were dried under vacuum for 3-5 days, and their average mass per mL solution taken as the concentration (usually in mg/mL). AFM was used regularly for measuring the thickness of the as-synthesized GO nanosheets. To prepare AFM samples, 25 μL of 0.002 mg/mL solution was drop cast on mica ($2\text{ cm} \times 2\text{ cm}$) and dried in a fume hood overnight.

2.1.4 Fabrication of electrodes.

Glassy carbon electrodes (GCEs) with a geometrical area of 0.07cm^2 were used as support for preparing biosensor or supercapacitor electrodes in this work. *First*, GCE was carefully polished with alumina slurry (1 μm , 0.3 μm and 0.05 μm , respectively). Immediately after polish, GCE was rinsed and sonicated in ethanol and Milli-Q water for 3 min each to remove the alumina residues from the electrode surface. The freshly polished

and clean electrode was dried under a slowing nitrogen atmosphere. *Second*, 20 μL of nanocomposite was cast onto the GCE surface, and the electrode was left for dry overnight.

2.1.5 Evaluation of electrochemical supercapacitive performances.

The specific capacitance was calculated from the Galvanostatic discharging curves, according to the following equation.

$$C_s = \frac{I \times \Delta t}{\Delta V \times m} \quad (2.1)$$

Where C_s is the specific capacitance, I is the current applied, Δt is the discharging time, ΔV is the potential window, and m is the mass of the electroactive material.

The energy density (E) of various materials was estimated using the following expression.

$$E = \frac{1}{2} C V^2 \quad (2.2)$$

Where E , C , and V are the energy density (W h kg^{-1}), specific capacitance (F g^{-1}), and the potential window applied (V), respectively.

2.2 Instrumental techniques

A variety of techniques were employed in preparation and characterization of materials and construction and functional tests of sensors and devices. The techniques that need particular emphasis include synthetic chemistry for nanoparticles and graphene, AFM, TEM, XPS and XRD for materials characterization, and electrochemistry and photoelectrochemistry for functional tests.

2.2.1 Electrochemistry

Electrochemistry is the branch of physical chemistry, in which chemical reactions taking place at interfaces of electrode/electrolyte can be studied. These reactions involve electric charges moving between the electrode and the electrolyte (or ionic species in a solution). Electrochemistry deals with the interaction between electrical energy and chemical changes¹.

When a chemical reaction is caused by an externally supplied current, as in electrolysis, or if an electric current is generated by a spontaneous chemical reaction as in a battery, it is called an electrochemical reaction. In contrast, chemical reactions where electrons are transferred directly between molecules and/or atoms are called oxidation-reduction or redox reactions². In general, electrochemistry describes the overall reactions when individual redox reactions are separate but connected by an external electric circuit and an intervening electrolyte.

Electrochemistry as a branch of chemistry, it has been applied in different fields, such as chemical sensors, energy conversion and storage, catalysis and corrosion³. Demanded by various applications, many electrochemical techniques have been developed and updated in the past several decades. For instance, the techniques such as cyclic voltammetry (CV), chronoamperometry, linear sweep voltammetry (LSV), and differential pulse voltammetry (DPV) are well developed and have been mostly widely used. In the present project, we have mainly explored CV, chronoamperometry and constant-current charge-discharge methods.

CV is a common method for initial studies of electrochemical systems, which uses a three-electrode setup to analyze the potentials at which reactions occur in a specific system⁴. Several different voltage-time functions sometimes denoted as excitation signals can drive to the working electrode, such as linear scan, differential pulse, square wave, etc^{1,4}. Linear sweep voltammetry (LSV) is the simplest method among these potential sweep techniques. The most useful method is CV as schematically shown in Fig. 2.1.

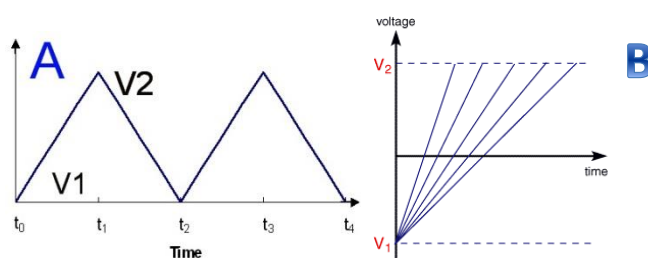


Fig. 2.1 Cyclic voltammetry curve, showing changes of potential as a function of time⁷.

In this case, the potential is initially swept from V_1 , and the slope is the scan rate (Fig.2.1B shown different scan rates). On arriving at V_2 , the potential sweep is reversed with the same speed until returned to the original potential V_1 . The diagram of CV is current vs. potential as a function, and the scan rates can vary from a few mV/s to thousands of V/s.

2.2.2 Electron microscopy

Electron microscopy has emerged as a very powerful tool to characterize nanomaterials, due to its capability to provide very useful structural and morphologic information about materials such as shape and size⁵.

With the development, macroscopically structural characterization is not enough for scientific research. Electron microscopy especially TEM, it is one of the most powerful techniques to characterize materials at the nanometer-scale even atomic-level feature, Due to the small de Broglie wavelength of electrons, TEM is capable of imaging specimens at resolutions up to the atomic level. TEM has multiple imaging modes that enable examination of specimens from various aspects. The structure of materials, the growing of crystal constituents and analysis of element distribution could be achieved⁵.

TEM utilizes energetic electrons to provide morphologic, compositional and crystallographic information on samples. By now, nanometer scale even atomic-level analysis of materials could be achieved by TEM. At a maximum potential magnification of 0.4 nanometer, TEMs are among the most powerful microscopes. TEMs produce high-resolution, two-dimensional images, allowing for a wide range of educational, science and industry applications. The working principle of TEM is shown schematically in Fig. 2.2, a high-energy electron beam transmits through the sample. The transmission of electron beam is highly dependent on the properties of the materials examined. Such properties include electron density, chemical composition, etc. For example, porous material allows more electrons to pass through while dense material allows much less. As a result, a specimen with a non-uniform density can be examined by TEM. Whatever part is transmitted is projected into an image for the user to see.

As shown in Fig. 2.2, the structure of a TEM instrument mainly includes five parts: electron source, electromagnetic lenses, sample, detectors and vacuum system. The electron source is an electron gun that consists of a cathode and an anode. According to different working principles of electron emitting, there are two kinds of electron gun. One is the negative electron gun made of W or LaB₆, and the other is field emission gun (FEG)⁵.

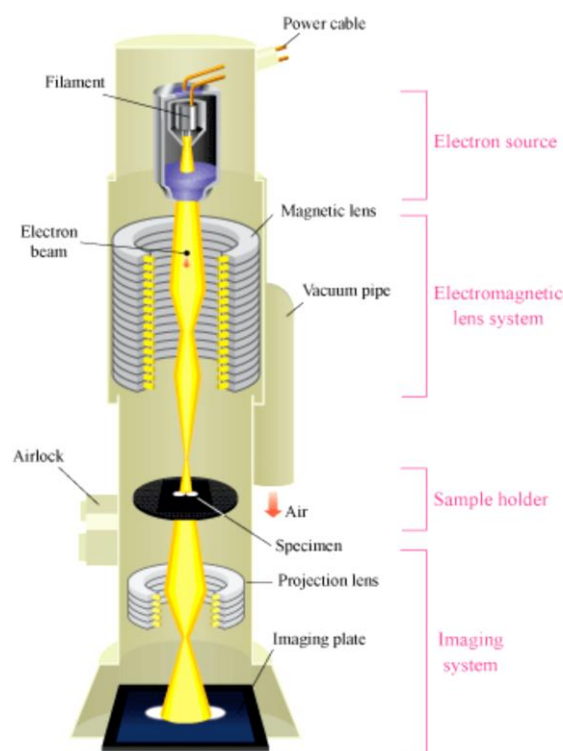


Fig. 2.2 Schematic view of the structures of a TEM instrument

In general, at least double electromagnetic lenses are used in all TEM instruments. In the new-generation TEM, a mini-condense lens is also equipped to improve imaging resolution. These lenses can be classified as the condenser lens, the objective lens, and the projector lens. The condenser lenses are responsible for primary beam formation, while the objective lenses focus the beam that comes through the sample itself (in STEM scanning mode, there are also objective lenses above the sample to make the incident electron beam convergent). The projector lenses are used to expand the beam onto the phosphor screen or other imaging device, such as film. The magnification of the TEM is due to the ratio of the distances between the specimen and the objective lens' image plane. Detector (e.g. electron detector and X-ray detector): Electron beam hits the sample, some electrons will pass through a thin-section specimen of a material, electrons are scattered and absorbed within the specimen. A sophisticated system of electromagnetic lenses focuses the scattered electrons into an image or a diffraction pattern, or a nano-analytical spectrum, depending on the mode of operations.

2.2.3 X-ray diffraction techniques

X-ray diffraction technique has become a common method for characterizing solid materials since the second half of the 20th century⁶. The basis for this method was created by W. Friedrich, P. Knipping, M. von Laue, W. H. Bragg and W. L. Bragg along with P. P. Ewald during their studies of condensed crystalline matters. The method has been used for determining the degree of crystallinity in solid samples, as well as identifying the individual phases present. It is even possible to evaluate the relative amount of the phases and crystallite size.

In X-ray diffraction, a solid sample with X-ray waves at an angle. Depending on the arrangement of the atoms and their distances relative to one another, the diffracted waves may interfere in a constructive, destructive or partially destructive manner. Diffraction happens when the waves excite atoms and are emitted in a random direction. The Bragg's law is the key equation for X-ray diffraction techniques as it describes the conditions necessary for constructive interference⁶.

$$n \lambda = 2 d \sin(\theta) \quad (2.3)$$

Where n is the diffraction order, λ the wavelength of the x-rays, d the interatomic distance and θ the incident angle of the x-ray on the sample. A simple illustration of Bragg's law applied on two planes can be shown in Fig. 2.3.

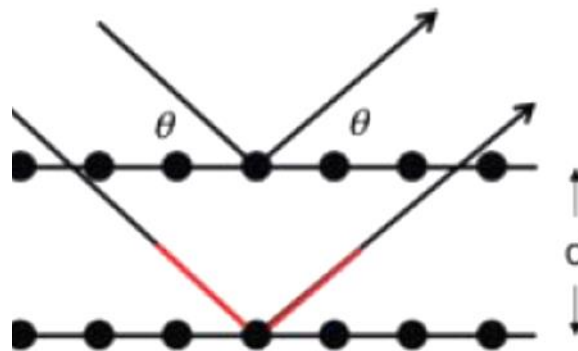


Fig. 2.3. X-ray diffraction on a two-plane system, with periodically placed atoms.

2.2.4 X-ray photoelectron spectroscopy

X-ray photoelectron spectroscopy (XPS) is a technique used to get information about the surface composition of materials⁷. The instrument uses an X-ray gun to excite core electrons in the material causing them to be emitted with a kinetic energy equal to the difference between the binding energy of the electron and the energy of the X-ray photon. The detector counts the emitted

electrons and separates them by their kinetic energy. A principle sketch of a XPS instrument is shown in Fig 2.4. Since the energy of the X-ray photons are known, the binding energy of the electrons can be calculated and used to determine the identity and relative quantity of different atoms on the surface. Further analysis of the peaks can be used to distinguish between the different types of bonds present.

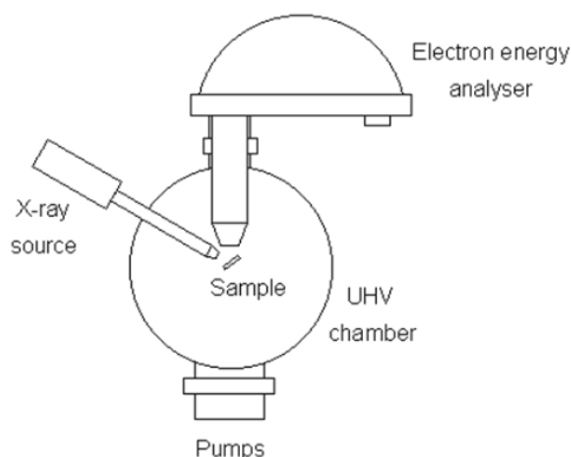


Fig. 2.4 Principle sketch of the insides of an XPS instrument with an X-ray source firing on the sample while the emitted electrons are detected by an electron energy analyzer.

2.2.5 Atomic force microscopy

Atomic force microscopy (AFM) is an amazing technique, which allows us to see and measure surface structures with unprecedented resolution and accuracy. AFM is rather different from other microscopes, because it does not form an image by focusing light or electron onto surface. AFM physically feels a sample surface via a sharp probe, building up a map of the height and structural variations of the sample surface. The working principles of AFM can be simplified illustrated in Fig. 2.5. Generally, the probe, typically a piezoelectric element, is made of silicon or silicon nitride cantilever coating with a much smaller integrated tip. The deflection from bending of cantilever depends on the forces acting between tip and sample, and is detected by a laser focused on the cantilever. The most common AFM operation modes, according to the nature of the tip motion, are the contact mode and tapping mode.⁸

Working of AFM

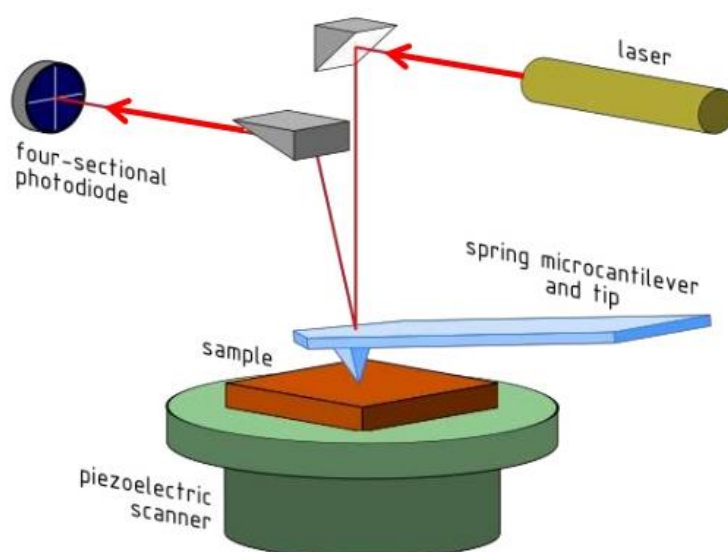


Fig. 2.5 Working principles of an AFM instrument.

References

1. <https://en.wikipedia.org/wiki/Electrochemistry>
2. D. Pletcher, R. Greff, R. Peat, L. M. Peter, J. Robinson, Southampton Electrochemistry Group, *Instrumental methods in electrochemistry*, Woodhead Publishing, **2001**.
3. A. J. Bard et al., *Electrochemical Methods: Fundamentals and Applications* (2nd ed.). Wiley. ISBN 0-471-04372-9, **2001**.
4. R. S. Nicholson, *Anal. Chem.* 1965, **37**, 1351–1355.
5. https://en.wikipedia.org/wiki/Transmission_electron_microscopy
6. M. J. Wilson, X-ray powder diffraction methods." *A handbook of determinative methods in clay mineralogy* (1987): 26-98.
7. *Practical Surface Analysis by Auger and X-ray Photoelectron Spectroscopy*, 2nd edition Wiley & Sons, 1992, Chichester, UK ISBN 0-471-26279-X.
8. P. Eaton, W. Paul, *Atomic force microscopy*. Oxford University Press, 2010.

Part 2. Prussian Blue functionalized graphene composites for electrochemical sensing and energy applications

As mentioned in [Part 1](#), graphene paper as an attractive material was widely used in flexible substrate, supercapacitor and sensor, especially in electrochemical sensors. In this part, we have explored the combination of redox active *Prussian Blue* (PB) nanostructures with chemically exfoliated graphene to prepare multifunctional composites as electrochemical catalysts and supercapacitor electrode materials.

Prussian blue (PB), as a non-enzymatic but enzyme mimicking catalyst, has been explored for applications in chemical sensors, biosensors, energy devices and water quality monitoring, due to the fact that PB and its analogues are considered as promising energy storage materials, because the theoretical specific capacity of PB can be as high as 170 mA h g^{-1} . In addition, the facile synthetic procedure, nontoxicity and low cost of PB based materials make them have potential favouring for large-scale production and multifunctional applications. In [Chapter.3](#), high-quality PB nanocube-rGO hybrids were successfully synthesized by using $\text{K}_4\text{Fe}(\text{CN})_6$ as the only iron-source. Simultaneous reduction and functionalization of GO have been achieved by a one-step procedure with the green nature of reactions. The as-synthesized PB nanocubes were wrapped by rGO nanosheets to form an interlocked stable structure. This unique structured microcomposite not only can act as an electron mediator, but also can stabilize PB nanocubes in electrochemical environments, which altogether enables these hybrid materials to hold multifunctional applications. Given the fact that PB displays low conductivity, in [Chapter 4](#), AuNPs was used as the core material, PB was coated on AuNPs surface in nanoscale, and thus core-shell structural Au@PB NPs was successful synthesized to enhance conductivity. More importantly, the size-effect of AuNPs for self-catalysis formation of Au@PB NPs is not clear at present in terms of detailed mechanisms, thus in [Chapter 4](#) one key focus was on studying size-effect of using AuNPs as catalyst for self-catalysis formation of Au@PB NPs. Another focus is on the size-dependent electrocatalysis of H_2O_2 reduction by the as-synthesized core-shell NPs. In [Chapter 5](#), as the synthesized core-shell structured Au@PB nanoparticles were loaded on single-layer GO nanosheets, then the resulting hybrid nanosheets was assembled into free-standing graphene papers directly used as electrochemical sensors. These graphene-paper based electrodes displayed high performances in electrocatalytic reduction of hydrogen peroxide.

Chapter 3: Interlocked graphene-*Prussian blue* hybrid composites enable multifunctional electrochemical applications

3.1 Introduction

Prussian blue (PB), as a non-enzymatic but enzyme mimicking catalyst, has been explored for applications in chemical sensors¹⁻³, biosensors⁴⁻⁸, energy devices^{9,10} and water quality monitoring¹¹. PB and its analogues are considered as promising energy storage materials, because the theoretical specific capacity of PB can be as high as 170 mA h g⁻¹⁹. In addition, the facile synthetic procedure, nontoxicity and low cost of PB based materials make them hold potential favouring for large-scale production and multifunctional applications. However, to date these great potentials have been far from exploitation, as the practically achieved specific capacity of PB is much lower than theoretical expectation. PB also suffers from low Coulombic efficiency and poor cycling stability, which has limited its practical utilization as energy materials. This has largely originated in the poor process used in the PB crystal growth, in which coordinated water is hardly avoided and occupies most vacancies of the PB crystal. Moreover, the water-occupied vacancies may induce a lattice distortion, which dramatically affects both the specific capacity and Coulombic efficiency, and deteriorates overall electrochemical performances. In most cases, PB prepared by the direct precipitation reaction of the M^{m+} cations and the [M(CN)₆]ⁿ⁻ anions in a neutral aqueous solution always contains a large number of vacancies occupied by coordinated water, because of the fast precipitation process. However, a recent report showed that high-quality PB nanocubes or/and analogues without coordinated water can be synthesized by employing Na₄Fe(CN)₆ as a single iron-source precursor, and the resulting material was tested as cathode electrodes for sodium-ion battery with impressive electrochemical performances^{12,13}. This was achieved by a slow process for growth of PB crystals, so that the number of vacancies occupied by coordinated water is dramatically reduced or even completely eliminated in some cases.

As noted in [Chapter 1](#), graphene holds considerable promise for its potential applications in many technological fields such as nanoelectronics^{14,15}, sensors¹⁶⁻¹⁸, functional nanocomposites^{8, 19, 20}, and energy devices²¹⁻²⁵. Graphene has been prepared by a variety of methods, including mechanical exfoliation^{26, 27}, modified Hummers' methods^{28, 29}, and chemical vapour deposition (CVD)^{15, 30}. Among these methods, wet-chemical reduction of exfoliated GO is an efficient approach to large-scale production of graphene nanosheets at low cost. However, the most

commonly used methods for reduction of GO are carried out using hydrazine and its derivatives^{31, 32} as reducing agents. The use of highly toxic and dangerously unstable hydrazine or dimethyl hydrazine to reduce GO is not desirable for many applications. Recently, mild conditions were reported to reduce GO using gentle reducing agents such as L-ascorbic acid³³, reducing sugars³⁴ and others. Among many green reducing agents, glucose is of particular interest in reducing GO because of its high ability, relatively low-cost, and enabling environmentally friendly reactions. In this work, we used glucose as a co-reducing agent. Based on the fact that GO is an efficient electron acceptor³⁵⁻³⁸, GO can be reduced by electron-rich materials such as metals, metal ions, biomolecules or bacteria. This has been demonstrated by several recent reports^{2, 37, 39}. In general, to obtain rGO based functional hybrid materials two steps including reduction and functionalization are normally involved. For example, PB functionalized graphene materials were prepared by mixed PB nanoparticles (PBNPs) directly with rGO, so that PBNPs were confined by electrostatic attraction in rGO papers⁸. Zhang et al⁴⁰ and Qian et al.⁴¹ used various reducing agents to reduce GO and Fe^{3+} to prepare rGO-PB hybrid materials. In the present work, we report the preparation of high-quality PB nanocube-rGO hybrids by using $\text{K}_4\text{Fe}(\text{CN})_6$ as the only iron-source. As schematically illustrated in Fig.3.1, simultaneous reduction and functionalization of GO have been achieved by a one-step procedure with the green nature of reactions. The as-synthesized PB nanocubes were wrapped by rGO nanosheets to form an interlocked stable structure. This unique structured microcomposite not only can act as an electron mediator, but also can stabilize PB nanocubes in electrochemical environments, which altogether enables these hybrid materials to hold multifunctional applications.

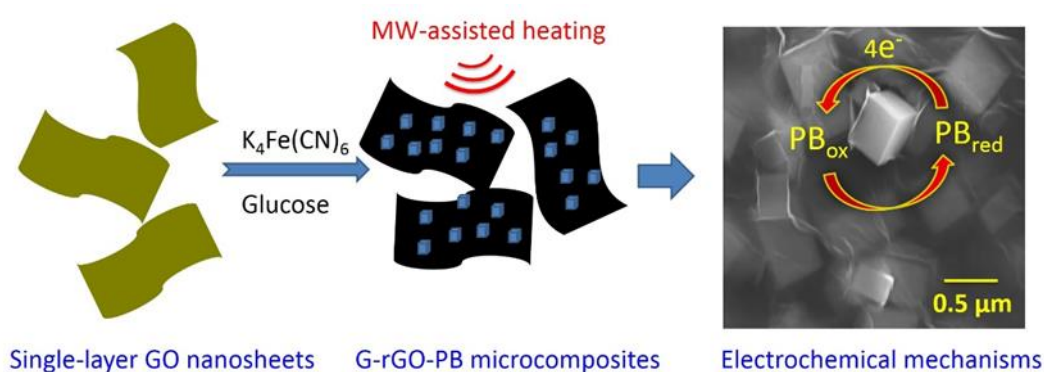


Fig. 3.1 The schematic preparation procedure and electrochemical mechanisms of G-rGO-PBs.

3.2 Synthesis of G-rGO-PB composite

To synthesize high-quality PB modified rGO (G-rGO-PB), 2 mL GO (1 mg/mL) solution was mixed with 10 mL $K_4Fe(CN)_6$ (10 mM), 2 mL (40 mg/mL) glucose and 1 mL 0.5 M HCl. The mixed solution was stirred for 10 min and then heated at 60 °C in a microwave for 3h. The raw product was collected and purified by centrifugation and filtration. rGO-PB was prepared in the same procedure but in the absence of glucose and is used as a reference sample.

3.3. Results and discussion

3.3.1 One-step eco-friendly synthesis of G-PB-rGO composites

High quality and stable GO was prepared by the modified Hummer's method². GO was well dispersed in pure water, and its UV-vis spectrum is shown in Fig. 3.2 (brown curve). We compared the efficiency of glucose and PB precursor for the reduction of GO. In comparison with PB-rGO (Fig. 3.2), GO was further reduced in the presence of glucose. The glucose-rGO (G-rGO) exhibits an absorption peak at 260 nm, while the PB-rGO retains a shoulder peak at 300 nm due to the $n-\pi^*$ transitions of C=O bonds. This indicates that glucose is a stronger reducing agent for GO reduction. However, PB precursor offers electroactive functionalization of GO, as evidenced by the new absorption peak around 725 nm from the PB component⁸. Therefore, we used both PB precursor and glucose as co-reducing agents to simultaneously reduce GO and functionalize rGO in microwave-assisted one-step synthesis to obtain G-PB-rGO composite. To gain more details, Raman spectra were recorded (Fig. 3.3). The D band of GO, rGO-PB and G-rGO-PB that originated in the defects of graphitic planes is located at 1363, 1363 and 1365 cm^{-1} , respectively; and the G band related to the in-plane vibrations of sp^2 is observed at 1594, 1594 and 1595 cm^{-1} . The I_D/I_G ratio of GO, rGO-PB and G-rGO-PB is 1.6, 1.4, and 1.1 respectively, which significantly decreases and indicates that GO was better reduced by the additional presence of glucose to restore the graphitic feature.

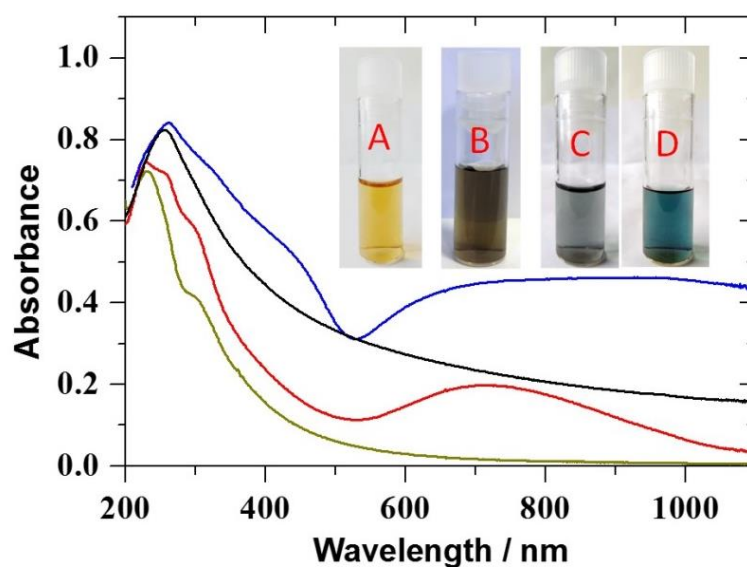


Fig. 3.2 UV-vis spectra of GO (brown curve), rGO-PB (red curve), glucose reduced graphene oxide (black curve) and G-rGO-PB (blue curve). Insets show digital photographs of GO (A), rGO (B), rGO-PB (C) and G-rGO-PB (D) solutions.

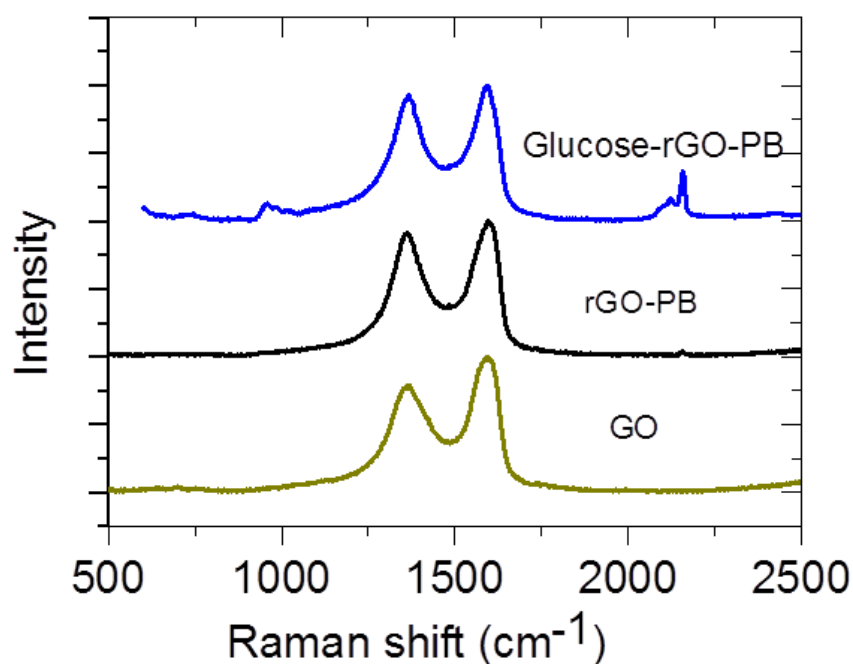
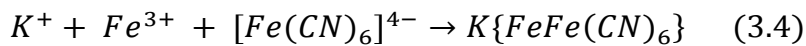
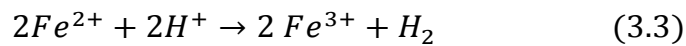


Fig. 3.3 Raman spectra of GO, rGO-PB and Glucose-rGO-PB.

The reaction mechanisms are also discussed. Because of its large stability constant ($K_s = 1.0 \times 10^{35}$), $[\text{Fe}(\text{CN})_6]^{4-}$ anions are very stable in neutral solutions at room temperature, and almost there is no free Fe^{2+} ions detectable¹³. However, Fe^{2+} will get free from $\text{K}_4\text{Fe}(\text{CN})_6$

crystal in acid media (pH~1.7), and it is then oxidized to Fe^{3+} . The released electrons together with H^+ would react with oxygen-containing groups on GO, leading to the partial reduction of GO to rGO at room temperature. In the meantime, once Fe^{3+} ions were generated, they strongly interacted with carboxyl groups of GO and adsorbed on GO via electrostatic and coordinating interactions⁴². In other words, this means that Fe^{3+} would be confined (or coordinated) on the surface of GO. Furthermore, the confined Fe^{3+} ions reacted with $[Fe(CN)_6]^{4-}$ to form PB cubes. This enables to form PB nanostructures wrapped with rGO nanosheets. The key reactions could be described by the following chemical equations.



Clearly, this solution-processed procedure allows the formation of PB cubes on GO and GO reduction in one step. The advantages likely include reactions occurred at low temperatures, no toxic reducing agents involved, low cost, and highly conductive composite obtained. To illustrate the $K_4Fe(CN)_6$ role that provides electrons for reduction of GO, different control experiments were designed and performed. Our observations include: 1) GO is not to be reduced in the absence of $K_4Fe(CN)_6$ in neutral solutions. 2) The presence of acid is essential for GO reduction by $K_4Fe(CN)_6$. When HCl is at low concentrations or there is no HCl, only very little PB was generated although GO was still partially reduced. This is due to the fact that free Fe^{2+} ions dissociate from $K_4Fe(CN)_6$ only occurs in acidic media. 3) Microwave plays a significant role as well. GO can be reduced by $K_4Fe(CN)_6$ in acid media at room temperature, but it takes much longer (at least 24 h). 4) The introduction of glucose as a co-reducing agent significantly enhanced the conductivity of composites by an improved reduction of GO.

3.3.2 Structural characterization of G-rGO-PB composites

The as-synthesized composites were examined *first* by powder X-ray diffraction (Fig. 3.4). In the XRD patterns, the peaks at $2\theta=17.5^\circ$, 24.8° , 35.3° , 39.6° , and 43.6° correspond to the (2 0 0), (2

2 0), (4 0 0), (4 2 0), and (4 2 2) reflections, respectively. Both rGO-PB and G-rGO-PB patterns exhibit the characteristic diffractions of mixed-valence compound with a face-centred cubic structure (JCPDS card no. 73-0687), which indicates that PB cubes prepared by microwave were highly crystallized. Compared to GO, for rGO-PB samples the peak at $2\theta=10.5$ almost disappears, which is the evidence that GO was reduced by glucose and Fe^{2+} . To further investigate the interaction between PB and rGO, PB was prepared by directly mixed FeCl_3 with $\text{K}_4[\text{Fe}(\text{CN})_6]$, as shown in Fig. 3.4, the diffraction peaks for such samples are broadening with lower intensity due to the smaller size of powder particles and poor crystallinity. The diffraction peaks of all rGO-PB samples are found to have a slight shift, which may be due to the distortion of PB lattices arising from the vacancies occupied by coordinated water in PB. It shows that high-quality PB nanocubes with a small number of vacancies and low interstitial water content were prepared by using $\text{K}_4\text{Fe}(\text{CN})_6$ as the only iron-source.

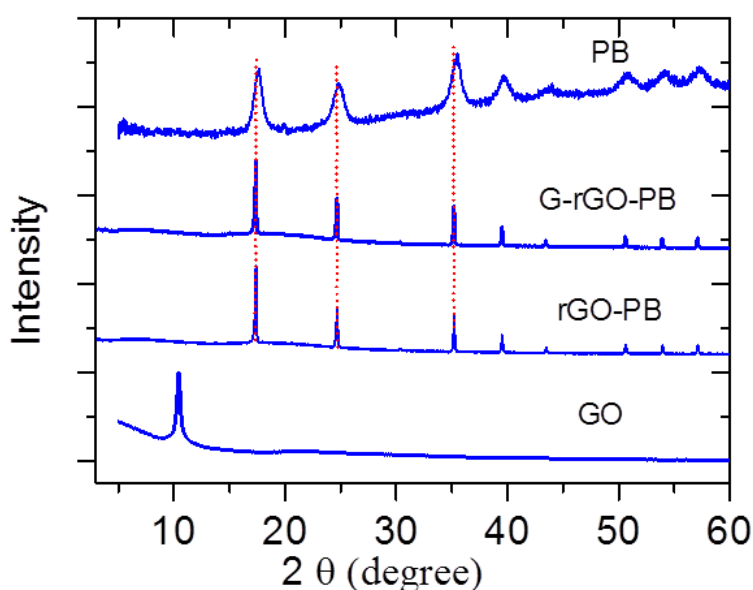


Fig. 3.4 XRD patterns of different samples including pure PB, GO alone, rGO-PB and G-rGO-PB composites.

The samples were *further* analyzed by X-ray photoelectron spectroscopy (XPS). The XPS spectrum of GO (supporting information) shows intensive O 1s but relatively weak C 1s peaks, and the C 1s XPS spectrum of GO confirms various oxygen-containing groups (OCGs) such as C=O and C–O existing on GO, which indicates that GO has abundant OCGs on the surface of GO sheet. The ratio of C/O was determined as about 3:2. The XPS survey spectrum of G-rGO-PB show that, not only O 1s peak significantly decreases and C 1s peak obviously increases, but also the peaks at

398.3 eV corresponding to N1s and peaks at 708.2 eV corresponding to Fe 2p are observed, which suggests the introduction of PB nanocubes into rGO planes (Fig. 3.5). The C 1s XPS spectrum of G-rGO-PB shows different carbon atoms in different functional groups: the non-oxygenated ring C/(C–C) (284.7 eV), the C in C–O bonds (286.8 eV), and the carboxylate carbon(C=O) (287.6 eV). The main peak at 284.8 eV was clearly seen, an indicative of only partial reduction of GO. Compared to GO, the signal of C–O in the C 1s spectrum of G-rGO-PB becomes much weaker, and the calculated ratio of C/O changed to about 2:1. These results conclude that considerable deoxygenation occurred by glucose and Fe²⁺ reduction, resulting in the recovery of graphitic planes on rGO, where a number of OCGs remain on the graphene plane that can serve as the anchoring sites for the growth of PB nanocubes. The high-resolution Fe 2p spin–orbit doublet spectra of PB/rGO composites were recorded. The binding energies of Fe p_{3/2} and Fe 2p_{1/2} were observed at 712.3 and 721.2 eV, respectively, which correspond to the Fe³⁺ ions. The peak at 708.4 eV is due to Fe²⁺ 2p_{3/2} in PB cubes. The ratio of Fe³⁺/Fe²⁺ was determined as approximately 1.6 to 0.9, which is largely expected for PB materials. These results confirm the formation of PB that has well-defined crystalline structure. The high-resolution N 1s spectrum of G-rGO-PB is de-convoluted into three peaks with the binding energy of 397.5, 399.5, and 403.1 eV, respectively. The peak at 397.5 eV can be attributed to Fe–C≡N bonds of PB cubes, and other peaks (including pyrrolic N₂ and pyridine N-oxide N₃) reflect the diverse forms of nitrogen functional groups. The peak for Fe–C≡N is predominant in intensity, suggesting that nitrogen atoms detected are mainly from PB.

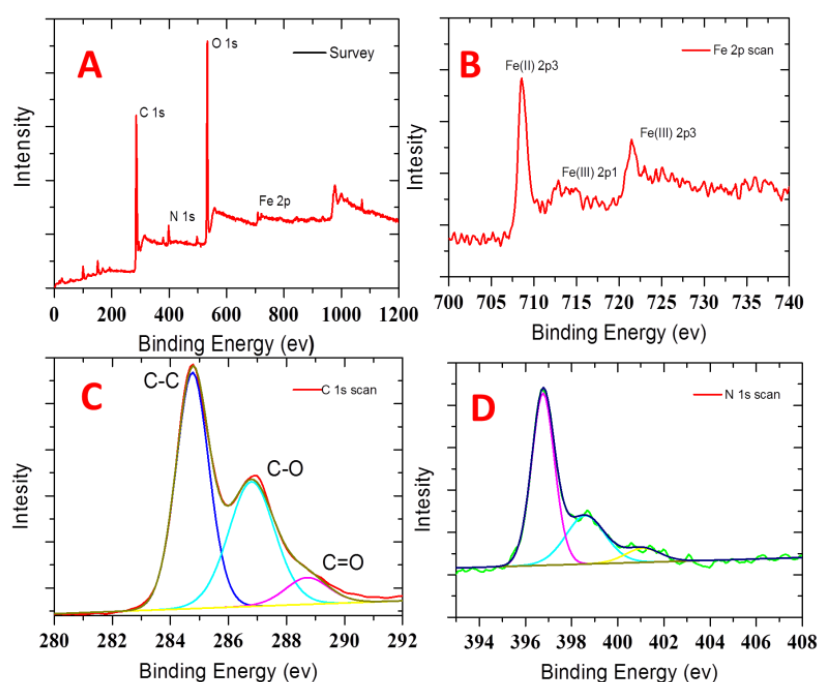


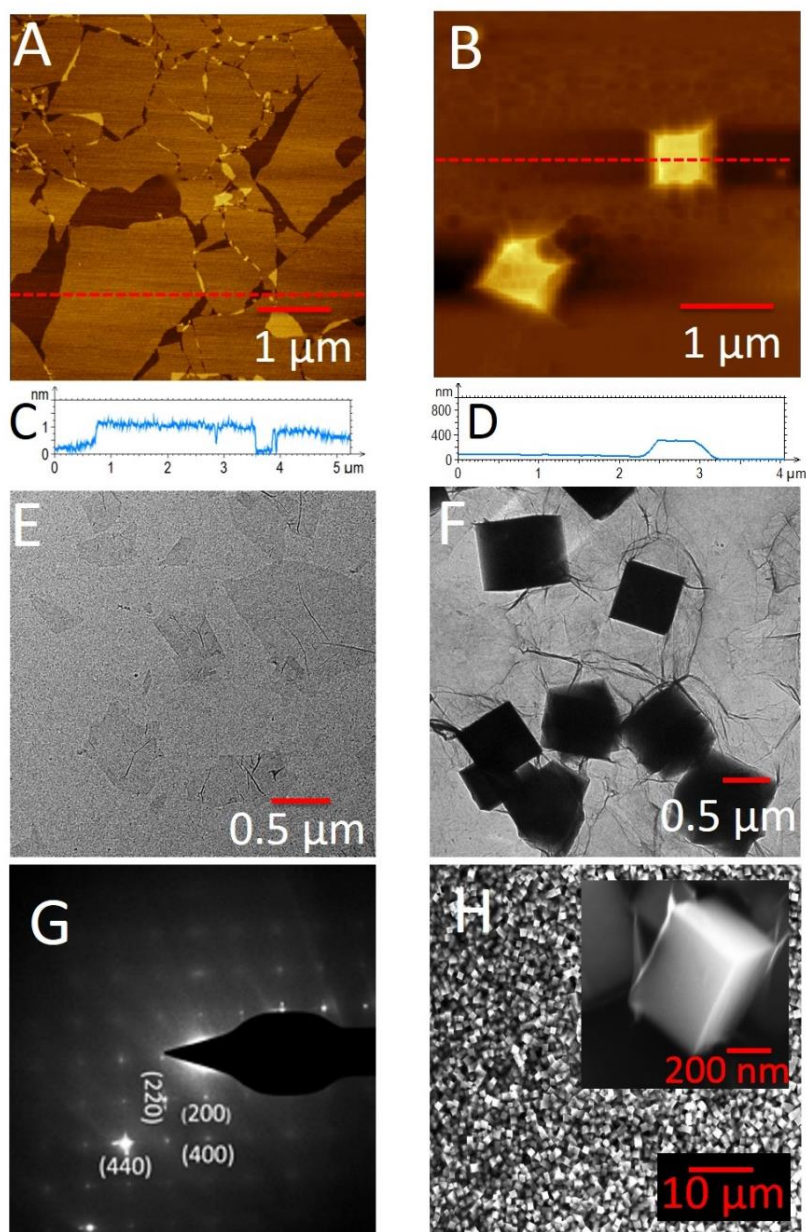
Fig. 3.5 XPS spectra of G-rGO-PB.

Fig. 3.6 AFM (A) and TEM (E) images of single layer GO; (C) and (D) cross-sectional profiles of GO and G-rGO-PB; AFM (B) and TEM (F) images of G-rGO-PB. (G) Corresponding SAED pattern of G-rGO-PB. (H) SEM images of G-rGO-PB.

Microscopy techniques were also used to characterize the structures of samples. As we expected, single layer GO sheets with the lateral dimension in the range of 0.5 to 5 μm were firstly obtained, as indicated by AFM (Fig. 3.6A) and TEM images (Fig. 3.6E). In comparison, as can be seen in FE-SEM images of the final product, G-rGO-PB (Fig. 3.6), high quality cubic PB nanocrystals with regular cubic shape and the size about 500 nm was wrapped by

rGO nanosheets. Comparing SEM images of PB with those for rGO-PB and G-rGO-PB (Fig. 3.6), it is found that the size distribution of PB nanocubes wrapped by rGO is more uniform than naked PB cubes. The most likely reason is that Fe^{3+} was locked by $-\text{OOH}$ groups and GO induced the directed growth of PB crystals on its surface. In contrast, the growth of PB crystals in the absence of GO nanosheets took place randomly. AFM and TEM images thus confirm the presence of distributed PB nanocubes in graphene matrix (Fig. 3.6). A TEM image of nanocubes with regular cubic shape is shown in Fig. 3.6F. The selected area electron diffraction (SAED) pattern (Fig. 3.6G) taken from an individual nanocube can be indexed to the (2 0 0), (2 2 0), (4 0 0) and (4 4 0) lattice planes of PB, which confirms that the PB nanocubes in the rGO-PB composite are single-crystalline. This result is clearly consistent with the XRD analysis (Fig. 3.4).

Moreover, there were no isolated PB nanocubes observed, but all PB nanocubes were interlocked by the rGO sheets—that can be found in all samples, indicating the formation of rGO-PB composites (Fig. 3.6). The results demonstrate that the PB nanocubes can be embedded into a graphene matrix consisting of individual rGO nanosheets, leading to a highly stable interlocked composite structure.

In order to investigate the elemental distribution in G-rGO-PB composites, scanning electron microscopy (SEM) and mapping analysis were performed. SEM mapping images of C, O, and Fe elements are provided in Fig. 3.7. All atoms were distributed uniformly in the composite, and it is also suggested that PB nanocubes have a high coverage on rGO sheets.

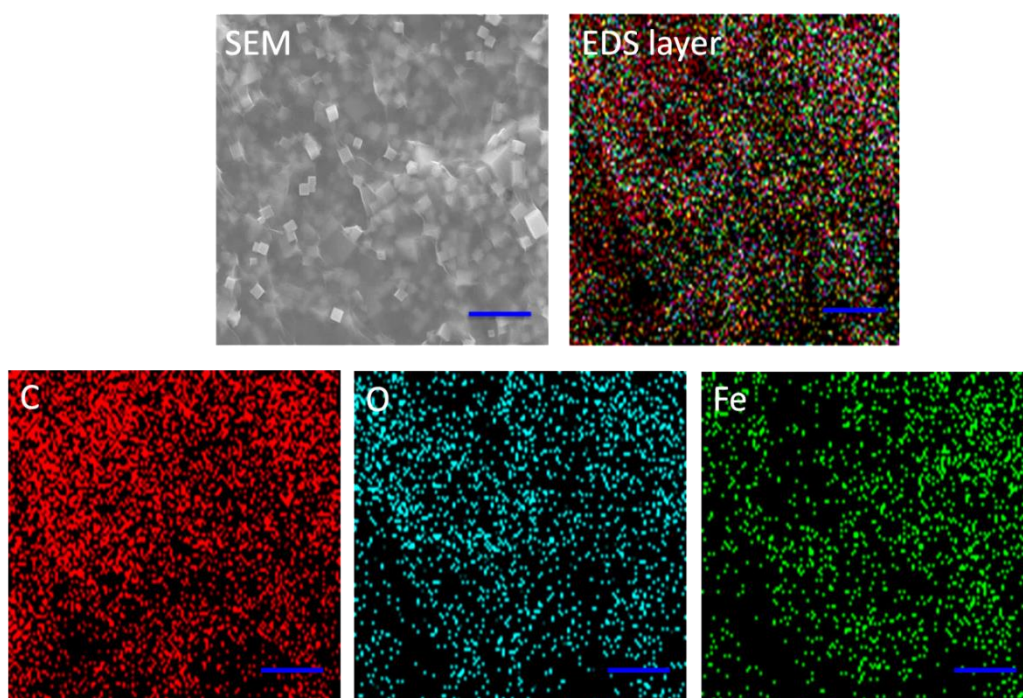


Fig. 3.7 EDX mapping images of G-rGO-PB composites. The scale bars: 5 μm .

3.3.3 Electroactivity of G-rGO-PB composites

To study the electrochemical behaviour of G-rGO-PB hybrid nanomaterials, the as-prepared PB, rGO-PB, and G-rGO-PB coated electrodes were evaluated by a three-electrode configuration in 0.1 M KCl aqueous electrolyte with the potential window of -0.4 to 0.8 V and the scan rate of 50 mV s^{-1} . Representative cyclic voltammograms (CVs) are compared in Fig. 3.8. The CV of pure rGO electrodes shows nearly rectangular shape, suggesting ideal electrical double-layer capacitive (EDLC) behaviour. The PB, rGO-PB and G-rGO-PB electrodes display evident redox couples with reversible redox peak profiles. The pair of redox peaks are observed at the formal potential of around 0.21 V (vs SCE), as expected for PB materials. In addition to the redox peaks from the PB, the CVs of rGO-PB and G-rGO-PB electrodes also show the significant expansion rectangular capacitive responses with much boosted current, revealing the effective combination of the electroactive component (PB) and capacitive rGO component. Although PB, rGO-PB and G-rGO-PB electrodes show comparably high electrochemical activity, their electron transfer kinetics are notably different. The peak separation (ΔE_p) of PB, rGO-PB and G-rGO-PB is found to be 0.49 , 0.11 and 0.10 V at a scan rate of 50 mV/s, respectively. The rate constant (k_s) was thus calculated by the Laviron method as 0.04 s^{-1} , 3.8 s^{-1} , and 65 s^{-1} corresponding to PB, rGO-PB and G-rGO-PB, respectively⁴³. These results demonstrate that the overpotential of redox process of the Fe(II/III) at G-rGO-PB electrode is notably lowered and the electron transfer rate is significantly enhanced, because GO was highly reduced in the presence of glucose to improve electrical conductivity, and further PB nanocubes were attached to rGO to form a synergistic hybrid network favouring electronic coupling for interfacial electron transfer. In order to further investigate the electrochemical behaviour of G-rGO-PB hybrid composites, PB and G-rGO-PB electrodes were tested further by electrochemical impedance spectroscopy (EIS) with the results compared in Fig. 3.9. The EIS spectra were fitted with the appropriate equivalent circuits. Due to all PB cubes were networked by rGO sheets, the charge transfer resistance (R_{ct}) of G-rGO-PB (~ 0.09 k Ω) is at least a 60-fold lower than that for pure PB cubes (~ 6.7 k Ω). This observation is consistent with the results obtained from CVs (Fig. 3.8) and also suggests that G-rGO-PB is a promising material for supercapacitor electrodes or as building blocks for electrochemical sensors, both of which have been tested.

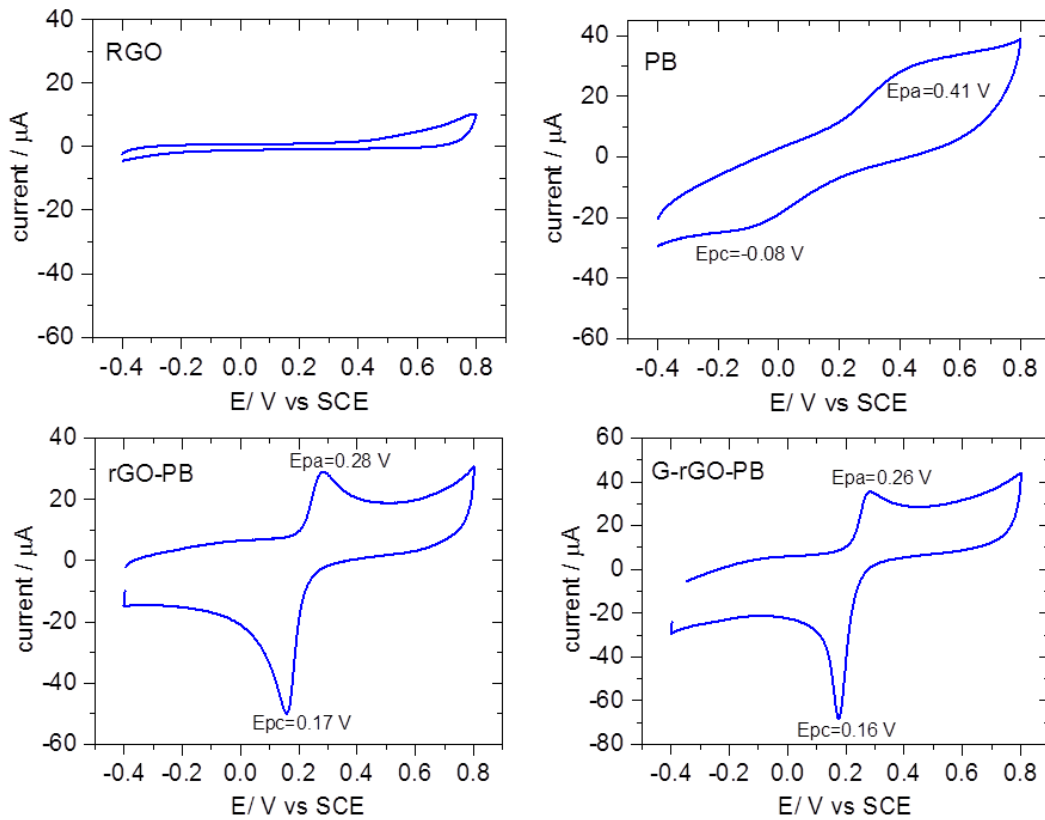


Fig. 3.8 Cyclic voltammograms of different materials based electrodes in Ar-saturated 0.1 M KCl, obtained with a scan rate of 50 mV/s.

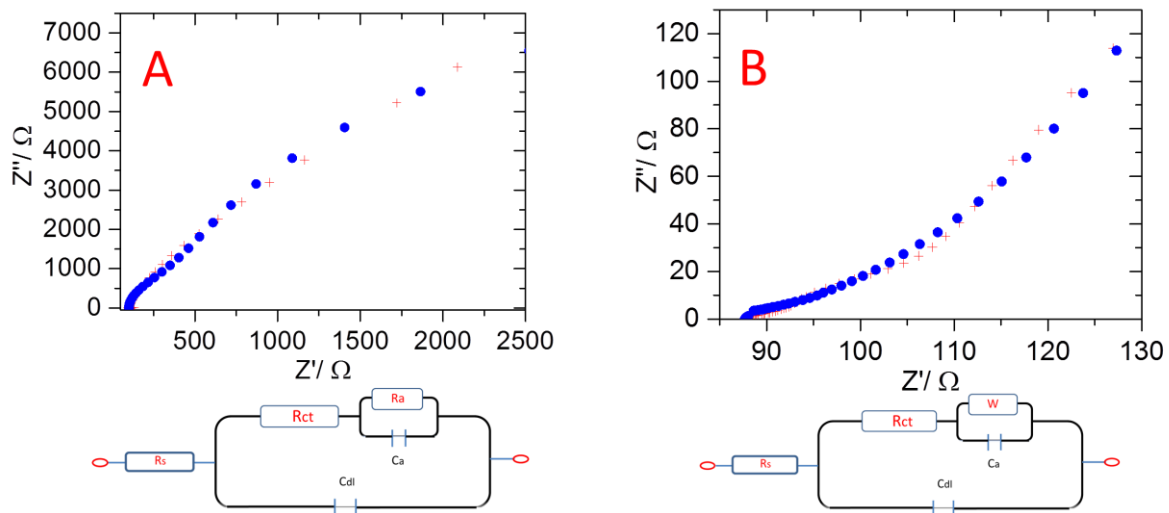


Fig. 3.9 Typical Nyquist plots obtained for PB (A) and G-rGO-PB (B) and represents the circuit used in the fitting of the EIS, electrode in 0.1 M KCl solutions at a fixed potential of 0.2 V (vs. SCE).

3.3.4 Application of hybrid composites

3.3.4.1 Supercapacitor electrodes

The CVs of as-prepared PB, rGO-PB and G-rGO-PB in 1 M KCl electrolyte with the potential window from -0.4 to 0.8 V (vs. SCE) were recorded. The capacitive performance of G-rGO-PB electrodes was further investigated with galvanostatic charge–discharge cycles. Figure 3.10, compare charge–discharge curves of rGO-PB and G-rGO-PB electrodes at different applied current densities. The specific capacitance (C_{sp}) of respective materials was calculated from the discharge curves under different experimental conditions, and the results are compared in Table 3.1. PB and its analogues are considered as promising energy storage materials, because of their high theoretical capacity. In our tests, however, the C_{sp} of pure PB materials is very low, only 4.42 F g^{-1} even at a low current density of 0.25 A g^{-1} (Table 3.1) as well as poor cycling stability was observed (Fig. 3.10D). This is mainly due to its poor conductivity and limited stability in neutral solutions. In contrast, the C_{sp} of G-rGO-PB electrodes at 0.25 A g^{-1} can reach $428.83 \pm 5 \text{ F g}^{-1}$, which is significantly higher if compared to pure rGO (14.7 F g^{-1}) and rGO-PB ($165.83 \pm 2 \text{ F g}^{-1}$) under the present testing conditions. This is because rGO nanosheets not only can interlock PB cubes but also can enhance the overall conductivity. In addition, G-rGO-PB electrodes show good cycling performance. For example, after 1000 continuous charge-discharge cycles at 2 A/g , C_{sp} was maintained at about 94% (238.13 F g^{-1}) of the initial capacitance. In the same condition, pure PB only retained approximately 50% of its specific capacitance. The results suggest that rGO not only served as electrically conductive support but also protected PB and improved PB stability in electrochemical environments. In addition, the C_{sp} of G-rGO-PB is higher than the theoretical capacity of pure PB. The significant enhancement in electrochemical performance by G-rGO-PB composite is attributed to positive synergetic interactions between the two components, in which the PB nanocubes contribute large pseudo-capacitance and rGO offers high electric double-layer capacitance and conductance.

Table 3.1 Comparison of specific capacitance and energy density obtained with various materials and current densities applied.

Materials	Current density applied	Specific capacitance	Energy density
	(A g ⁻¹)	(F g ⁻¹)	(W h kg ⁻¹)
PB	1.00	1.17	0.42
	0.25	4.48	1.60
rGO	1.00	1.47	0.53
	0.25	11.04	3.98
rGO-PB	1.00	40	14.40
	0.25	165.83	59.7
G-rGO-PB	1.00	385	138.60
	0.25	428.83	154.38

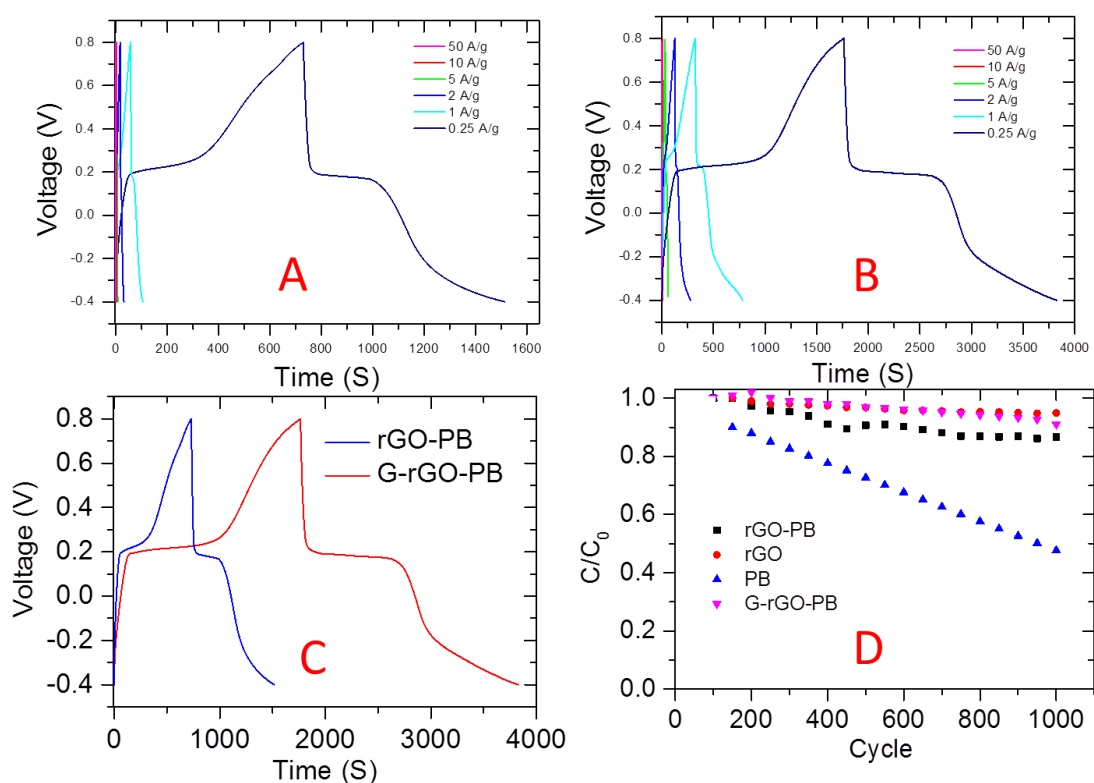


Fig. 3.10 Electrochemical performances of hybrid composites: (A) and (B) charge-discharge curves of rGO-PB G-rGO-PB in Ar-saturated 1 M KCl solution with applied various current density. (C) charge-discharge curves of rGO-PB (blue curve) and G-rGO-PB (red curve) in Ar-saturated 1 M KCl solution at 0.25 A g⁻¹. (D) Cycling stability of supercapacitor electrodes (C_{sp} vs the number of cycles).

3.3.4.2 Biosensing electrocatalysis

To qualitatively evaluate the electrocatalytic activity, CVs of the rGO-PB and G-rGO-PB sensors in 0.1 M KCl solutions containing 500 μM H_2O_2 were *first* recorded (Fig. 3.11A and B). While electrocatalytic reduction of H_2O_2 by rGO-PB started at 0.2 V (vs SCE) and tended to reach a maximum current at potentials more negative than -0.1 V, G-rGO-PB invoked electrocatalytic reduction of H_2O_2 starting at 0.3 V (vs SCE) with a maximum response at potentials more negative than -0.1 V. In order to quantitatively evaluate the performance of electrocatalytic sensing to H_2O_2 , both chronoamperometry and differential pulse voltammetry (DPV) were used in measurements. Chronoamperometric responses were recorded at -0.1 V with successive additions of H_2O_2 . Typical current-time curves are shown in Fig. 3.11C. Both rGO-PB and G-rGO-PB electrodes displayed steady-state responses upon successive addition of H_2O_2 . A subsequent addition of H_2O_2 to a stirring 0.1 M KCl solution resulted in a remarkable increase in the reduction current, which shows the electrocatalytic activity of the modified electrodes towards the reduction of H_2O_2 . The linear relationship between the H_2O_2 concentration and catalytic current is found in the range of 1.6 to 70 μM at G-rGO-PB electrodes (Fig. 3.11D), with a detect limit of 0.5 μM . The linear regression equation with a high correlation coefficient (R) of 0.998 is obtained, and the sensitivity is estimated as $1.5 \text{ A cm}^{-2} \text{ M}^{-1}$, over 3-fold higher than that for rGO-PB ($\approx 0.5 \text{ A cm}^{-2} \text{ M}^{-1}$).

To further verify the performance, some characteristic tests of G-rGO-PB composites were performed. The relative standard deviation for 3 repeated measurements of 50 μM H_2O_2 was 3.4%, which illustrated that the electrochemistry response of G-rGO-PB toward the reduction of H_2O_2 was highly reproducible. In order to explore the specific detection of H_2O_2 using the present materials, the interferences of common ions (1 mM Na^+ , Mg^{2+} , and Ca^{2+}) and small molecules (e.g. dopamine, urea acid and ascorbic acid) were investigated. The non-enzymatic chronoamperometric detections of 10 μM H_2O_2 were performed at -0.1 V with successive additions of H_2O_2 and possible interference species. The typical current-time curve suggests that no significant interference for determination of H_2O_2 was detected upon the presence of these selected ions and compounds. Thus, the composite holds potential for use of detections of H_2O_2 in practical mixture samples. Moreover, for most PB based electrochemical sensors Nafion is often used to protect the material and to eliminate redox interferences. However, the Nafion film could slow down interfacial electron transfer between PB and support electrode as well as affect mass transportation of analytes. In the present case, the composite is prepared in the form of interlocked structures. Such structural

configuration not only can stabilize PB cubes but also appears to improve the selectivity of H_2O_2 detection.

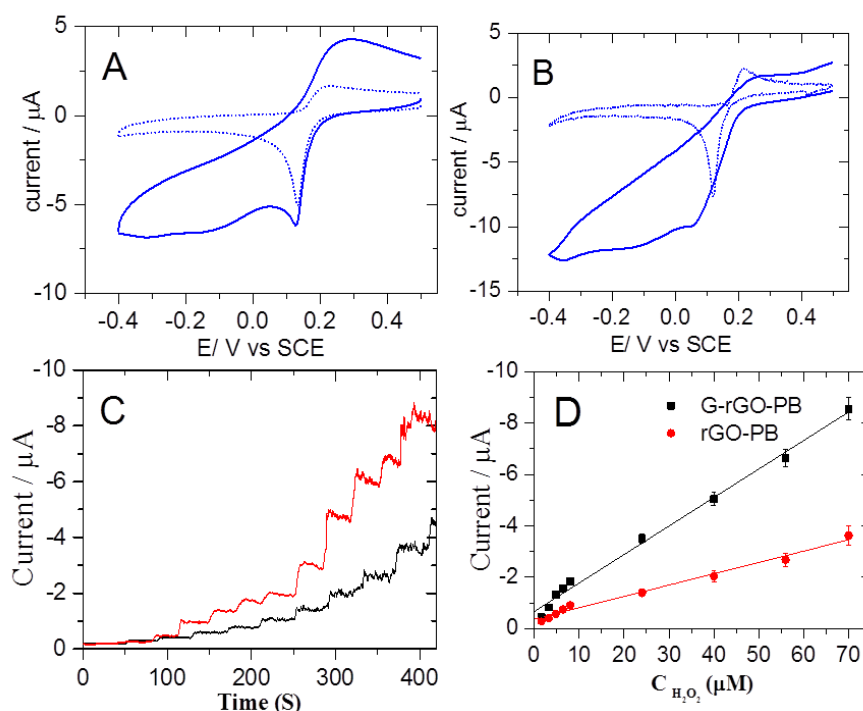


Fig. 3.11 CVs of rGO-PB (A) and G-rGO-PB (B) in Ar-saturated 0.1 M KCl (dot) and contained 500 μM H_2O_2 (solid) at 10 mV /S; (C) Amperometric responses of the rGO-PB (black curve) and G-rGO-PB (red curve) electrodes to successive additions of H_2O_2 at -0.10 V into the stirred Ar-saturated 0.1 M KCl solution. (D) The calibration curves of the current response to different concentrations of H_2O_2 .

3.4. Conclusions

A novel, green and low-cost method has been explored in this work to prepare high quality *Prussian blue* nanostructure decorated graphene hybrid materials. Graphene oxide is able to be reduced under mild conditions (low temperature, green reducing agent) without the use of any toxic reagents, accompanied by the formation of PB nanocubes in the one-step procedure. High quality *Prussian blue* nanocubes with a regular cubic shape and approximately 500 nm are wrapped by rGO nanosheets to form interlocked stable composite. The possible reaction mechanisms are discussed in detail. Interlocked graphene-*Prussian Blue* nanocomposites display high performances, when they are tested in biosensing electrocatalysis and as supercapacitor electrode material. Such structural configuration is intriguing, because it can not only stabilize PB cubes but also offer the high selectivity of H_2O_2 detection and high specific capacitance and charge-discharge cycling stability. Therefore, such hybrid composites could be a promising candidate for multiple

electrochemical applications, particularly in building Nafion-free electrochemical sensors and high-performance supercapacitor electrodes. Although this kind composite give high performance for electrochemical sensor and supercapacitor, the productivity still need further improve, as well as with some drawbacks, such as based on commercial electrode as support substrate. In the next step, we used freestanding graphene paper as substrate for construction of flexible biosensor electrodes.

References

1. Q. Chi and S. Dong. *Anal. Chim. Acta*, 1995, **310**, 429-436.
2. L. Liu, L. Shi, Z. Chu, J. Peng and Q. Jin, *Sens. Actuators B Chem.*, 2014, **202**, 820-826.
3. G. Zhao, J. Feng, Q. Zhang, S. Li and H. Chen. *Chem. Mater.*, 2005, **17**, 3154-3159.
4. F. Arduini, F. Ricci, C. S. Tuta, D. Moscone, A. Amine and G. Palleschi, *Anal. Chim. Acta*, 2006, **580**, 155-162
5. Z. Gao, Y. Qu, T. Li, N. K. Shrestha and Y. Y. Song. *Sci. Rep.-UK*, 2014, **4**, 6891.
6. N. C. Sekar, S. A. M. Shaegh, S. H. Ng, L. Ge and S. N. Tan, *Sens. Actuators B Chem.*, 2014, **204**, 414-420.
7. G. Wang, L. Chen, Y. Zhu, X. He, G. Xu and X. Zhang, *Analyst*, 2014, **139**, 5297-5303.
8. N. Zhu, S. Han, S. Gan, J. Ulstrup and Q. Chi, *Adv. Funct. Mater.*, 2013, **23** 5297-5306.
9. M. Okubo, D. Asakura, Y. Mizuno, J. D. Kim, T. Mizokawa, T. Kudo and I. Honma, *J. Phys. Chem. Lett.*, 2010, **1**, 2063-2071.
10. M. Pasta, C.D. Wessells, R.A. Huggins and Y. Cui, *Nat. Commun.*, 2012, **3**, 1149.
11. J. Hao, W. Yang, Z. Zhang and J. Tang, *Nanoscale*, 2015, **7**, 10498-10503.
12. Y. Yang, Y. Cao, X. Wang, G. Fang and S. Wang, *Biosens. Bioelectron.*, 2015, **64**, 247-254.
13. Y. You, X. Wu, Y. Yin and Y. Guo, *Energy Environ. Sci.*, 2014, **7**, 1643-1647.
14. C. Berger, Z. Song, T. Li, X. Li, A. Y. Ogbazghi, R. Feng, Z. Dai, A. Marchenkov, E. H. Conrad, P. N. First and W. A. Heer, *J. Phys. Chem. B*, 2004, **108**, 19912-19916.
15. N. Cernetic, S.F. Wu, J.A. Davies, B.W. Krueger, D.O. Hutchins, X.D. Xu, H. Ma and A.K.Y. Jen., *Adv. Funct. Mater.*, 2014, **24**, 3464-3470.
16. X. Dong, H. Xu, X. Wang, Y. Huang, M.B. Chan-Park, H. Zhang, L. Wang, W. Huang and P. Chen, *ACS Nano*, 2012, **6**, 3206-3213.
17. S. Li, N. Xia, X. Lv, M. Zhao, B. Yuan and H. Pang, *Sens. Actuators B chem.*, 2014, **190**, 809-817.
18. Y. Song, K. Qu, C. Zhao, J. Ren and X. Qu, *Adv. Mater.*, 2010, **22**, 2206-2210.
19. M. Klein, A. Varvak, E. Segal, B. Markovskiy, I.N. Pulidindi, N. Perkas and A. Gedanken, *Green Chem.*, 2015, **17**, 2418-2425.
20. Y. Zhang, Z.R. Tang, X. Fu and Y. Xu, *ACS Nano*, 2010, **4**, 7303-7314.
21. L. Liu, L. Shi, Z. Chu, J. Peng and W. Jin, *Sens. Actuators B Chem.*, 2014, **202**, 820-826.
22. Y. Wang, S. Tong, X. Xu, B. Ozyilmaz and K.P. Loh, *Adv. Mater.*, 2011, **23**, 1514-1518.
23. J. Xiong, W. Zhu, H. Li, W. Ding, Y. Chao, P. Wu, S. Xun, M. Zhang and H. Li, *Green Chem.*, 2015, **17**, 1647-1656.
24. G. Xu, J. Han, B. Ding, P. Nie, J. Pan, H. Dou, H. Li and X. Zhang, *Green Chem.*, 2015, **17**, 1668-1674.
25. X. Yang, J. Zhu, L. Qiu and D. Li, *Adv. Mater.*, 2011, **23**, 1514-1518
26. X. Li, G. Zhang, X. Bai, X. Sun, W. Wang, E. Wang and H. Dai, *Nat. Nanotechnol.*, 2008, **3**, 538-542.
27. K. S. Novoselov, A. K. Geim, S. V. Morozov, D. Jiang, Y. Zhang, S. V. Dubonos, I. V. Grigorieva and A. A. Firsov, *Science*, 2004, **306**, 666-669.
28. C. Chen, Q. Yang, Y. Yang, W. Lv, Y. Wen, P.X. Hou, M. Wang and H. Cheng, *Adv. Mater.*, 2009, **21**, 3007-3011.

29. O. C. Compton, D. A. Dikin, K. W. Putz, L. C. Brinson and S. T. Nguyen, *Adv. Mater.*, 2010, **22**, 892-896
30. Y. Wu, Y. Lin, A.A. Bol, K.A. Jenkins, F. Xia, D.B. Farmer, Y. Zhu and P. Avouris. *Nature*, 2011, **472**, 74-78.
31. S.H. Domingues, I.N. Kholmanov, T. Kim, J. Kim, C. Tan, H. Chou, Z.A. Alieva, R. Piner, A.J. Zarbin and R.S. Ruoff. *Carbon*, 2013, **63**, 454-459.
32. S. Park, J. An, J. R. Potts, A. Velamakanni, S. Murali and R. S. Ruoff. *Carbon*, 2013, **49**, 3019-3023.
33. J. Zhang, H. Yang, G. Shen, P. Cheng, J. Zhang and S. Guo. *Chem. Commun.*, 2010, **46**, 1112-1114.
34. C. Zhu, S. Guo, Y. Fang, S. Dong. *ACS Nano*, **2010**, 4, 2429-2437.
35. O. Akhavan and E. Ghaderi, *Carbon*, 2012, **50**, 1853-1860.
36. E. C. Salas, Z. Sun, A. Luttge and J. M. Tour. *ACS Nano*, 2010, **4**, 4852-4856.
37. P. Guo, F. Xiao, Q. Liu, H. Liu, Y. Guo, J. Gong, S. Wang and Y. Liu. *Sci. Rep.-UK*, 2013, **3**, 3499.
38. Z. Fan, W. Kai, J. Yan, T. Wei, L. Zhi, J. Feng, Y. Ren, L. Song and F. Wei, *ACS Nano*, 2011, **5**, 191-198.
39. X. Mei, H. Zheng and J. Ouyang. *J. Mater. Chem.*, 2012, **22**, 9109-9116.
40. L. Zhang, A. Zhang, D. Du and Y. Lin, *Nanoscale*, 2012, **4**, 4674-4679.
41. L. Qian, R. Zheng and L. Zheng, *J. Nanoparticle Res.*, 2013, **15**, 1806.
42. L. Wang, Y. Ye, H. Zhu, Y. Song, S. He, F. Xu and H. Hou, *Nanotechnology*, 2012, **23**. 455502.
43. P. S. Jensen, Q. Chi, J. Zhang and J. Ulstrup. *J. Phys. Chem. C*, 2009, **113**, 13993-14000.

Chapter 4. Size dependent self-catalytic growth and electrochemical catalysis of Au@PB core-shell nanoparticles

4.1. Introduction

In Chapter 3, *Prussian blue* nanocube functionalized graphene was synthesized via the one-pot method. Although these kinds of composites give high performance for electrochemical sensor and supercapacitor, large-size PB cubes (500 nm) resulted in lowered catalysis efficiency. Thus, *Prussian blue* nanoparticles (PBNPs) have become a subject of intense interest, because of their intriguing physical and chemical properties different from their bulk counterparts and hence novel applications in catalysis¹⁻², energy devices³⁻⁴, drug delivery⁵⁻⁶, separation devices⁷⁻⁸ and sensors⁹⁻¹³. In particular, electrocatalytic applications of PBNPs have received increasing attention recently¹. As compared to their bulk counterparts and *Prussian blue* films, PBNPs often have superior or even new catalytic properties following from their nanometer size that give them increased surface-to-volume ratios and chemical potentials. The size of nanoparticles plays a pivotal role in determining their electrocatalytic properties, and understanding how the size affects their catalytic properties remains a central goal in nanocatalysis research. Size-dependent reactions were investigated extensively¹⁴⁻²⁰, but size effect in electrocatalysis was not mentioned so much²¹⁻²², especially distinct PB size effect is not reported.

It is known that *PB* has low solubility, indicating that added Fe^{2+} to $[\text{Fe}(\text{CN})_6]^{3-}$ immediately causes the formation of *PB* precipitate. For this kind of rapid reaction, it is difficult to obtain controlled shape and well dispersed uniform size distribution of PBNPs, and the conductivity which is very important in electrochemical reaction process is also concerned. To overcome those problems, polymer protection²³ was used to synthesize core-shell structural *PB@PVP* NPs, that using polymer as shell blocks the PBNPs growth. It is easy to control the size and shape, but the conductivity of *PB@PVP* NPs was even worse than that of pure PBNPs and it probably will affect the electrochemical activity as the shell could block the electron transfer.

Core-shell structured nanoparticles have been subjected for extensive studies recently. The combination of two or more different elements into core-shell NPs allows not only significant improvement in their properties, but also makes it possible to obtain unique properties that cannot be achieved with single component NPs. Au nanoparticles (AuNPs)

are well known to exhibit various colors arising from surface plasmon absorption and size-dependent specific catalytic, optical properties, high conductivity and good biological compatibility, and they are widely used as the core to prepare core-shell structured NPs²⁴⁻²⁹, Here we prepare a new type core-shell structural NPs that is using AuNPs as core and PB as shell and study their electrocatalytic properties. AuNPs as a representative catalyst has been applied in different areas and the size-effect of AuNPs has also become a subject of intensive interest. Self-catalysed formation of core-shell structure Au@Prussian blue nanoparticles (Au@PB NPs) has been previously reported, but the size-effect for Au@PB NPs is still not clear. In this research PB was used as shell materials, and Au@PB NPs with well-defined shape and size-control was successfully synthesized. The working principle for self-catalytic formation of Au@PB NPs is shown in Fig.4.1. AuNPs acted as both a catalyst and a core, Fe^{3+} was first captured on the surface of AuNPs by electrostatic attraction, as AuNPs were protected by citrate with negative charges. Fe^{3+} was then catalytically reduced to Fe^{2+} , and Fe^{2+} finally reacted with $\text{Fe}(\text{CN})_6^{3-}$ to form the PB film attached to AuNPs surfaces.

In this part, we have studied and demonstrated that: 1) AuNPs was used as a core, and PB as a shell to fabricate core-shell structured PB functional AuNPs (Au@PB NPs), with the aim to overcome problems like difficult to get controlled shape, well dispersed uniform size distribution of PBNPs, and poor conductivity; 2) with the facile reactions, using AuNPs as a catalytic agent and two kinds of Fe^{3+} species (FeCl_3 and $\text{K}_3\text{Fe}(\text{CN})_6$) as PB precursors enables an easy way to synthesize size-controllable, highly stable, water soluble, and biologically compatible Au@PB NPs; 3) 3 nm to 42 nm AuNPs were used to systematically investigate the size effect of AuNPs as core and catalyst to prepare Au@PB NPs and demonstrated that the smallest AuNPs have the highest activity for self-catalytic formation of Au@PB NPs; and 4) Au@PB NPs with various sizes were exploited to study size-dependent electrocatalytic activity towards reduction of hydrogen peroxide (H_2O_2).

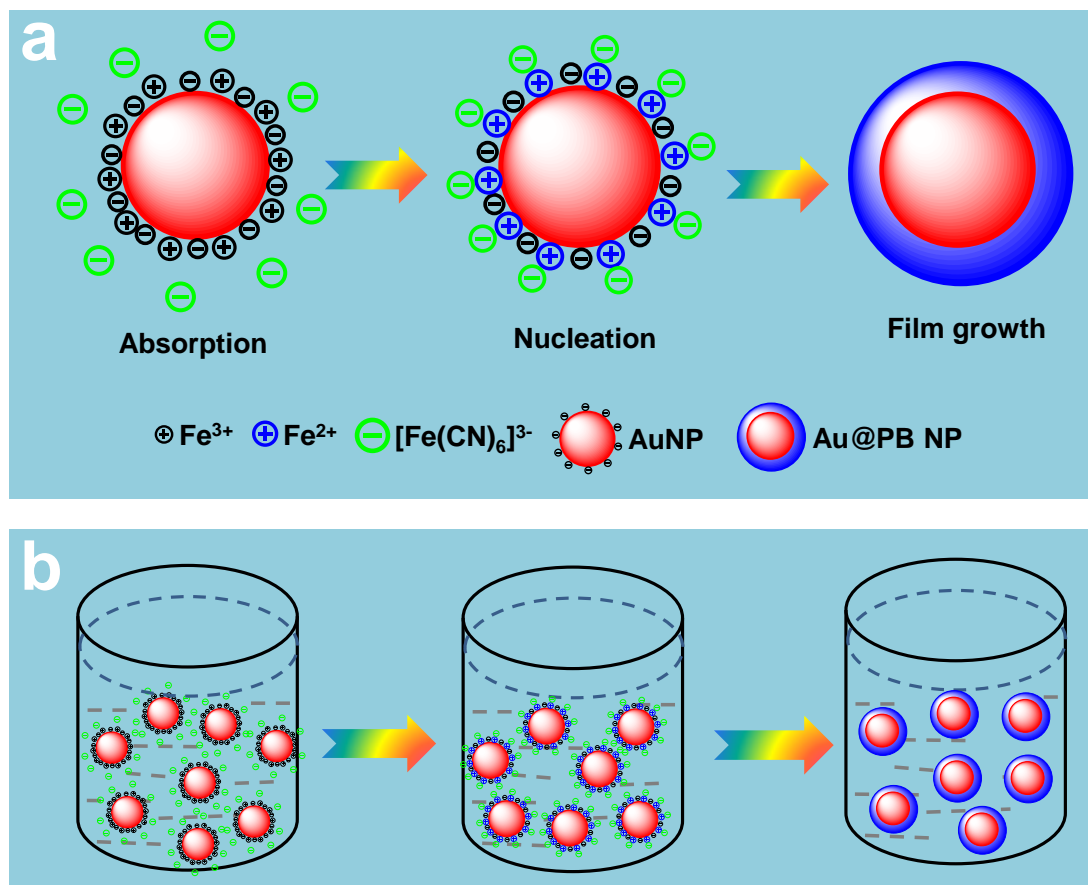


Fig. 4.1 Schematic illustration of the formation mechanisms of core-shell Au@PB nanoparticles. (a) Focused on a single nanoparticle, and (b) numerous nanoparticles in solutions. The reactions involve the two key steps: the adsorption and reduction of Fe(III) ions on the AuNPs surface, which allows ferricyanide ions to access the gold nanoparticle surface, followed by the conversion of Fe(II) to form PB layers.

4.2. Experimental section

4.2.1 Synthesis of AuNPs.

Different size citrate protected AuNPs were prepared according to previous reports (3 nm³¹; 6 nm, 14 nm and 20 nm AuNPs³²⁻³³; 34 nm and 42 nm³⁴). The size and morphology of the synthesized AuNPs were confirmed by TEM analysis, and the concentration of AuNPs was estimated according to a previous report³⁴.

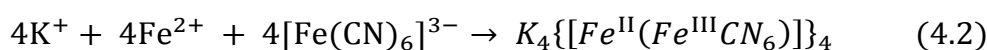
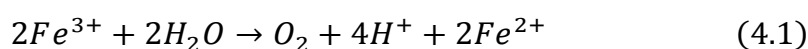
4.2.2 Synthesis and purification of Au@PB core/shell nanoparticles.

In a typical experiment, in order to keep the fixed population of nanoparticles, the 10 mL mixture solution containing 1.0 mM FeCl₃, 1.0 mM K₃Fe(CN)₆, 0.1 M KCl and 0.025 M HCl was slowly added to 10 mL 1.25 nM AuNPs solution under vigorous stirring. Upon the addition of the mixture solution, the colour of AuNPs solution changed rapidly from red to dark-blue. After 30 min, the product was purified by centrifugation and filtration and then re-dispersed in 10 mL Milli-Q water as a stock solution.

4.3. Results and discussion

4.3.1 Self-catalytic formation of Au@PB nanoparticles.

Citrate-protected AuNPs were prepared according to previous reports³¹⁻³⁴ with some modifications. The UV-vis spectra (Fig. 4.2) and transmission electron microscopy (TEM) images (Fig. 4.3) of AuNPs strongly suggest that different sizes (3 nm, 6 nm, 13 nm, 20 nm, 32 nm and 42 nm) of AuNPs were obtained. After slowly adding PB precursors into the AuNPs solution, the colour of the solution completely changed to dark-blue. The overall reactions can be described in eq.1 and eq.2. AuNPs act as good catalyst for reaction 4.1 that is thermodynamically unfavourable because the standard free energy is 173 KJ/mol, and the driving force is thus most likely provided by reaction 4.2. The standard free energy of reaction 4.2 is -177 KJ/mol. According to the reaction 4.2, PB films formed on the surface of AuNPs by replacing the protecting agent, citrate.



Comparing the UV-vis spectrum of AuNPs (a) with that of Au@PB NPs (b) in Fig. 4.2, the characteristic absorption peak of unmodified AuNPs appears at around 520 nm as expected, but the characteristic absorption peak of the product shifts to 700 nm. This is a strong indication that PB was obtained. EDX results (Fig.4.5) further supports the formation of PB layers. In other words, the yield of PB increased by increasing AuNPs as shown in

Fig. 4.4. The characteristic absorption peak of AuNPs at 520 nm significantly decreased, but not completely disappeared, which is other evidence that AuNPs acted as an important catalyst for eq(4.1). It is also suggested that PB formed a thin film coated on the surface of AuNPs and blocked the surface plasmon resonance of AuNPs, resulting in the decrease in the 520 nm plasmon peak. As a reference, if AuNPs and PBNPs were directly mixed, the absorption of AuNPs at 520 nm did not change (**Fig.4.2c**), which is distinct from the spectrum of core-shell structured Au@PB NPs (**Fig. 4.2d**).

As-prepared Au@PB NPs were also characterized by TEM (**Fig.4.5**). All AuNPs were covered by PB, consistent with our proposed formation mechanism (**Fig. 4.1**). To further test the proposed formation mechanism, in a control experiment positively charged polymer (PVP) protected AuNPs were used to replace citrate protected AuNPs for the synthesis of Au@PB NPs. PB was still obtained, but only separate PB NPs and AuNPs rather than core-shell structured NPs were produced.

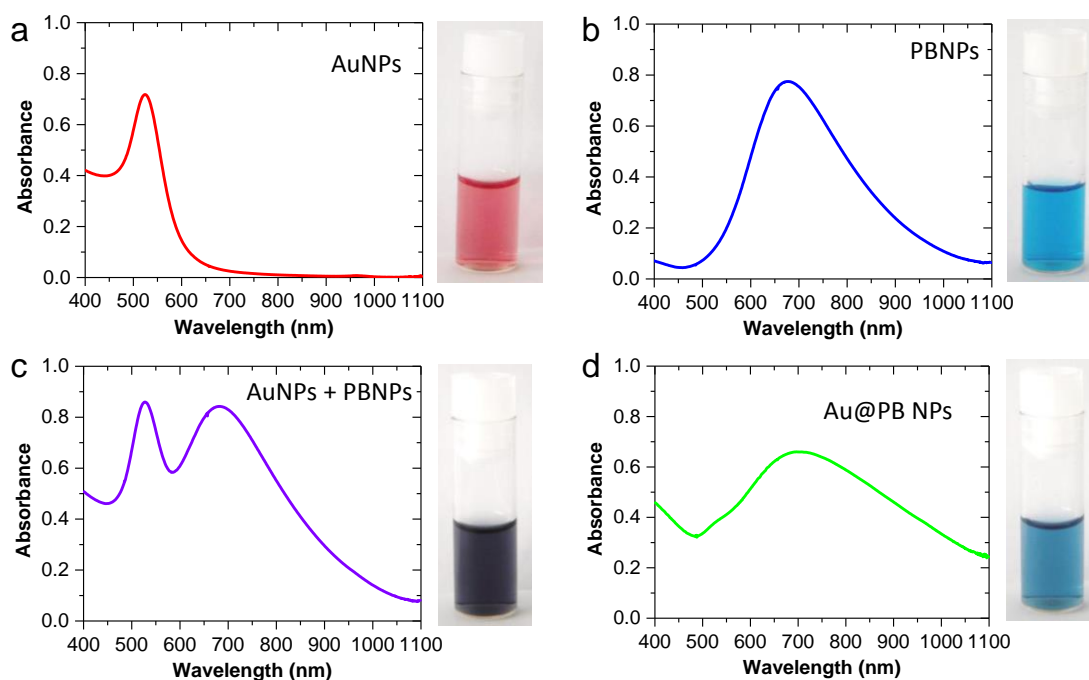


Fig. 4.2 UV-vis spectra and digital photographs of various colloid nanoparticle suspensions. (a) Pure gold nanoparticles (AuNPs); (b) pure *Prussian Blue* nanoparticle (PBNPs); (c) a physical mixture of AuNPs and PBNPs solutions (1:1, v/v); and (d) core-shell nanoparticles (Au@PB NPs).

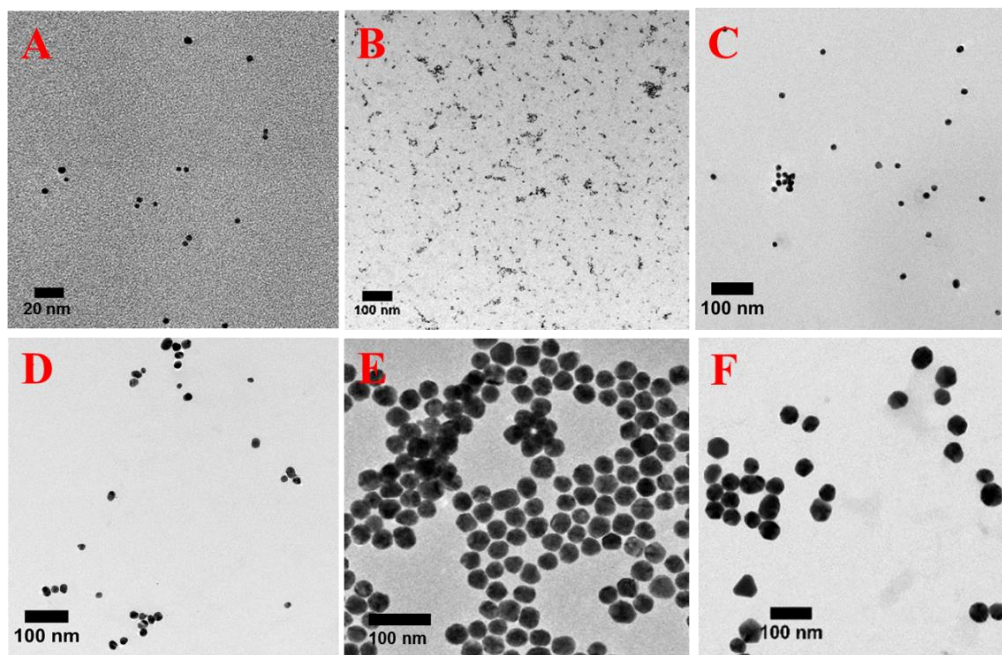


Fig. 4.3 TEM images of AuNPs with different sizes: (A) 3 nm, (B) 6 nm, (C) 13 nm, (D) 20 nm, (E) 34 nm and (F) 42 nm.

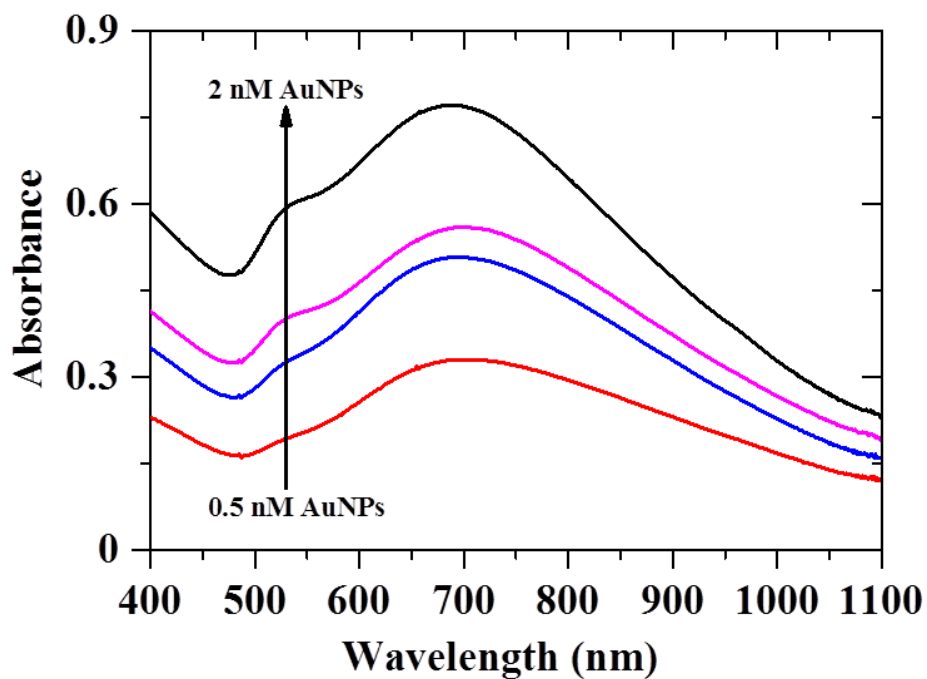


Fig. 4.4 UV-vis spectra of Au@PB NPs prepared from different amounts of 6 nm AuNPs and fixed 1 mM PB precursor solution.

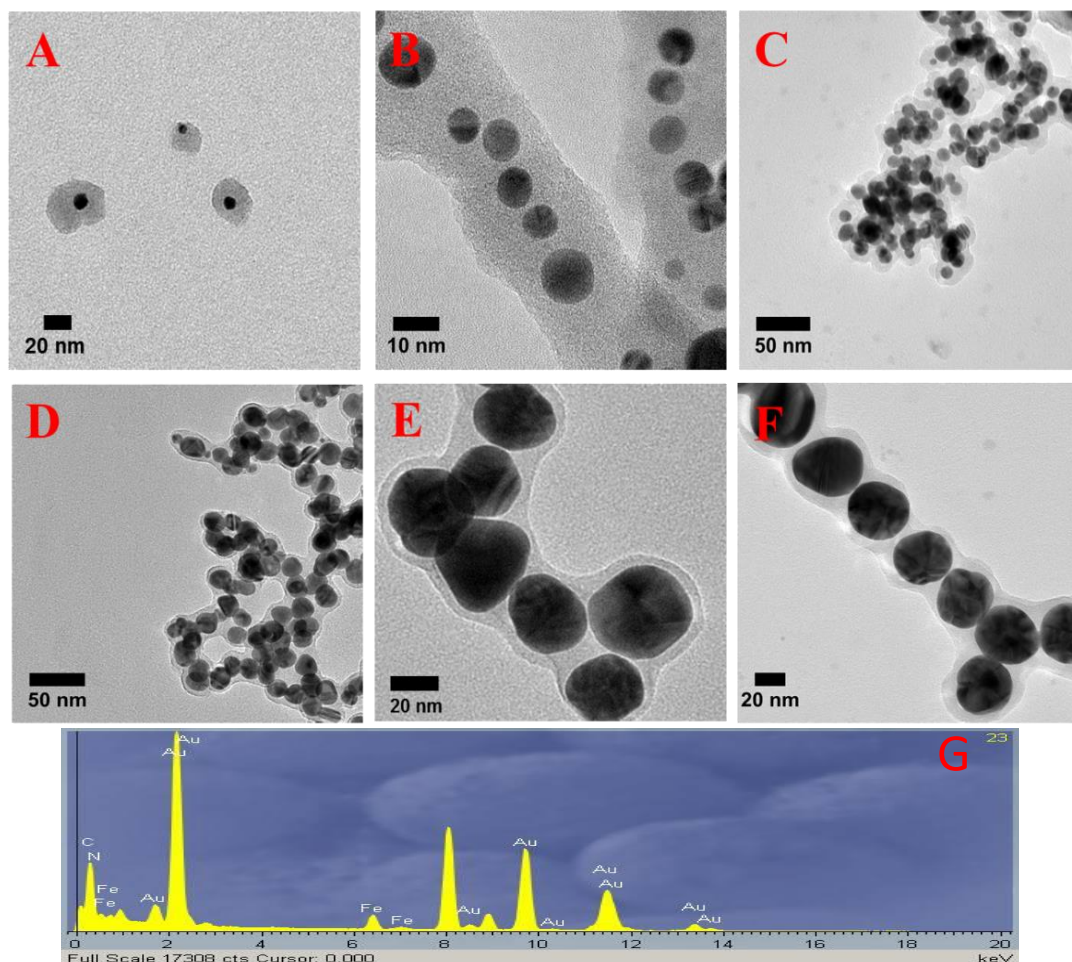


Fig. 4.5 HRTEM images of Au@PB NPs prepared from different sizes of AuNPs: (A) 3 nm, (B) 6 nm, (C) 13 nm, (D) 20 nm, (E) 34 nm and (F) 42 nm; (G): the EDX spectrum of Au@PB NPs.

4.3.2 Structural mapping of Au@PB nanoparticles.

UV-vis spectra of Au@PB NPs that were synthesized from different sizes of AuNPs are shown in Fig.4.6. All sizes of AuNPs showed high performance for catalysis PB precursor to form Au@PB NPs, but the characteristic absorption of Au@PB NPs with different sizes were red-shifted from around 700 nm to 710 nm, 750 and 770 nm, respectively. More interestingly, the A_{PB}/A_{AuNPs} ratio decreased with increasing the size of AuNPs, which is most likely due to the decrease in the thickness of PB films with increasing the AuNP size.

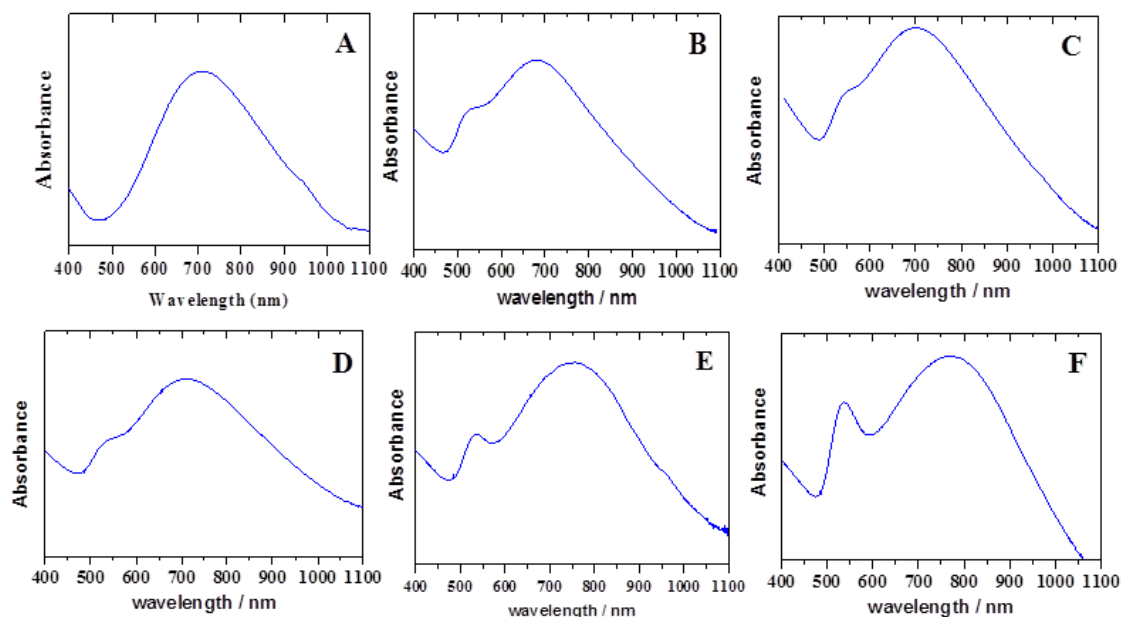


Fig. 4.6 UV-Vis spectra of Au@PB NPs prepared by different sizes of AuNPs: (A) 3 nm, (B) 6 nm, (C) 13 nm, (D) 20 nm, (E) 34 nm and (F) 42 nm

In order to study the size-effect of AuNPs for formation of Au@PB NPs in detail, TEM was used to characterize the shape and size of the Au@PB NPs. We can clearly see the size of Au@PB grown to 23 nm, 18 nm, 23 nm, 28 nm, 41 nm, and 48 nm, corresponding to (3–42 nm) AuNPs (as shown in Fig.4.5). Moreover, the thickness of the PB films was estimated to be 10 nm, 6 nm, 5 nm, 4 nm, 3.5 nm and 3 nm, respectively. The thickness of PB films decreased with increasing AuNP size. The 3 nm AuNPs thus showed the highest activity for self-catalysed formation of Au@PB NPs. The most likely reason is that small sizes of AuNPs have higher surface-to-volume ratio than that for larger AuNPs, leading to higher catalytic activities. Furthermore, the 48 nm Au@PB NPs were used as an example for characterizations by high-angle annular dark-field scanning TEM (HAADF-STEM) and elemental mapping of Au@PB core-shell NPs (Fig. 4.7). From the EDS mapping of Au@PB NPs, AuNPs with a size of 42 are located in the centre. The outer shells are composed of mainly elemental Fe and the thickness of the shell is about 6 nm. N element was also found on the shell by EDS linear scanning, with the cross-sectional profile of the elemental distribution of Au, Fe and N in an Au@PB NP shown in Fig.4.8. All results thus suggest that different sizes of Au@PB NPs with various thickness PB film were successfully synthesized by using AuNPs self-controlled catalytic procedure with the formation process of Au@PB NPs following size effect of the AuNPs.

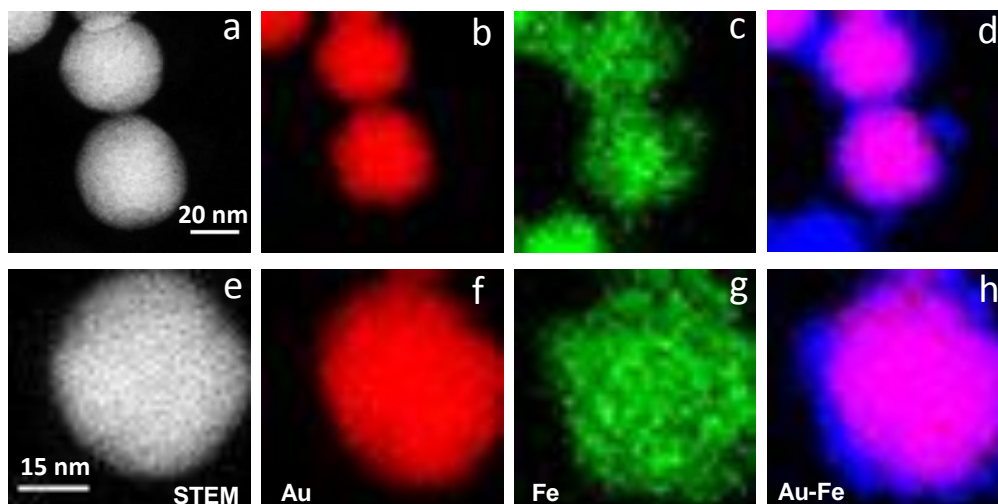


Fig. 4.7 EDS mapping of elemental distribution for 48 nm Au@PB nanoparticles. (a) and (e) STEM images, (b) & (f) for gold, (c) & (g) for iron, (d) and (h) for both gold and iron.

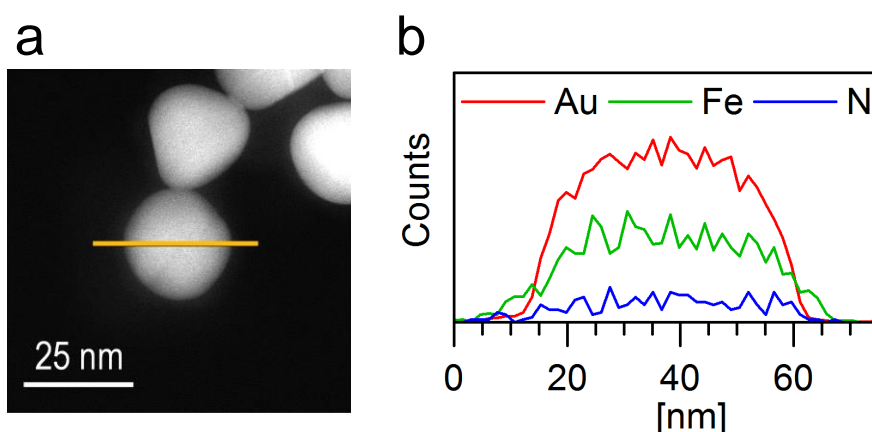


Fig. 4.8 (a) A TEM image of 48 nm Au@PB NPs and (b) the cross-sectional profiles of the elemental distribution of Au, Fe and N in an single Au@PB nanoparticle.

4.3.3 Electroactivity of Au@PB nanoparticles.

To evaluate the electrochemical behaviour of the different sized Au@PB NPs, cyclic voltammograms (CVs) of Au@PB NPs/GCE in 0.1 M KCl solution were recorded. As shown in Fig. 4.9, one pair of well-defined redox peaks are observed at 0.15 V, while no obvious response was found at the control electrode, Nafion/GCE in which there was no core-shell NPs, indicating that the PB layer on AuNP retained good electrochemical activity. In addition, the effects of scan rates on responses were studied (Fig. 4.9). Both the redox peak currents increased with increasing scan rate. The relationship between the peak currents (I_p) and scan rate (v) was evaluated by a series of plots of I_p versus v^x with $x = 0.5-1.0$. The best linear fit with a best linear coefficient (R)

is obtained for $x = 0.8$, indicating a mixed surface and diffusion controlled electrochemical process. Every size of Au@PB NPs gives high electrochemical activity, but the peak separation (ΔE_p) of different size Au@PB NPs is different, 70 mV, 132 mV, 112 mV, 211 mV, 230 mV and 248 mV are corresponding to (3-42 nm) AuNPs with scan rate in 500 mV/s as shown in Fig.4.10. The apparent rate constants (k_s) were estimated by the Laviron's method³⁰ as 310 s^{-1} , 614 s^{-1} , 338 s^{-1} , 190 s^{-1} , 133 s^{-1} and 101 s^{-1} , respectively. The relationship of sizes of Au@PB NPs with rate constant is shown in Fig. 4.12C, it decreased with increasing the size of Au@PB NPs, indicating Au@PB NPs prepared by 3 nm AuNPs give faster electron transfer rate than other sizes. This will be further discussed later.

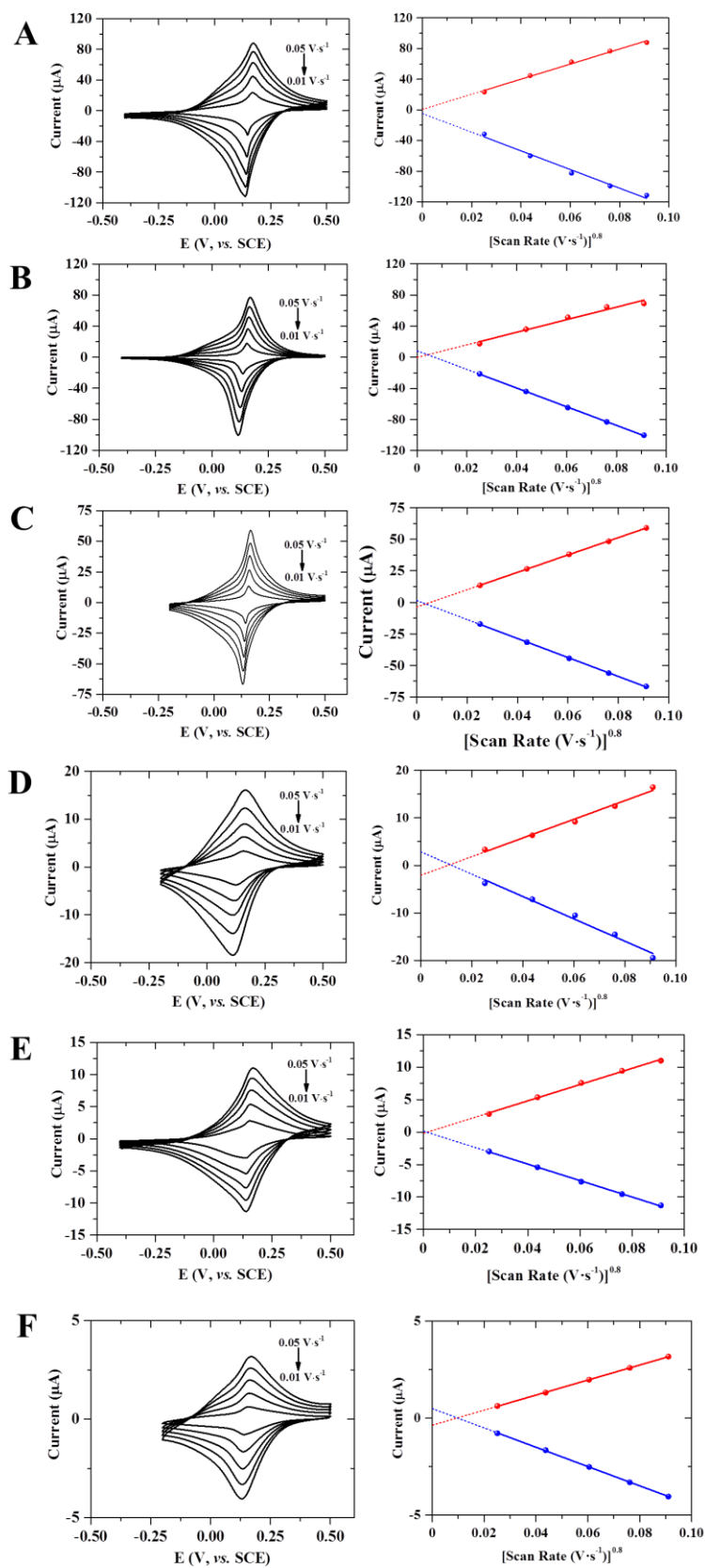


Fig. 4.9 CVs of Au@PB NPs prepared by different sizes of AuNPs (A, 3 nm; B, 6 nm; C, 13 nm; D, 20 nm; E, 34 nm and F, 42 nm) with scan rates ranging from $0.01 \text{ V}\cdot\text{s}^{-1}$ to $0.05 \text{ V}\cdot\text{s}^{-1}$. AuNPs@PB was drop-casted on GCE surfaces. Electrolyte: 0.1 M KCl. The corresponding relations between the anodic/cathodic peak currents and the scan rates are also shown (right).

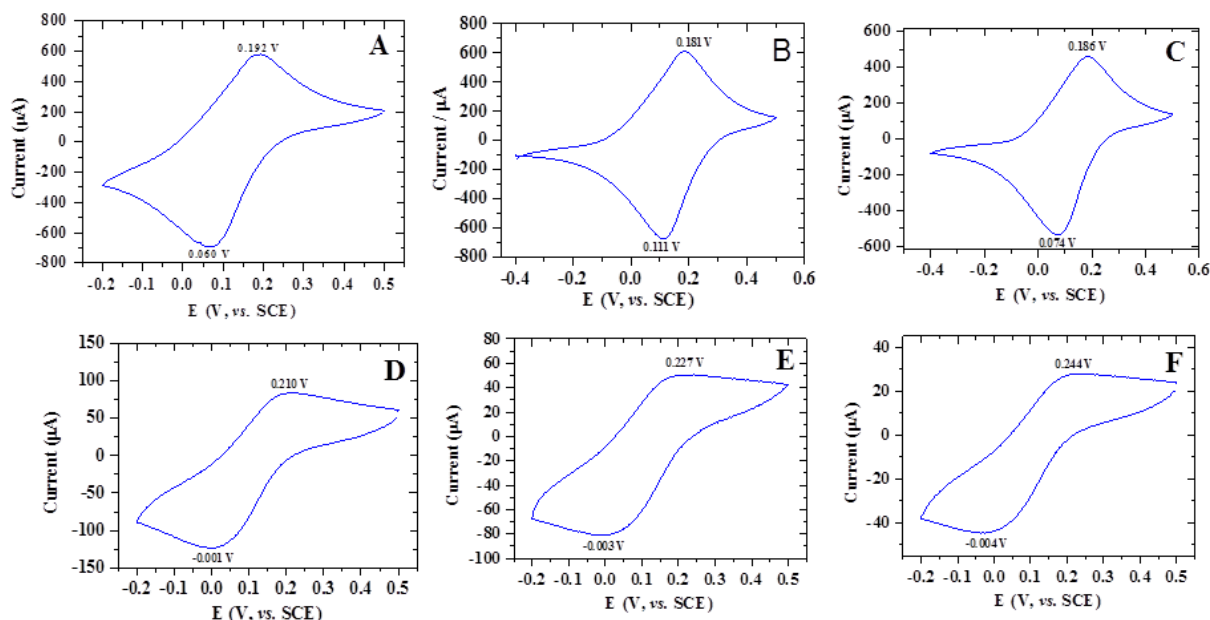


Fig. 4.10 CVs of Au@PB NPs prepared by different sizes of AuNPs (A, 3 nm; B, 6 nm; C, 13 nm; D, 20 nm; E, 34 nm and F, 42 nm) at a scan rate of $0.5 \text{ V}\cdot\text{s}^{-1}$. AuNPs@PB were drop-casted on GCE surfaces. Electrolyte: 0.1 M KCl.

4.3.4 Size-dependent electrochemical catalysis of Au@PB nanoparticles toward reduction of H_2O_2 .

As all sizes Au@PB NPs displayed high performance electrochemical activity as shown in Figs. 4.9 and 4.10, they would be good candidates for studying size effects in electrocatalysis. All the size Au@PB NPs exhibited electrocatalytic activity, electrocatalytic reduction of H_2O_2 started at 0.3 V and tended to reach a maximum effect at potentials more negative than -0.1 V . The electrocatalytic current increases with increasing H_2O_2 concentration (Fig. 4.11A) as expected. To study size effects of Au@PB NPs on electrocatalytic reduction of H_2O_2 in detail, chronoamperometric detection of H_2O_2 was further performed at a fixed potential of -0.1 V . Fig. 4.11B shows a typical steady state response of a Nafion/Au@PB NPs films modified GCE electrode upon successive addition of H_2O_2 . The current density varying with the concentration of H_2O_2 was calculated, and the results are shown in Fig. 4.12A. The current density decreased with increasing the size of Au@PB NPs, i.e. 3.0, 6.6, 3.4, 2.1, 1.2 and 0.8 ($\text{Acm}^{-2} \text{ M}^{-1}$), respectively. The relationship of sizes of Au@PB NPs with relative catalytic efficiency is shown in Fig. 4.12B. The electrocatalytic efficiency decreased with increasing the NP size, with 18 nm Au@PB NPs displaying the highest efficiency. All the

results are further compared in Table 4.1. From Table 4.1 and Fig. 4.12, we can conclude that the electrocatalytic activity of Au@PB NPs towards reduction H_2O_2 significantly depends the NP size.

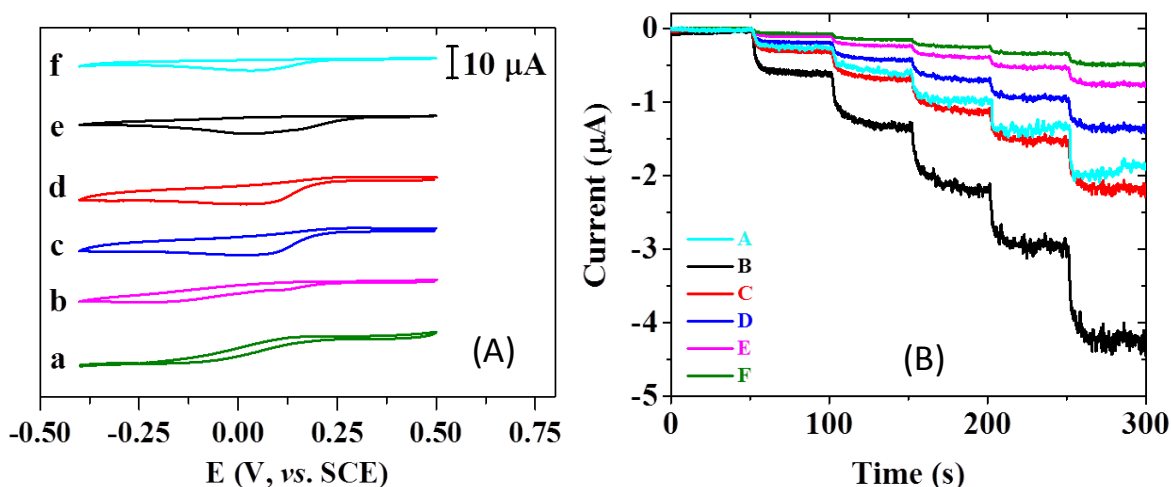


Fig. 4.11 (A) Qualitative evaluation of electrocatalytic activity of Au@PB NPs prepared by different sizes of AuNPs (a), 3 nm; (b), 6 nm; (c), 13 nm; (d), 20 nm; (e), 34 nm and (f), 42 nm). Cyclic voltammograms obtained in 0.1 M KCl containing 0.5 mM H_2O_2 with a scan rate of 10 mV s^{-1} . (B) Amperometric responses of AuNPs@PB prepared by different sizes of AuNPs (A, 3 nm; B, 6 nm; C, 13 nm; D, 20 nm; E, 34 nm and F, 42 nm) to the electrocatalytic reduction of 1.6 μM , 3.2 μM , 4.8 μM , 6.4 μM and 9.6 μM H_2O_2 . H_2O_2 concentration was adjusted by adding freshly-prepared H_2O_2 aq. into the three-electrode cell per 50 s. AuNPs@PB were drop-casted on GCE surfaces. Electrolyte: 0.1 M KCl.

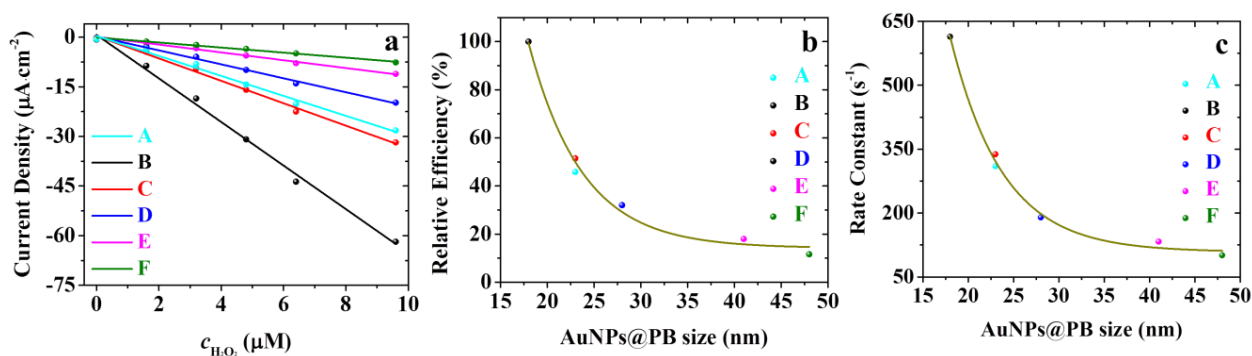


Fig. 4.12 Quantitative evaluation of size-dependent electrocatalytic activity for AuNPs@PB prepared with different sizes of AuNPs (A, 3 nm; B, 6 nm; C, 13 nm; D, 20 nm; E, 34 nm and F, 42 nm). (a) The dependence of current density on H_2O_2 concentration, (b) relative electrocatalytic efficiency, and (c) the relation of interfacial electron transfer with AuNPs@PB size.

Table 4.1 Comparison of physiochemical properties and electrocatalytic activity of differently sized Au@PB NPs.

No.	AuNPs (nm)	PB Shell Thickness (nm)	AuNPs@PB (nm)	Rate Constant (s ⁻¹)	Current Density (A·cm ⁻² ·M ⁻¹)	Relative Catalytic Activity (%)
#1	3±0.5	10±3	23±3	310±20	3.0±0.4	45.8
#2	6±1	6±2	18±2	614±30	6.6±0.5	100
#3	13±2	5±2	23±2	338±20	3.4±0.4	51.5
#4	20±2	4±1	28±3	190±15	2.1±0.3	32.0
#5	34±3	3.5±1	41±4	133±10	1.2±0.3	18.0
#6	42±3	3±1	48±4	101±10	0.8±0.2	11.6

4.4. Conclusions

We have successfully synthesized core-shell structural Au@PB NPs with the size largely controlled by using different sized AuNPs. The core-shell nanoparticles could offer some advantages including size-controllability, highly stability, water solubility, and high conductivity. The possible mechanism of self-catalysed formation of Au@PB NPs was investigated in detail. Au@PB NPs can be used as an electrocatalyst for reduction of hydrogen peroxide, which clearly displays size-dependent enhancement of electrocatalytic activity with decreasing the overall particle size and in turn facilitating interfacial electron transfer.

References

1. G. Wang, L. Chen, Y. Zhu, X. He, G. Xu and X. Zhang, *Analyst*, 2014, **139**, 5297-5303.
2. L. Shen, Z. Wang and L. Chen, *Chem. Eur. J.*, 2014, **20**, 12559-12562.
3. C. Zhao, C. Shen, F. Xin, Z. Sun and W. Han, *Mater. Lett.*, 2014, **137**, 52-55.
4. G. Fu, W. Liu, Y. Li, Y. Jin, L. Jiang, X. Liang, S. Feng and Z. Dai, *Bioconjugate Chem.*, 2014, **25**, 1655-1663.
5. L. Cheng, H. Gong, W. Zhu, J. Liu, X. Wang, G. Liu and Z. Liu, *Biomaterials*, 2014, **35**, 9844-9852.
6. S. Jang, S.B. Hong, H. Yang, K. Lee, J. Moon, B. Seo, Y. Huh and C. Roh, *Nanomaterials*, 2014, **4**, 894-901.
7. T. Arun and R. Joseyphus, *J. Mater. Sci.*, 2014, **49**, 7014-7022.
8. Z. Gao, Y. Qu, T. Li, N. Shrestha and Y. Song, *Sci. Rep.-UK*, 2014, **4**, 6891.
9. G. Zhao, J. Feng, Q. Zhang, S. Li and H. Chen, *Chem. Mater.*, 2005, **17**, 3154-3159.

10. P.A. Fiorito, V.R. Goncales, E.A. Ponzio and S.I.C. Torresi, *Chem. Commun.*, 2005, **3**, 366-368.
11. N. Zhu, S. Han, S. Gan, J. Ulstrup and Q. Chi, *Adv. Funct. Mater.*, 2013, **23**, 5297-5306.
12. Q. Chi and S. Dong, *Anal. Chim. Acta*, 1995, **310**, 429-436.
13. O. Choi and Z. Hu, *Environ. Sci. Technol.*, 2008, **42**, 4583-4588.
14. S. Huang, Y. Lin, T. Hor and G. Jin, *J. Am. Chem. Soc.*, 2013, **135**, 8125-8128.
15. W. Kaden, W. Kunkel, M.D. Kane, F.S. Roberts and S.L. Anderson, *J. Am. Chem. Soc.*, 2010, **132**, 13097-13099.
16. Z. Xu, F. Xiao, S.K. Purnell, O. Alexeev and S. Kawi, *Nature*, 1994, **372**, 346-348.
17. C. Wang, R. Thompson, P. Ohodnicki, J. Baltrus and C. Matranga, *J. Mater. Chem.*, 2011, **21**, 13452-13457.
18. S. Bonanni, K. Ait-Mansour, W. Harbich and H. Brune, *J. Am. Chem. Soc.*, 2014, **136**, 8702-8707.
19. Q. Wu, H. Kang, B.N. Oh and J. Kim, *J. Phys. Chem. C*, 2012, **116**, 8020-8026.
20. P.C. Pandey and A.K. Pandey, *Analyst*, 2012, **137**, 3306-3313.
21. C. Koenigsmann, W.P. Zhou, R. R. Adzic, E. Sutter and S. S. Wong, *Nano Lett.*, 2010, **10**, 2806-2811.
22. T. Uemura and S. Kitagawa, *J. Am. Chem. Soc.*, 2003, **125**, 7814-7815.
23. P. S. Jensen, Q. Chi, J. Zhang and J. Ulstrup, *J. Phys. Chem. C*, 2009, **113**, 13993-14000
24. Y. Qi, M. Chen, S. Liang, W. Yang and J. Zhao, *Appl. Surf. Sci.*, 2008, **254**, 1684-1690.
25. Y. Qi, M. Chen, S. Liang, J. Zhao and W. Yang, *J. Colloids Surf. A*, 2007, **302**, 383-387.
26. W. Lu, B. Wang, J. Zeng, X. Wang, S. Zhang and J. Hou, *Langmuir*, 2005, **21**, 3684-3687.
27. C. Gu, H. Xu, M. Park and C. Shannon, *Langmuir*, 2009, **25**, 410-414.
28. R. Guzel, Z. Ustundag, H. Eksi, S. Keskin, B. Taner, Z. G. Durgun, A. A. I. Turan and A. O. Solak, *J. Colloid Interface Sci.*, 2010, **351**, 35-42.
29. R. Chen, Q. Zhang, Y. Gu, L. Tang, C. Li and Z. Zhang, *Anal. Chim. Acta*, 2015, **853**, 579-587.
30. N. R. Jana, L. Gearheart and C. J. Murphy, *Langmuir*, 2001, **17**, 6782-6786.
31. K. Nguyen Tri, S. W. Kim, D.-H. Yoo, E. J. Kim, S. H. Hahn, *Appl. Catal. A*, 2014, **469**, 159-164.
32. M. Zhang, X. Cao, H. Li, F. Guan, J. Guo, F. Shen, Y. Luo, C. Sun and L. Zhang, *Food Chem.*, 2012, **135**, 1894-1900.
33. N. G. Bastus, J. Comenge and V. Puentes, *Langmuir*, 2011, **27**, 11098.
34. W. Haiss, N. T. Thanh, J. Aveyard and D. G. Fernig, *Anal. Chem.*, 2007, **79**, 4215-4221.

Chapter 5. Free-standing and flexible graphene papers as disposable non-enzymatic electrochemical sensors

5.1. Introduction

As described in Chapters 1 and 3, two-dimensional (2D) graphene papers have attracted significant interest in a wide range of fields from physics, materials science, and sensors to environmental engineering. Such materials not only largely retain the core properties of individual graphene sheets, but also add collective properties or/and synergistic functionality resulting from purpose-driven assembly or/and functional doping with desirable components. The advantages of low mass density, high flexibility, large surface area, robust mechanical strength, and high electrical conductivity make graphene-derived composite materials hold great promise to meet a number of requirements in modern technologies, especially graphene supported materials for electrochemical sensing applications¹⁻⁴.

Prussian Blue (PB) and its analogues show good chemical stability and high electrocatalytic activity. Those are also low-cost materials, with potential scalability of mass production⁵. PB and its analogues are therefore attractive materials in catalysis⁶, energy devices⁷, drug delivery⁸, separation devices⁹, and sensors¹⁰⁻¹¹. In particular, electrocatalytic applications of PBNPs have received increasing attention recently. In the present work, we have explored AuNPs as a catalyst and a core material to prepare a new type of core-shell nanostructured NPs, Au@PBNPs, with the aim of improving the conductivity and size control. Moreover, we have used Au@PBNPs to functionalize graphene papers as freestanding electrochemical sensors. These electrodes can display high performances in electrocatalytic reduction of hydrogen peroxide.

5.2. Experimental section

5.2.2 Synthesis of AuNPs.

Prior to use, all glassware was thoroughly cleaned by boiling in nitric acid, rinsed with Milli-Q water, and dried in an oven. AuNP (13 nm) solution was prepared as described¹². Briefly, 100 mL of 1 mM HAuCl₄ was added to a 250 mL round-bottom flask, and the solution heated to boiling under vigorous stirring. Rapid addition of 10 mL of 38.8 mM sodium citrate to the vortex of the solution caused the colour of the solution to change from pale yellow to claret-red. Boiling was

continued for 10 min. The heating mantle was then removed, but stirring was kept for an additional 15 min.

5.2.3 Synthesis and purification of Au@PB core/shell nanoparticles.

The synthesis of Au@PB NPs dispersions was inspired by an early report⁸, but with significant modifications. In a typical experiment, 10 mL AuNP solution prepared as above step was mixed with a 10 mL mixture of 1.0 mM FeCl₃, 1.0 mM K₃[Fe(CN)₆], 0.1 M KCl and 0.025 M HCl under vigorous stirring. The colour of the AuNP solution changed from red to dark-blue upon addition of the mixture solution. After 30 min, the product was centrifuged at 12000 rpm for 10 min, the supernatant was discarded to remove unreacted reagents, and the sediment was re-dispersed in 10 mL Milli-Q water. The procedure was repeated at least three times. The samples were further purified by filtration using polycarbonate membrane (diameter 47 mm, 0.2 μm pores), and the product was finally dispersed in 10 mL Milli-Q water as a stock solution.

5.2.4 Preparation of graphene oxide.

GO was prepared by the modified Hummer's method according to our previous report⁶. The experimental details are also provided in the Chapter 2. The quality of single-layer GO nanosheets was checked regularly by AFM. An example of AFM images is shown in supporting information.

5.2.5 Preparation of graphene papers.

10 mL of 1 mg/mL GO solution was first mixed with different volumes of Au@PB NP solutions and stirred for 1h, then centrifuged at 8000 rpm for 10 min. The supernatant was discarded to remove free Au@PB NPs. The sediment was re-dispersed in Milli-Q water by sonication and a blue solution obtained. The solution mixture of Au@PB NPs/GO was vacuum filtered to prepare Au@PB NPs/GO papers. GO nanosheets were assembled into a layer-by-layer structure, in which π-π stacking has re-ordered the monolayer of GO nanosheets to graphite-like structures. The number of layers can be controlled by the concentration and volume of mixture solution. In order to improve the mechanical property of the graphene paper, an AAO (anodic aluminium oxide) membrane was selected to use in the filtration, as this material releases Al³⁺, which is a strong cross-linker for connecting monolayer GO sheets¹³. In order to enhance the conductivity of the GO hybrid paper, Au@PB NPs/GO paper was reduced by placing the paper in an autoclave together

with the hydrazine solution and heating at 180 °C overnight. After cooling to room temperature the paper was taken out. The rGO paper was further annealed at 190 °C to remove residual hydrazine and further enhance the conductivity. As expected, the amount of oxygen-containing groups was significantly reduced, as indicated by the increased C/O ratio estimated from the XPS analysis. The resulting paper was cut into small pieces for different tests. A similar procedure was used to prepare pure graphene and AuNPs/graphene papers as reference samples. The whole procedure is schematically illustrated in Fig. 5.1.

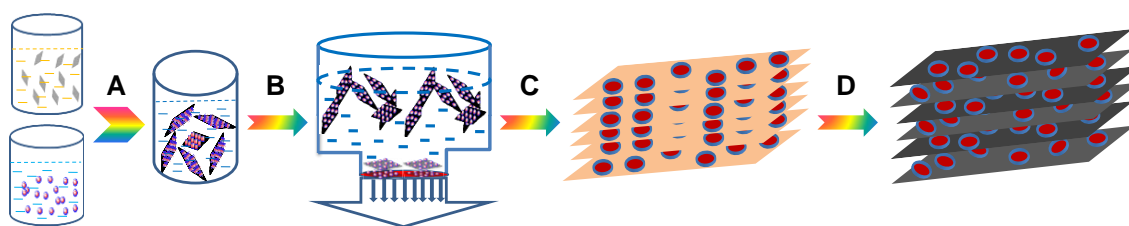


Fig. 5.1 Schematic representation of the experimental procedure for preparation of RGO papers functionalized with Au@PB NPs in a sandwich-like structure. The four steps are: the two components are mixed (A), transferred to a vacuum filter (B), vacuum filtration to form GO paper (C) and hydrothermal vapor reduction of GO paper to rGO paper (D). Not drawn to scale.

5.3. Results and discussion

5.3.1 Synthesis, electronic properties, and structures of core/shell Au@PB NPs

As described in the Experimental section, the synthesis of Au@PB NPs dispersions was based on a previously reported procedure⁸ with modifications. The resulting samples were characterized by XPS, UV-vis spectroscopy and TEM. By comparing the UV-vis spectra of AuNPs and Au@PB NPs, Fig. 5.2A and Fig. 5.2B, the characteristic surface plasmon absorption peak of pure AuNPs was found around 520 nm. After coating with a PB layer, the absorption peak appears around 700 nm, an indication that the absorbance from PB dominates, but the 520 nm AuNP peak is still clearly visible as a shoulder in the UV-vis spectrum (Fig 5. 2B).

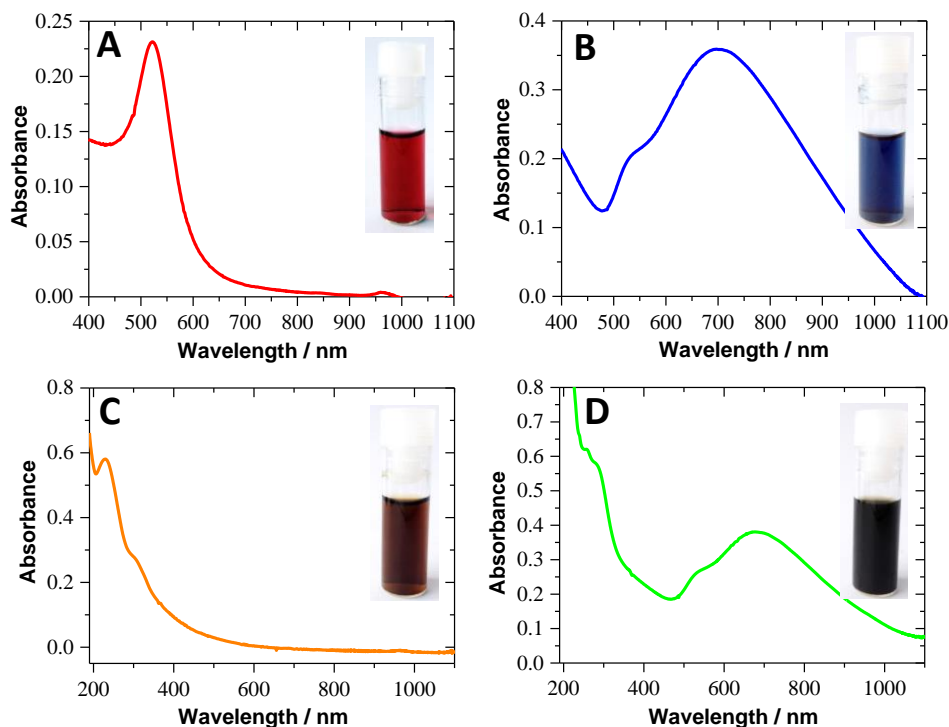


Fig. 5.2 UV-vis spectra and digital photographs of various colloid suspensions: (A) pure AuNPs, B) core/shell Au@PB NPs, C) pure GO and D) Au@PBNPs attached to GO sheets. All suspensions were in 0.1 M KCl solution.

XPS was used to analyze Au@PB NPs samples in detail, Fig. 5.3. As indicated in the survey spectrum (Fig. 5.3A), all expected elements were detected. The Au 4f and Fe 2p spectra are shown largely as expected. In particular, the high-resolution Fe 2p spin-orbit doublet spectra were recorded, and the binding energy of Fe $2p^{3/2}$ and Fe $2p^{1/2}$ observed at 712.3 and 721.2 eV, respectively, corresponding to Fe²⁺ ions. The peak at 708.4 eV is due to Fe³⁺ $2p^{3/2}$ in the form of $[\text{Fe}(\text{CN})_6]^{3-}$. These observations support that the PB layer was formed on core AuNPs as a shell, which is directly proven by TEM as described below (Fig. 5.4).

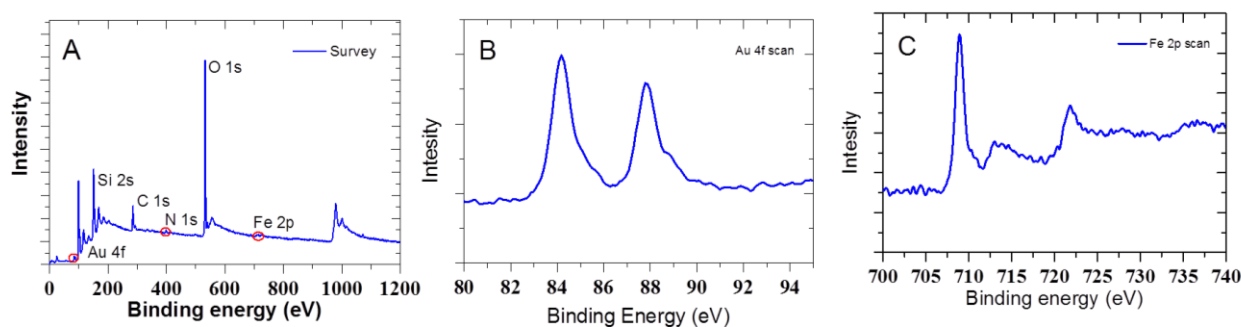


Fig. 5.3 XPS spectra of core/shell nanoparticles (Au@PB NPs) samples. (A) XPS survey spectrum, (B) the Au 4f scan spectrum, and (C) Fe 2p region spectrum.

From TEM images and size-distribution analysis of the AuNPs (Fig. 5.4A-C) and Au@PB NPs (Fig. 5.4D-F), it is concluded that the AuNP (13 nm) is located in the centre as a core, while the PB layer with a thickness ≈ 5 nm covers the AuNP as a shell.

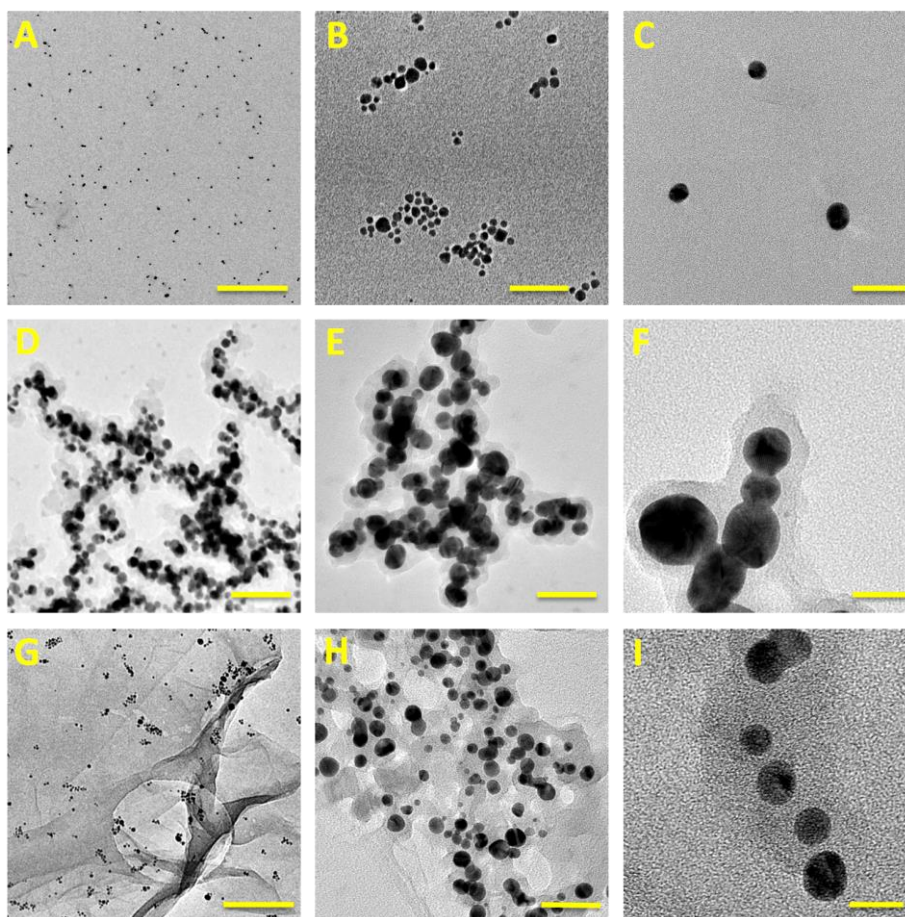


Fig. 5.4 TEM images of different types of nanoparticles with various magnifications: (A)-(C) Pure AuNPs; (D)-(F) core/shell Au@PB NPs; (G), and (H)-(I) Core/shell Au@PB NPs on GO sheets. Scale bars: (A) 500, (B) 50, (C) 25; (D) 100, (E) 50, (F) 20; (G) 200, (H) 50, (I) 25 nm.

5.3.2 Preparation of Au@PB NP/graphene papers

High-quality GO was synthesized by a modified Hummer's method according to our previous report, (detailed in Chapter 2). AFM images (supporting information) show that the extension of the GO sheets ranges from 0.5 to 5 μm , with the thickness about 1.2 nm. As expected, the UV-vis spectrum, Fig. 5.2C shows two characteristic peaks, at 230 and 300 nm. XPS spectrum was shown

in supporting information present XPS survey and C 1s spectra of GO samples. The XPS spectra exhibit a relatively high O1s and a weak C1s peak, while the C1s XPS spectra show various oxygen carbon groups including C=O and C–O, which indicates that oxygen-containing groups (OCGs) are abundantly present on the GO sheet surface, providing active sites for attaching positively charged molecular groups and nanoparticles via electrostatic interaction. From the UV-vis spectra of Au@PB NPs/GO (Fig. 5.2D), three characteristic peaks at 230, 300, and 700 nm are observed, which correspond to GO and Au@PB NPs, respectively. It was imaged by TEM that the combination between Au@PB NPs and GO had indeed occurred. It can be seen from the images in Fig. 5.4G, H and I that most Au@PB NPs were loaded onto the GO sheet surface. As noted, this could be due to the presence of a large number of OCGs on the GO surface bridging the contact between GO and Au@PB NPs. Au@PB NPs are most likely attached to GO by electrostatic attraction. Different ratios of GO to Au@PB NPs were investigated. The UV-vis spectra of the mixed solutions with different ratios (v/v) are shown in Fig. 5.5A. Fig. 5.5B shows a plot of the ratio of PB absorbance (700 nm) to GO absorbance (230 nm) at different GO/Au@PB NPs ratios (v/v). When the mixture ratio reached 1:9, the A_{700}/A_{230} ratio does not change further, suggesting that all active sites on the GO sheet surface are occupied by Au@PB NPs, and no more nanoparticles can be adsorbed.

As described in Section 5.2.5, we used the hybrid materials characterized above to prepare graphene papers via vacuum filtration. The resulting graphene paper is robust and free-standing (Fig. 5.6A), and can be rolled or/and bent (Fig. 5.6B). They can also be cut into any shapes with various sizes. For the use of electrochemical sensors, the paper was cut into rectangular pieces (typically 0.4 cm x 2 cm) (Fig. 5.6C) that was directly used as working electrodes.

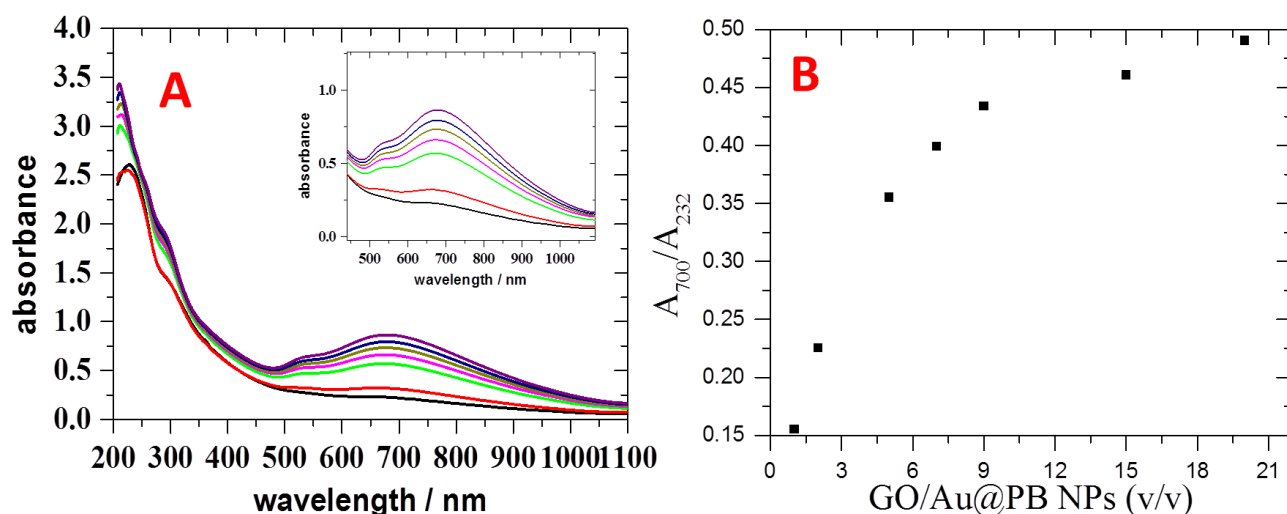


Fig. 5.5 UV-vis spectroscopic analysis of Au@PB NPs decorated GO nanosheets. (A) UV-vis spectra

of Au@PB NPs-GO solutions for different ratios of Au@PB NPs to GO (v/v). The inset in shows enlarged spectra in the wavelength 450 to 1100 nm, mainly contributed by the PB component. (B) A plot of A_{700}/A_{232} for various ratios of Au@PB NPs to GO.

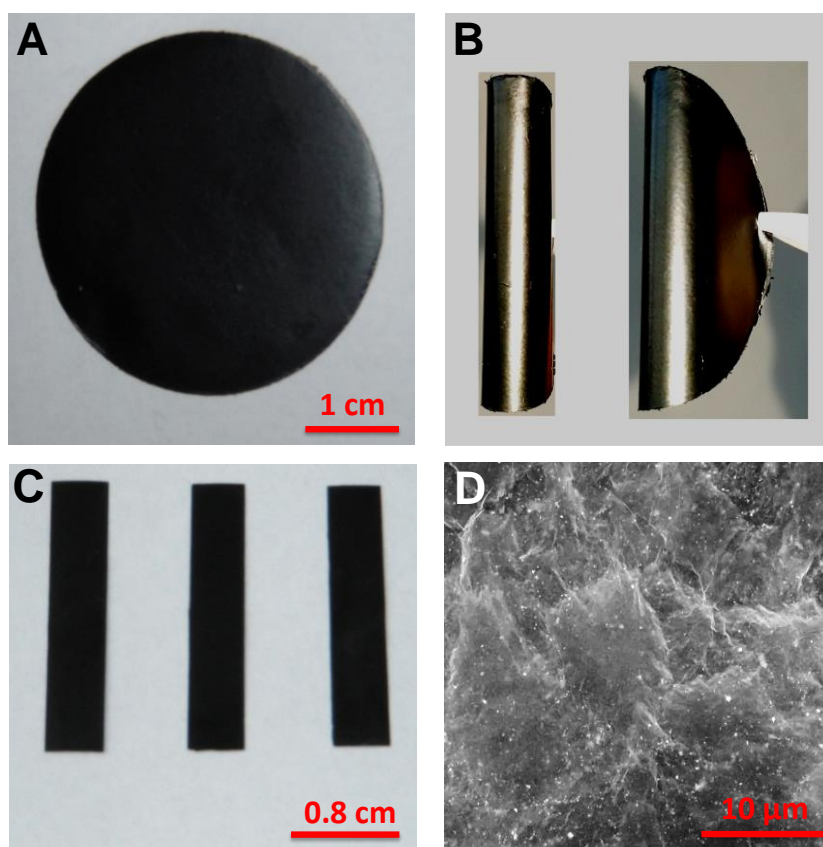


Fig. 5.6 Digital photographs and SEM image of RGO paper functionalized with Au@PB NPs: (A) as-filtered RGO paper, (B) rolled and bent RGO papers, (C) disposable electrodes (or sensors) cut from RGO paper, and (D) SEM image of the surface of RGO paper.

5.3.3 Characterization of Au@PB NPs graphene paper

The surface of Au@PB NPs/graphene paper is relatively smooth (Fig.5.6D). Au@PB NPs attached onto the graphene paper are clearly observed by SEM. In order to verify that Au@PB NPs were doped into the graphene paper, cross sectional SEM of graphene papers was investigated. Fig.5.7 shows the layer-by-layer sandwich-like structure of Au@PB NP decorated graphene paper. Au@PB NPs are distributed on the surface of the graphene sheet. Compared with GO paper, the graphene paper reduced by hydrazine hydrate vapour is thicker, the thickness of GO paper and graphene paper being 6 μm and 20 μm , respectively, but the lateral sizes have shrunk slightly. This is because the hydrazine hydrate vapour opens pores between the GO sheets during the reduction process¹⁴. This kind of structure can promote ion and molecular transport through graphene paper.

SEM EDS-mapping (Fig.5.8) was used to further observe the sandwich structure. Each chemical element (Au, Fe, C, N and O) was found to be uniformly distributed on the graphene paper. XPS was also used to examine the element distribution with different depth from the graphene paper surface. The survey spectra and Au 4f spectra were collected during the depth profiling up to 500 nm of a nominal etching depth into the paper from both sides. Both Fe and Au were found in each etching step in the XPS spectra. This indicates that the Au@PB NPs were successfully doped into interlayers of the graphene paper. This could be substantiated additionally by high-resolution cross sectional SEM images. Compared to the XPS spectrum of GO paper, graphene paper has a much higher C/O ratio suggesting that GO was reduced effectively, but there is still a considerable amount of oxygen-containing groups present mainly carboxylic groups at the edges of nanosheets. These remaining groups could play a crucial role in the electrostatic binding of the Au@PB NPs which is related to the amount of OCGs. In addition, this causes a slight increase in the C/Au ratio. We believe that this arises from a decrease in the number of defects in the RGO nanosheets, so that the number of active sites for Au@PB NP binding was also decreased and induced partial loss of Au@PB NPs.

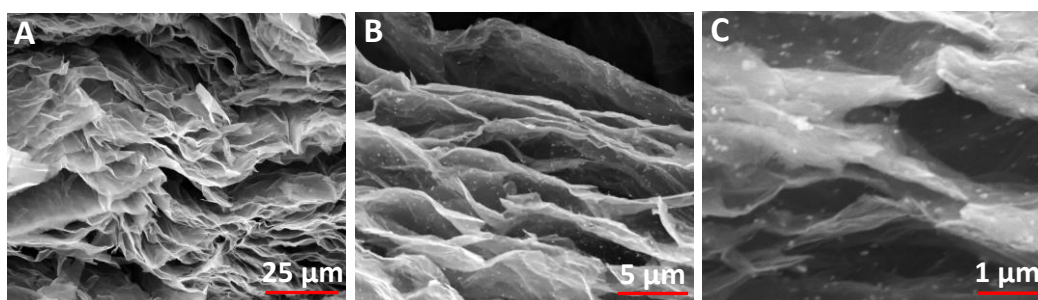


Fig. 5.7 Cross-sectional SEM images of Au@PB NP decorated RGO papers with various magnifications. The parameters used in recording SEM images are: voltage 10 KV, a work distance 12.9 mM and a typical spot size 3.0 μ M.

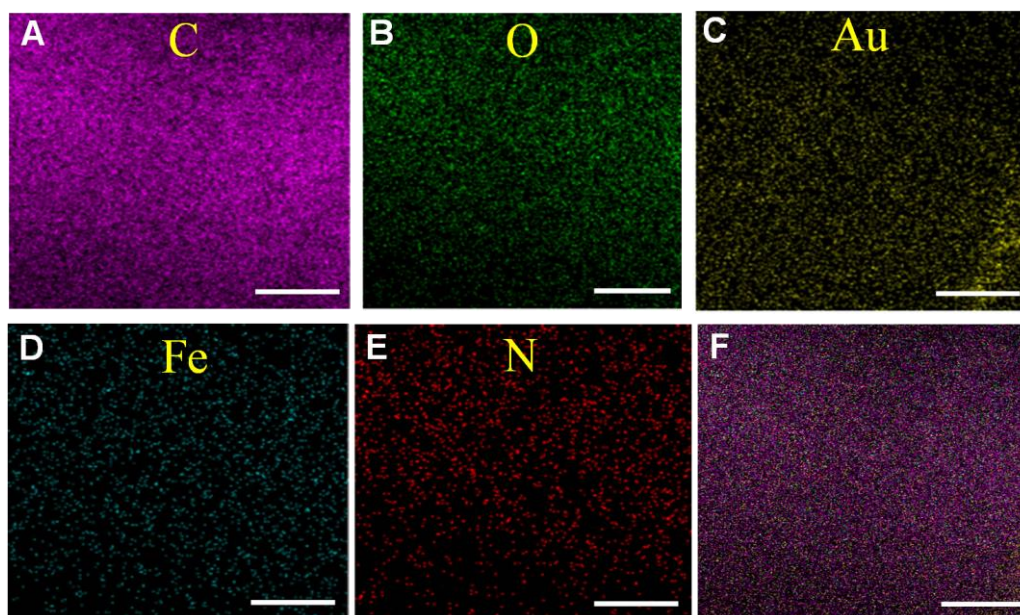


Fig. 5.8 Cross-sectional SEM elemental mapping images. Scale bars: 10 μm .

5.3.4 Electroactivity of Au@PB NP graphene paper

To evaluate the electrochemical behaviour of the Au@PB NP/graphene paper, Au@PB NPs/RGO, pure RGO, and AuNP/RGO papers were cut into rectangular pieces as free-standing working electrodes with an active area of 0.09 cm^2 (i.e. $0.3\text{ cm} \times 0.3\text{ cm}$). Cyclic voltammograms (CVs) of each electrode in 0.1 M KCl solution were recorded with a SCE as reference electrode. As shown in Fig. 5.9A (blue line), a single pair of well-defined redox peaks was observed at 0.18 V (vs SCE). This signal originates from the PB shell. No obvious response was found for pure RGO papers (red curve in Fig. 5.9A) or AuNP/RGO papers (black curve in Fig. 5.9A), indicating that the PB shell after heat treatment retains good electrochemical properties. In addition, the effects of scan rates on the voltammetric responses were studied, Fig. 5.9B. Both redox peak currents were found to increase with increasing scan rate. The relationship between the peak currents (I_p) and scan rate (v) evaluated by a series of plots of I_p versus v^x with $x = 0.5\text{--}1.0$ is obtained for $x = 0.8$, indicating that both surface confinement and diffusion control the electrochemical process, diffusion most likely being random electron hopping rather than nanoparticle diffusion. Conductivity is also a critical factor for fabricating an electrode. The resistance of graphene paper is about $200\ \Omega/\text{cm}$, but decreases to $100\ \Omega/\text{cm}$ in the presence of AuNPs. The apparent resistance of Au@PB NPs/graphene paper, measured by a simple voltmeter, is approximately $132\ \Omega/\text{cm}$.

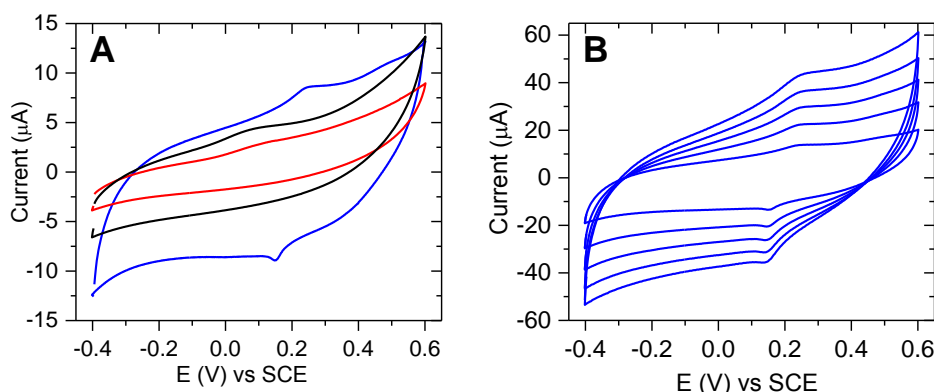


Fig. 5.9 Voltammetric evaluations of Au@PB NP functionalized RGO papers. (A) Comparison of cyclic voltammograms (CVs) of pure RGO paper (red curve), AuNP-RGO paper (black curve) and Au@PB NP RGO paper (blue one). Scan rate 50 mV s^{-1} ; (B) CVs of Au@PB NP RGO papers with higher scan rates of 100 to 500 mV s^{-1} . Electrolyte: 0.1 M KCl.

5.3.5 Electrocatalytic reduction of H_2O_2 by Au@PB NP graphene papers.

CVs of the Au@PB NPs graphene paper in 0.1 M KCl solutions containing different concentrations of H_2O_2 were recorded. As shown in Fig. 5.10A, Electrocatalytic reduction of H_2O_2 on Au@PB NPs graphene/paper electrodes starts at 0.3 V (vs SCE) and tends to reach a maximum effect at potentials more negative than -0.1 V . In order to evaluate the electroanalytical performance for H_2O_2 reduction, chronoamperometric detection of H_2O_2 at -0.1 V with successive addition of H_2O_2 was performed. As shown in Fig. 5.10B, Au@PB NPs/graphene paper displays a typical steady state response of the modified electrode on successive addition of H_2O_2 at -0.1 V . Subsequent addition of hydrogen peroxide to the stirred 0.1 M KCl results in a remarkable increase in the reduction current, which demonstrates strong catalytic properties of the free-standing electrode towards the reduction of H_2O_2 . The linear range of Au@PB NPs graphene paper is from 1 to $30 \mu\text{M H}_2\text{O}_2$ (Fig. 5.10C) with a linear correlation coefficient (R) of 0.995. The response time is less than 10 s, and the sensitivity $5 \text{ A cm}^{-2} \text{ M}^{-1}$, which is higher than previous report, the most possibility because graphene oxide paper was reduced by hydrazine vapour, it will be extremely enhance the electrode work area.

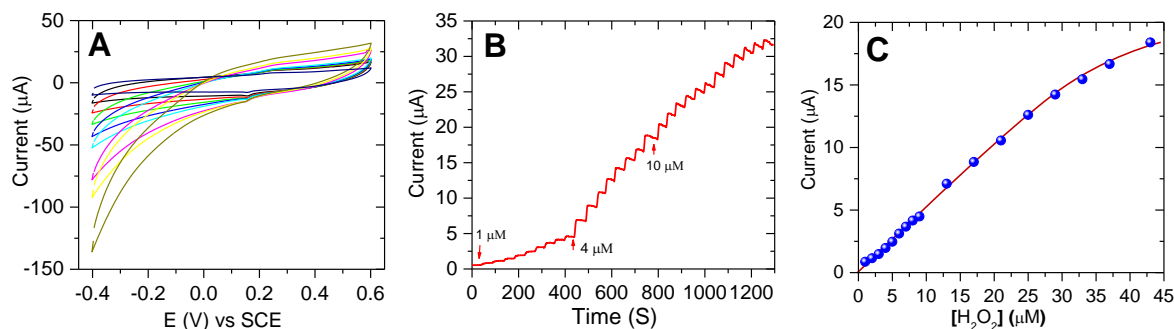


Fig. 5.10 Voltammetric and amperometric responses of Au@PBNP graphene paper electrodes to electrocatalytic reduction of hydrogen peroxide (H_2O_2): (A) CVs of Au@PBNP RGO paper in the presence of various H_2O_2 concentrations from 0.1 to 1 mM, scan rate 20 mV s^{-1} ; (B) amperometric responses to H_2O_2 addition with the working electrode potential fixed at -0.1 V in a stirred solution; (C) the calibration curve of the current response to $[\text{H}_2\text{O}_2]$. Electrolyte: 0.1 M KCl .

In addition, we have investigated the effects of the number of graphene layers on the electrocatalytic sensitivity of H_2O_2 . The number of graphene layers can be controlled roughly by adjusting the concentration of GO starting solutions used in the preparation of GO papers. For example, a series of GO solutions with various concentrations of $0.5\text{--}2.0 \text{ mg/ml}$ were used to prepare graphene papers. In general, the thinner graphene papers give rise to a slightly enhanced sensitivity towards electrocatalytic detection of H_2O_2 , but their mechanical strength is deteriorated dramatically, causing material handling problem. It is thus concluded that, under our experimental conditions GO suspension with the concentration of 1 mg/ml formed the most practical graphene papers with an optimum balance between their electrocatalytic sensitivity and mechanical strength.

5.4. Conclusions

Water-dispersible and highly stable core-shell structural Au@PB nanoparticles were successfully synthesized and used to functionalize graphene nanosheets. With the doping of Au@PB NPs, conductive, functional, mechanically strong, and flexible free-standing graphene papers can be fabricated. The functionalized graphene paper can be cut into disposable electrodes with high performances for electrochemical reduction detection of hydrogen peroxide. The new electrochemical detection configuration offers a non-traditional approach to facile and portable monitoring of chemical and biological environments. Finally, it is noticed that the core-shell nature of Au@PB NPs could pose new interests and challenges regarding their electronic and optical properties, as well as the ways the Au core and PB shell interact, and the whole Au@PB NP hybrid

interacts with the graphene support. Understanding of these issues is of crucial in offering novel insight and should be a main focus in ongoing research.

References

1. H. Gao, and H. Duan, *Biosens. Bioelectron.*, 2014, **65**, 404-419.
2. Y. Song, Y. Luo, C. Zhu, H. Li, D. Du and Y. Lin, *Biosens. Bioelectron.*, 2016, **76**, 195-212.
3. M. Carbone, L. Gorton, R. Antiochia, *Electroanalysis*, 2015, **27**, 16-31.
4. A.T. Lawal, *Talanta*, 2015, **131**, 424-443.
5. M. Okubo, D. Asakura, Y. Mizuno, J. D. Kim, T. Mizokawa, T. Kudo and I. Honma, *J. Phy. Chem. Lett.*, 2010, **1**, 2063-2071.
6. G. Wang, L. Chen, Y. Zhu, X. He, G. Xu and X. Zhang, *Analyst*, 2014, **139**, 5297-5303.
7. L. Shen, Z. Wang and L. Chen, *Chem. Eur. J.*, 2010, **20**, 12559-12562.
8. L. Cheng, H. Gong, W. Zhu, J. Liu, X. Wang, G. Liu and Z. Liu, *Biomaterials*, 2014, **35**, (2014) 9844-9852.
9. S. Jang, S. Hong, H. Yang, K. Lee, J. Moon, B. K. Seo, Y.S. Huh and C. Roh, *Nanomaterials*, 2014, **4**, 894-901.
10. Z. Gao, Y. Qu, T. Li, N.K. Shrestha and Y. Song, *Sci. Rep.-UK*, 2014, **4**, 6891.
11. N. Zhu, S. Han, S. Gan, J. Ulstrup and Q. Chi, *Adv. Funct. Mater.*, 2013, **23** 5297-5306.
12. M. Zhang, X. Cao, H. Li, F. Guan, J. Guo, F. Shen, Y. Luo, C. Sun and L. Zhang, *Food Chem.*, 2012, **135**, 1894-1900.
13. C.N. Yeh, K. Raidongia, J.J. Shao, Q.H. Yang and J.X. Huang, *Nat. Chem.*, 2015, **7**, 166-170.
14. Z. Niu, J. Chen, H. Huang, J. Ma and X. Chen, *Adv. Mater.*, 2012, **24**, 4144-4150.

Part 3. Low cost template methods for synthesis of 2D layered and nanoporous transition metal oxide nanosheets

Metal oxides (MOs) are one of the key family materials in a variety of current demanding needs for sensor, catalysis, energy storage and conversion, optical electronics and piezoelectric mechanics, arising from their versatile functionalities. Fine engineered MOs with specific nanostructures and robust macroscopic morphology are proven to boost their performances, but the design and controlled synthesis of such materials in a cost-effective and facile way is still a tremendous challenge. By exploiting the advantages of intrinsic structures of GO paper, serving as a sacrificial template, we have shown the feasibility of preparing 2D layered and free-standing MO materials with desirable structures. Systematic structural characterizations suggest that these MO materials are nanostructured, ultralight and porous papers. In Chapter 6, we generally report a new method for preparation of various MO papers (CuO, NiO, ZnO, Co₃O₄, Fe₂O₃ and Mn₃O₄). CuO as a representative, the assembled principle of CuO paper was studied in detail. To our surprise, the growth of CuO papers follows an Oriented-attachment mechanism (a non-conventional crystallization process) rather than traditional Ostwald ripening growth process. As a versatile material, CuO displays high performance for electrochemical sensor, supercapacitor and photocathode. In Chapter 7, GO paper was used as sacrificial template to generate the 2D nanoporous hybrid CuO/ZnO nanosheets. The size of CuO/ZnO nanosheets is about 50 nm and the size of porous is from 5 nm to 10 nm, and the thickness of single-layer CuO/ZnO nanosheet is only 2 nm (equivalent to 3-4 atom layers). The as-synthesized nano-hybrid material with high surface area and bimodal pores can play key roles by providing shorter diffusion paths and rapid mass transport of electrolyte, which could be further improved by providing more active sites for electrochemical reactions. These hybrid MO nanosheets displayed high performance as non-enzymatic sensor for detection of glucose with low potential (0.3 V vs SCE), high sensitivity (3.85 A M⁻¹ cm⁻²), a wide linear range (5 μM to 3 mM), and low detection limit of 0.5 μM. In Chapter 8, the similar method was used to prepare 2D NiO nanosheets, and the resulting nanosheets were deposited on a screen printed electrode for fabrication of electrochemical sensor for detection of urea. Electrochemical studies indicate that the 2D NiO nanosheets exhibited excellent stability and high electrocatalytic activity for the oxidation of urea in alkaline solutions.

Chapter 6. Ultralight and semi-transparent metal oxide papers composed of nanoporous monolayers for lightweight energy and sensing applications

6.1 Introduction

Due to their versatile functionalities, metal oxides (MOs) have become one of the key family materials for a range of demanding needs from sensors, catalysis, energy storage and conversion, optical electronics to piezoelectric mechanics¹⁻⁶. Many transition metals are earth abundant, and thus offer favorable opportunity for their scale-up production. Previous studies have shown that physicochemical properties of MOs, particularly their electronic and optical features, are significantly dependent on their grain size and morphology^{7, 8}. In general, fine engineered MOs with specific structure and morphology have displayed enhanced performances. For example, nanoengineered MO building blocks not only have a large surface-to-volume ratio and a nanometer size^{9, 10}, but also facilitate their self-assembly into a macroscopic material needed for practical applications^{11, 12}. On the other hand, nanoscale MO building blocks such as nanoparticles, nanosheets, nanorods and nanotubes could often undergo *densification* and suffer *significant loss* of specific surface areas during the self-assembly, so that the resulting macroscopic material cannot match expected properties and performances. To overcome these critical problems, recent efforts have focused on the development of rationally designed and directed assembly methods. For example, Dou and coworkers reported an impressive approach, based on employing lamellar reverse micelles, to generalize self-assembly of scalable 2D transition MO nanosheets¹². Another example is demonstrated by Hwang and coworkers, they used graphene nanosheets as a platform for the 2D ordered assembly of TiO₂ nanoparticles¹³. These studies have inspired related researches on controlled assembly of nanobuilding blocks into macroscopic 2D or three-dimensional (3D) ordered MO materials¹⁴⁻¹⁶. Similar strategy was previously used in fabrication of macroscale 2D and 3D graphene materials from graphene nanosheets¹⁷⁻¹⁹.

The exploration of graphene nanosheet derived materials as soft templates to prepare MO nanosheets is an emerging and interesting approach^{14, 20-23}. Ordered meso- or microstructured MO nanosheets can be synthesized and have potentials for use in a wide range of applications. Some MO ensembles were systematically characterized, but the formation mechanism of macroscopic MO structures is far from fully understood²². A deep investigation into the underlying mechanisms and further gaining tailoring their structures are thus highly desirable. In addition, to date few cases (or none) have demonstrated the capacity to assemble *ultralight, free-standing, semi-transparent*

and *flexible* macroscopic MO materials with ultrafine nanostructures. Such MO materials are increasingly demanded by fabrication of lightweight, flexible and wearable sensors and energy devices.

In this section, we have explored the structural advantages of graphene oxide (GO) paper as a sacrificial template, which has a well-defined layer structure, to simultaneously synthesize and assemble ultrafine nanostructured MOs (with research focus on CuO, ZnO, Co₃O₄, NiO, Fe₂O₃ and Mn₃O₄). We have successfully prepared free-standing MO papers that consist of ultrathin and porous 2D MO monolayers. We also provide a general understanding of how MO clusters grow into porous nanosheets. The unique nanostructured MO papers have an ultralow density and desirable ability facilitating ion and/or solute diffusion in electrochemical or photoelectrochemical environments. CuO papers were used as a main target for the proof-of-concept tests of multifunctional applications. The results have shown that CuO paper is a highly efficient material for solar water splitting, non-enzymatic electrochemical sensing of glucose, and supercapacitor energy storage. In particular, the CuO paper based photocathodes have shown high efficiency in photoelectrochemical (PEC) water reduction, reflected by high solar conversion efficiency and photocurrent density-to-weight ratio. These observations offer promises for cost-effective lightweight applications of these newly synthesized MO materials.

6.2 Results and discussion

6.2.1 Preparation of metal oxide

The overall preparation of MO materials is schematically illustrated in Fig. 6.1 (the top panel). GO paper was prepared according to our previous procedure²⁴⁻²⁶ and used as a starting material. The *d*-space between the GO layers in the GO paper is approximately 1 nm, which is potentially suitable for accommodation of some metal ions. In addition, it is well known that both the graphitic planes and edges of individual GO nanosheets contain a significant number of oxygen-containing groups (OCGs)²⁷. These functional groups provide chemically active sites for confining metal ions or loading small nanoparticles. A variety of metal ions (e.g. Fe³⁺, Zn²⁺, Cu²⁺, Co²⁺, Mg²⁺ and Ni²⁺) can be captured inside GO paper *via* electrostatic attraction between OCGs and metal cations. In a typical preparation procedure, we immersed a piece of GO paper in a salt solution containing specific metal ions for a given period. After the absorption of metal ions, the Mⁿ⁺-GO paper was removed from the salt solution, followed by rinsing with water to remove those loosely (or

physically) adsorbed ions. The M^{n+} -GO paper was then annealed in air (or nitrogen atmosphere) to sacrifice carbon components and to proceed nucleation, crystallization and growth of pure MO material. As a result of space-confined synthesis, the MO material duplicates the morphology of the GO paper (e.g. those MO papers in Fig. 6.2a, 6.2d, 6.2g and 6.2j), except its size shrinks by approximately 13.6% due to the decomposition of GO layers. Various MO papers prepared by the present method are free-standing and ultralight (surprisingly, even much lighter than GO nanopowders or GO papers), as demonstrated by Fig. 6.1 (the bottom panel).

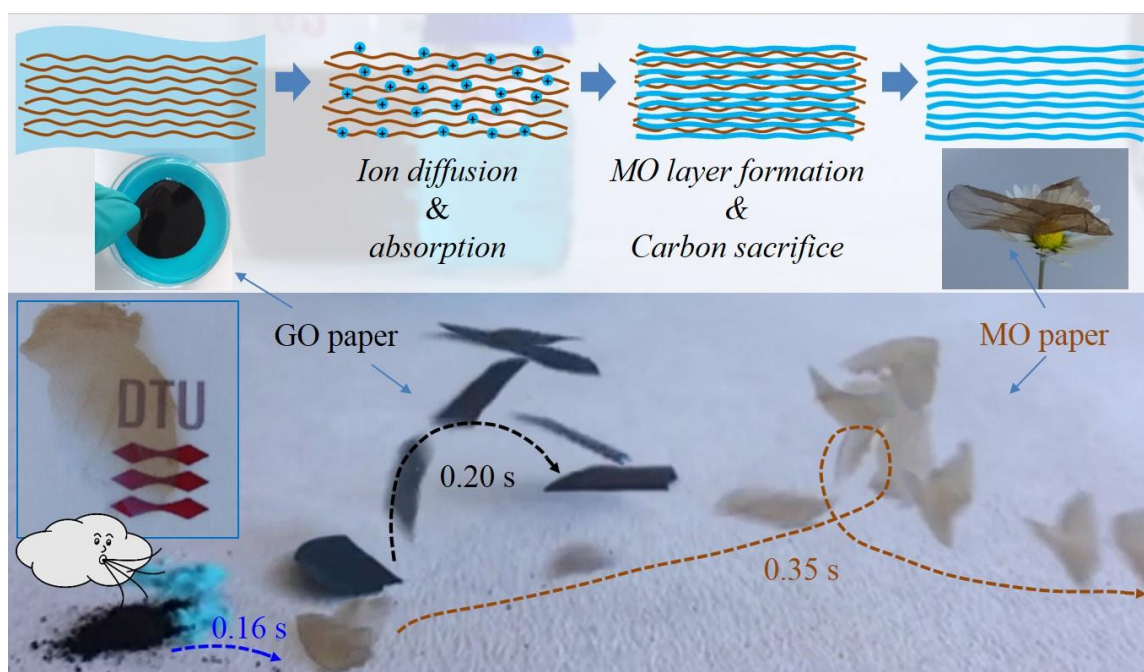


Fig. 6.1 The sketch illustrating the synthesis of MO papers and material appearances (blue powders and solution: Cu_2SO_4 , black powders and papers: GO, light brown papers: CuO); Bottom panel: the 10 photographs successively recorded within 0.35 s were superimposed to demonstrate lightweight materials (including both CuO and GO papers) being blown away. The inset shows a piece of semi-transparent CuO paper partially covering on a university logo (the logo size is 8 mm \times 12 mm).

6.2.2 Structural characterization of metal oxide materials

We performed systematic analysis of the morphology and microscopic structures of MO materials using a wide range of microscopy and spectroscopy, including scanning electron microscope (SEM), transmission electron microscope (TEM), atomic force microscopy (AFM), X-ray diffraction (XRD) and X-ray photoelectron spectroscopy (XPS). For example, digital photos, SEM images and TEM images for a series of as-prepared MO papers are shown in Fig. 6.2. Thanks to the template effect of the GO paper, the MO materials retain the freestanding paper form and

have a graphite-like layered structure. The XRD and XPS analyses clearly reveal that ultrapure MO crystals were formed (Fig. 6.3). The XRD patterns can be assigned to PDF#65-5745, PDF#18-0803, PDF#43-1003, PDF#48-1548, PDF#36-1451 and PDF#33-0664, corresponding to NiO, Mn_3O_4 , Co_3O_4 , CuO, ZnO and Fe_2O_3 , respectively. The size of their grains is in the range 7 to 50 nm, depending on the type of metals (Fig. 6.4). This most likely originates in their different crystallization kinetics associated directly with the activation energy of MO crystal formation. Overall, all MO papers have the similar graphite-like nano/microstructures as revealed by the SEM and TEM. By controlling the thickness of GO papers, the MO papers with a thickness of 4–16 μm (but not limited to this range) can be prepared. In contrast, in our control experiments, if we did not use template or if we used GO nanosheets and aerogels as templates, then we could not obtain freestanding MO papers with ultrafine-grained nanostructures. These observations indicate that GO paper plays an essential role in the formation of layered MO papers. With six different types of metal ions as examples, this template method could constitute a general strategy for design and synthesis of freestanding 2D porous MO materials.

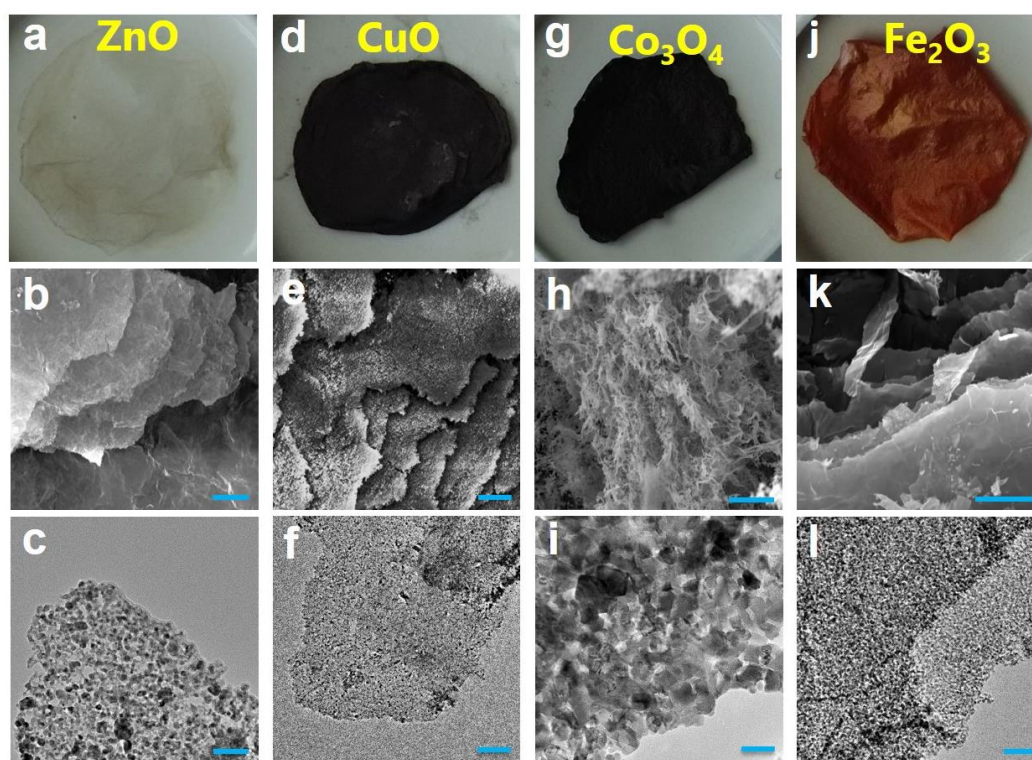


Fig. 6.2 Photographs (top panel: (a), (d), (g) and (j)) and microscopy images (middle panel: SEM images (b), (e), (h) and (k); lower panel: TEM images (c), (f), (i) and (l)) of the as-synthesized metal oxide papers. (a–c) ZnO, (d–f) CuO, (g–i) Co_3O_4 and (j–l) Fe_2O_3 papers papers. Scale bars: 10 μm (b), 100 nm (c); 15 μm (e), 500 nm (f); 5 μm (h), 100 nm (i); 5 μm (k), 100 nm (l).

6.2.3 The growth principle of metal oxide

MO monolayers in the MO paper have an ultrathin nanoporous structure as revealed by high-resolution TEM (HRTEM) images (Figs. 6.2 and 6.4). It is well known that the growth of MO nanocrystals follows the Ostwald ripening kinetics and is largely a random nucleation process, when the synthesis is in the absence of templates (e.g. surfactants). The morphology of MO crystals is thus difficult to control. To overcome this problem, surfactants are widely used to control the MO nanocrystals growth. However, Ostwald ripening is mainly driven by the minimization of total surface free energy. As a consequence, the formations of spherical particles with large size (hundreds of nm) are predominantly favored over ultrafine nanocrystals²⁸⁻³⁰. In contrast, we have obtained an ultrafine-grained nanostructure (sub-10 nm) and a well-defined micromorphology in the form of 2D freestanding MO papers using the present synthesis method. In the rest of this work, our focus is to use the CuO paper as an example for studying the formation mechanism of such a unique structure and for evaluating its multiple electrochemical applications.

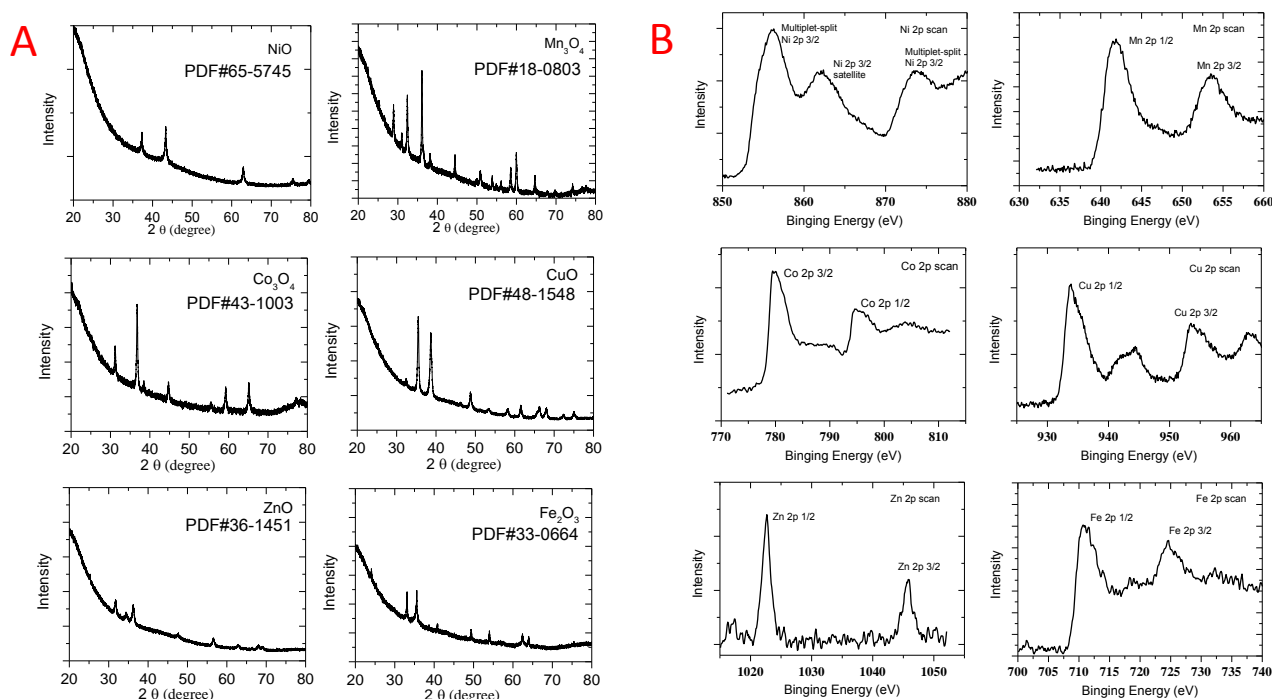


Fig. 6.3 (A) XRD patterns and (B) XPS spectra of as-synthesized six types of MO papers.

A combination of thermogravimetric analysis (TGA) and microscopy imaging can offer crucial clues for understanding the possible formation mechanisms of MO papers. For the TGA analysis, both dried Cu^{2+} -GO and pure GO papers were heated under the same experimental condition. When

the samples were heated in air from room temperature to 600 °C, the differential scanning calorimetry (DSC) measurements show that both samples exhibit a similar exothermic peak around 210 °C (Fig. 6.5a), attributed to the decomposition of OCGs on GO^{31, 32}, but the Cu²⁺-GO paper occurred at a notably lower decomposition temperature by approximately 10 °C (i.e. $\Delta T \approx 10$ °C) and with a less weight loss (~3.1%) compared to pure GO paper. For further comparison, we performed similar TGA and DSC in a N₂ atmosphere instead of air. To our surprise, the same phenomenon was observed for these two samples. This observation clearly indicates that external oxygen from air is not essential for the formation of MO papers. Instead, the GO nanosheets can serve as the oxygen donor, while the absorbed Cu²⁺ ions act as the oxygen acceptor during the thermal reduction of GO. As a result, Cu_xO (x = 1 or 2, which is identified by XPS spectra and discussed later) nanoclusters were crystallized between the GO layers (TEM images in the insets of Fig. 6.5a) and grow by expanding the interplanar spacing of the GO paper. The TGA curve shows that the first-stage weight loss of Cu²⁺-GO paper started at ~180 °C, in which the Cu_xO clusters were formed and attached to GO layers as revealed by the TEM image (inset *i* in Figure 6.5a). The Cu_xO clusters maintained their size at around 5 nm until the annealing temperature elevated to 400 °C (insets *ii* and *iii* in Fig. 6.5a), in which the Cu²⁺-GO paper was subjected to the second-stage weight loss.

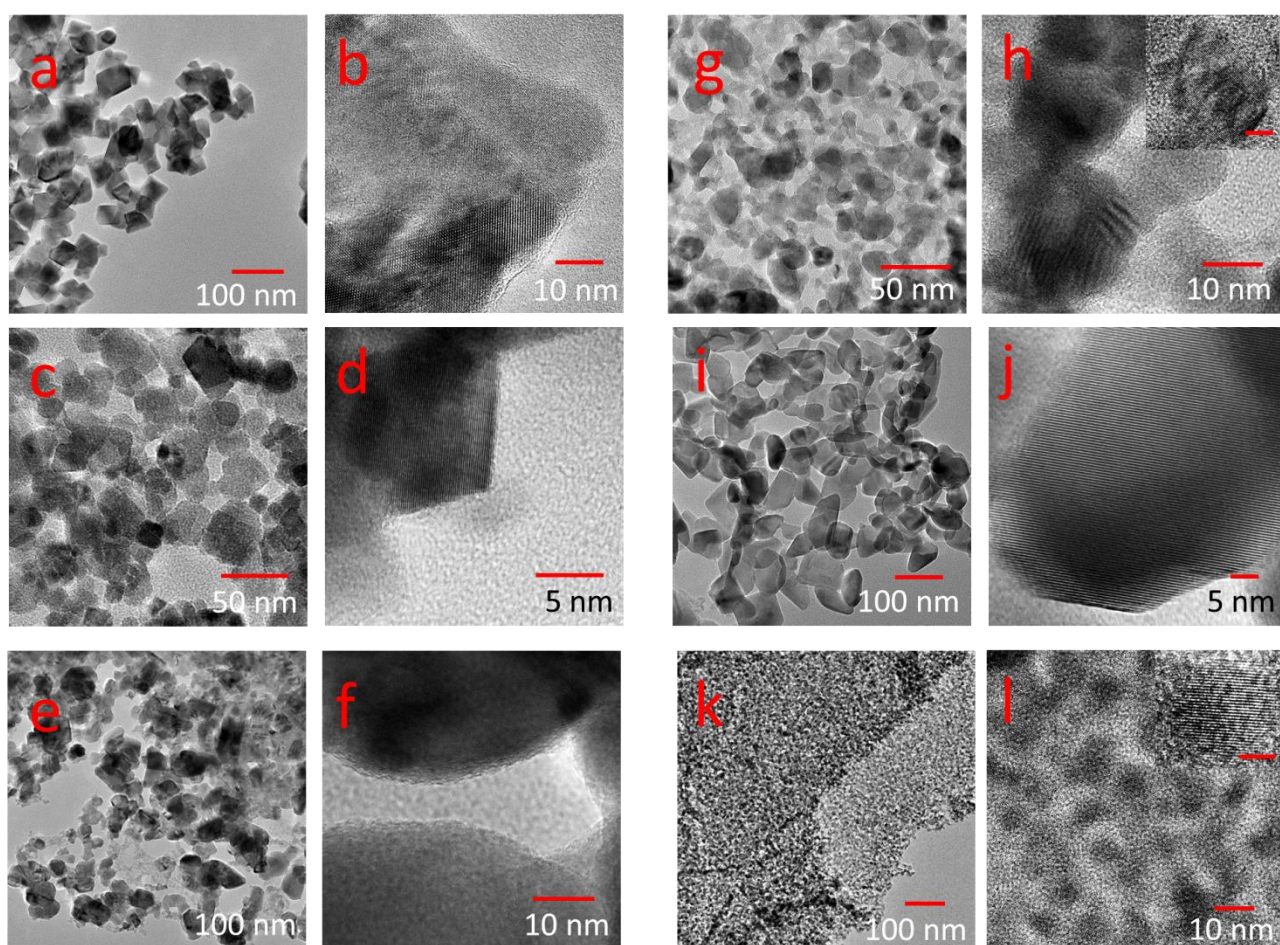


Fig. 6.4 TEM images of nanostructures of metal oxide layers at higher resolution: (a) and (b) Co_3O_4 , (c) and (d) NiO , (e) and (f) CuO , (g) and (h) ZnO , (i) and (j) Mn_3O_4 and (k) and (l) Fe_2O_3 , respectively.

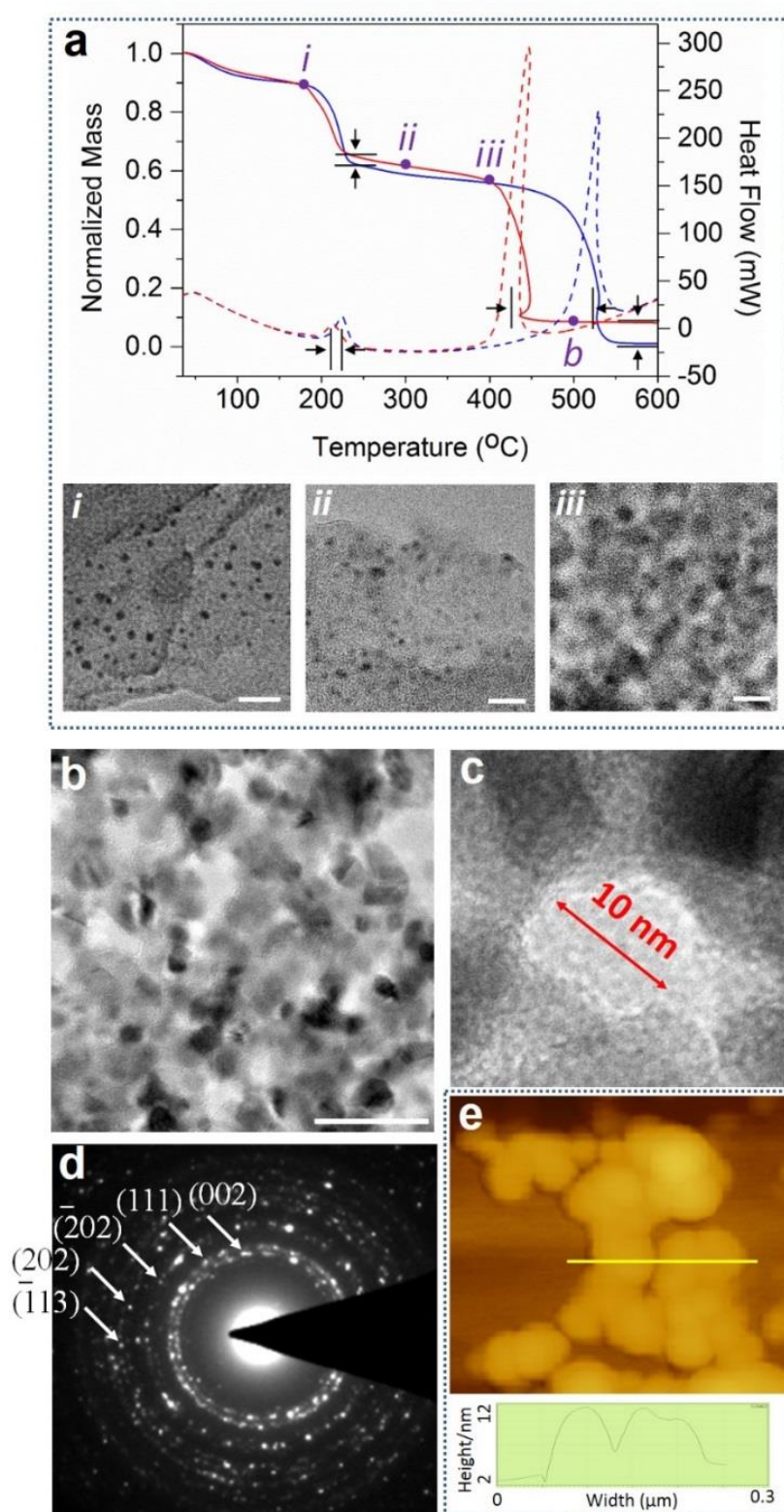


Fig. 6.5 (a) TGA (solid lines) and DSC (dash lines) of Cu²⁺-GO (red lines) and pure GO (blue lines) papers annealed in air. Insets are the TEM images of the Cu²⁺-GO paper after heated at different temperatures, corresponding to the points marked on the TGA curve. Scale bars: 20 nm (i), 40 nm (ii) and 15 nm (iii). (b–d) TEM images and corresponding selected area electron diffraction (SAED)

pattern of Cu^{2+} -GO paper annealed at 500 °C; the scale bar in (b) is 40 nm. The SAED pattern indicates the presence of CuO crystalline structures. (e) AFM image and a corresponding height profile of the 2D CuO monolayer sheets.

The second exothermic process was reflects the decomposition of carbon components of GO paper. The Cu^{2+} -GO paper decomposed at much lower temperatures ($\Delta T \approx 100$ °C) and faster than pure GO paper (Fig. 6.5a), because the crystallization and growth of Cu_xO in the Cu^{2+} -GO paper disrupted the ordered layer structure of GO paper. Owing to the sacrifice of the GO layers, Cu_xO clusters started to grow and to connect to their neighbors to form a 2D network after annealing at 400 °C or higher temperatures. Cupric oxide (CuO) networks composed of ~15 nm nanocrystals were fully formed after annealed at 500 °C (Fig. 6.5b–d). The network consists of the monolayers that have a thickness of ~10 nm as measured by AFM (Fig. 6.5e) and an average pore size of ~10 nm determined by the nitrogen adsorption-desorption isotherms (based on the Brunauer-Emmett-Teller (BET) method). The BET surface area of CuO networks was estimated as $61.1 \pm 0.2 \text{ m}^2 \text{ g}^{-1}$. These results confirm the polycrystalline nature and nanoporous structure of CuO monolayers. Owing to this ultrathin and nanoporous structural characteristics, the CuO papers have an ultralow apparent density of approximately $65 \pm 4 \text{ mg cm}^{-3}$, which is calculated on the basis of the precise mass determination by a quartz crystal microbalance (QCM). The value is at least one order of magnitude lower than the density of bulk CuO powders composed of similar-size particles³³ and the CuO paper is even more than 27 times lighter than pure GO papers³⁴.

We further discuss the formation mechanism of porous MO networks in this section, based on the experimental observations. We propose the growth process of the MO crystals in Fig. 6.6 with Cu_xO as an example. The crystallization and growth of Cu_xO nanocrystals, as well as the enlargement and disruption of GO layers are schematically illustrated in Fig. 6.6 a–c. During the nucleation and crystallization of clusters (Fig. 6.6b), Cu^{2+} ions accept a limited amount of oxygen species only from GO layers, leading to a partial aggregation into $\text{Cu}^{2+}\text{--O--Cu}^{2+}$ complexes. They are, however, confined and protected by GO layers from reaching a steady state by blocking the passage of environmental O_2 in air. In contrast, the progressive thermal activation caused the $\text{Cu}^{2+} \rightarrow \text{Cu}^+$ reduction with oxygen elimination³⁵. Cuprous oxide (Cu_2O) was therefore identified at this stage. Spontaneous self-organization/self-recrystallization of adjacent Cu_2O clusters was observed. As disclosed by the TEM image (the inset in Fig. 6.6c and Fig. 6.7), the Cu_2O clusters attached to each other along the common crystallographic orientations (highlighted by parallel yellow and blue lines in the inset of Fig. 6.6c) to form a larger crystal. This observation strongly suggests that the growth of Cu_2O clusters follows an Oriented-attachment mechanism (a non-

conventional crystallization mechanism)^{36, 37}. During the coarsening process, GO paper was gradually destroyed so that dioxygen (O_2) was allowed to diffuse into the GO paper interlayers. Cu_2O was consequently fully oxidized to CuO , as evidenced by the Cu 2p XPS spectra and XRD patterns (Fig. 6.3).

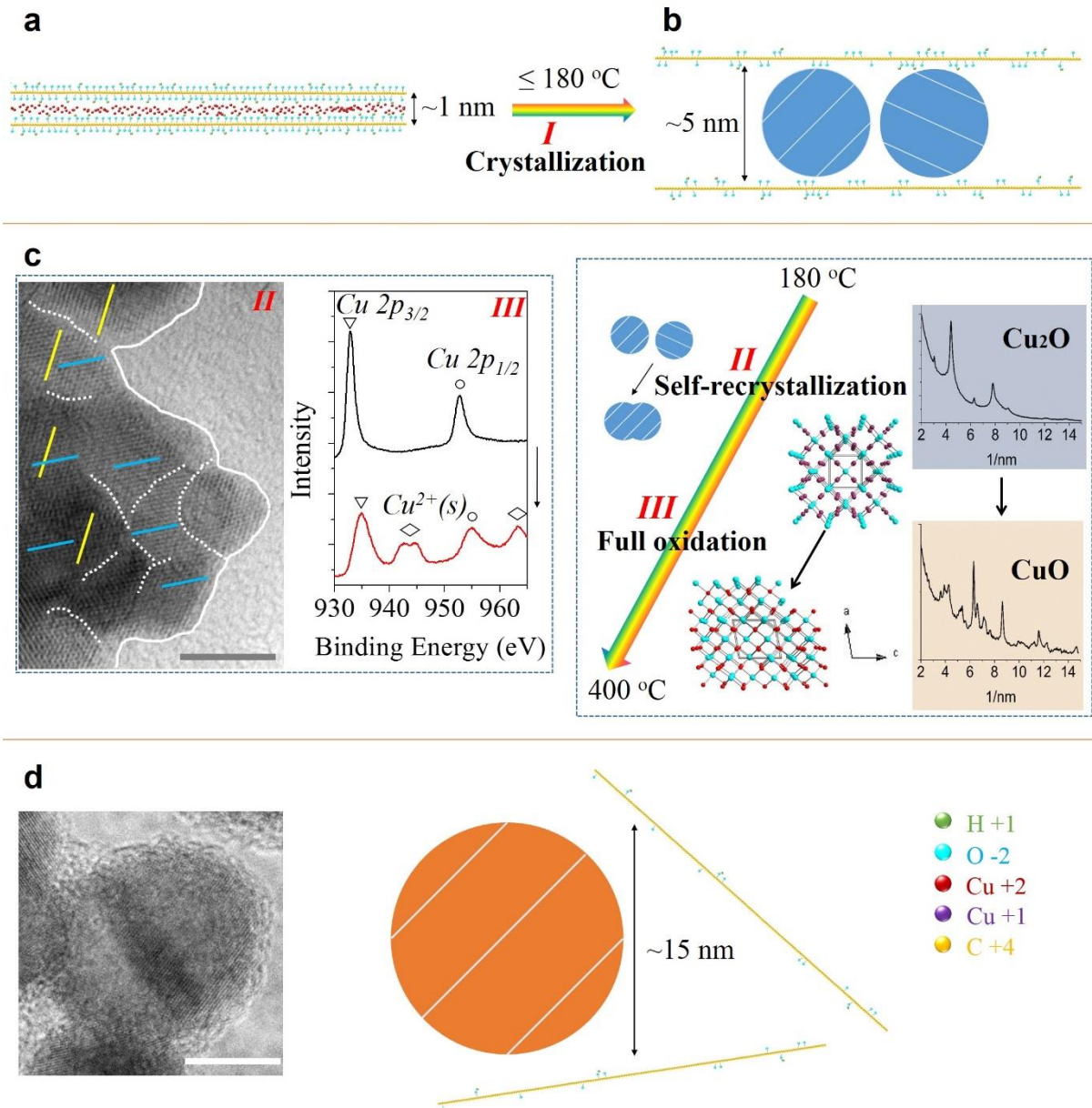


Fig. 6.6 Schematic illustration of the proposed oriented-attachment mechanism for the growth of MO crystals. (a) The interlayer structure of Cu^{2+} -GO paper before annealing. (b) The interlayer structure of Cu^{2+} -GO paper after annealing at $180 \text{ }^\circ\text{C}$. (c) TEM image (sample treatment, ST: $300 \text{ }^\circ\text{C}$), XPS spectra and XRD patterns (ST: 180 and $400 \text{ }^\circ\text{C}$) indicating the self-recrystallization *via* the oriented attachment mechanism and full oxidation of Cu_2O clusters into CuO . The raw TEM image is provided in Figure 6.7. Scale bar is 5 nm . (d) Illustration and TEM image (ST: $500 \text{ }^\circ\text{C}$) of the as-prepared CuO crystal annealed upon $400 \text{ }^\circ\text{C}$. Scale bar: 10 nm . Not drawn to scale.

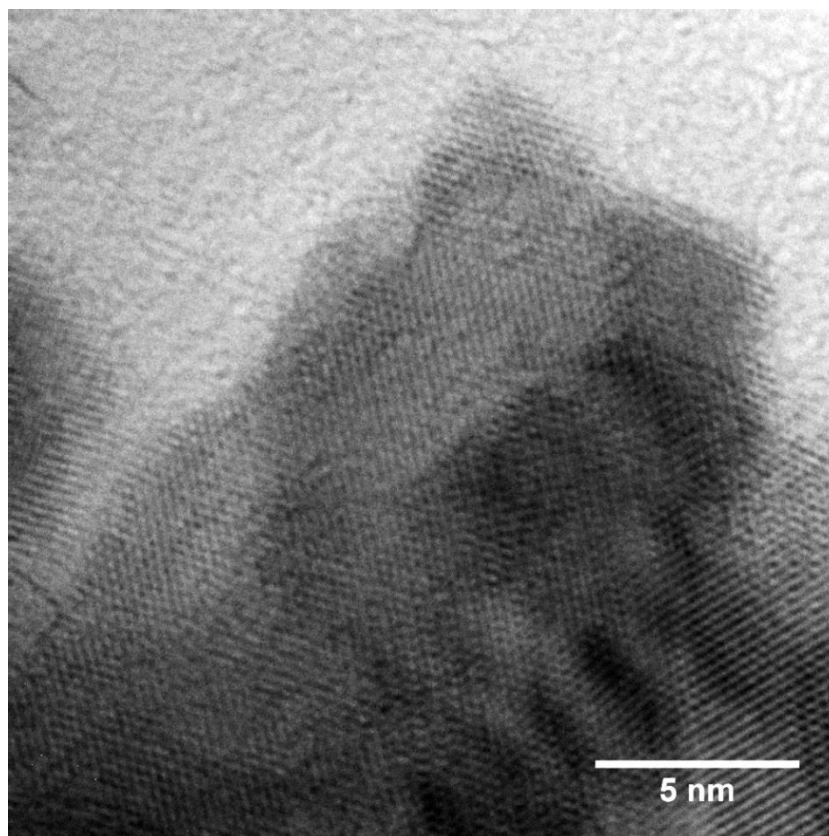


Fig. 6.7 A representative TEM image of CuO samples treated at 400 °C for 4.5 h. Larger crystals are formed by the assembly of smaller clusters.

In the following stage, the 15-nm CuO particles attached to their neighbors in the confined nanoscale space to form a network. However, because the aggregation had already reached saturation, further reorientation and self-organization/self-recrystallization of nanocrystals were restricted. Given the fact that metal ions are confined within GO paper and their total amount is constant, it is largely ruled out that the MO could undergo diffusion-controlled Ostwald ripening growth process. In other words, the solo oriented attachment mechanism is solely responsible for the growth of MO crystals³⁷. These results in a significant difference in structures between the MO samples synthesized by GO paper template and reference MO samples prepared by other templates. In short, the solo oriented attachment mechanism can well explain the formation of monolayered nanoporous MO.

The monolayer nanoporous structure could play a key role in providing shorter diffusion paths and rapid electrolyte transport in electrochemical reactions. The as-prepared MO papers are thus expected to exhibit high electrochemical performances. Among these MOs, CuO is one of the earliest, most Earth-abundant, and cheapest semiconductor materials investigated for energy related

technological applications. It has been proven that it is a versatile candidate that holds promising applications in various fields such as photocatalysis and supercapacitors³⁸⁻⁴¹.

6.3. Applications

6.3.1 Application of CuO as photocathode

To demonstrate the application perspective of the as-synthesized materials, we *first* tested the CuO paper as the photocathode for PEC water splitting. Nanocrystalline CuO is an attractive p-type semiconductor for PEC applications. Its conduction band edge has a more negative potential than the potential needed for water reduction to generate hydrogen, which makes this material a promising photocathode material for water splitting. The indirect transition bandgap of the CuO paper is estimated from the Tauc plot as ≈ 1.34 eV, further making it a good candidate for solar water splitting as the CuO paper can absorb photons from the solar spectrum. In the meantime, the band gap of 1.34 eV is higher than the thermodynamic potential for water splitting (1.23 eV). We fabricated photocathodes by directly casting the CuO paper on an ITO electrode and tested their PEC performances for water splitting. As shown in Fig. 6.8a, CuO paper can be steady wet-casted on various substrates such as soft human fingers or hard ITO owing to the high flexibility of nanoporous CuO layers. Therefore, the CuO paper can be integrated likely with a wide range of current collector materials including ITO, rough copper mesh, porous carbon and flexible conductive polymers. In addition, the transparency of CuO papers can be adjusted by controlling the thickness of GO paper template. In other words, the amount/mass/thickness of the as-prepared MO papers can be largely controlled. Fig. 6.8b shows the transmission spectra of a series of CuO paper/ITO photocathodes (named No.2–No.8) with various thicknesses. Their transmission in the visible-light region varies from 50% to 5%. The semi-transparent photoelectrodes are highly desirable in photovoltaic applications^{42, 43}.

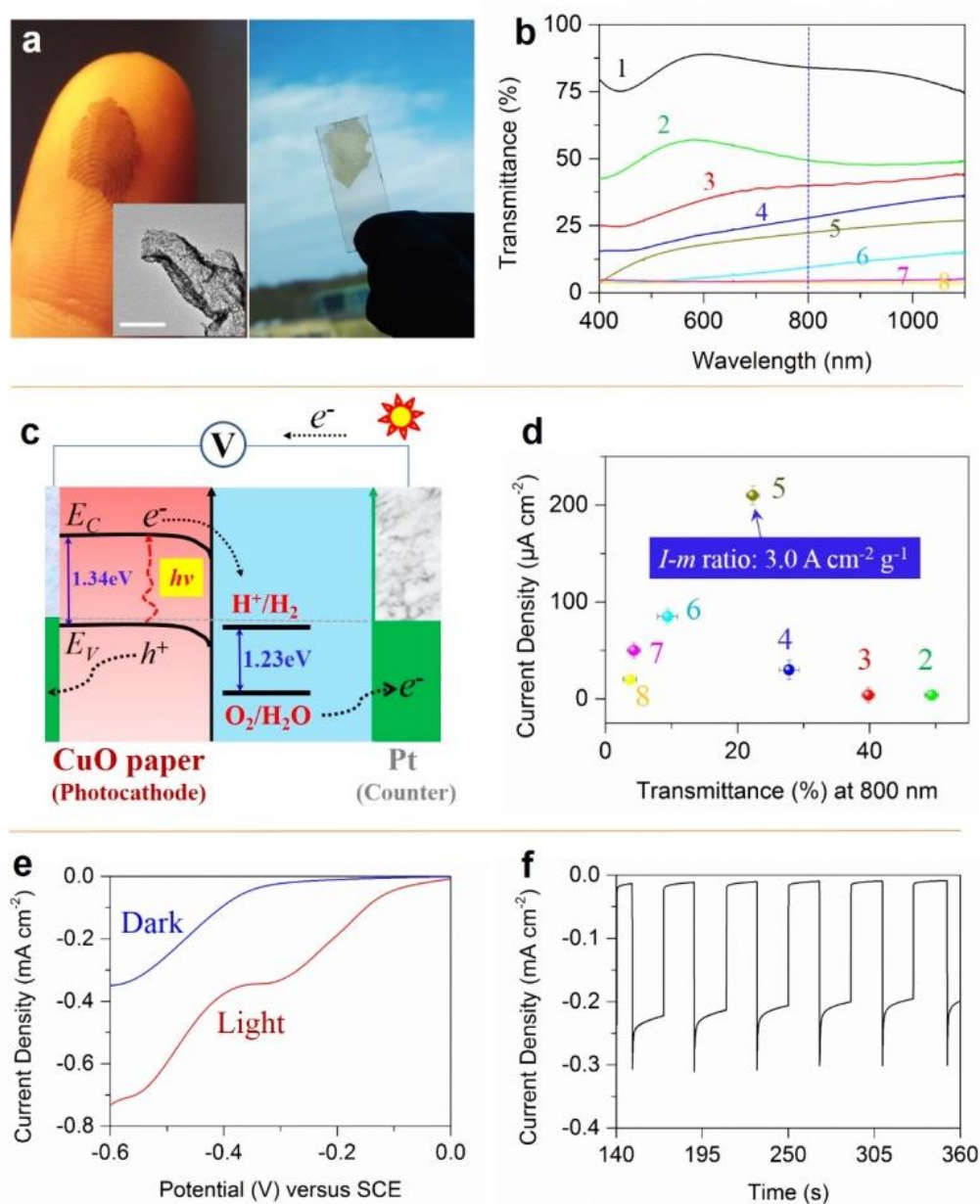


Fig. 6.8 (a) Photographs of CuO papers wet-casted on a finger and an ITO. Inset is a TEM image demonstrating a highly flexible CuO nanoporous monolayer. Scale bar: 400 nm. (b) Transmission spectra of a series of CuO paper/ITO photocathodes. Spectrum 1 was obtained at bare ITO electrodes as a reference. CuO paper/ITO photocathodes with decreasing transparency in the visible light range upon increasing the film thickness are continuously numbered top-down. (c) Schematic illustration of the operation principles of light-driven water splitting for a PEC cell based on CuO paper/ITO photocathode; e^- and h^+ denote electron and hole, respectively. (d) Current density of a series of CuO paper/ITO photocathodes as a function of their transmittance at 800 nm. The photocurrent density was recorded at -0.5 V (vs SCE) in 0.5 M Na_2SO_4 under light illumination of 100 mW cm^{-2} , where a Pt wire and saturated calomel electrode (SCE) were used as a counter and reference electrode, respectively. The current density-weight (I - m) ratio obtained photocathode No.5 is highlighted. (e) Linear sweep voltammograms collected at a scan rate of 10 mV s^{-1} from photocathode No.5 at 100 mW cm^{-2} . (f) Amperometric I - t curves of the photocathode No.5 at an applied voltage of -0.5 V upon light on/off cycles.

The CuO paper/ITO photocathodes with an active surface area of 0.8 cm^2 were employed in the one-step excitation PEC water splitting (Fig. 6.8c). The mean photocurrent density measured for photocathodes No.2–No.8 is compared in Fig. 6.8d. The highest net photocurrent generated (by photocathode No.5) can be up to $210 \mu\text{A cm}^{-2}$. Since the ITO surface was also exposed to the electrolyte due to the nanoporous nature of CuO paper, the photocurrent generated by the bare ITO electrode as a background current must be measured. However, the result shows that bare ITO electrodes only generate negligible photocurrent compared to CuO paper coated ITO electrodes.

The systematic measurements were performed at photocathode No.5, with the key results shown in Fig. 6.8e and f. Linear sweep voltammograms (LSV) and net $I-t$ curves were collected in the dark and under visible-light illumination (100 mW cm^{-2} , $\lambda > 400 \text{ nm}$) in $0.5 \text{ M Na}_2\text{SO}_4$ electrolyte. A considerable photocurrent was generated rapidly on light illumination, and the electrode exhibited fast and stable On-Off switching (Fig. 6.8f). We also observed a transient photocurrent in response to chopped illumination (Fig. 6.8f). The instantaneous photocurrent (I_0) measured immediately after the visible-light illumination was switched on is associated with a surface electron-hole recombination. After the transient phase, the steady-state photocurrent (I_{ss}) arising from the flux of electrons that are successfully transferred to the electrolyte was obtained.⁴⁴ The charge transfer efficiency (η_{trans}) can be estimated from the ratio of transition to steady photocurrents (i.e. $\eta_{\text{trans}} = I_{ss}/I_0$). The η_{trans} calculated from Fig. 6.8f is about 70%, indicating a good electrode/electrolyte contact even without employing co-catalyst such as Pt nanoparticles⁴⁵. This should be attributed to the nanoporous structure of CuO papers.

We further calculated the solar conversion efficiency (η_{conv}), or the efficiency of photon-to-hydrogen generation, based on the measured I_{ss} values according to the following equation^{46, 47}

$$\eta_{\text{conv}} = I_{ss}(1.23 - V)/J_{\text{light}} \quad (6.1)$$

Where V is the applied potential, and J_{light} the intensity of light irradiation. The conversion efficiency of photocathode No.5 is as high as 0.36%, which is a considerable improvement compared to those previously obtained at co-catalyst-free photoelectrodes (for example, 0.15% for ZnO:N nanowires⁴⁷, 0.1% for gold nanorods⁴⁸, 0.12 for Si and TiO₂ nanotrees⁴⁹, 0.1% for ZnO thin film⁵⁰ and 0.1% for TiO₂ nanorods⁵¹). In addition, the conversion efficiency of CuO papers could be further improved by using co-catalysts or conductive chemical agents, though it is beyond the scope of the present work but should constitute an interesting ongoing research effort.

More importantly, it is worth noting that only $\sim 70 \mu\text{g}$ CuO paper was used in the construction of photocathode No.5. In most previous reports, in contrast, the amount of photoactive materials (m) needed for the construction of a photoelectrode with the similar efficiency is normally in the range from tens of milli grams to several grams. To date, the current density-to-active material mass ratio has rarely been reported in literature. In response to current environmental and energy concerns, however, lightweight materials could offer unique advantages to meet special needs in some areas such as wearable devices, spaceship, and army or astronaut clothing's. In fact, lightweight materials have especially been identified as necessary and important by the U.S. Department of Energy, in order to fulfill the Energy Efficiency programs.⁵² In the present case, we calculated the I_{ss} - m ratio of photocathode No.5 to be as high as $3.0 \text{ A cm}^{-2} \text{ g}^{-1}$, which is more than one order of magnitude higher than the value estimated from previously reported solar water splitting materials (0.125^{49} , 0.25^{53} , $\sim 0.2 \text{ A cm}^{-2} \text{ g}^{-1}$ ⁵⁴).

6.3.2 Application of CuO as supercapacitor electrode materials

Cyclic voltammetry (CV) and galvanostatic charge-discharge (GCD) measurements were conducted with a three-electrode system as described above. Fig. 6.9a shows CVs of the as-prepared CuO paper electrodes in 1 M KOH aqueous electrolyte at different scan rates ranging from 5–175 mV s^{-1} . The pair of strong anodic and cathodic peaks is associated with the *Faradaic* redox reaction of the $\text{Cu}^+/\text{Cu}^{2+}$ transition. This suggests the hybrid contribution of the double-layer capacitance and redox reaction from Cu paper electrodes². It is also notable that the shape of CV curves remained almost unchanged with increasing scan rate. This suggests high rate capability of the electrode. The hybrid capacitive performance of the CuO paper electrodes was further investigated by GCD measurements. Fig. 6.9b shows GCD curves of the electrodes in 1 M KOH aqueous electrolyte with increasing the constant current density from 2 to 20 A g^{-1} in the potential window of -0.1 to 0.5 V (vs saturated calomel electrode, SCE). Notably, the dynamic voltage drop is extremely low, which is not observed at conventional metal oxide based electrodes. This observation indicates that the CuO paper-based capacitor has low equivalent series resistance. The specific capacitance (SC) of the electrodes was calculated from the discharging curves. As shown in Fig. 6.9c, the SC value for CuO paper electrodes at 2 A g^{-1} reaches 323 F g^{-1} , which is remarkably higher than that of normal CuO bulk electrode (78 F g^{-1})². The SC of the electrode at 20 A g^{-1} is 200 F g^{-1} , which is as much as 62% of that at 2 A g^{-1} . In addition, the CuO paper electrodes show high cycling stability, as shown in Fig. 6.9d. After 1000 continuous cycles at 10 A g^{-1} , the SC

retained 83% (200.13 F g^{-1}). The results demonstrate that the CuO papers are very suitable for fabrication of supercapacitor electrodes which can be used in fast charge-discharge cycles, stilling retaining a significantly high specific capacitance.

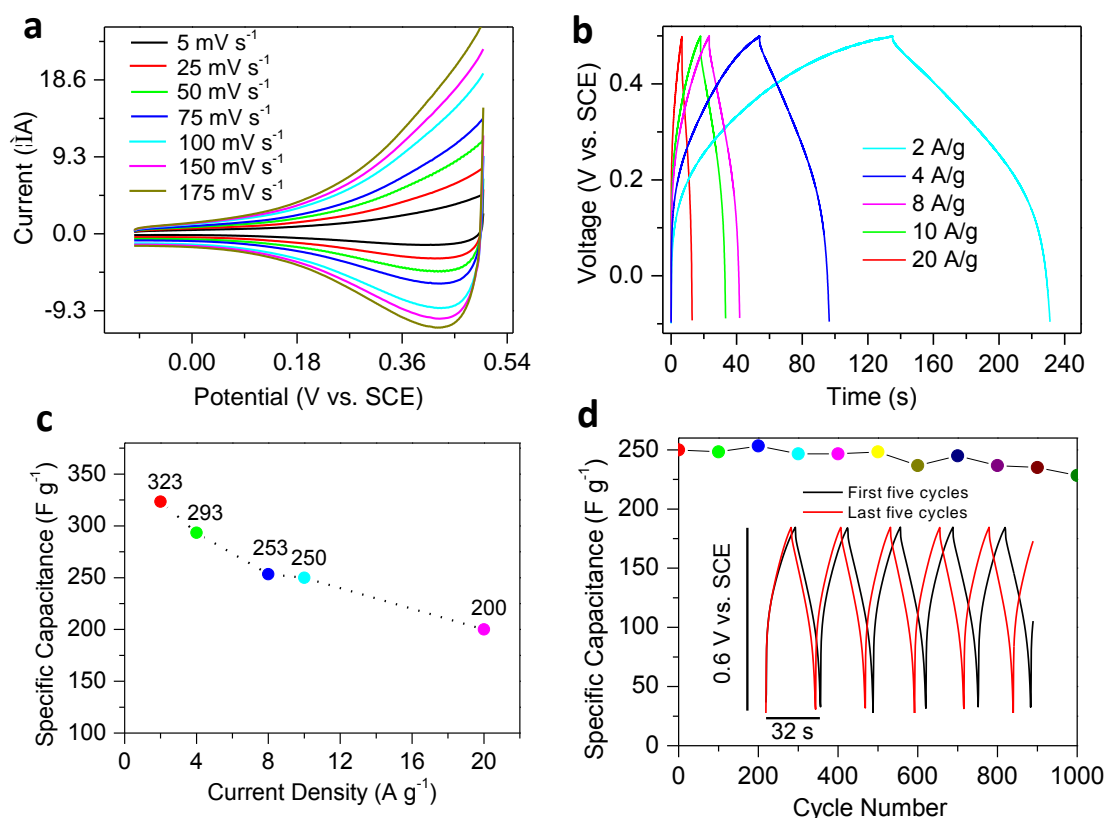


Fig. 6.9 Supercapacitor performances of CuO paper electrodes: (a) CVs obtained with various scan rates. (b) Galvanostatic charge-discharge curves at different applied current densities. (c) Dependence of the specific gravimetric capacitances as a function of the applied current density. (d) Cycling stability at a high current density of 10 A g^{-1} . Inset in (d) shows the first and last five charge-discharge cycles.

6.5. Conclusions

In summary, we have reported here a general method for the high-yield and possibly large-scale synthesis of ultralight, freestanding and nanoporous MO papers. Six types of MO papers including ZnO, CuO, Co_3O_4 , Fe_2O_3 , Mn_3O_4 and NiO are demonstrated as examples. The MO papers consist of nanoporous monolayers, which are attributed to the confined synthesis facilitated by the sacrificial GO paper as a template. We have discussed the formation mechanism of the unique nanostructured MO papers in detail. We suggest a non-conventional oriented attachment mechanism that can well explain the formation of the unique structured MO materials. In our proof-

of-the-concept studies, the CuO papers were directly used to fabricate photocathodes for photoelectrochemical water splitting. These CuO paper based photocathodes have demonstrated clear advantages for lightweight electrochemical applications. Straightforward structural improvement to a material can lead to a significant enhancement in the photocurrent-weight ratio. Besides, when used as supercapacitor electrodes the CuO paper exhibits a large specific capacitance (323 F g^{-1} at 2 A g^{-1}) and good cycling stability.

References

- 1 J. A. Rodriguez, M. F. Garcia, *Synthesis, Properties and Applications of Oxide Nanomaterials*, 2007, John Wiley and Sons, Hoboken, New Jersey.
- 2 J. P. Jolivet, *Metal Oxide Chemistry and Synthesis from Solution to Solid State*, 2000, Wiley Chichester.
- 3 A. J. Zarur and J. Ying, *Nature*, 2000, **403**, 65-67.
- 4 M. V. Reddy, G. V. S. Rao and B. V. R. Chowdari, *Chem. Rev.*, 2013, **113**, 5364-5475.
- 5 H. J. Kim and J. H. Lee, *Sens. Actuators B Chem.*, 2014, **192**, 607-627.
- 6 T. Athar, A. A. Khan, S. K. Vishwakarma, A. Razzaq and A. Ahemd, *Rev. Adv. Sci. Eng.*, 2015, **4**, 258-276.
- 7 S. Barth, F. Hernandez-Ramirez, J. D. Holmes and A. Romano-Rodriguez, *Prog. Mater. Sci.*, 2010, **55**, 563-627.
- 8 Q. Zhang, K. Zhang, D. Xu, G. Yang, H. Huang, F. Nie, C. Liu, S. Yang, *Prog. Mater. Sci.*, 2014, **60**, 208-337.
- 9 F. E. Osterloh, *Chem. Soc. Rev.*, 2013, **42**, 2294-2320.
- 10 R. S. Devan, R. A. Patil, J. Lin and Y. Ma, *Adv. Funct. Mater.*, 2012, **22**, 3326-3370.
- 11 D. Ling, N. Lee and T. Hyeon, *Acc. Chem. Res.*, 2015, **48**, 1276-1285.
- 12 Z. Sun, T. Liao, Y. Dou, S. Hwang, M. S. Park, L. Jiang, J. H. Kim and S. Dou, *Nat. Commun.*, 2014, **5**, 3813.
- 13 J. M. Lee, I. Y. Kim, S. Y. Han, T. W. Kim and S. J. Hwang, *Chem. Eur. J.*, 2012, **18**, 13800-13809.
- 14 H. Cao, X. Zhou, C. Zheng and Z. Liu, *ACS Appl. Mater. Inter.*, 2015, **7**, 11984-11990.
- 15 S. E. Moosavifard, M. F. El-Kady, M. S. Rahmanifar, R. B. Kaner and M. F. Mousavi, *ACS Appl. Mater. Inter.*, 2015, **7**, 4851-4860.
- 16 C. Hou, M. Zhang, T. Kasama, C. Engelbrekt, L. Zhang and H. Wang, Q. Chi, *Adv. Mater.*, 2016, **28**, 4097-4104.
- 17 H. Chen, M. B. Muller, K. J. Gilmore, G. G. Wallace and D. Li, *Adv. Mater.*, 2008, **20**, 3557-3561.
- 18 C. Hou, H. Wang, Q. Zhang, Y. Li and M. Zhu, *Adv. Mater.*, 2014, **26**, 5018-5024.
- 19 C. N. Ye, K. Raidongia, J. Shao, Q. H. Yang and J. Huang, *Nat. Chem.*, 2015, **7**, 166-169.
- 20 S. Takenaka, S. Miyake, S. Uwai, H. Matsune and M. Kishida, *J. Phys. Chem. C*, 2015, **119**, 12445-12454.
- 21 R. Boston, A. Bell, V. P. Ting, A. T. Rhead, T. Nakayama, C. F. J. Faul and S. R. Hall, *CrystEngComm*, 2015, **17**, 6094-6097.
- 22 X. Li, W. Qi, D. Mei, M. L. Sushko, I. Aksay and J. Liu, *Adv. Mater.*, 2012, **24**, 5136-5141.
- 23 H. Wang, Y. Fu, X. Wang, J. Gao, Y. Zhang and Q. Zhao, *J. Alloy Compd.*, 2015, **639**, 352-358.
- 24 M. Zhang, A. Halder, C. Hou, J. Ulstrup and Q. Chi, *Bioelectrochemistry*, 2016, **109**, 87-94.
- 25 N. Zhu, S. Han, S. Gan, J. Ulstrup and Q. Chi, *Adv. Funct. Mater.*, 2013, **23**, 5297-5306.
- 26 J. Mu, C. Hou, H. Wang, Y. Li, Q. Zhang and M. Zhu, *Sci. Adv.*, 2015, **1**, e1500533.
- 27 K. N. Kudin, B. Ozbas, H. C. Schniepp, R. K. Prud'homme, I. A. Aksay and R. Car, *Nano Lett.*, 2008, **8**, 36-41.
- 28 H. G. Yang and H. Zeng, *J. Phys. Chem. B.*, 2004, **108**, 3492-3495.
- 29 C. Hou, H. Yu, Q. Zhang, Y. Li and H. Wang, *J. Alloy. Compd.*, 2010, **491**, 431-435.
- 30 Z. Wang, L. Zhou and X. Lou, *Adv. Mater.*, 2012, **24**, 1903.

- 31 C. Zeng, Z. Tang, B. Guo and L. Zhang, *Phys. Chem. Chem. Phys.*, 2012, **14**, 9838-9845.
- 32 S. Ye, and J. Feng, *Poly. Chem.*, 2013, **4**, 1765-1768.
- 33 <http://www.us-nano.com/inc/sdetail/485>
- 34 D. A. Dikin, S. Stankovich, E. J. Zimney, R. D. Piner, G. H. B. Dommett, G. Evmenenko, S. T. Nguyen and R. S. Ruoff, *Nature*, **2007**, *448*, 457-460.
- 35 F. X. L. I. Xamena, P. Fiscaro, G. Berlier, A. Zecchina, G. T. Palomino, C. Prestipino, S. Bordiga, E. Giamello and C. Lamberti, *J. Phys. Chem. B*, 2003, **107**, 7036-7044.
- 36 J. Zhang, F. Huang and Z. Lin, *Nanoscale*, 2010, **2**, 18-34.
- 37 M. Niederberger and H. Colfen, *Phys. Chem. Chem. Phys.*, 2006, **8**, 3271-3287.
- 38 D. Barreca, P. Fornasiero, A. Gasparotto, V. Gombac, C. Maccato, T. Montini and E. Tondello, *ChemSusChem*, 2009, **2**, 230-233.
- 39 A. Kargar, Y. Jing, S. J. Kim, C. T. Riley, X. Pan and D. Wang, *ACS Nano*, 2013, **7**, 11112-11120.
- 40 G. Wang, J. Huang, S. Chen, Y. Gao and D. Cao, *J. Power Sources*, 2011, **196**, 5756-5760.
- 41 V. D. Patake, S. S. Joshi, C. D. Lokhande and O. S. Joo, *Mater. Chem. Phys.*, 2009, **114**, 6-9.
- 42 Y. Sun, Z. Sun, S. Gao, H. Cheng, Q. Liu, J. Piao, T. Yao, C. Wu, S. Hu, S. Wei and Y. Xie, *Nat. Commun.*, 2012, **3**, 1057
- 43 J. Brillat, J. H. Yum, M. Cornuz, T. Hisatomi, R. Solaraska, J. Augustynski, M. Graetzel and K. Sivula, *Nat. Photonics*, 2012, **6**, 823-827.
- 44 H. K. Dunn, J. M. Feckl, A. Muller, D. Fattakhova-Rohlfing, S. G. Morehead, J. Roos, L. M. Peter, C. Scheu and T. Bein, *Phys. Chem. Chem. Phys.*, 2014, **16**, 24610-24620.
- 45 A. Paracchino, V. Laporte, K. Sivula, M. Graetzel and E. Thimsen, *Nat. Mater.*, 2011, **10**, 456-461.
- 46 B. Parkinson, *Acc. Chem. Res.*, 1984, **17**, 431.
- 47 X. Yang, A. Wolcott, G. Wang, A. Sobo, R. C. Fitzmorris, F. Qian, J. Zhang and Y. Li, *Nano Lett.*, 2009, **9**, 2331-2336.
- 48 S. Mubeen, J. Lee, N. Singh, S. Kramer, G. D. Stucky and M. Moskovits, *Nat. Nanotechnol.*, 2013, **8**, 247-252.
- 49 C. Liu, J. Tang, H. Chen, B. Liu and P. D. Yang, *Nano Lett.*, 2013, **13**, 2989-2992.
- 50 A. Wolcott, W. A. Smith, T. R. Kuykendall, Y. Zhao and J. Zhang, *Adv. Funct. Mater.*, 2009, **19**, 1849-1856.
- 51 A. Wolcott, W. A. Smith, T. R. Kuykendall, Y. Zhao and J. Zhang, *Small*, 2009, **5**, 104-111.
- 52 <http://energy.gov/eere/office-energy-efficiency-renewable-energy>
- 53 Q. X. Jia, K. Iwashina and A. Kudo, *PNAS*, 2012, **109**, 11564.

Chapter 7. Bottom-up method for synthesis of 2D nanoporous hybrid CuO/ZnO nanosheets for non-enzymatic biosensor

7.1. Introduction

CuO/ZnO based multi-functional nanohybrid materials were widely used in various applications, such as gas sensors¹, chemical sensors², biosensors³⁻⁵, photo degradation⁶⁻⁸, catalysis⁹⁻¹⁰, energy storage¹¹, memory application¹², especially application in non-enzymatic sensors for detection of glucose¹³⁻¹⁴. The heterostructured ZnO–CuO composite material has been extensively used for sensing application due to its high sensitivity and fast response time originated in the extension of the electron depletion layer through the formation of p-n junction¹⁵⁻¹⁶.

As we mentioned in Chapter 6, various MOs were successfully synthesized using GO paper as a template, CuO paper displayed high performance for supercapacitor and photocathode, which suggests that the morphology and structure of MOs can significantly influence their physicochemical properties. In this chapter, we used scalable two-dimensional (2D) GO papers as templates to synthesize layer-by-layer nanoporous 2D heterostructured ZnO–CuO nanosheet and furthermore used them for ultrasensitive non-enzymatic detection of glucose.

GO papers were prepared by vacuum filtration of GO solution. Metal cation (Cu^{2+} and Zn^{2+}) was loaded on GO paper via physical absorption^{17, 18} and electrostatic interaction between oxygen groups and metal cations. During annealing in air, CuO/ZnO nucleation process was initiated and the porous CuO/ZnO nanoclusters formed between the GO layers. D-spacing of GO paper interlayers restricted the MO expansion in the Z axis, which resulted in the formation of ultrathin 2D nanosheets. After removing GO by heating, MO papers maintained the layer-by-layer, ultrathin and nanoporous structure. More interestingly, the as-prepared ZnO–CuO composite material by using GO paper as a template can provide better chances for continuous growth of p-n junction at the nanoscale, which could be very useful for electrochemical and photoelectrochemical applications.

7.2. Experimental section

Preparation of 2D nanoporous MO nanosheets: GO paper was used as a platform for the synthesis of 2D MO nanosheets. GO was synthesized by the procedure described in section 2.1.3. Briefly, the GO paper was fabricated by vacuum filtration of GO solution and further dried at room

temperature. The GO paper was then immersed in 0.1 M Cu^{2+} and Zn^{2+} solution for 48 h, and rinsed carefully by Milli-Q water. After that, the sample was heated from room temperature to 500 °C at a rate of 10 °C min^{-1} and held at this temperature for 4 h under air atmosphere. After cooling down to room temperature, paper-like sample was collected and characterized by SEM. The sample was dispersed in ultrapure ethanol by sonication, and further drop-cast on different substrates for structural characterization with TEM, XRD, XPS. Such samples were also used in electrochemical measurements.

7.3 Results and discussion

7.3.1 Preparation of CuO/ZnO 2D hybrid nanosheets

High-quality GO was synthesized by a modify Hummer's method according to our previous work¹⁹⁻²¹ (detailed in Chapter.2). AFM images (Fig. S2) clearly show that the size of the GO sheets ranges from 0.5 to 5 μm , and the thickness is about 1.2 nm. As expected, the UV-vis spectrum is characterized by the two main peaks at 230 and 300 nm (Fig. S3). Fig S1A and Fig.S1B presents XPS survey and C 1s spectra of GO. The XPS spectra of GO exhibits a relatively high O1s and a weak C1s peak, while the C1s XPS spectra of GO show various oxygen-containing carbon groups (OCGs) including C=O and C–O, which indicates that OCGs are abundantly present on the GO sheet surfaces, providing attaching site for positively charged molecular groups and nanoparticles²²⁻²³. Vacuum filtration of GO solutions was used to prepare GO paper, and then it was immersed into Cu^{2+} solution, Zn^{2+} solution or a mixture of Cu^{2+} and Zn^{2+} solution for 48 h, after careful rinsing with Milli-Q water it was dried in air. Metal ions modified GO paper was transferred into oven for annealing at 500 °C for 5 h, the MO paper largely retained the same shape but its color changed to white, black, and light back, respectively, corresponding to ZnO, CuO, and CuO/ZnO samples.

7.3.2 Characterization of metal oxides

The as-synthesized composites were examined *first* by powder X-ray diffraction (Fig. 7.1). In the XRD pattern of ZnO, a definite line broadening of the XRD peaks indicates that the prepared material is composed of particles with nanoscale sizes. From this XRD pattern analysis, we can obtain the key parameters regarding the peak intensity, position and width, full-width at half-maximum (FWHM). The diffraction peaks located at $2\theta=31.7^\circ$, 34.4° , and 36.3° are assigned the index as the hexagonal Wurtzite phase of ZnO (PDF #36-1451). Similarly, in the XRD pattern of

CuO the peaks at $2\theta=35.4^\circ$, 38.7° and 48.7° correspond to the (002), (111), and (-202,) reflections of CuO. Both exhibit the characteristic diffractions of mixed-valence compounds with a face-centred cubic structure, and all diffraction peaks can be readily assigned to the standard phase of monoclinic (PDF #48-1548) without any characteristic peak originated in possible impurities such as Cu_2O or $\text{Cu}(\text{OH})_2$. In the hybrid of CuO/ZnO, it displays both CuO and ZnO diffractions. And XPS was also used to confirm that hybrid 2D porous CuO/ZnO was obtained (Fig. 7.2). The binding energies of Cu $2p_{3/2}$, Zn $2p_{3/2}$, and O 1s are identified at 933.63, 1021.9, and 529.67 eV, respectively. The high-resolution Cu scan, $2p_{3/2}$ and Cu $2p_{1/2}$ appeared in 934.9 eV and 945.9 eV (Fig. 7.2 B) indicate that Cu is in the Cu^{2+} oxidation state. The XPS measurements thus verify the structures consisting of CuO and ZnO, furthermore, the atom ratio of Cu with Zn is calculated as approximately 1:1, which is consistent with the concentration ratio of the mixed solution. This clearly suggests that each cation had equal opportunity to diffuse into the interlayers of GO paper and to be captured. It should be mentioned that carbon was detected by XPS (Fig. 7.2) and could come from residual graphene which was not completely burned out during the annealing.

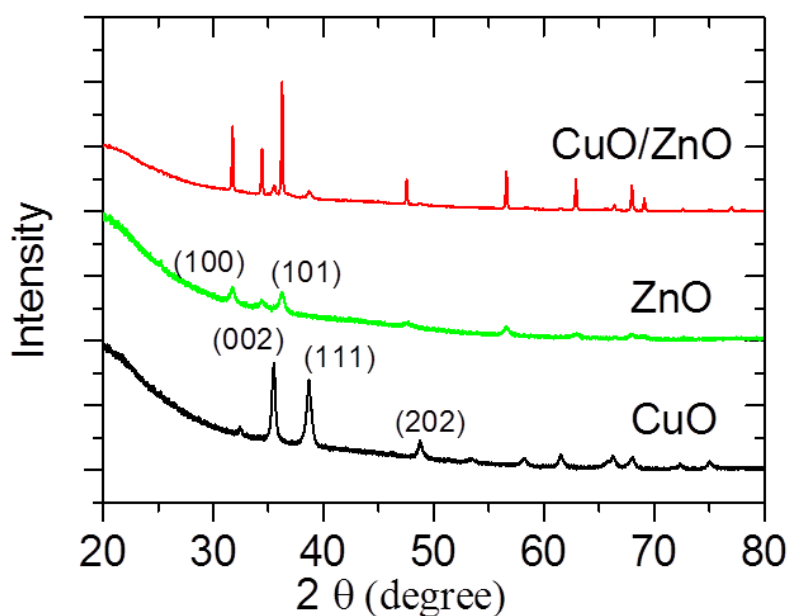


Fig. 7.1 XRD patterns of 2D porous CuO, ZnO and CuO/ZnO nanosheets.

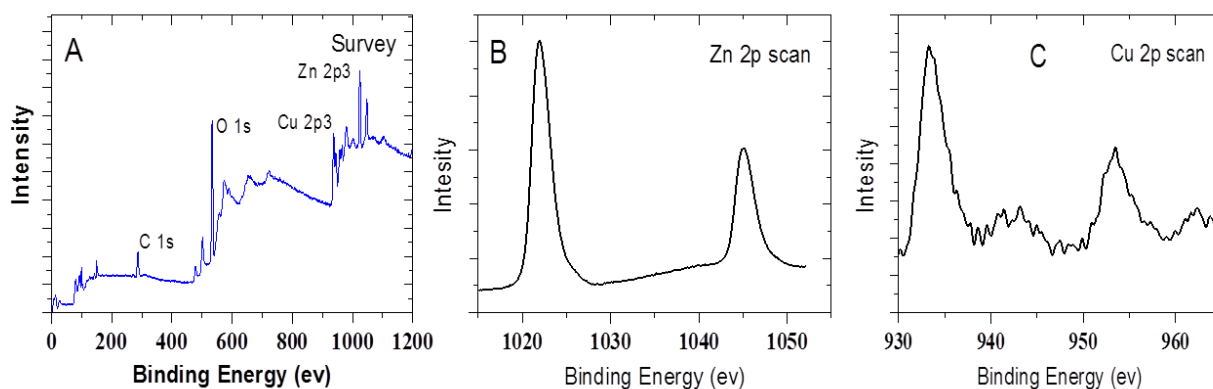


Fig. 7.2 XPS spectra of 2D nanoporous CuO-ZnO nanosheet samples. (A) Survey spectrum, (B) high-resolution Zn 2p scan and (C) high-resolution Cu 2p scan.

In general, CuO/ZnO oxide was synthesized by chemical methods, the shape of most products is nanocubic or nanoparticle and protecting ligands are necessary for preventing aggregation. Due to the fast grow process and no restriction in the growth direction, it is difficult to control the morphology of the metal oxide. In contrast, in the present case hybrid CuO/ZnO displayed ultrathin 2D nanosheet, the size is about 20 nm and 50 nm corresponding to ZnO and CuO according to the TEM image shown in Fig. 7.3C. In addition, high-resolution TEM image (Fig. 7.3D) suggests that highly nanoporous structure (the pore size from 5 to 50 nm) formed by the network of CuO/ZnO nanosheets. There are probably two reasons that nanoporous structure is formed. One is that CuO/ZnO nanosheets were connected each other during the growth process, the other is that GO has a lot of defects or pores which would affect the growth of CuO/ZnO nanosheets. Such kinds of nanoporous structure normally give rise to a high specific surface area and plenty of pores with even distribution, which is very helpful for ion diffusion. High-resolution TEM image of CuO/ZnO in Fig. 7.3E shows lattice fringes with interplanar spacing of 0.25 nm and 0.28 nm corresponding to the CuO 002 lattice face and ZnO 100 lattice face. The selected area electron diffraction (SAED) is shown in Fig. 7.3E, and it is in good agreement with the XRD patterns and illustrated a polycrystalline structure of CuO/ZnO. The thickness of the most ZnO/CuO nanosheets is about 2-5 nm (3-7 layers of single layer MO) as measured by AFM (the image in Fig. 7.3F and the cross-sectional profile in Fig. 7.3G). In addition, the SEM images (in Fig. 7.3A and Fig. 7.3B) of CuO/ZnO reveal the layer-by-layer structural feature in microscale. Moreover, the density of 2D nanoporous CuO/ZnO nanosheet was estimated as about 50 mg cm^{-3} by quartz crystal microbalance (QCM), which is at least 10 times lighter than normal CuO powder composed of similar size particles.

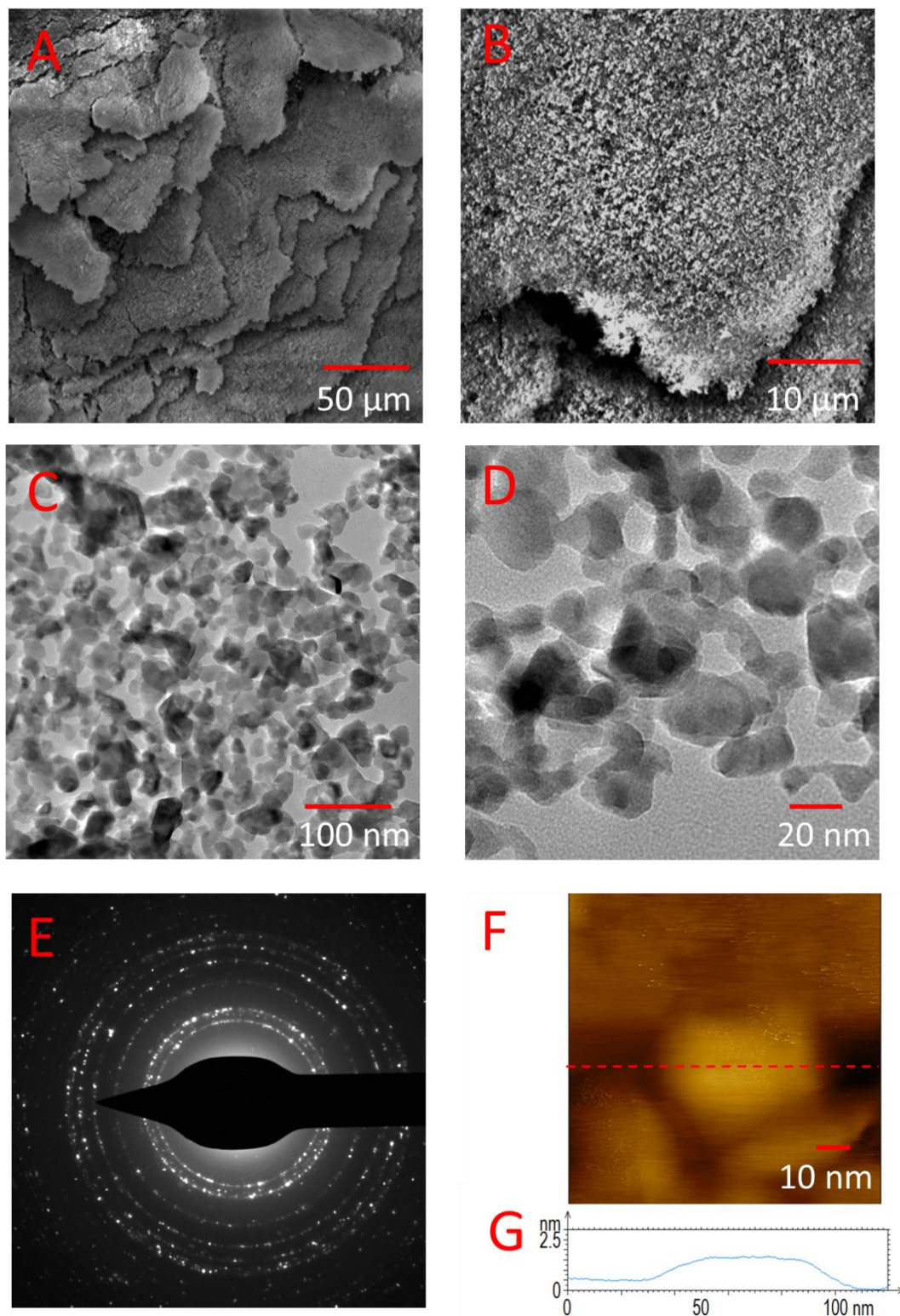


Fig. 7.3 SEM images with different magnifications (A and B), TEM images (C and D), SAED (E) and AFM image (F) with corresponding cross-sectional profile along the line marked in the AFM image (G) of 2D porous CuO/ZnO nanosheet.

In order to investigate the elemental distribution of Cu and Zn in the 2D nanoporous CuO/ZnO hybrid nanosheets, scanning electron microscopy (SEM) and EDX mapping analysis were performed for single MO sheets. SEM mapping images of C, O, Cu and Zn elements are shown in Fig. 7.4. All atoms were distributed uniformly in the nanocomposite, suggesting that structurally uniform CuO/ZnO hybrid nanosheets were obtained.

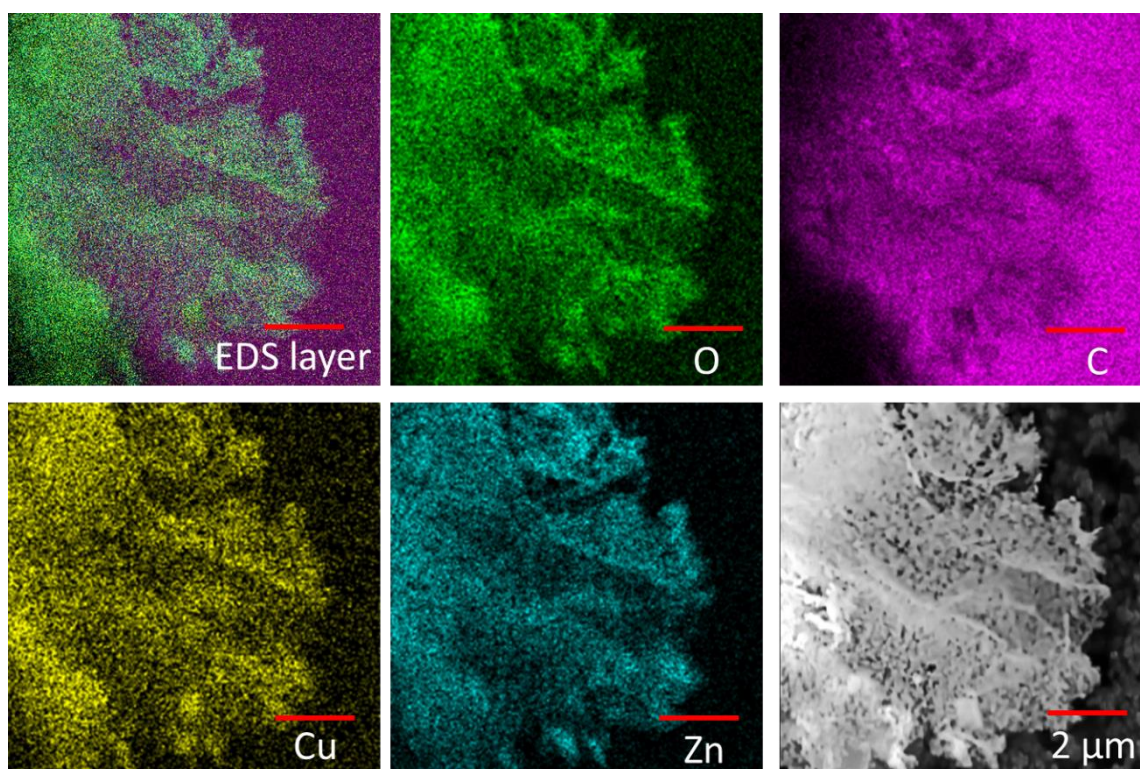


Fig. 7.4 EDX mapping images of 2D porous CuO/ZnO nanosheet.

The BET surface area of as-obtained CuO/ZnO hybrid materials is estimated as approximately $80 \text{ m}^2 \text{ g}^{-1}$ (Fig. 7.5), with the average pore size of $\sim 10 \text{ nm}$. These pores are featured by the bimodal arrangement, which could play a key role in providing shorter diffusion paths and rapid transport of electrolyte ions as well as providing more active sites for electrochemical reactions. In addition, from XRD and XPS analyses, it appears that rGO was not completely removed. Graphene most likely exists as a film coated on metal oxide surfaces or edges to enhance the overall conductivity, in turn beneficial for electron transfer. Given these striking nanostructured properties, the 2D CuO/ZnO hybrid nanosheets may exhibit good electrochemical performance as a non-enzymatic sensing material for detection of glucose.

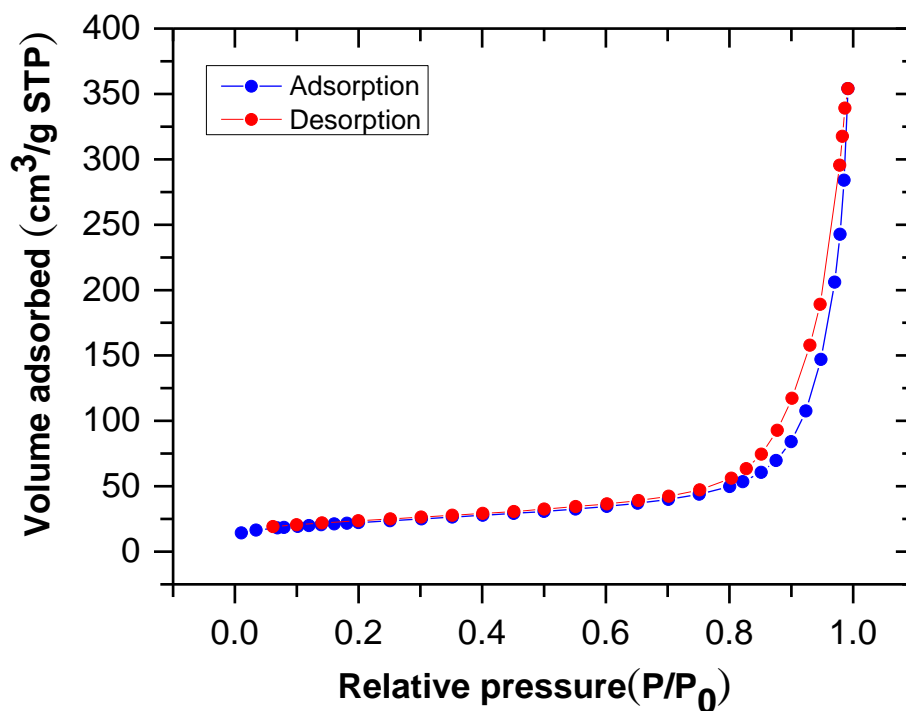


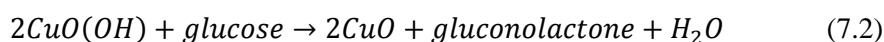
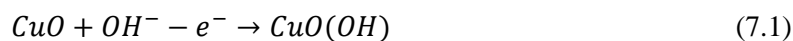
Fig. 7.5. Nitrogen adsorption-desorption isotherms of CuO/ZnO papers.

7.4 Application of 2D porous CuO/ZnO nanosheets

Accurate detection of glucose is important for clinical diagnostics in diabetes control and analytical applications in biotechnology, environmental pollution control, and food industry. Amperometric glucose biosensor which can satisfy the requirements of clinic blood glucose level measurement, glucose oxidase (GOx) modified electrode is the most common class of amperometric biosensors for glucose detection because GOx enables catalytic oxidation of glucose with high sensitivity and selectivity^{3, 24} However, these enzyme modified electrodes have some disadvantages, for instance, the instability of the electrode and unsatisfactory reproducibility, the complicated immobilization procedure, and the expensive enzymes are that easily lose activation. For addressing such issues, the development of non-enzymatic sensors with high sensitivity and stability, and interference-free glucose determination is critical.

Due to the fact that CuO/ZnO hybrid materials displayed high specific area, 2D porous nanosheets are promising electrode materials for non-enzymatic sensor used for glucose detection. Cyclic voltammetry of 2D porous CuO, ZnO and CuO/ZnO nanosheet modified glassy carbon (GCE) electrodes in 40 mL 0.1 M NaOH or KOH solution without and with 1 mM glucose were studied (Fig.7.6A). Compared the CV without and with 1 mM glucose, obvious reduction peaks

around 0.6 V (vs SCE) can be observed in blank NaOH solution, which corresponding to the Cu(II)/Cu(III) redox couple according to previous studies (except for pure ZnO nanosheet electrode), the reaction process can be depicted as eq(7.1). After injection of glucose into the electrolyte solution, Cu (III)(OOH) obtains an electron and acts as an electron acceptor. Electrons are transferred from glucose to the electrode which leads to increase of the peak current, with the reaction process following eq(7.2). The oxide current dramatically increased, which suggests a kinetic limitation in the reaction between the redox sites of the CuO and CuO/ZnO modified electrode and glucose. The starting reaction potential for glucose oxidation can be lowered to 0.25 V (vs SCE).



In order to evaluate the performance of electrochemical analysis for glucose, the non-enzymatic chronoamperometric detections of glucose at 0.6 V (vs. SCE) was performed with successive addition of glucose. Fig. 7.6B shows the I-t curves of different 2D porous ZnO, CuO and CuO/ZnO nanosheet modified GCE electrodes in 0.1 M NaOH solution by successive addition of different concentrations of glucose. Both CuO and CuO/ZnO show typical steady-step response with very low noise, significant increase in the oxidation current, which shows the electrocatalytic activity of the modified electrodes towards the oxidation of glucose. A linear relationship between the glucose concentration and catalytic current is found in the range of 4 to 140 μM at the CuO/ZnO modified electrodes (Fig. 7.6C), with detection limit of 0.5 μM . The linear regression equation with a high correlation coefficient (R) of 0.998 is obtained, and the sensitivity estimated as 500 $\mu\text{A cm}^{-2} \text{mM}^{-1}$, over 6 fold higher than that for pure CuO ($\approx 84 \mu\text{A cm}^{-2} \text{mM}^{-1}$). It is possible that assembly CuO with ZnO to heterostructures, which the formation of a p-n junction could result in the extension of the space charge region, which locally narrows the conducting channel for the charge carriers in the ZnO, thus making the p-n junction more sensitive to glucose induced charge transfer. The application of CuO/ZnO for glucose sensors thus involves two types of sensing behavior: adsorption-induced surface depletion and chemical conversion with a change in the electrical potential. Another mechanism is that the heterostructures could expand the active area of CuO.

Reproducibility, selectivity and stability: To further test the performance, some characteristics tests on 2D porous CuO/ZnO nanosheets are performed. *First*, the intra-electrode and inter-

electrode reproducibility of 2D porous CuO/ZnO nanosheet for nonenzymatic glucose sensing were evaluated. The relative standard deviations (RSD) are no more than 8.7 % for the current response, indicating a satisfaction electrode-to-electrode reproducibility. Additionally, the RSD of 3.5% (S/N = 3) for 50 μ M of glucose demonstrates good single-electrode reproducibility. In order to explore the specific detection of glucose in real sample using the proposed approach based on 2D nanoporous CuO/ZnO nanosheet modified electrode, the I-t curve of 2D CuO/ZnO nanosheet modified GCE electrodes in 0.1 M NaOH solution by successive addition of 50 μ M of glucose and different interfering agents, as shown in Fig.7.6D. Some common interfering species in human serum, such as uric acid (UA), ascorbic acid (AA), dopamine acid (DA), nicotinamide adenine dinucleotide (NADH), Mg, K, Na and Ca ions, were chosen for tests. As clearly seen in Fig.7.6D, the current responses of interfering species have little effect compared to glucose, it is indicated that 10 times concentration interferences high in bloods is no response for detection 50 μ M glucose. The good selectivity of 2D nanoporous CuO/ZnO nanosheet against some reducing compounds, such as AA, can be ascribed to the obvious repulsion of negatively charged CuO and ZnO (the isoelectric point both are about 9.5) and the negatively charged AA (deprotonated) under highly basic conditions¹⁴. The good selectivity of 2D porous CuO/ZnO nanosheet electrodes for glucose and against other interfering materials can be ascribed to the synergetic action of well-designed 2D porous structure and high surface area structure, which provides maximum numbers of active free paths to the glucose molecules and facilitates faster electron transfer (electronic kinetics).

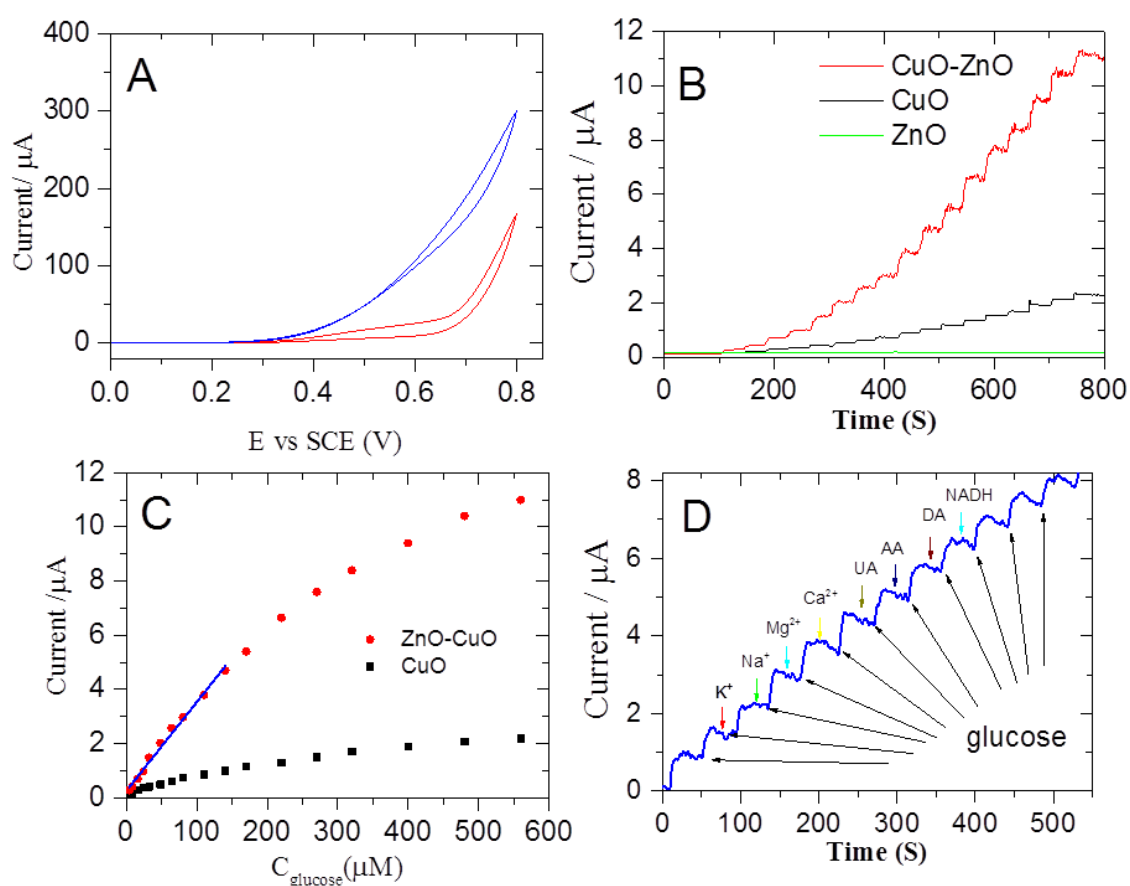


Fig. 7.6. (A) CVs of CuO/ZnO in 0.1 M NaOH (red line) and with 1 mM glucose (blue line) with a scan rate of 50 mV/s; (B) amperometric responses to glucose addition with the different concentrations, with the working electrode potential fixed at +0.6 V (vs SCE) in a stirred solution; (C) the calibration curve of the current response to glucose; and (D) amperometric responses to different interference and glucose addition with the CuO/ZnO modified electrode potential fixed at +0.6 V (vs SCE) in a stirred solution.

7.5 Conclusions

2D CuO/ZnO heterostructures were successfully synthesized via using graphene oxide paper as sacrificial template, display high porous and layer-by-layer structure. The resulting material shows high-performance towards detection of glucose in terms of sensitivity and selectivity. The material preparation method could be applied to prepare other 2D porous metal oxide nanosheets that can be used for non-enzymatic sensors, photocatalytic degradation of organic pollutants, and energy conversion and storage.

References

- 1 W. J. Park, K. J. Choi, M. H. Kim, B. H. Koo, J. L. Lee and J. M. Baik, *ACS Appl. Mater. Inter.*, 2013, **15**, 6802-6807.

- 2 M. M. Rahman, A. Jamal, S. B. Khan and M. Faisal, *ACS Appl. Mater. Inter.*, 2011, **4**, 1346-1351.
- 3 C. Karuppiyah, M. Velmurugan, S. M. Chen, S. H. Tsai, B. Lou, M. A. Ali and F. M. A. Al-Hemaid, *Sens. Actuator B-Chem.*, 2015, **221**, 1299-1306.
- 4 K. Khun, Z. H. Ibutopo, X. Liu, N. A. Mansor, A. P. F. Turner, V. Beni and M.J. Willander, *J. Nanosci. Nanotechnol.*, 2014, **9**, 6646-6652.
- 5 T. Soejima, K. Takada and S. Ito, *Appl. Surf. Sci.*, 2013, **277**, 192-200.
- 6 M. T. Qamar, M. Aslam, I. M. I. Ismail, N. Salah, A. Hameed, *ACS Appl. Mater. Inter.*, 2015, **16**, 8757-8769.
- 7 S. Kuriakose and B. Satpati, S. Mohapatra, *Phys. Chem. Chem. Phys.*, 2015, **38**, 25172-25181.
- 8 C. Zhang, L. Yin, L. Zhang, Y. Qi and N. Lun, *Mater. Lett.*, 2012, **1**, 303-307.
- 9 J. Sun, G. Yang, Y. Yoneyama and N. Tsubaki, *ACS Catal.*, 2014, **10**, 3346-3356.
- 10 T. Witoon, T. Permsirivanich, N. Kanjanasontorn, C. Akkaraphataworn, A. Seubsai, K. Faungnawakij, C. Warakulwit, M. Chareonpanich and J. Limtrakul, *Catal. Sci. Technol.*, 2015, **4**, 2347-2357.
- 11 A. Kargar, Y. Jing, S. J. Kim, C. T. Riley, X. Pan and D. Wang, *ACS Nano*, 2013, **12**, 11112-11120.
- 12 B.S. Kang, S. E. Ahn, M.J. Lee, G. Steftinovich, K.H. Kim, Y. Xian, W.X. Lee, Y. Park, I.G. Baek and B.H. Park, *Adv. Mater.*, 2008, **16**, 3066-3069.
- 13 B. Cai, Y. Zhou, M. Zhao, H. Cai, Z. Ye, L. Wang and J. Huang, *Appl. Phys. A-Mater.*, 2015, **3**, 989-996.
- 14 C. Zhou, L. Xu, J. Song, R. Xing, S. Xu, D. Liu and H. Song, *Sci. Rep.-UK*, 2014, **4**, 7382.
- 15 C. Wang, J. Zhu, S. Liang, H. Bi, Q. Han, X. Liu and X. Wang, *J. Mater. Chem. A*, 2014, **43**, 18635-18643.
- 16 A. Ghosh, B. B. Show, S. Ghosh, N. Mukherjee, G. Bhattacharya, S. K. Datta and A. Mondal, *RSC Adv.*, 2014, **93**, 51569-51575.
- 17 J. Chen, Y. Fu, Q. An, S. Lo, S. Huang, W. Hung, C. Hu, K. R. Lee and J. Lai, *Nanoscale*, 2013, **19**, 9081-9088.
- 18 B. G. Choi, Park, H.; T.J. Park, M.H. Yang, J.S. Kim, S. Y. Jang, N. S. Heo, S. Y. Lee, J. Kong and W.H. Hong, *ACS Nano*, 2010, **5**, 2910-2918.
- 19 S. Watcharotone, D. A. Dikin, S. Stankovich, R. Piner, I. Jung, G. H. B. Dommett, G. Evmenenko, S. Wu, S. Chen, C. Liu, S.T. Nguyen and R. S. Ruoff, *Nano Lett.*, 2007, **7**, 1888-1892.
- 20 M. Zhang, A. Halder, C. Hou, J. Ulstrup and Q. Chi, *Bioelectrochemistry*, 2016, **109**, 87-94.
- 21 J. Mu, C. Hou, H. Wang, Y. Li, Q. Zhang and M. Zhu, *Sci. Adv.*, 2015, **1**, e1500533
- 22 B. Zhan, C. Liu, H. Chen, H. Shi, L. Wang, P. Chen, W. Huang and X. Dong, *Nanoscale*, 2014, **6**, 7424-7429.
- 23 R. R. Nair, H. Wu, P. N. Jayaram, I. V. Grigorieva and A. K. Geim, *Science*, 2012, **335**, 442-444.

Chapter 8. Graphene oxide templated synthesis of nickel oxide nanosheets for enzymeless detection of urea

8.1 Introduction

Control and regulation of metabolic end products is very important for a healthy human life. Urea is one of the most concerned compounds in the human metabolism. Therefore, monitoring of the urea amount in different products is very essential for the agricultural and environmental industries. Urea is also an important industrial chemical widely used in fertilizers as a source of nitrogen and is an important raw material for the chemical industry. Due to its high nitrogen level (46% nitrogen by mass), urea has been illegally added into feed stuffs and foods to artificially boost their crude protein content since the protein levels are estimated by the conventional standard Kjeldahl or Dumas tests without identifying nitrogen sources. An increase in the urea level (the normal range in blood is 15–40 mg dL⁻¹) causes renal failure, urinary tract obstruction, dehydration, shock, burns, gastrointestinal bleeding, etc. Traditionally, different types of analysis means have been developed for melamine detection, such as high-performance liquid chromatography (HPLC), liquid chromatography/mass spectrometry (LC-MS), gas chromatography/mass spectrometry (GC-MS), enzyme-linked immunosorbent assay (ELISA) and capillary electrophoresis. These methods could have high sensitivity and good accuracy, but require complicated and time-consuming steps, expensive instrumentation and specific skills for operation, which limit their wide applications. Therefore, developing a rapid, simple, convenient and sensitive method for the determination of urea has become increasingly important. Although there are several reports^{1, 2} of enzyme based biosensors for urea detection, but they suffer from major drawbacks due to high cost of enzymes and lack of long-term stability. Development of a sensitive, selective, reliable and low-cost material based biosensor is of great importance for the diagnosis and management of urea. In recent years nanomaterial based electrochemical biosensors have attracted wide popularity and applicability due to their good selectivity, portability, inexpensiveness and simplicity^{3,4}.

Non-enzymatic biosensors with metal oxide based electrocatalysts have received widespread interest for the high sensitivity and stability of the sensing responses⁵. Different low-cost metal oxides such as NiO, CuO, ZnO, and Co₃O₄ with well-defined redox properties⁶, have been employed for direct electrocatalytic oxidation and determination of many biochemically important compounds such as urea, glucose, and dopamine^{6, 7}. In particular, Ni-based catalysts have exhibited

excellent catalytic abilities for different biosensing applications⁸⁻¹³. However, most of sensor platforms had to attach the nanostructure to a conductive supporting substrate such as graphene, carbon nanotube and ITO to enhance the current signal. Detection of urea by using conductive supporting agent free 2D NiO nanosheet was not previously reported. This work aims to introduce NiO nanosheet based electrochemical sensor for the detection of urea. In our report, layer-by-layer nanoporous 2D NiO nanosheet was prepared by using graphene oxide paper as a sacrificial template and assembled into conductive agent-free electrochemical sensor for detection of urea. Ni²⁺ was loaded on graphene oxide paper via electrostatic attraction between oxygen-containing groups and adsorbed cations. During high-temperature annealing process in air atmosphere, NiO nucleation and crystal growth were proceeded to produce a highly porous NiO nanosheet. This is due to the space-confined synthesis. D-spacing of interlayers in the graphene paper enables to restrict the MO growth in the Z axis, leading to the X- and Y-direction expansion to form 2D ultrathin nanosheets. After removing graphene oxide template by high-temperature heating, the NiO could retain layer-by-layer and ultrathin structural features duplicated from graphene oxide paper, meanwhile the nanopores were introduced. Moreover, the resulting material is ultralight with a density of 70 mg cm⁻³ approximately 10 times lighter than most commercial NiO products.

8.2 Experimental section

Preparation of 2D porous NiO nanosheets: Graphene oxide (GO) paper was used as a template for the synthesis of 2D nickel oxide nanosheets. GO was synthesized by a previously reported method by our group¹⁴. The GO paper was fabricated by using vacuum filtration of GO solutions and further dried in room temperature. Then, the GO paper was immersed in 0.1 M Ni²⁺ solution for 48 h, and washed carefully with Milli-Q water. After that, the sample was heated from room temperature to 500 °C at a rate of 10°C min⁻¹ and maintained at 500 °C for 4 h under air atmosphere. After cooling to room temperature, paper-like sample was collected and was directly characterized by SEM. The sample was dispersed in ultrapure ethanol by sonication and further drop-cast on different substrates for structural characterizations by TEM, XRD, XPS as well as such sample was used for electrochemical measurements.

8.3 Results and discussion

8.3.1 Synthesis of 2D nanoporous NiO nanosheets

Graphene-like 2D materials with few nanometers thickness and several micro-meters of lateral size have attracted huge attention in recent years. Owing to large surface-to-volume ratio and the quantum-confinement effect, these few atom thick 2D nanosheets exhibited unique physical and chemical properties different from the bulk materials¹⁵. Consequently, these 2D nanomaterials have shown their wide range of applications in sensing, solar cells, energy-storing devices, photocatalytic systems, and others¹⁶⁻¹⁹. In General, there are two different ways for the synthesis of 2D nanosheets, i.e. one is top-down approach and the other is bottom-up approach. In top-down approaches, 2D nanosheets are exfoliated from the bulk crystal materials by using chemical reactions or mechanical force²⁰⁻²¹. In bottom-up approaches, 2D nanosheets are grown by directly starting from atoms, ions, or molecules. Top-down approaches are very popular and well-established in this regard due to their simple synthetic strategies. And most of the recently developed 2D materials are first prepared by the exfoliation from their bulk material. However, the major challenge is to synthesize a 2D material from non-layer layer structured bulk material²². Bottom-up approaches can be an ideal way to face this challenge. And choice of an ideal 2D template for the synthesis of 2D nanostructures is very significant in this regard. In this work, taking NiO as an example, we establish the bottom-up synthesis of 2D NiO nanosheets by using graphene paper as a template.

In our bottom-up synthesis procedure, we chose graphene oxide (GO) paper as the 2D template, and designed a new synthesis route following which NiO can duplicate the shape of 2D GO paper. GO has widely been used as the template for the growth and self-assembly of various inorganic nanomaterials^{5, 6}, but for most of the cases the resulting products were usually composed of nanoparticles loaded on the GO sheets based composites. However, the ideal duplication of 2D nanostructure of GO has not been achieved. Using our method, uniform 2D NiO nanosheets with a lateral size of only ≈ 50 nm were successfully prepared by using GO paper template. For the bottom-up synthesis of 2D NiO based on GO paper, thin layer of acetate of nickel was deposited on the GO paper in the solution and form a composite. Next, GO was removed from the composite by calcination at 500 °C, while the acetate of nickel was converted into the 2D NiO sheets. GO paper acts as a superior 2D template to direct the growth and self-assembly of nickel oxide due to its high dispersibility in water, and availability of a large number of oxygen-containing functional groups,

which provide strong attraction to the inorganic materials. As an example of the improved characteristic of 2D -NiO nanosheets, they were used for electrochemical sensing of urea, and showed much higher sensitivity compared with other materials.

8.3.2 Structural characterization of nanosheets

The as-prepared 2D NiO nanosheets were analyzed by X-ray diffraction technique to get the information about their crystal structures. Fig. 8.1A shows the X-ray diffraction (XRD) patterns of the 2D NiO nanosheets. The diffraction peaks at $2\theta = 37.2^\circ$, 43.2° , and 62.6° are corresponding to the (1 1 1), (2 0 0), (2 2 0) planes of the 2D structure of NiO sheets, respectively. No impurity-phase peak was detected, suggesting that the product is highly pure NiO crystals.

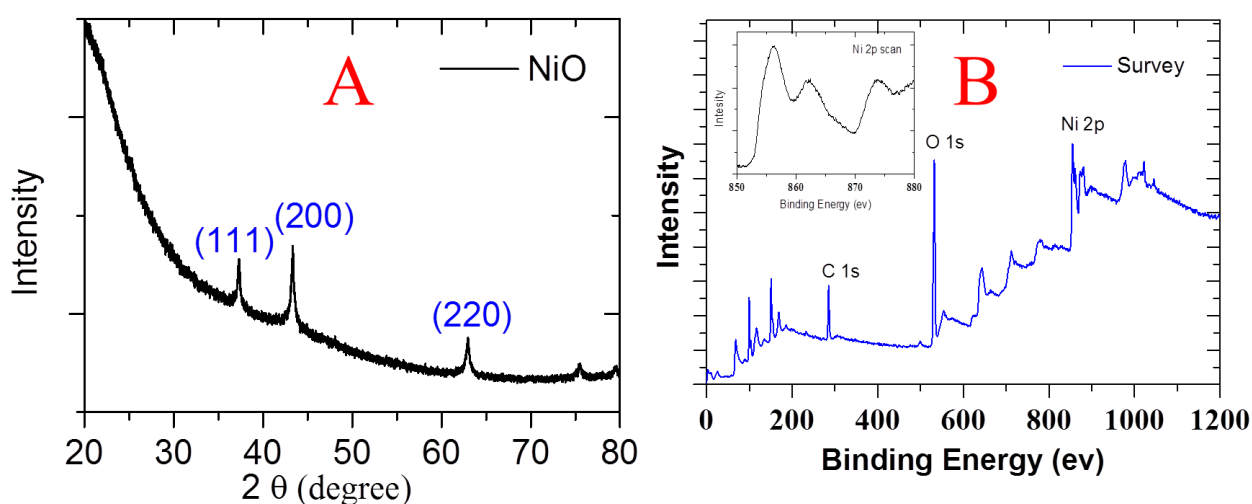


Fig. 8.1. XRD pattern (A) and XPS spectrum (B) of 2D NiO nanosheets. Inset is the expanded view of Ni 2p peak.

X-ray photoelectron spectroscopy (XPS) was also carried out to investigate the chemical states of bonded elements in the 2D NiO nanosheets. As shown in Fig. 8.1B, the survey XPS spectrum displays a set of peaks corresponding to C 1s, O 1s, and Ni 2p bindings, respectively. It should be noted that C 1s (285.1 eV) is ascribed to a carbon-based substrate, which is an indication remaining part of the sacrificial GO template. The peak at ~531.6 eV and ~855.7 eV are attributed to O 1s and Ni 2p spectra from NiO nanosheets.

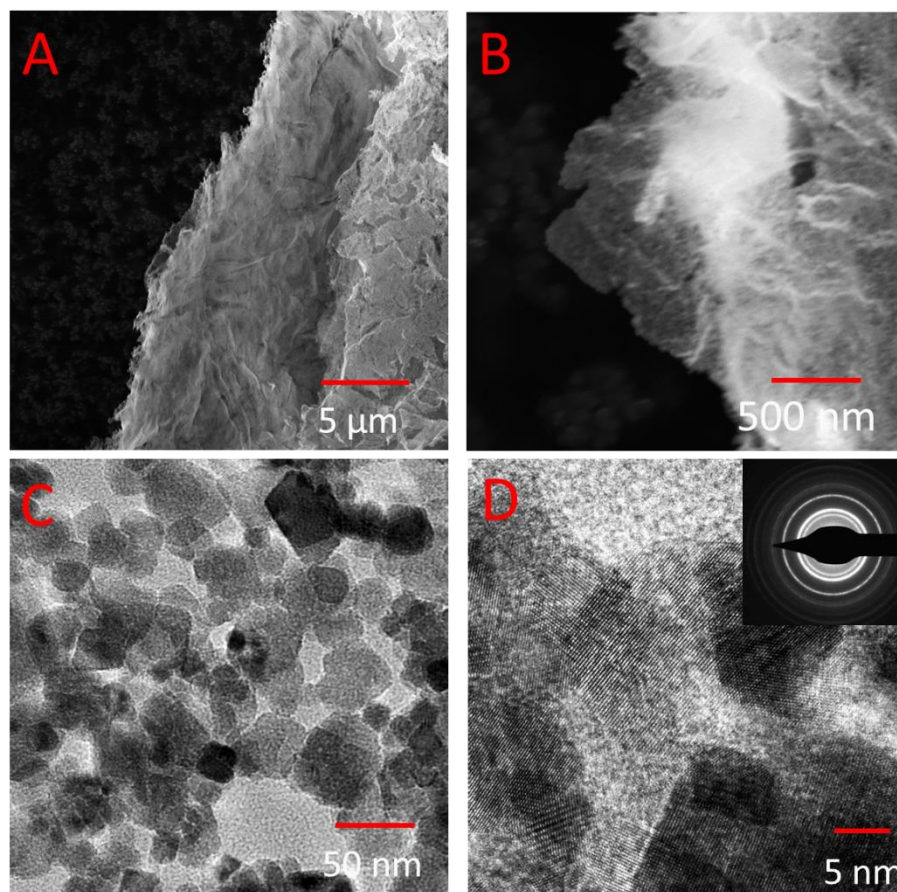


Fig. 8.2. (A) Low and (B) high magnification SEM images of 2D NiO nanosheets, (C) HRTEM image of 2D NiO nanosheets, (D) HRTEM image and SAED pattern of 2D NiO nanosheets

SEM and TEM were performed to characterize the structure and the morphology of the as-synthesized 2D-NiO nanosheets. Fig. 8.2A and B show the SEM images to reveal the layered and porous structures. Fig. 8.2C shows a typical TEM image of 2D NiO nanosheets. It is clearly seen from the pictures that all the 2D nanosheets are ≈ 50 nm in the lateral dimension. And the high resolution TEM (HRTEM) image (Fig. 8.2D) shows the transparent nature of the nanosheets. The inset in Fig. 8.2D displays selected area electron diffraction (SAED) patterns of NiO nanosheets. Consistent with the XRD results, several well-defined rings corresponding to the certain diffraction planes of NiO are found, suggesting that the NiO nanosheets have a well-defined crystalline structure. According to the HRTEM image (Fig. 8.2D), moreover, the building blocks of NiO nanosheets are consisting of numerous NiO nanocrystals with a well-defined lattice spacing of 0.28 nm corresponding to the (1 1 1) lattice plane of NiO. The NiO nanosheets were further analyzed by taking elemental mapping images to evaluate the element distribution (Fig. 8.3B-D), which further supports the layered structural feature of NiO nanosheets.

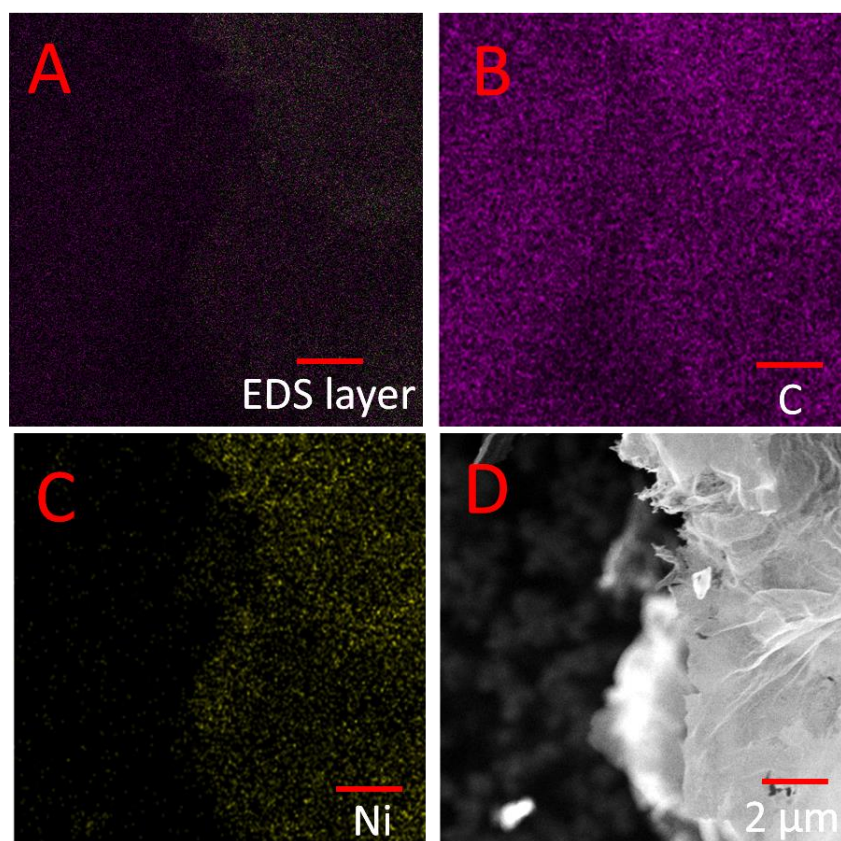


Fig. 8.3. (A) SEM image of 2D NiO nanosheets, (B) EDS mapping of the corresponding SEM image (A) of 2D NiO nanosheets, (C) Carbon elemental mapping, (D) Nickel elemental mapping.

8.3.3 Electrochemical characterization of 2D NiO nanosheets

Figure 8.4 represents the cyclic voltammograms (CVs) of the NiO nanosheets modified glass carbon in argon saturated 0.1 M NaOH solution at a scan rate from 10 to 300 mV s^{-1} . 2D NiO nanosheets display a pair of well-defined redox peaks with anodic peak and cathodic peak at +0.47 V and +0.42 V (vs SCE), respectively. Apparently, the NiO nanosheets show much better electrochemical activity with the smaller peak potential separation of 50 mV. The couple of peaks are recognized as the redox reaction of $\text{Ni}^{2+}/\text{Ni}^{3+}$ couple on the electrode surface in the medium^{23,24}. From Fig. 8.4A, it is clearly seen that the anodic peak has a positive shift and the cathodic peak has a slight negative shift with increasing scan rate. This fact indicates a quasi-reversible electron transfer for the electrochemical reaction. Moreover, the relationship between peak currents (I_p) and scan rate (v) was evaluated by a series of plots of I_p versus v^x with $x = 0.5-1.0$. The best linear fit (i.e., with the best regression coefficient (R)) is achieved for $x = 0.7$, demonstrating that both

surface and diffusion control electrochemical processes are involved here, due to the nanoporous structural nature of 2D NiO nanosheets.

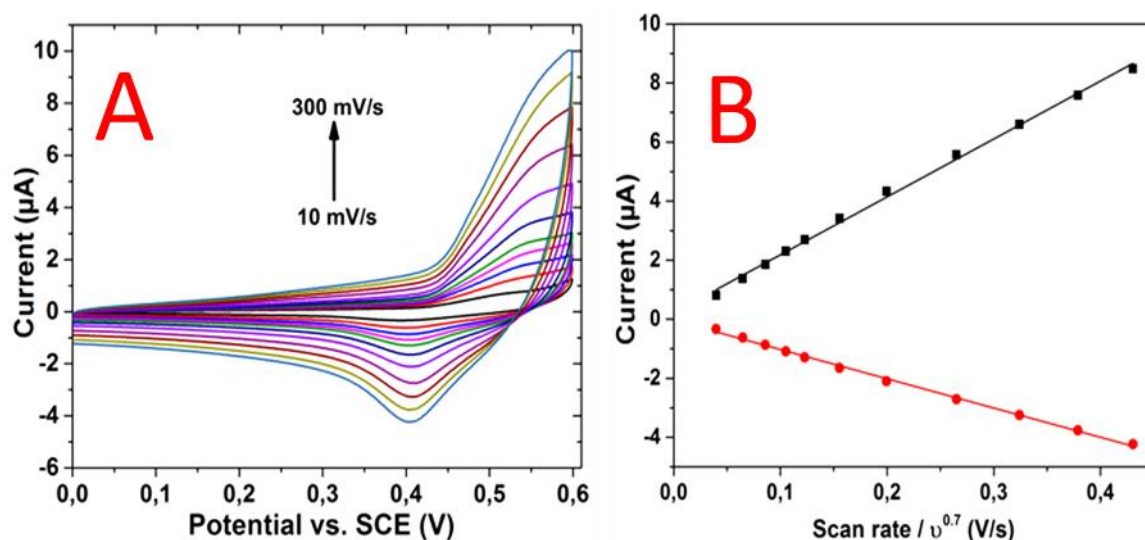
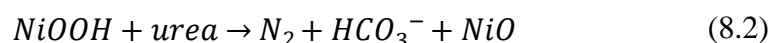


Fig. 8.4. (A) CVs of the 2D NiO nanosheets/GCE electrode in 0.1 M NaOH electrolyte with different scan rates, (B) Relationship between the redox peak current and scan rate.

8.3.4 Non-enzymatic urea sensing response

The CV technique was used to investigate the electrochemical behavior of the 2D-NiO nanosheets/GCE in 0.1 M NaOH without and with the presence of urea. The presence of redox peak from the cyclic voltammogram of 2D NiO nanosheets/GCE in presence of urea is a clear indication for the feasibility of electrocatalytic oxidation of urea on this electrode. After the addition of urea into the electrolyte solution, the anodic peak current exhibited a remarkable increase accompanying with a slight positive shift of anodic peak potential, and a decrease of the cathodic peak (Fig. 8.5A), suggesting excellent electrocatalytic activity of 2D NiO nanosheets towards urea oxidation. The oxidation of urea was electrocatalyzed by the $\text{Ni}^{2+}/\text{Ni}^{3+}$ redox couple as described in eq. (8.1) and eq. (8.2).



The electro-oxidation of urea consumes Ni^{3+} and further helps in the slight decrease of cathodic peak current. On the other side, the oxidation of urea on electrode surface would certainly induce

adsorption of urea and the oxidized intermediates on active sites of 2D-NiO nanosheets, which may sluggish the kinetics of the redox reaction and give rise to a slight positive shift of the anodic peak²⁴.

For amperometric sensing measurements, the change of current is continuously measured with the addition of analyte at a constant potential. The electrochemical sensing performance of 2D-NiO nanosheets/GCE sensor was evaluated here by amperometric measurements. The amperometric response of the 2D-NiO nanosheets /GCE sensor to the successive step-wise addition of urea was carried out at an applied potential of 0.5 V. Fig.8.5Ba shows a typical current-time plot of the as prepared sensing material on successive addition of urea. As the urea was added into the stirring buffer solution, the sensor responded rapidly to the substrates. Fast response was obtained after each addition of analyte. The response was highly stable, and the increase periodically in the current was obtained. The amperometric response was saturated for higher concentration of urea. The non-enzymatic urea biosensor could response linearly from 4.4 to 181.6 μM and it has a dynamic concentration range from 4.4 to 513.4 μM (Fig. 8.5C).

8.3.5 Interference study

Selectivity is one of the most important characteristics in evaluating the overall performance of an electrochemical sensor. The possible interference from various organic and ionic species related to urea detection was investigated for 2D NiO nanosheets based electrodes. In the sample analysis, co-existence of other electroactive species, such as ascorbic acid (AA), glucose, and dopamine (DA), might affect the detection of urea. Therefore, the effects of interfering species (e.g., DA, AA, Na, K, Ca, Mg, Vitamin C and Glucose) on the 2D-NiO nanosheets /GCE sensor were examined at their physiological concentration. From the amperometric analysis, the current responses of interfering species have little effect compared to glucose, it is indicated that 250 μM of AA, DA, Na, K, Ca, Mg and 25 μM glucose no response for detection 25 μM urea. Which indicated that the 2D NiO nanosheets based electrodes are quite stable for the detection of urea without detectable interference from these species (Fig. 8.5D).

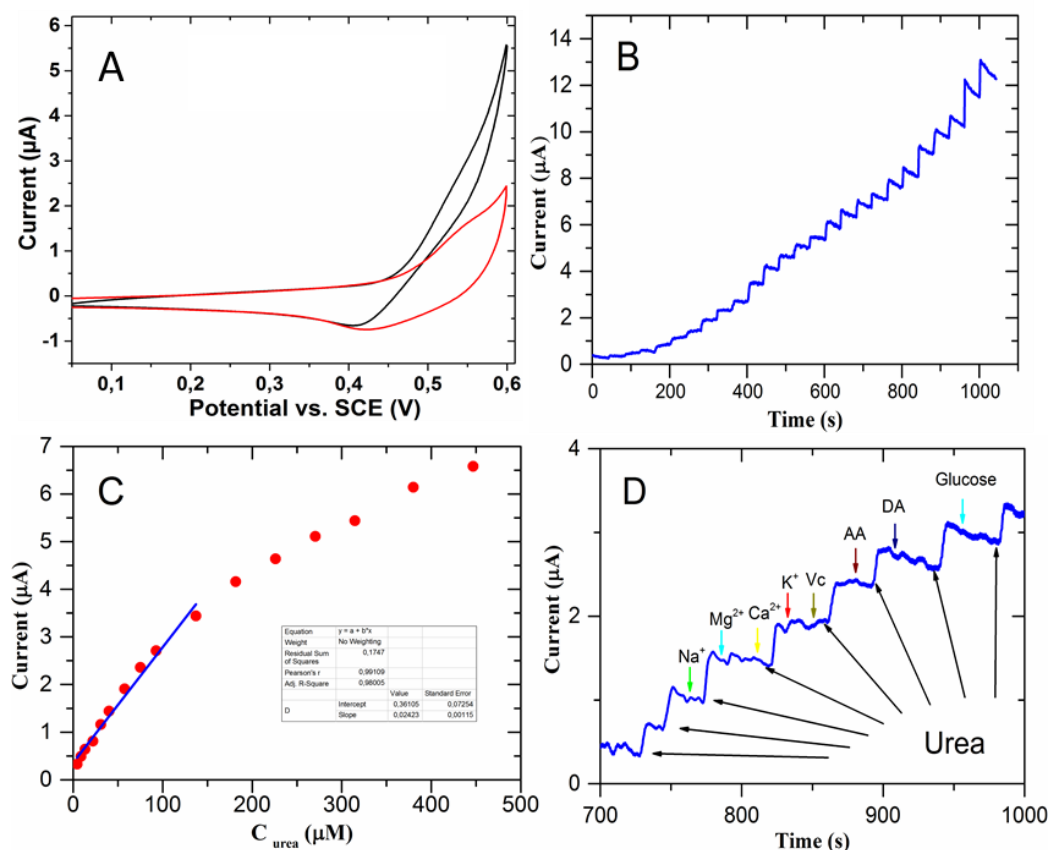


Fig. 8.5. (A) CVs of the 2D NiO nanosheets/GCE electrode in 0.1 M NaOH electrolyte in the absence (red curve) and presence (black curve) of urea. (B) Amperometric $i-t$ curve for the response to successive addition of urea into the electrolyte solution. (C) Calibration plot of the urea concentration vs current. (D) The amperometric response to the addition of 25 μM urea and different interfering species with specific concentrations (the concentration of AA, DA, Na, K, Ca and Mg is 250 μM ; VC and glucose 25 μM).

8.4 Conclusions

In summary, a simple and low-cost method has been developed to synthesize 2D NiO nanosheets with graphene oxide paper as a template. The as-prepared 2D NiO nanosheets was successfully utilized for the fabrication of an enzymeless electrochemical urea sensor, which showed advantages of high sensitivity, fast response time, and good stability for non-enzymatic determination of urea. The simple bottom-up preparation procedure using GO paper and enhanced electrocatalytic performance could potentially pave the way for materials preparation and construction of inexpensive, reproducible, and highly sensitive urea sensors.

References

- 1 T. Ghosh, P. Sarkar, A. P. F. Turner, *Bioelectrochemistry*, 2015, **102**, 1–9.

- 2 R. S. Dey, S. Gupta, R. Paira and C. R. Raj, *ACS Appl. Mater. Inter.*, 2010, **2**, 1355–1360.
- 3 M. Zhang, A. Halder, C. Hou, J. Ulstrup and Q. Chi, *Bioelectrochemistry*, 2016, **109**, 87–94.
- 4 M. Zhang, C. Hou, A. Halder, J. Ulstrup and Q. Chi, *Biosens. Bioelectron.*, 2017, **87**, 570–577
- 5 K. Shavanova, Y. Bakakina, I. Burkova and I. Shtpliuk, *Sensors*, 2016, **16**, 223.
- 6 Y. Lin, J. Ren and X. Qu, *Acc. Chem. Res.*, 2014, **47**, 1097–105.
- 7 Y. Mu, D. Jia, Y. He, Y. Miao and H. Wu, *Biosens. Bioelectron.*, 2011, **26**, 2948–2952.
- 8 M. Wu, S. Meng, Q. Wang, W. Si, W. Huang and X. Dong, *ACS Appl. Mater. Inter.*, 2015, **7**, 21089–21904.
- 9 B. Yuan, C. Xu, D. Deng, Y. Xing, L. Liu, H. Pang and D. Zhang, *Electrochim. Acta*, 2013, **88**, 708–712.
- 10 Y. Zhang, Y. Wang, J. Jia and J. Wang, *Sens. Actuators B Chem.*, 2012, **171**, 580–587.
- 11 X. Zhu, Q. Jiao, C. Zhang, X. Zuo, Y. Liang and J. Nan, *Microchim. Acta*, 2013, **180**, 477–483.
- 12 Y. Zhang, X. Xiao, Y. Sun, Y. Shi, Z. Li and L. Wang, *Electroanalysis*, 2013, **25**, 959–966.
- 13 Z. Wang, Y. Hu, W. Yang, M. Zhou and X. Hu, *Sensors*, 2012, **12**, 4860–4869.
- 14 N. Zhu, S. Han, S. Gan, J. Ulstrup and Q. Chi, *Adv. Funct. Mater.*, 2013, **23**, 5297–5306.
- 15 Z. Huang, A. Zhou, J. Wu, Y. Chen, X. Lan, H. Bai and L. Li, *Adv. Mater.*, 2016, **28**, 1703–1708.
- 16 C. Lin, Y. Lai, H. Chen, J. Chen, C. Kung, R. Vittal and K. Ho, *Energy Environ. Sci.*, 2011, **4**, 3448–3455.
- 17 J. Zhu, L. Cao, Y. Wu, Y. Gong, Z. Liu, H. Hoster, Y. Zhang, S. Yang, Q. Yan and P. Ajayan, *Nano Lett.*, 2013, **13**, 5408–5413.
- 18 P. Niu, L. Zhang, G. Liu and H. Cheng, *Adv. Funct. Mater.*, 2012, **22**, 4763–4770.
- 19 X. Huang, C. Tan, Z. Yin and H. Zhang, *Adv. Mater.*, 2014, **26**, 2185–2204.
- 20 Z. Zeng, Z. Yin, X. Huang, Q. He, G. Gu and H. Zhang, *Angew. Chemie Int. Ed.*, 2011, **50**, 11093–11097.
- 21 Z. Q. Sun, T. Liao, Y. Dou, S. Hwang, M. Park, L. Jiang, J. Kim and S. Dou, *Nat Commun.*, 2014, **5**, 3813.
- 22 C. Tan and H. Zhang, *Nat. Commun.*, 2015, **6**, 7873.
- 23 S. Ci. T. Huang, Z. Wen, S. Cui, S. Mao, D. Steeber and J. Chen, *Biosens. Bioelectron.*, 2014, **54**, 251–257.
- 24 L. Zheng, J. Zhang and J. Song, *Electrochim. Acta*, 2009, **54**, 4559–4565.

Appendix A. Characterization data of GO material

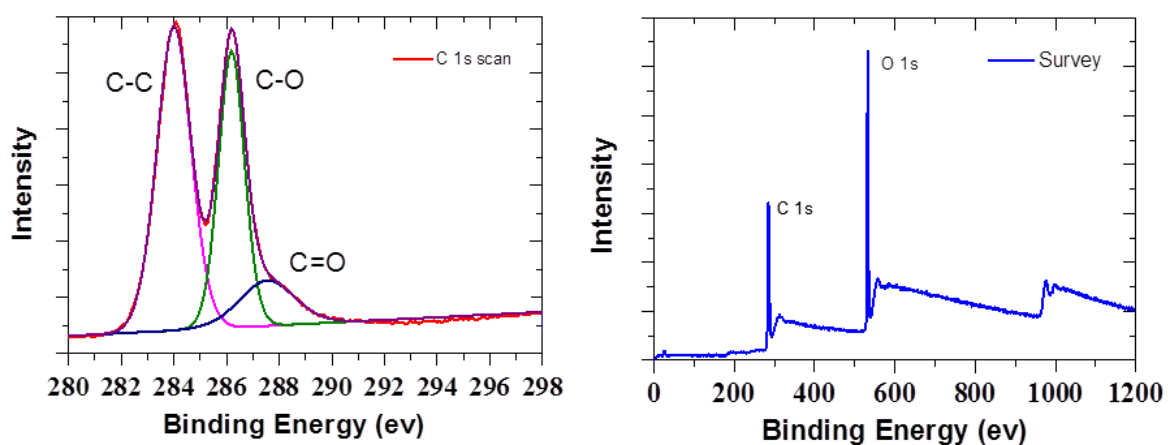


Figure S1. XPS spectra of pure GO: C 1s scan (left) and survey spectrum (right).

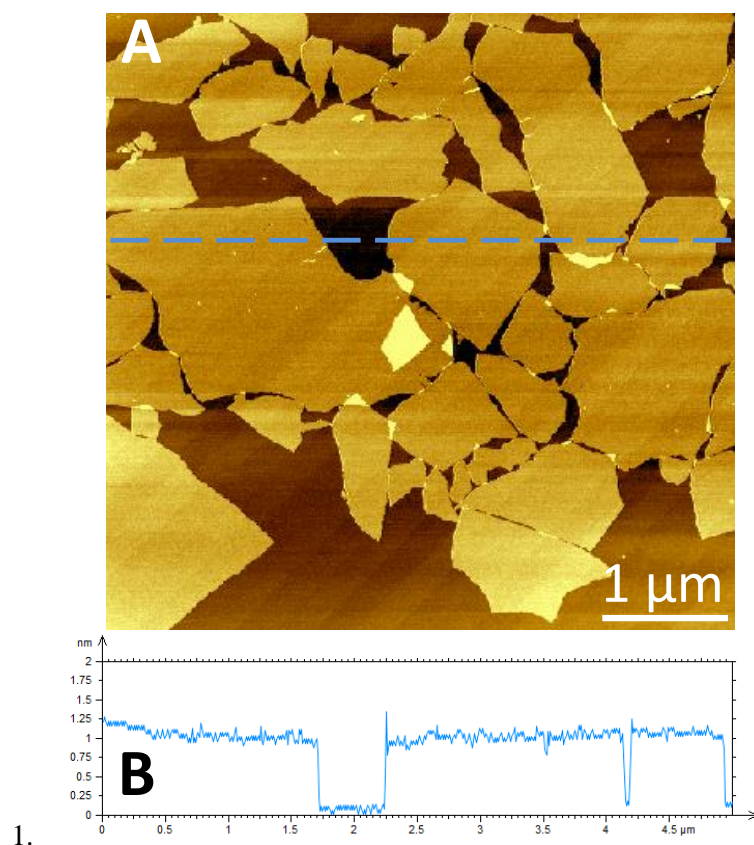


Figure S2. (A) AFM image of GO nanosheets and (B) cross-sectional profile corresponding to the line marked in the AFM image (A).

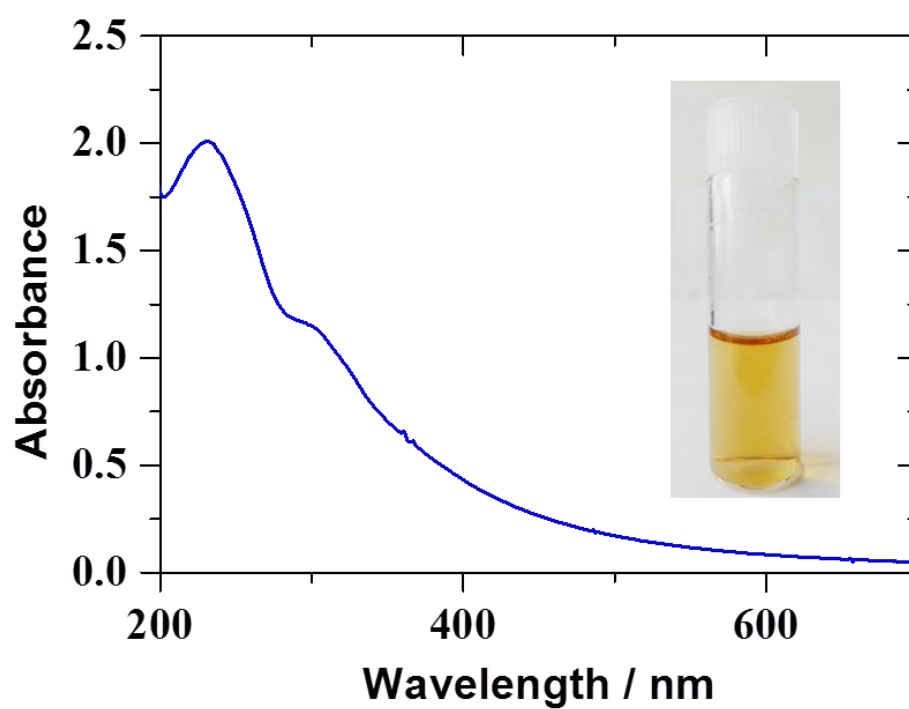


Figure S3. UV-vis spectrum of graphene oxide solution, and insert shows digital photographs of GO

Appendix B. Publication and dissemination

Only the publications accomplished during the PhD study are included.

1. Peer-reviewed journal articles published or accepted

1. Zhang MW, Halder A, Hou CY, Ulstrup J, Chi QJ. *Interlocked graphene–Prussian blue hybrid composites enable multifunctional electrochemical applications*. ***Biosensors & Bioelectronics***, 2017, 89, 570-577. (IF: 7.47)
2. Zhang MW, Hou CY, Halder A, Chi QJ. *Graphene papers: smart architecture and specific functionalization for biomimetics, electrocatalytic sensing and energy storage*. ***Materials Chemistry Frontiers***, 2017, 1, 37-60.
3. Zhang MW, Hou CY, Halder A, Chi QJ. *Ultralight, flexible and semi-transparent metal oxide papers for photoelectrochemical water splitting*. ***ACS Applied Materials & Interfaces***, 2017, 9, DOI: 10.1021/acsami.6b14036. (IF: 7.15)
4. Zhang MW, Halder A, Hou CY, Ulstrup J, Chi QJ. *Free-standing and flexible graphene papers as disposable non-enzymatic electrochemical sensors*. ***Bioelectrochemistry*** 2016, 109, 87-94. (IF: 4.17)
5. Halder A, Zhang MW, Chi QJ. *Graphene-metal oxide hybrid nanostructured materials for electrocatalytic sensing and sustainable energy storage*. ***Review in Advanced Sciences and Engineering***, 2016, 5, 4-31. (Co-the first author, equal contribution)
6. Hou CY, Zhang MW, Kasama T, Engelbrekt C, Zhang LL, Wang HZ, Chi QJ. *Reagent-free synthesis and plasmonic antioxidation of unique nanostructured metal-metal oxide core-shell microfibers*. ***Advanced Materials***, 2016, 28, 4097-4104. (IF: 18.96)
7. Hou CY, Zhang MW, Zhang LL, Tang YY, Wang HZ, Chi QJ. *Reagent-free electrophoretic synthesis of few-atom-thick metal oxide nanosheets*. ***Chemistry of Materials***, 2017, DOI: 10.1021/acs.chemmater.7b00188. (IF: 9.41) (This work was highlighted by ChemistryViews: [http://www.chemistryviews.org/details/news/10461439/Fast and Green Way to Metal-Oxide Nanosheets.html#.WJhEazfZWqw.email](http://www.chemistryviews.org/details/news/10461439/Fast_and_Green_Way_to_Metal-Oxide_Nanosheets.html#.WJhEazfZWqw.email))
8. Halder A, Zhang MW, Chi QJ. *Electroactive and biocompatible functionalization of graphene for the development of biosensing platforms*. ***Biosensors & Bioelectronics***, 2017, 87, 764-771 (IF: 7.47)
9. Guo F, Chen J, Zhang MW, Gao BF, Lin BZ, Chen YL, *Deprotonation of g-C₃N₄ with Na*

- ions for efficient non sacrificial water splitting under visible light. *Journal of Materials Chemistry A*, 2016, 4, 10806-10809. (IF: 8.26)
10. Rui YC, Wang YQ, Zhang QH, Chi QJ, Zhang MW, Wang HZ, Li YG, Hou CY, *In-situ construction of three-dimensional titania network on Ti foil toward enhanced performance of flexible dye-sensitized solar cells. Applied Surface Science*, 2016, 380, 210-217. (IF: 3.15).
 11. Li HZ, Wang JM, Shi QW, Zhang MW, Hou CY, Shi GY, Wang HZ, Zhang QH, Li YG, Chi QJ *Constructing three-dimensional quasi-vertical nanosheet architectures from self-assemble two-dimensional $WO_3 \cdot 2H_2O$ for efficient electrochromic devices. Applied Surface Science*, 2016, 380, 281-287. (IF: 3.15).
 12. Huang W, Xiao XX, Engelbrekt C, Zhang MW, Ulstrup J, Ci LJ, Feng JK, Si PC, Chi QJ. *Graphene encapsulated Fe_3O_4 nanorods assembled into a mesoporous hybrid composite used as high-performance lithium-ion battery anode material. Materials Chemistry Frontiers*, 2017, DOI: 10.1039/C6QM00252H.
 13. Hou C, Zhang MW, Halder A, Chi QJ. *Graphene templated nanostructures for multifunctional electrochemical applications. Electrochim. Acta*, 2017, accepted for publication. (IF: 4.80).

2. Book Chapters

1. Hou C, Zhang MW, Chi QJ. *Design, Assembly, and Fabrication of Two-Dimensional Nanomaterials into Functional Biomimetic Device Systems*. In "Two-dimensional Materials - Synthesis, Characterization and Potential Applications". Chapter 11: pp 247-270; InTech Press, August 2016.
2. Halder A, Zhang MW, Chi QJ. *Electrocatalytic applications of graphene-metal oxide nanohybrid materials*. In "Advanced Catalytic Materials", ISBN 978-953-51-4596-7 (Edited by Luis Enrique Noreña Franco), Chapter 14: pp379-413; InTech Press, March 2016.
3. Zhang MW, Halder A, Cao XY, Hou C, Chi QJ. *Graphene paper based electrochemical sensors*. In "Electrochemical Sensors", ISBN 978-953-51-5287-3, 2017, accepted in press.

3. International conference contributions

1. Zhang MW, Ulstrup J, Chi QJ. *One-step Facile Functionalization of Graphene for Highly Active Electrocatalysis*. XXIII International Symposium on Bioelectrochemistry and Bioenergetics, 2015 Sweden (poster presentation).

2. Zhang MW, Ulstrup J, Chi QJ. *Microwave-assisted synthesis of graphene-Prussian Blue networked nanocomposites for electrocatalysis*. The 6th Symposium on Carbon and Related Nanomaterials, 2015 Denmark (**poster presentation**).
3. Zhang MW, Halder A, Hou CY, Chi JQ. *Nanoparticle functionalized and sandwich structured graphene papers as flexible electrochemical sensors*. The 67th ISE Annual meeting, 2016 Hoge, Netherlands. (**Oral presentation**)
4. Chi Q, Zhang MW, Halder A, Hou C. *Electrochemical nanomaterials synthesized using graphene as scaffolds or templates for analytical and sensing applications*. In *ISE (International Society of Electrochemistry) Annual meeting 2016, August 2016, Hague, Netherlands*. (**Invited talk for Chi QJ**)
5. Hou C, Zhang MW, Engelbrekt C, Chi QJ. *Reagent-free electrolytic synthesis of metal-metal oxide core-shell microfibers with plasmonic anti-oxidation functionality*. In *ISE Annual meeting 2016, Hague, Netherlands*. (**Poster presentation by Hou C**)
6. Halder A, Zhang MW, Chi QJ. *Electroactive polymer functionalized graphene nanocomposites as a biosensing platform*. In *Biosensors 2016-26th Anniversary World Congress on Biosensors, April 2016, Göthenburg, Sweden*. (**Poster presentation by Halder A**)

4. Manuscripts in submission or preparation

14. Zhang MW, Hou CY, Halder A, Chi, QJ. *Graphene paper as template to synthesis, layer-by-layer nanoporous CuO/ZnO 2D nanosheet for ultrasensitive non-enzymatic sensor for detection of glucose and environmental application*. (in submission)
15. Halder A, Zhang MW, Hou CY, Chi, QJ. *Conductive agent-free nanoporous nickel oxide as non-enzymatic sensor for detection of urea*. (the co-first author, in submission)
16. Zhang MW, Cao XY, Engelbrekt C, Hou CY, Chi, QJ. *Self-controlled formation and size-dependent electrocatalysis of Au@PB core/shell nanoparticles*. (in preparation)
17. Zhang MW, Hou CY, Halder A, Chi, QJ. *Graphene paper as a template for synthesis of porous Co nanosheets as a high efficient electrocatalyst*. (in preparation)
18. Halder A, Zhang MW, Olsen G, Chi QJ. *Biocompatible electroactive engineering graphene with dopamine for highly sensitive detection of melamine*. (in preparation)
19. Xiao XX, Engelbrekt C, Zhang MW, Li ZS, Ulstrup J, Zhang JD, Si PC, *Facile synthesis of tungsten disulfide/poly(3,4-ethylenedioxythiophene) composites on nanoporous gold and its electrochemical catalysis of the dihydrogen evolution*. (in submission)

-
20. Sun HY, Zhang MW, Mujtaba J, Yesibolati MN, Canepa S, Zhang JD, Norby P, Mølhave K, Zhu J. *Modulation of Oxygen Vacancies in Hierarchical Co₃O₄ Mesoporous Nanostructures for Electrochemical Applications in Lithium Storage and Oxygen Evolution Reaction.* (in submission)

Appendix C. The first pages of six peer-reviewed articles

1. *Materials Chemistry Frontiers*
2. *Biosensors & Bioelectronics*
3. *ACS Applied Materials & Interfaces*
4. *Bioelectrochemistry*
5. *Advanced Materials*
6. *Chemistry of Materials*

REVIEW

CrossMark
click for updatesCite this: *Mater. Chem. Front.*,
2017, 1, 37

Graphene papers: smart architecture and specific functionalization for biomimetics, electrocatalytic sensing and energy storage

Minwei Zhang,^{†a} Chengyi Hou,^{†ab} Arnab Halder,^a Hongzhi Wang^{*b} and Qijin Chi^{*a}

Paper is an attractively assembled form of materials and has accompanied our daily life almost everywhere. Two-dimensional layered materials, especially graphene, have unique intrinsic structures to be exploited for smart architecture of macroscopic papers that are offering many newly emerging applications. Research advances in graphene based papers in the past few years have created a new category of composite materials. This review aims at offering an up-to-date comprehensive summary of graphene-supported papers, with the emphasis on smart assembly and purpose-driven specific functionalization for their critical applications associated with sensing, environmental and energy technologies. The contents of this review are based on a balance combination of our own studies and selected research studies done by worldwide academic groups. We first give a brief introduction to graphene as a versatile building block and to the current status of research studies on graphene papers. This is followed by addressing some crucial methods of how to prepare graphene papers. We then summarize multiple possibilities of functionalizing graphene papers, membranes or films. Finally, we evaluate some key applications of graphene papers in the areas of chemical/electrochemical sensors, biomimetics and energy storage devices, just before leading to our concluding remarks and perspectives.

Received 28th July 2016,
Accepted 11th September 2016

DOI: 10.1039/c6qm00145a

rsc.li/frontiers-materials

1. Introduction

Graphene has attracted much attention from researchers, from physicists, chemists to material scientists in the past decade. It is a material structurally characterized as a two-dimensional (2D) sheet of carbon atoms arranged in a hexagonal configuration with atoms bonded by sp^2 bonds. In 2004, Geim, Novoselov and co-workers at the University of Manchester first reported that graphene nanosheets exfoliated from bulk graphite using Scotch tape can stably exist and can be studied for their unique electronic and optical properties.¹ Although an apparently rigid 2D material, graphene is not completely flat, but rather exhibits ripples that even provide the possibility for confining nanoparticles and molecules. In the case of graphene oxide (GO), and its reduced form (reduced graphene oxide, rGO), the structure is even more complicated. Owing to the oxygenated functional groups existing on both the basal planes and at their edges, GO (or rGO) has a hybrid structure comprised of a mixture of sp^2 and sp^3 hybridized carbon atoms.^{2,3}

Several methods have been developed for the preparation of graphene, such as peeling-off graphite, liquid phase exfoliation,⁴⁻⁶ chemical vapour deposition (CVD),⁷⁻⁹ wet-chemical reduction of GO,¹⁰⁻¹² graphitization of silicon carbide,¹³ unzipping of carbon nanotubes,^{14,15} and bottom-up organic synthesis.^{16,17} These methods, all of which produce graphene with different size, shape, chemical composition, and environment, have different requirements for functionalization. Since 2004, graphene has been studied for its potential applications in electronics, energy storage and conversion (*e.g.* supercapacitors, batteries, fuel cells, and solar cells), and bioscience/biotechnologies because of its unique physicochemical properties such as high surface area (theoretically $2630 \text{ m}^2 \text{ g}^{-1}$ for single-layer graphene sheets), excellent thermal and electrical conductivity, and robust mechanical strength.

The mass production of high-quality GO has been achieved by chemical oxidation and exfoliation of low-cost graphite, based on the modified Hummers' method, and a stable suspension of GO can be obtained by ultrasonic treatment of graphite oxide or GO in water, which has therefore become a widely-used precursor for the solution-processing synthesis of graphene based nanomaterials. The abundant hydroxyl and epoxy groups on the basal plane and the carboxyl groups at the sheet edges are normally introduced during the wet-chemical synthesis of GO. These functional groups not only facilitate the

^a Department of Chemistry, Technical University of Denmark, DK-2800, Kongens Lyngby, Denmark. E-mail: cq@kemi.dtu.dk

^b State Key Laboratory for Modification of Chemical Fibers and Polymer Materials, College of Materials Science and Engineering, Donghua University, Shanghai 201620, P. R. China. E-mail: wanghz@dhu.edu.cn

[†] These authors contributed equally to this work.



ELSEVIER

Contents lists available at ScienceDirect

Biosensors and Bioelectronics

journal homepage: www.elsevier.com/locate/bios

Interlocked graphene–Prussian blue hybrid composites enable multifunctional electrochemical applications

Minwei Zhang, Chengyi Hou, Arnab Halder, Jens Ulstrup, Qijin Chi*

Department of Chemistry, Technical University of Denmark, DK-2800 Kongens Lyngby, Denmark

ARTICLE INFO

Article history:

Received 1 December 2015

Received in revised form

13 February 2016

Accepted 16 February 2016

Available online 17 February 2016

Keywords:

One-pot synthesis

Prussian blue

Graphene

Biosensor

Supercapacitor

ABSTRACT

There has been increasing interest recently in mixed-valence inorganic nanostructure functionalized graphene composites, represented by Prussian blue, because they can cost-effectively apply to biosensors and energy devices. In this work, we present a one-pot green method to synthesize interlocked graphene–Prussian Blue hybrid composites as high-performance materials for biosensors and supercapacitor electrodes. Given the fact that graphene oxide (GO) can act as an electron acceptor, we used iron(II) and glucose as co-reducing agents to reduce GO under mild reaction conditions without introducing toxic agents. High quality Prussian blue nanocubes with no or little coordinated water were generated simultaneously. Reduced graphene oxide (rGO) was thus functionalized by Prussian blue nanocubes via chemical bonding to form a kind of interlocked microstructure with high stability and good conductivity. The as-synthesized composites were tested for biosensing of hydrogen peroxide (H₂O₂) and as supercapacitor electrode materials. The specific capacitance of the microcomposite based electrodes can reach 428 F g⁻¹, with good cycling stability. The microcomposite also displays high performance catalysis towards electroreduction of H₂O₂ with a high sensitivity of 1.5 A cm⁻² M⁻¹.

© 2016 Elsevier B.V. All rights reserved.

1. Introduction

Prussian blue (PB), as a non-enzymatic but enzyme mimicking catalyst, has been explored for applications in chemical sensors (Chi and Dong 1995; Liu et al., 2014a, 2014b; Yang et al., 2015a, 2015b; Zhao et al., 2005), biosensors (Arduini et al., 2006; Gao et al., 2014; Sekar et al., 2014; Wang et al., 2014; Zhu et al., 2013), energy devices (Okubo et al., 2010; Pasta et al., 2012) and water quality monitoring (Hao et al., 2015). PB and its analogs are considered as promising energy storage materials, because the theoretical specific capacity of PB can be as high as 170 mA h g⁻¹ (Okubo et al., 2010). In addition, the facile synthetic procedure, nontoxicity and low cost of PB based materials make them have potential favoring for large-scale production and multifunctional applications. However, to date these great potentials have been far from exploitation, as the practically achieved specific capacity of PB is much lower than theoretical expectation. PB also suffers from low Coulombic efficiency and poor cycling stability, which has limited its practical utilization as energy materials. This has largely originated in the poor process used in PB crystal growth, in which coordinated water is hardly avoided and occupies most vacancies of the PB crystal. Moreover, the water-occupied vacancies may

induce a lattice distortion, which dramatically affects specific capacity and Coulombic efficiency, and deteriorates overall electrochemical performances. In most cases, PB prepared by the direct precipitation reaction of the M^{m+} cations and the [M(CN)₆]ⁿ⁻ anions in a neutral aqueous solution always contains a large number of vacancies occupied by coordinated water, because of the fast precipitation process. However, a recent report showed that high-quality PB nanocubes or/and analogs without coordinated water can be synthesized by employing Na₄Fe(CN)₆ as a single iron-source precursor, and the resulting material was tested as cathode electrodes for sodium-ion battery with impressive electrochemical performances (Yang et al., 2015a, 2015b; You et al., 2014). This was achieved by a slow process for growth of PB crystals, so that the number of vacancies occupied by coordinated water is dramatically reduced or even completely eliminated in some cases.

Graphene-based materials have captured great attention among physicists, chemists and materials scientists. Graphene is a two-dimensional (2D) sheet of carbon atoms in a hexagonal configuration connected by sp² bonds. This unique nanostructure holds considerable promise for its potential applications in many technological fields such as nanoelectronics (Berger et al., 2004; Cernetic et al., 2014), sensors (Dong et al., 2012; Li et al., 2014; Song et al., 2010), functional nanocomposites (Klein et al., 2015; Zhang et al., 2010a, 2010b; Zhu et al., 2013), and energy devices (Liu et al., 2014a, 2014b; Wang et al., 2011; Xiong et al., 2015; Xu

* Corresponding author.

E-mail address: cq@kemi.dtu.dk (Q. Chi).

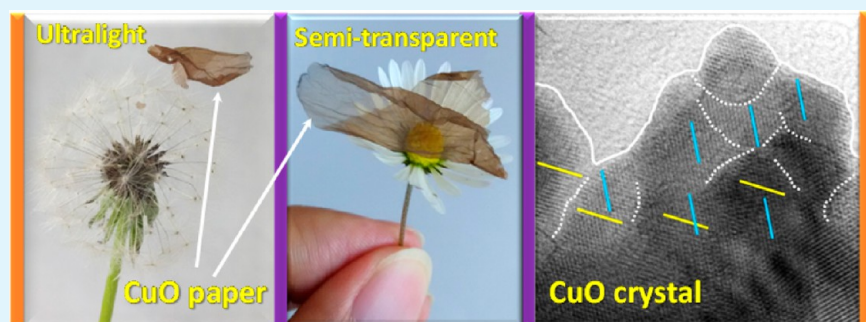
Ultralight, Flexible, and Semi-Transparent Metal Oxide Papers for Photoelectrochemical Water Splitting

Minwei Zhang,^{†,§} Chengyi Hou,^{†,‡,§} Arnab Halder,[†] and Qijin Chi^{*,†}

[†]Department of Chemistry, Technical University of Denmark, DK-2800 Kongens Lyngby, Denmark

[‡]The State Key Laboratory for Modification of Chemical Fibers and Polymer Materials, College of Materials Science and Engineering, Donghua University, Shanghai 201620, China

 Supporting Information



ABSTRACT: Thanks to their versatile functionality, metal oxides (MOs) constitute one of the key family materials in a variety of current demands for sensor, catalysis, energy storage and conversion, optical electronics, and piezoelectric mechanics. Much effort has focused on engineering specific nanostructure and macroscopic morphology of MOs that aims to enhance their performances, but the design and controlled synthesis of ultrafine nanostructured MOs in a cost-effective and facile way remains a challenge. In this work, we have exploited the advantages of intrinsic structures of graphene oxide (GO) papers, serving as a sacrificial template, to design and synthesize two-dimensional (2D) layered and free-standing MO papers with ultrafine nanostructures. Physicochemical characterizations showed that these MO materials are nanostructured, porous, flexible, and ultralight. The as-synthesized materials were tested for their potential application in photoelectrochemical (PEC) energy conversion. In terms of PEC water splitting, copper oxide papers were used as an example and exhibited excellent performances with an extremely high photocurrent-to-weight ratio of $3 \text{ A cm}^{-2} \text{ g}^{-1}$. We have also shown that the synthesis method is generally valid for many earth-abundant transition metals including copper, nickel, iron, cobalt, and manganese.

KEYWORDS: 2D nanomaterial, graphene oxide paper, templated synthesis, ultralight metal oxide, photoelectrochemical water splitting, hydrogen generation

1. INTRODUCTION

Due to their versatile functionality, metal oxides (MOs) have become one of the key family materials for a range of increasing demands from sensor, catalysis, energy storage and conversion, and optical electronics to piezoelectric mechanics.^{1–6} The fact that many transition metals are earth abundant offers advantageous opportunity for scale-up production of MO nanomaterials. It has been noticed that physicochemical properties of MOs, their electronic and optical features in particular, are significantly dependent on grain size and morphology.^{7,8} For example, compared to their bulk materials nanostructured MOs with large surface-to-volume ratio and nanometer grain size can display much enhanced photoelectrochemical performance.^{9,10} The bottom-up assembly of MO nanostructures into a macroscopic form is needed for many practical applications of MO materials.^{11,12} However, nanoscale MO building blocks such as nanoparticles, nanosheets, nanorods, and nanotubes often undergo *densification*

and suffer *significant loss* of specific surface areas during the assembly process. To overcome these critical challenges, recent efforts have focused on the development of controlled assembly methods. For example, Dou and co-workers reported an impressive approach, based on employing lamellar reverse micelle templates, to generalize template-induced self-assembly of scalable two-dimensional (2D) transition MO nanosheets.¹³ Another example was demonstrated by Hwang and co-workers, in which they used graphene nanosheets as a platform for the 2D ordered assembly of TiO_2 nanoparticles.¹⁴ These templating methods have in general inspired other researches to create macroscopic 2D or three-dimensional (3D) MO materials.^{15–19}

Received: November 2, 2016

Accepted: January 10, 2017

Published: January 10, 2017



Free-standing and flexible graphene papers as disposable non-enzymatic electrochemical sensors☆



Minwei Zhang, Arnab Halder, Chengyi Hou, Jens Ulstrup, Qijin Chi *

Department of Chemistry, Technical University of Denmark, DK-2800 Kongens Lyngby, Denmark

ARTICLE INFO

Article history:

Received 11 October 2015

Received in revised form 26 January 2016

Accepted 15 February 2016

Available online 16 February 2016

Keywords:

Graphene paper

Electrochemistry

Disposable sensors

Flexible 2D materials

Electroactive nanoparticles

Core/shell nanoparticles

ABSTRACT

We have explored AuNPs (13 nm) both as a catalyst and as a core for synthesizing water-dispersible and highly stable core-shell structural gold@Prussian blue (Au@PB) nanoparticles (NPs). Systematic characterization by transmission electron microscopy (TEM) and X-ray photoelectron spectroscopy (XPS) disclosed AuNPs coated uniformly by a 5 nm thick PB layer. Au@PB NPs were attached to single-layer graphene oxide (GO) to form Au@PB decorated GO sheets. The resulting hybrid material was filtered layer-by-layer into flexible and free-standing GO paper, which was further converted into conductive reduced GO (RGO)/Au@PB paper via hydrazine vapour reduction. High-resolution TEM images suggested that RGO papers are multiply sandwich-like structures functionalized with core-shell NPs. Resulting sandwich functionalized graphene papers have high conductivity, sufficient flexibility, and robust mechanical strength, which can be cut into free-standing electrodes. Such electrodes, used as non-enzymatic electrochemical sensors, were tested systematically for electrocatalytic sensing of hydrogen peroxide. The high performance was indicated by some of the key parameters, for example the linear H_2O_2 concentration response range (1–30 μM), the detection limit (100 nM), and the high amperometric sensitivity ($5 \text{ A cm}^{-2} \text{ M}^{-1}$). With the advantages of low cost and scalable production capacity, such graphene supported functional papers are of particular interest in the use as flexible disposable sensors.

© 2016 Elsevier B.V. All rights reserved.

1. Introduction

Two-dimensional (2D) graphene films, membranes or papers derived from graphene oxide (GO), reduced graphene oxide (RGO) or pristine graphene have attracted significant interest in a wide range of fields from physics, materials science, and sensors to environmental engineering. This is because such materials not only retain the core properties of individual graphene sheets, but also add collective properties or/and synergistic functionality resulting from purpose-driven assembly or/and functional doping with desirable components. The advantages of low mass density, supraflexibility, large surface area, tough mechanical strength, and high electrical conductivity make graphene-derived composite materials hold great promise to meet a number of requirements in modern technologies, especially graphene supported materials for electrochemical sensing applications [1–4].

Several techniques have been explored in the preparation of graphene papers. These include vacuum filtration of GO or RGO solutions [5,6], layer-by-layer (LBL) assembly [7,8], two-phase induced interfacial self-assembly [9,10], spin coating [11,12], electrophoretic deposition (EPD) [13,14], and chemical vapour deposition (CVD) [15,16]. Each method has its own advantages and shortcomings. Vacuum filtration is a simple and effective way to prepare pure or functionalized GO papers, which

can be transformed into conductive RGO papers, with low cost and ease of operation, although the procedure is time-consuming in some cases. Individual GO nanosheets tend to interact increasingly under the vacuum pressure towards self-assembly into multilayer membranes or paper, in which the nanosheets are connected via multiple interactions including π - π stacking, hydrogen bonding, ionic electrostatic attraction, and hydrophobic interaction.

Different materials have been exploited to endow graphene nanosheets or papers with specific functionality. The materials include polymers (PEI [17], PDDA [18], PANi [19] and PVDF [20]), and inorganic nanostructures (Au NPs [21], Ag NPs [22], Pt NPs [23], Au@Pt NPs [24], NiO or Ni(OH)₂ [14,25], V₂O₅ [26], Co₃O₄ [27], ZnO [28], TiO₂ [29] and Fe₃O₄ [30]). With high conductivity and mechanical strength, graphene paper can be used as free-standing electrodes for sensors or energy devices. Especially, graphene papers functionalized with metal nanoparticles, polymers or biomolecules are promising candidates for bioelectrochemical applications such as electrochemical biosensors and biofuel cells. For example, PtNPs/MnO₂ nanowire/graphene paper has been used as a free-standing electrode for detection of H₂O₂ [23]. Glucose sensors have been constructed in different ways based on PANi/AuNPs/graphene film-GOD composites (GOD = glucose oxidase) [31]. The resulting sensors have been used in the determination of glucose concentration in blood samples in the physiological range of 3.9–7.8 mM. Graphene paper electrodes decorated with gold nanoparticles have also been used as low-cost and robust impedimetric

☆ This is a part of Special Issue BES2015.

* Corresponding author.

E-mail address: cq@kemi.dtu.dk (Q. Chi).

Reagent-Free Synthesis and Plasmonic Antioxidation of Unique Nanostructured Metal–Metal Oxide Core–Shell Microfibers

Chengyi Hou, Minwei Zhang, Takeshi Kasama, Christian Engelbrekt, Lili Zhang, Hongzhi Wang,* and Qijin Chi*

Sunlight and dioxygen are two of the essential elements for life sustainability on Earth. In the evolution of modern science and technology, researchers have a long-standing interest in how to use earth-abundant materials such as metals and their oxides to store solar energy, to convert it, and even to produce dioxygen via biomimicking artificial photosynthesis. Efficient exploitation of these natural sources has become increasingly in demand for human survival and sustainable development, arising from current energy and environmental concerns. On the other hand, sunlight and dioxygen could invoke negative effects under certain circumstances. For example, random oxidation (or corrosion) of metals and degradation of metal oxides upon their exposure to sunlight and air have caused huge economic losses every year.^[1–3] Undesirable oxidation of active nanomaterials has also limited their use for many commercially important energy systems.^[4–8] Several strategies have been attempted to prevent active materials from oxidation, mainly by introducing protective coatings,^[9–11] such as inert atoms,^[12] polymers,^[13] and more recently graphene-based materials.^[14] However, the native functionality of such materials would be hindered by coated layers. Self-protection of active materials from oxygen or/and sunlight is thus highly desired, when operating in such environments, but it seems to be an unnatural event and has been rarely achieved.

Very recently, visible-light induced switching of the oxidation states of metal (oxide) was reported by Linic and co-workers.^[15] Although the mechanisms have not been fully understood, they believed that localized surface plasmon resonance (LSPR)-mediated energy transfer is a key reason for the observed phenomenon. This finding might inspire the development of new

ways toward achieving self-protection for active materials. In the presence of light, the random oxidization of active materials is generally accelerated.^[16–18] However, it was found that core–shell nanostructured materials containing a plasmonic core (e.g., Au, Ag, or Cu)^[19] and a metal (oxide) shell could undergo the opposite process, i.e., LSPR-mediated chemical reduction or decomposition of shell upon specific light irradiation.^[15] Such observations are obviously counter-intuitive and would inspire new research. It is noted that their experiments were performed in a nonoxygen environment.^[15] We have thus raised the question: can the LSPR-mediated photoswitching effect be efficient enough to prevent oxidation of active metals or oxides under oxygen and sunlight conditions? This question has yet to be answered and has motivated the present work.

We have first developed a new method to synthesize active core–shell microfibers, consisting of a core of copper nanoparticles and a shell of cuprous oxide nanowires (**Figure 1**). Such a unique structure is proven special and the key to study LSPR-mediated antioxidation effects. We show that this novel kind of heterostructural microfiber can be prepared in pure water via simultaneous anodic electrolysis and a direct current (DC) electrophoretic assembly. Secondly, we find that the resultant copper-oxide fibers are surprisingly stable in oxygen-containing aqueous solution upon simulated solar irradiation. In contrast, copper/cuprous oxide mixtures without such an organized structure are oxidized rapidly under the same conditions. Finally, all experimental evidence points to LSPR-mediated antioxidation being responsible for this unusual phenomenon and material stability. The as-designed core–shell microfibers could become a promising new catalyst for durable photocatalytic applications.

To probe LSPR-mediated oxidation protection effects, we use three key criteria to design the active fiber: (1) its core/shell structure should be actively responsive to oxygen, and at least one of the components is plasmonic, (2) the nanocomposite must have an open structure so that both core and shell components can interact with an oxygen-containing environment (the inset in **Figure 1**), and (3) the use of chemical reagents in the synthesis should be avoided or minimized in order to rule out side effects from surface coating, for example by surfactants or polymers. The first requirement is satisfied by using copper foil with high purity as a starting material. To meet the other two criteria, we have developed a reagent-free method to synthesize a unique kind of nanoparticle–nanowire core–shell structures in pure water.

There are a number of solution-processed methods developed for preparing metal (oxide) nanomaterials.^[20–23] However, most

Dr. C. Hou, Dr. M. Zhang, Dr. C. Engelbrekt,
Prof. Q. Chi

Department of Chemistry
Technical University of Denmark
DK-2800, Kongens Lyngby, Denmark
E-mail: cq@kemi.dtu.dk

Dr. T. Kasama, Dr. L. Zhang
Center for Electron Nanoscopy
Technical University of Denmark
DK-2800, Kongens Lyngby, Denmark

Dr. C. Hou, Prof. H. Wang
State Key Laboratory for Modification of Chemical Fibers and Polymer
Materials, College of Materials Science and Engineering
Donghua University
Shanghai 201620, P. R. China
E-mail: wanghz@dhu.edu.cn



DOI: 10.1002/adma.201505990

Reagent-Free Electrophoretic Synthesis of Few-Atom-Thick Metal Oxide Nanosheets

Chengyi Hou,^{*,†,‡} Minwei Zhang,^{‡,§} Lili Zhang,[§] Yingying Tang,[‡] Hongzhi Wang,[†] and Qijin Chi^{*,‡,§}

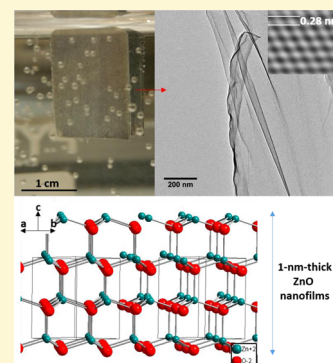
[†]State Key Laboratory for Modification of Chemical Fibers and Polymer Materials, College of Materials Science and Engineering, Donghua University, Shanghai 201620, People's Republic of China

[‡]Department of Chemistry, Technical University of Denmark, DK-2800 Kongens Lyngby, Denmark

[§]Center for Electron Nanoscopy, Technical University of Denmark, DK-2800 Kongens Lyngby, Denmark

S Supporting Information

ABSTRACT: Engineering traditional materials into the new form of atomic and free-standing two-dimensional structures is of both fundamental interest and practical significance, but it is in general facing challenges especially for metal oxide semiconductors. We herein report an ultragreen method for the cost-effective and fast preparation of atomic metal oxide nanosheets that can be further transformed into nanofilms. The method combines top-down building block synthesis and bottom-up electrophoretic assembly in water under ambient conditions, using only bulk metal and Milli-Q water without involving any additional reagents. The focus is on free-standing polycrystalline ZnO nanosheets that can be produced with a lateral dimension as large as 10 μm and a thickness of 1 nm (the thinnest free-standing metal oxide nanosheet ever reported). A new electrophoretic assembly mechanism dominated by intrinsic surface polarity was revealed. We also demonstrate potential applications of this approach for wet electronic systems as exemplified by facile and in situ fabrication of dielectric layers and cellular electrets.



INTRODUCTION

Two-dimensional (2D) nanomaterials have exhibited unique electronic and optical properties because of their quantum well band structure and large surface exposure.^{1–3} The recent rise of 2D nanomaterials, represented by graphene,⁴ phosphorene,⁵ MXene,⁶ hexagonal boron nitride (h-BN),⁷ and MoS₂,⁸ has offered emerging opportunities for the development of new-generation electronic and photonic technologies. The recent explosive development of these 2D nanomaterials has become feasible because of some facile and high-quality synthesis methods employed such as mechanical and liquid exfoliation, which is facilitated by the intrinsic 2D layered structures of starting materials.^{9–11} Other synthesis methods, including high-temperature (chemical vapor deposition¹² and thermal expansion¹³) and wet chemical (redox, solvothermal, or colloidal growth reactions^{14–16}) processes, have also been developed because of their capability of scaling up production, but they have suffered from some disadvantages. For example, in most cases, (1) strict reaction conditions and environmentally unfriendly reagents are needed for synthesis, (2) processes are rather complicated and costly, and (3) byproducts are usually generated in addition to the target product.

In spite of the drawbacks mentioned above, these existing methods would continue to play important roles in the synthesis of a novel class of 2D atomic nanomaterials that are intrinsically non-2D in their conventional crystal structure. The definition of 2D in these cases is that the materials can be isolated as free-standing few-atom-thick layers. This non-natural free-standing 2D form of traditional materials has attracted a

growing amount of attention because such a structure could exhibit unexpected and/or unpredictable new physicochemical properties. For instance, 2D polymers (also known as monolayers of molecular plywood), organic frameworks, and metal–organic frameworks have shown promising advantages for their application in the fields of molecular electronics, photoelectronics, and electrocatalysis.^{17–20} Free-standing 2D metals, including Pd,²¹ Ru,²² Au,²³ and Fe²⁴ nanosheets, have also been reported to be highly chemically active. Atomic metal oxide nanosheets have exhibited unusual energy band structure and outstanding electrochemical performance.^{25–28}

However, critical reaction conditions or chemical templates are often required to break materials' three-dimensional (3D) symmetry and foster anisotropy in 2D growth. In general, the facile and green synthesis of 2D atomic nanomaterials from nonlayered starting materials remains a challenge. The challenges are especially notable for metal oxide (MO) semiconductors that are functionally versatile and particularly important for electronics and photonics, because the lateral expansion of MO atomic nanosheets is highly restricted because of unfavorable energetic kinetics. The development of novel synthetic strategies toward efficient, simple, eco-friendly, and large-scale synthesis of such non-natural structures is highly desirable.

On the basis of alternative working principles, in this work, we have demonstrated an effective approach to the synthesis of

Received: January 15, 2017

Published: January 19, 2017